Very High Energy Gamma-Rays from Binary Systems

DICKINSON, HUGH,JOHN

Very High Energy Gamma-Rays from Binary Systems

by

Hugh John Dickinson

Submitted in conformity with the requirements

for the degree of Doctor of Philosophy

Department of Physics

University of Durham

United kingdom

Abstract

This thesis presents a study of the very high energy (VHE) γ-ray emission from X-ray binary systems using the H.E.S.S. imaging atmospheric Cherenkov array.

The historical background and basic principles of ground-based γ-ray astronomy are briefly reviewed and an overview of the design and capabilities of the H.E.S.S. telescope system is presented. The broadband observational properties of X-ray binary systems and their relevance in a broader astrophysical context is also discussed.

A review of the radiative emission mechanisms which relate to VHE γ-ray emission in X-ray binaries is presented, with emphasis given to the leptonic emission processes of synchrotron radiation and inverse-Compton scattering. Intrinsic absorption processes which act to attenuate the emitted flux of VHE γ-rays are also discussed. Three computer models are introduced which simulate aspects of the γ-ray emission and absorption in X-ray binary systems.

A detailed analysis of the VHE γ-ray emission from the X-ray binary LS 5039 is presented and the relevant procedures for data selection, γ-hadron separation and background estimation are discussed in some detail. Methods for the determination of detection significance and the calculation of γ-ray fluxes are also reviewed and results are derived which apply specifically to LS 5039. A detailed temporal analysis of the γ-ray signal from LS 5039 is presented, applying tests for secular, excess and periodic variability. Strong evidence is found for modulation of the observed γ-ray flux on the orbital period of $\sim$ 3.9 days. Following a brief discussion of the procedures required for spectral analysis of VHE γ-ray data, results are presented for LS 5039 which reveal evidence for spectral variability which is correlated with the observed γ-ray flux and therefore, the orbital phase of the binary system. The spectral and temporal characteristics of LS 5039 are then compared with the predictions of theoretical models in an attempt to explain the observed behaviour.

Contemporaneous X-ray and VHE γ-ray observations of three galactic microquasars using the *Rossi X-ray Timing Explorer* and H.E.S.S. are presented. Although no γ-ray detections are reported, the observations permit the derivation of upper limits to the VHE γ-ray flux which correspond to episodes of known X-ray behaviour. The X-ray characteristics of each target are compared with pre-existing observational data to infer the presence or otherwise of relativistic outflows at the H.E.S.S. observation epochs. The implications of the γ-ray non-detections are then discussed in the context of these inferred system properties.

The results of a survey of the VHE γ-ray emission associated with the positions of 125 known X-ray binaries are presented. Although no conclusive detections were obtained, tentative indications were found for a population of faint, spectrally hard γ-ray sources associated with high-mass X-ray binary systems. The inferred characteristics of the indicated population show broad agreement with the measured properties of known γ-ray-emitting X-ray binary systems like LS 5039.

Contents

Declaration

The material contained within this thesis has not previously been submitted for a degree at Durham University or any other university. The research reported within this thesis has been conducted by the author unless indicated otherwise.

Copyright Notice

Acknowledgements

The research presented in this thesis could not have been completed without the assistance and encouragement of numerous colleagues, friends and family members.

I am indebted to the members of the VHE γ-ray astronomy group at the University of Durham who generously gave their time, wisdom and experience. In particular, I thank Dr John Osborne and Dr Paula Chadwick for the patient and conscientious supervision they provided. Special thanks should also go to Dr Michael Daniel, whose seemingly encyclopaedic knowledge of VHE γ-ray astronomy proved invaluable during the somewhat desperate rush to submission!

Away from the office, I have been fortunate enough to enjoy the support and camaraderie of many friends who both enriched and enlightened the years I spent in Durham. I thank Dr Christos Hadjichristidis for his humbling generosity and for his friendly and open advice, which provided much needed reassurance during the inevitable moments of self doubt. Thanks also to Dr Ian Latham, whose formidable scientific insight was a profound influence upon the ultimate focus of my research and who miraculously kept a roof over my head as my projected completion date stubbornly refused to arrive. I would be unforgivably remiss if I failed to acknowledge the influence of my good friend, Dr Matthew Middleton. An outstanding scientist with a singular wit, Matthew is never too busy to help, and his enthusiasm for all aspects of life is infectious. An inspiring team mate, a dependable ally, and an honourable gentleman, I am privileged to call him my friend.

I am extremely grateful for continual and ongoing support and encouragement from my brother Owen Dickinson and my father John Dickinson. My sincere thanks to you both. This thesis would not exist without you.

Above all, this thesis is a tribute to my mother, Sara Dickinson, whose impeccable example sustained and motivated me when the prospect of success seemed like a distant memory or an unachievable goal. She taught me to believe in myself, never give up, and never settle for second best. She will always be my greatest inspiration.

Chapter 1

Introduction

1.1 Cosmic Rays

Ultimately, VHE γ-ray astronomy owes its existence to a discovery made by Victor Hess in 1912 [122]. Noting that balloon-borne electroscopes discharged more rapidly at higher altitudes, he deduced that the Earth was being bombarded by charged particles from outer space. We now recognize that these *cosmic rays* represent the remnants of some of the most energetic processes in the Universe.

The flux of cosmic rays we observe is dominated by protons and heavier nuclei, with only $\sim 2\%$ accounted for by electrons and 'exotic' particles. Of the remaining hadronic component almost 87% are protons, with elements such as helium, carbon and iron also contributing [163]. To first order, the cosmic ray spectrum is a power law ($dN(E)/dE \propto E^{-2.8}$) (Figure 1.1). It spans many decades of energy from a relatively innocuous 10^8eV up to the famous 'oh-my-god' particle, a proton with an energy of 3.2×10^{20}eV [235]. It displays two well known features, the *knee* and *ankle*, which are manifested as abrupt changes in spectral slope and variations in particle composition.

The knee is a slight steepening of the spectrum at $\sim 10^{16}$eV and is accompanied by a significant increase in the measured proportion of heavy nuclei. The origin of the knee is a subject of much debate, however a popular interpretation is that it represents the energy of those particles whose

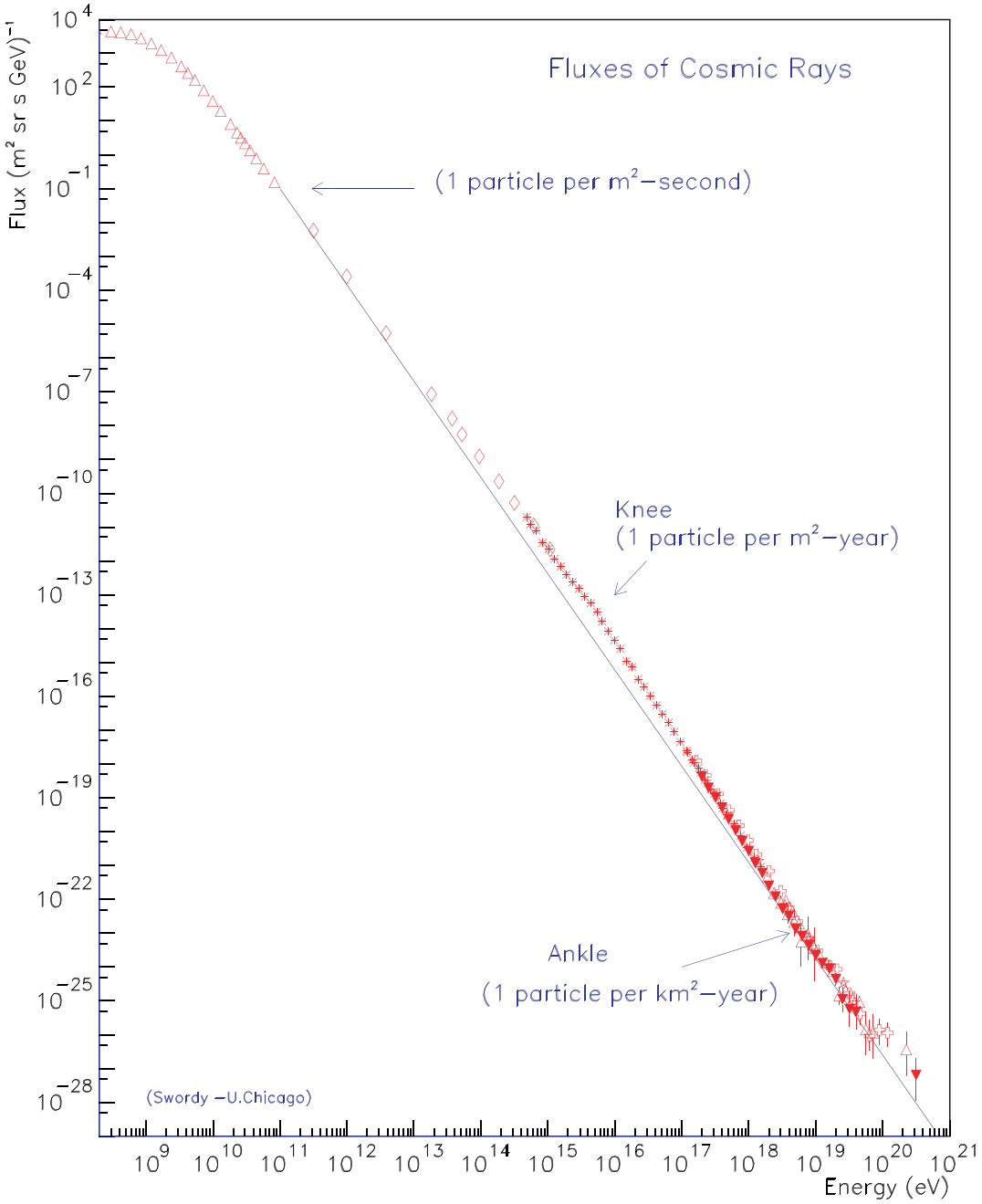

Figure 1.1: The cosmic ray spectrum [70]

gyroradii in the galactic magnetic field are too large for confinement. This would allow these cosmic rays to leak out of the Milky Way leading to the observed fall off in particle numbers [129].

The ankle in the cosmic ray spectrum occurs at $\sim 10^{18}$eV. This hardening of the spectral index is thought to indicate the transition between cosmic rays with galactic origin, and those produced at larger distances. At particle energies above $\sim$ 2 EeV, recent measurements using the Pierre Auger observatory [31], e.g. indicate an increasing proportion of heavy nuclei in the observed cosmic ray flux. The mechanisms responsible for the acceleration of these ultra-high energy cosmic rays remain a subject of continued active research [190].

1.2 Very High Energy γ-ray Astronomy

As charged particles, cosmic rays are subject to deflection by the galactic magnetic field. The gyroradius (or Larmor radius) of a relativistic proton with energy E moving in a magnetic field B is given by [163]

$$r_g \approx \frac{1}{3}\left(\frac{E}{1\text{ eV}}\right)\left(\frac{B}{10^{-9}\text{ T}}\right)^{-1} \quad \text{m.} \tag{1.1}$$

The average magnetic field of the Milky Way can be estimated via radio mapping of synchrotron radiation and is $\sim 10^{-9}$ T. Therefore, the physical extent of the galaxy ($\sim 10^{19}$m) implies that only the most energetic cosmic rays detected are likely to retain directional information regarding their point of origin [196]. Unfortunately, as Figure 1.1 clearly illustrates, the extremely low flux of these ultra high energy cosmic rays provides insufficient statistics for most directional analyses. Being unable to associate the observed (approximately isotropic) flux of cosmic rays with specific astrophysical objects is a serious hinderance. It forbids the incorporation of cosmic ray data into our picture of celestial phenomena which can be localised at other wavelengths and denies the insight which invariably arises when several avenues of investigation are combined.

Luckily, cosmic rays are not the sole products of the events which accelerate them. Indeed, the cataclysmic events capable of producing 10^8 TeV protons are thought to be powerful sources of electromagnetic radiation, neutrinos, and in some cases, gravitational waves. With currently

available detector technology, only the γ-ray emission component offers a viable insight into the highest energy processes involved.

Very High Energy (VHE) γ-ray astronomy is the study of photons with energies in excess of $\sim$ 100GeV. With zero electrical charge, γ-rays are able to travel directly from their source to the observer unaffected by magnetic fields. In environments harbouring particle acceleration on the scale of that to which cosmic rays are subjected, it is widely accepted that VHE γ-ray emission must take place. Consequently, observations in the 0.1-10 TeV band have the potential to unravel many enigmas which still surround the production of cosmic rays.

As a science only now coming of age, VHE γ-ray astronomy is becoming an invaluable probe of the most extreme regions in the Universe. The prototypical TeV source is the Crab nebula [90] and indeed, supernova remnants like the Crab are prime candidates for the source of the galactic cosmic ray flux. However, the catalogue of confirmed VHE sources is growing rapidly, with AGNs [16], X-ray binaries [18], and a number of as yet unidentified sources joining the increasing number supernova remnants detected in recent years [15, 17]. VHE γ-ray astronomy now stands alone from the search for cosmic ray emitters to which it owes its origins. It is a valuable tool which augments numerous separate multi-wavelength observational data and deepens our understanding of many physical processes at work in the Universe.

1.3 Ground Based VHE γ-ray Astronomy

Although satellite based experiments such as *Fermi* and *INTEGRAL* are capable of detecting photons in the TeV range, the extremely low photon fluxes at these energies require prohibitively large collection areas or integration times. In contrast, ground-based γ-ray telescopes utilise the Earth's atmosphere as a detection medium, resulting in an extremely large effective collection area. These ground-based systems do not detect the incident γ-rays directly, but rely upon Cherenkov radiation from showers of energetic particles produced when the a TeV photon strikes the atmosphere.

1.3.1 Cherenkov Radiation

Cherenkov radiation [56] occurs when a charged particle moving in some dielectric medium exceeds phase velocity ($v_p = c/n$, where $n > 1$ is the refractive index) of light in that medium.

Radiation from a point charge is characterised by the Poynting vector

$$\mathbf{S} = (c/4\pi)\mathbf{E} \times \mathbf{H}. \tag{1.2}$$

Its integral over some surface Σ is equal to the total energy flowing out of the volume enclosed by that surface.

$$\frac{dU}{dt} = \int_{\Sigma} \mathbf{S} \cdot d\mathbf{A} \tag{1.3}$$

The Liénard-Wiechart potentials ϕ and $\mathbf{A}$ describe respectively scalar and vector components of the electromagnetic fields a distance R from some relativistically moving charge q.

$$\phi = \left[\frac{q}{\kappa R}\right] \tag{1.4a}$$

$$\mathbf{A} = \left[\frac{q\mathbf{v}}{c\kappa R}\right] \tag{1.4b}$$

$$\kappa = 1 - \beta\cos\theta \tag{1.4c}$$

We define $\beta = |\mathbf{v}|/c$ and theta is the angle between the particle's velocity and the radius vector $\mathbf{R}$. Quantities inside the square brackets are evaluated such that

$$[Q] = Q(\mathbf{r}', t - \frac{1}{c}(\mathbf{r} - \mathbf{r}')). \tag{1.5}$$

This means the electromagnetic field at $\mathbf{r}$ at time t depends uniquely on the particle's behaviour at time $t' = (\mathbf{r} - \mathbf{r}')/c$ when it was at position $\mathbf{r}'$, since the information cannot have propagated a longer or shorter distance than that travelled by light in the time $t - t'$.

A particle which moves uniformly in a vacuum cannot radiate. To see this, consider the electric and magnetic fields at some distance R from the charge. These are found by differentiating the

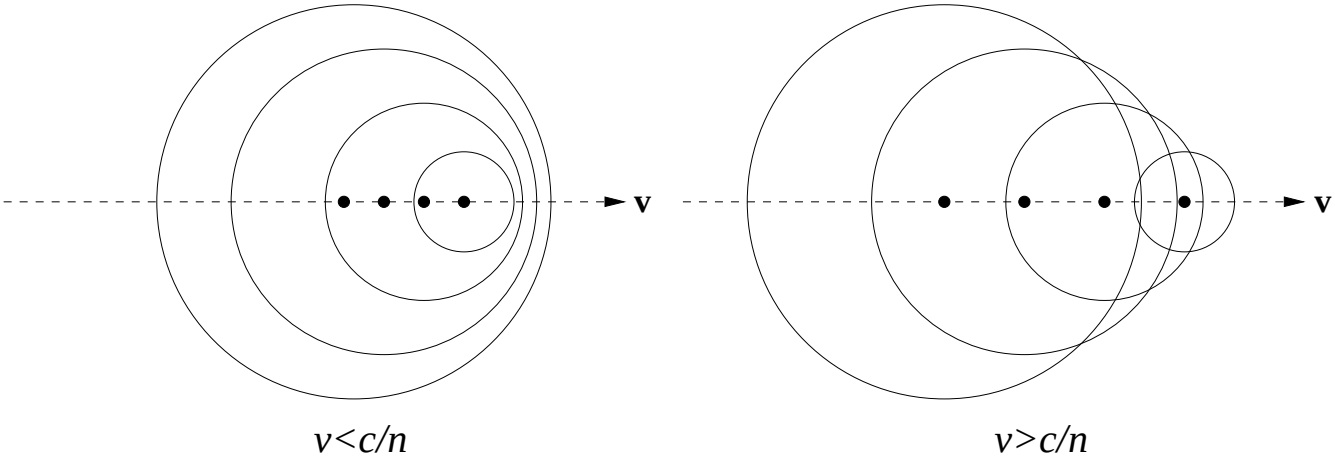

Figure 1.2: The Cherenkov cone. When a particle moves in some medium with a velocity greater than the phase velocity of light in that medium (right), the radiation from that particle is contained within a cone.

Liénard-Wiechart potentials (1.4). By inspection we see that if $\dot{\mathbf{u}} = 0$ then the field strengths

$$E, B \propto R^{-2} \tag{1.6}$$

This makes the integral (1.3) go to zero at large distances, since the surface area increases as R^2 while $\mathbf{S}$ decreases like R^{-4}, making the transfer of energy over long distances impossible.

In a dielectric however, (1.4c) is modified by the refractive index of the medium n, such that

$$\kappa = 1 - \beta n \cos\theta \tag{1.7}$$

Now, when $\cos\theta = (\beta n)^{-1}$, $\kappa \to 0$ and the field strengths E and B become infinite, allowing the charge to radiate.

Figure 1.2 illustrates the formation of the Cherenkov cone. Each point within the cone can now be influenced by the particle's behaviour at more than one position and time in the the past. The observed radiation front moves normally to the surface of the cone, the opening angle of which ψ, is defined by

$$\psi = \cos^{-1}\left(\frac{1}{\beta n}\right) \tag{1.8}$$

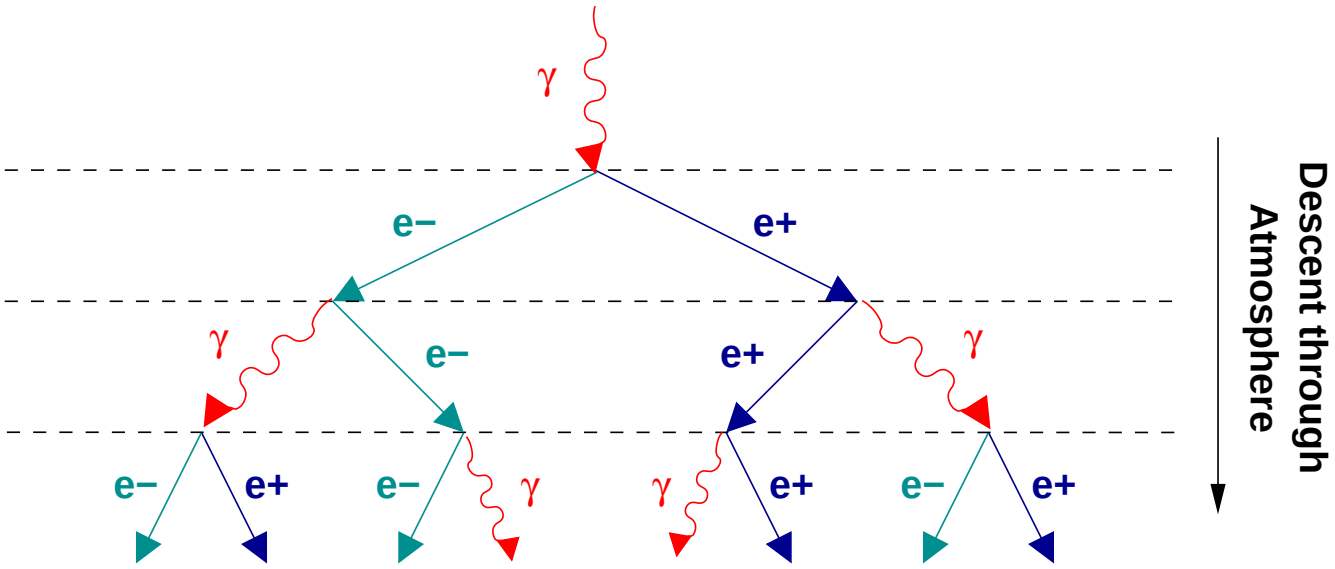

Figure 1.3: Schematic representation showing the formation of an extensive air-shower

In general, charged particles moving superluminally in the atmosphere emit Cherenkov light with a spectrum that peaks at the near-ultraviolet wavelengths. Pulses from individual particles are extremely faint and short-lived, but nonetheless measurable. The combined radiation from many emitting particles, though still too rapid to be visible to the eye, is comparatively straightforward to detect [See e.g. 218, 164].

1.3.2 Extensive Air-Showers

When a VHE γ-ray is incident upon the top of the atmosphere it can interact with the Coulomb field of an atom producing an electron-positron pair. This may then initiate a cascade or Extensive Air-Shower (EAS) of electrons, positrons and γ-rays (See Figure 1.3). Due to the extremely energetic nature of the progenitor photon, the charged particles in the shower move superluminally in the atmosphere and hence emit Cherenkov radiation as they descend. The shower propagates because for electrons and positrons created with energies > 84MeV, the dominant energy loss mechanism is through Bremsstrahlung, which produces more high-energy γ-rays to pair produce. The altitude at which the shower initiates depends upon the energy of the incident photon, with more energetic γ-rays penetrating further on average. The number of particles in the shower will eventually reach

a maximum of $\sim 10^5$ e^+, e^- pairs, before decaying away as energy losses prohibit further particle creation. If the initial γ-ray energy $\lesssim 20$ TeV, the shower decays before reaching the ground and only the emitted Cherenkov radiation transmits information about the progenitor to the observer.

1.3.3 γ-Hadron Separation

Unfortunately for VHE γ-ray astronomers, it is not only γ-ray photons that are capable of producing extensive air-showers. As mentioned in §1.1, the Earth is subject to constant bombardment from cosmic rays. These hadronic particles also carry charge and can be hugely energetic, producing Cherenkov-emitting cascades of their own. In fact, the Cherenkov light produced by the cosmic ray flux swamps the γ-ray signal, requiring some ingenuity to extract useful data from such a noisy background. Luckily, there are several properties of an EAS which differ according to the progenitor particle type, and several techniques have been developed which discard over $\gtrsim 99\%$ of the background while retaining $\sim$50% of the true signal [36].

Figure 1.4 illustrates the marked difference between a purely electromagnetic air-shower initiated by a VHE γ-ray and that produced by a hadronic progenitor. While the electromagnetic shower remains tightly confined as it descends, strong decays produce pions with large transverse momenta, leading to a more ragged, spread out particle distribution. Figure 1.5 illustrates how the contrasting modes of shower evolution lead to a discernible difference in the emitted Cherenkov light pools when they reach the ground.

1.3.4 The Imaging Atmospheric Cherenkov Technique

Indirect detection of high energy particles and photons via observation of the Cherenkov radiation from the air-showers they produce is known as the Atmospheric Cherenkov Technique (ACT). In order to effectively discriminate between hadronic and pure electromagnetic showers, an image of their light pools on the ground is required. This mapping of the distribution of Cherenkov radiation forms the basis of the Imaging Atmospheric Cherenkov Technique (IACT), and plays a large part in achieving the $\gtrsim 99\%$ background rejection seen in modern VHE γ-ray telescopes.

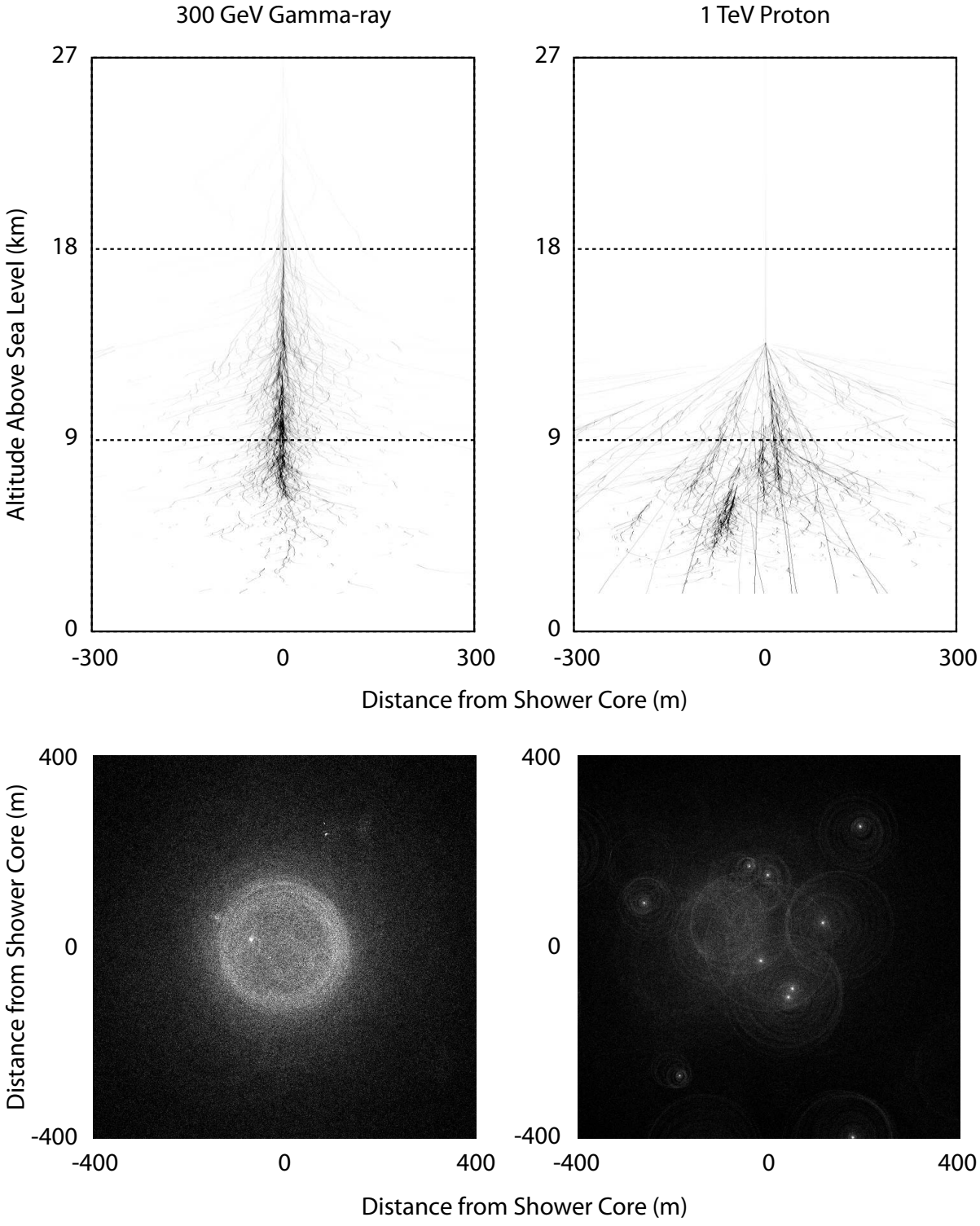

Figure 1.4: Electromagnetic (left) and hadronic (right) extensive air-showers. The lateral spread of the hadronic shower is due to the transverse momentum afforded to pions in strong interactions (Courtesy of Konrad Bernlöhr).

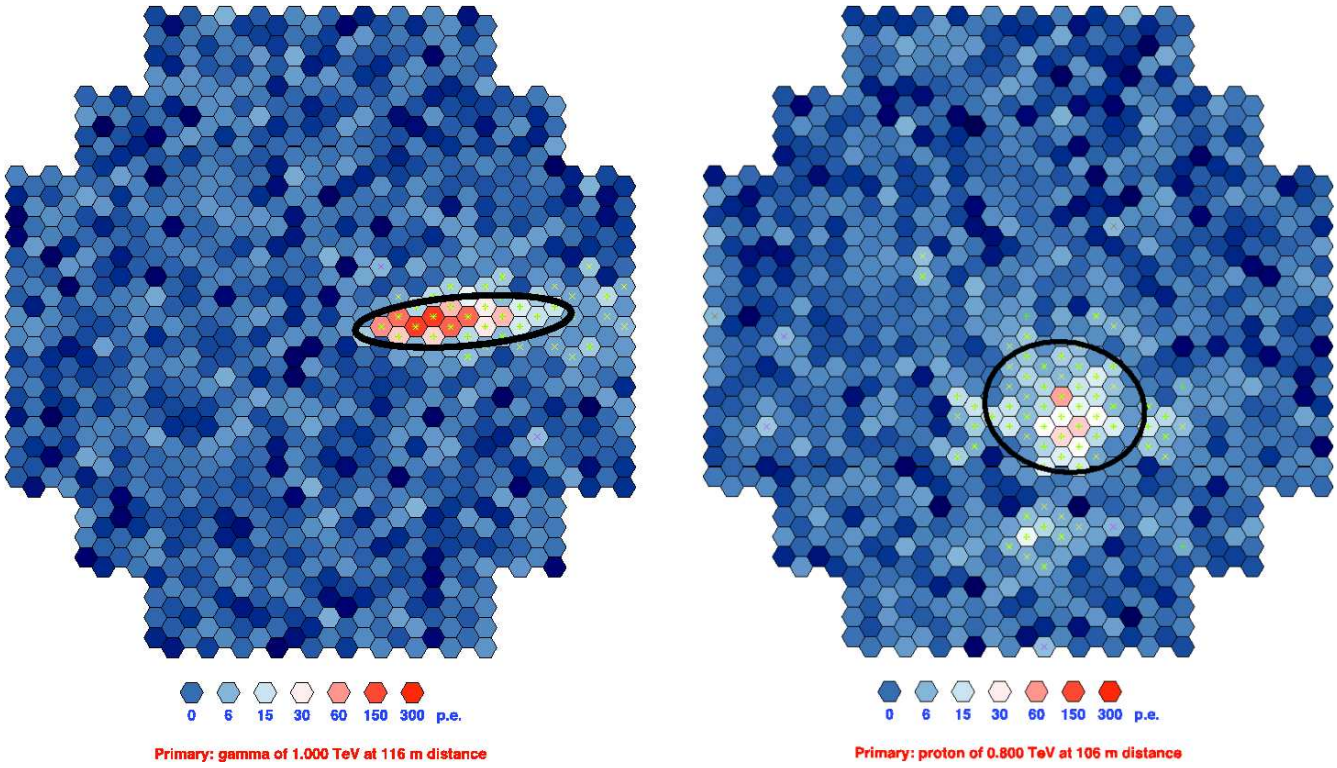

Figure 1.5: Illustration of the marked disparity between the Cherenkov images resulting from γ-ray initiated air showers (left), and those resulting from hadronic air showers (right).

Each γ-ray-initiated air-shower produces a roughly elliptical Cherenkov footprint at ground level. The precise configuration of this footprint is extremely useful in ascertaining the nature of the progenitor particle. The collimated electromagnetic showers produced by γ-ray showers produce a correspondingly compact light pool. Indeed, for the same primary energy, the radiation generated by the more disorganised hadron showers is up to three times weaker than for γ-ray initiated cascades [91].

Another observable characteristic of electromagnetic air showers is the phenomenon of annular focussing. The refractive index of the air increases with decreasing altitude, due to an increase in ambient density. The implied consequence of this (from (1.8)) is a widening of Cherenkov cone opening angle. Figure 1.6 demonstrates how this leads to a clearly observable ring structure in the lateral density function of the detected Cherenkov light. In contrast, the profiles measured from hadronic showers show no such pattern, since the effect is washed out by the lateral inconsistency of the shower itself.

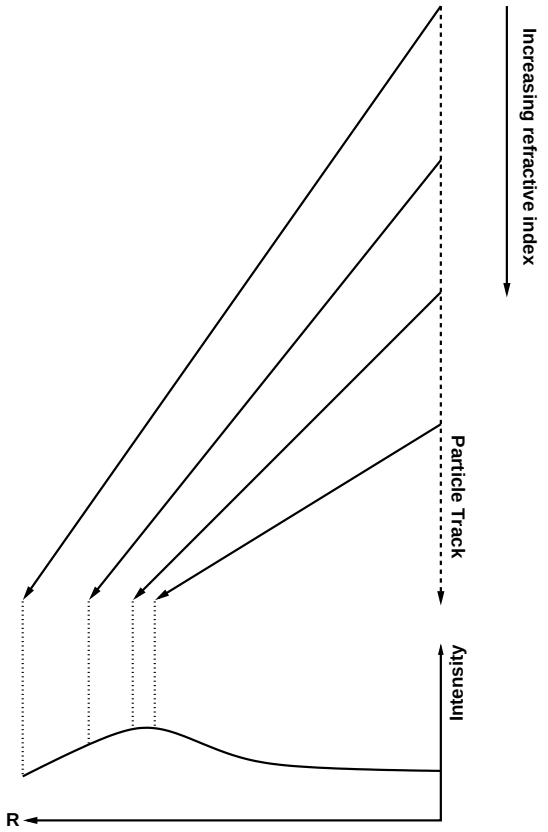

Figure 1.6: Annular focussing. The gradual increase in atmospheric refractive index as the air-shower descends concentrates the Cherenkov emission into a ring in electromagnetic showers.

1.3.5 The Hillas Parameters

Computer based discrimination between the Cherenkov images produced by hadronic and electromagnetic air-showers requires a parameterisation of the image properties. Through repeated Monte Carlo simulation of air shower development and the propagation of Cherenkov radiation, expected parameter ranges for each progenitor type may be defined. Selected parameter cuts may then be imposed on the observed shower images, with the aim of rejecting those showers which do not conform to γ-ray predictions.

The analyses described in this thesis utilise an image parameterisation scheme based on the second moments of the Cherenkov image [124]. Figure 1.7 demonstrates how these *Hillas parameters* are employed in the parametrisation of an elliptical image while their mathematical formulation is outlined in Appendix C. Figure 1.8 illustrates how the simulated probability distributions for

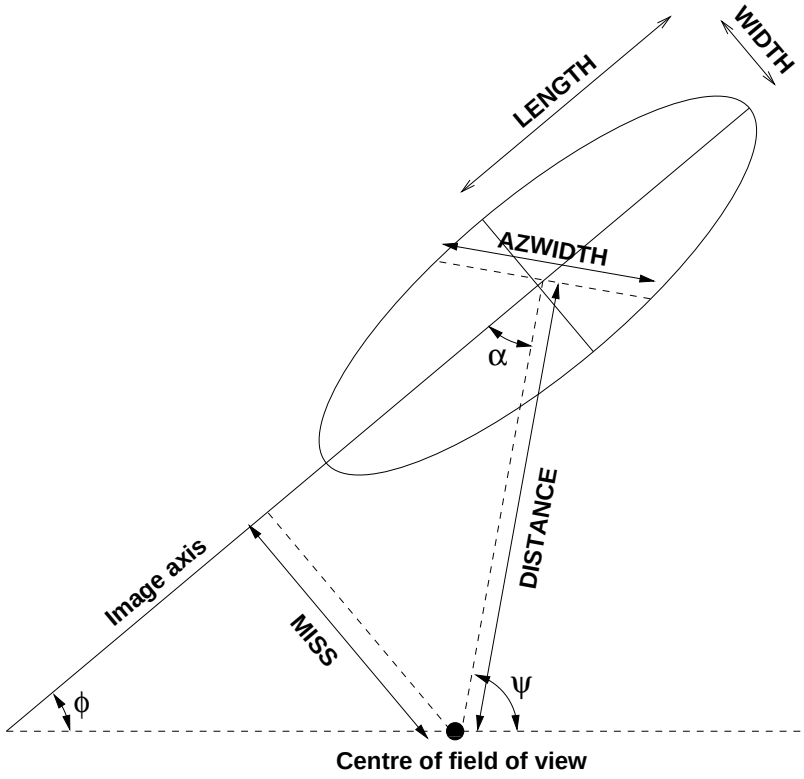

Figure 1.7: The Hillas parameters.

selected Hillas parameters vary for different progenitors. Evidently, the comparatively compact nature of the γ-ray showers makes the disparities between parameter distributions significant enough to allow effective rejection of unwanted events while retaining a large proportion of real detections [247].

1.3.6 Stereoscopic Techniques and Shower Reconstruction

Image analysis techniques have been shown successful in discriminating between the two main air-shower types. However, the technique is lacking in two areas. Firstly, false Cherenkov flashes can be produced by local superluminal particles such as muons produced by pion decays in the atmosphere. These signals, although intrinsically much weaker than the desired signal, are produced far nearer and in some cases closely resemble γ-ray initiated air-showers. Secondly, determining the point of origin of the air shower, and hence the progentitor γ-ray, is particularly difficult using a single telescope.

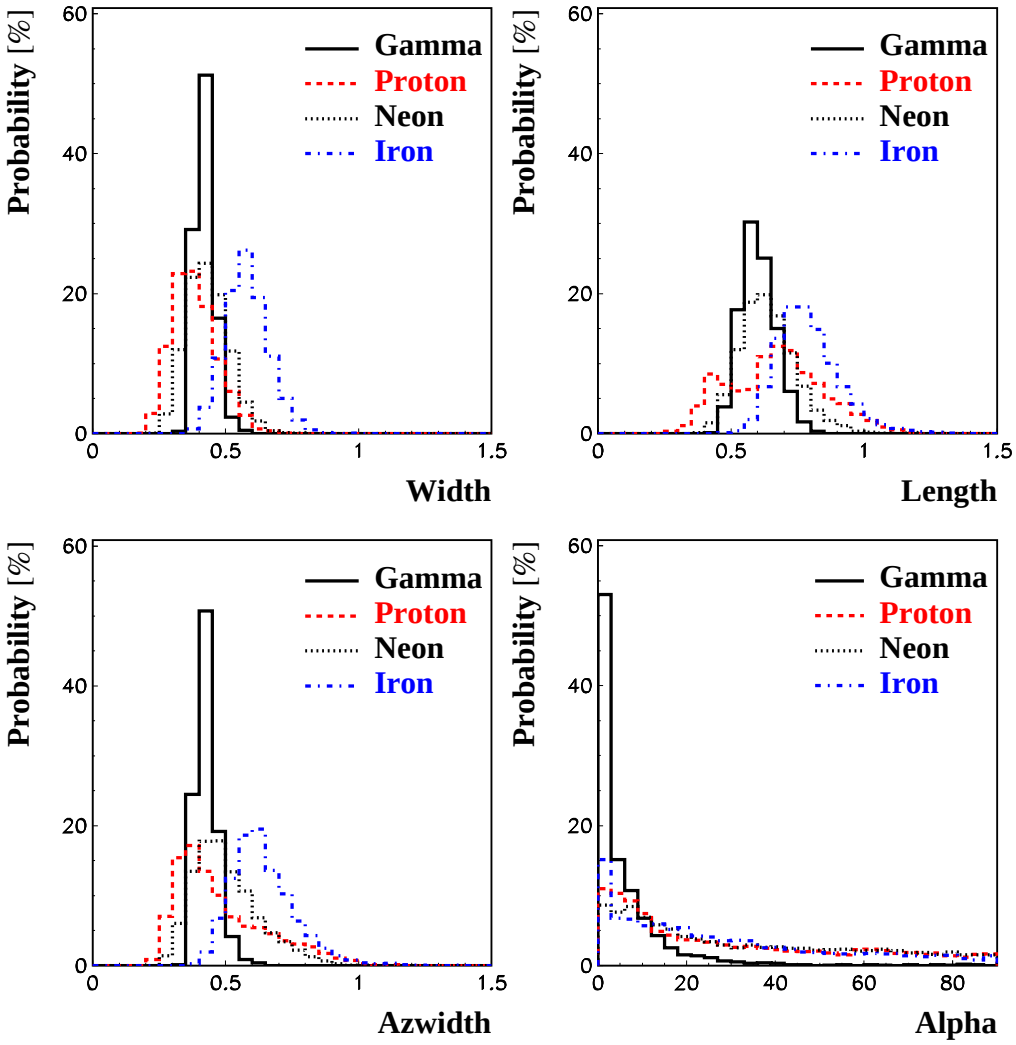

Figure 1.8: The effect of progenitor particle type on the probability distribution of image *length*, *width*, *azwidth* and α [119].

Both of these shortcomings are addressed by constructing an array of two or more separated Cherenkov telescopes. The contamination by local particles can be almost completely eliminated by imposing the criterion that several telescopes should register a detection simultaneously, or at least within some short ($\sim 10-100$ ns) time window. Due to the extremely faint Cherenkov flash it produces, a local particle will only be detected if it passes very close to, if not through, a telescope. By separating the telescopes sufficiently, one can ensure that a single particle cannot successfully trigger more than one detector. This n-fold coincidence technique can therefore eliminate all but the small number of accidental coincidences when separate particles trigger different telescopes within the required time-span. Of these events, many will be eliminated by the image analysis techniques discussed in §1.3.5.

With more than one telescope, the task of localising an air-shower's source becomes significantly easier. Figure 1.9 illustrates how the images recorded by several telescopes can be used to derive the point of origin of a detected Cherenkov pulse.

Unlike conventional optical telescopes, atmospheric Cherenkov telescopes do not attempt to image the γ-ray sky directly. Rather, the images they produce show the elliptical footprint of the Cherenkov pulse. Since this profile represents the cross section of the air shower's Cherenkov cone, its long axis will be approximately aligned with the direction of the shower axis. Accordingly, the intersection of the long axes of all the telescope images defines the projected sky position at which the arriving photon initiated the air-shower. As illustrated by Figure 1.4, simulations indicate that this generally corresponds to the celestial position of VHE γ-ray source. Furthermore, when the Cherenkov images are projected onto the ground plane of the telescope system, the intersection of their long axes yields the likely impact point of the shower.

For spatially unresolved or *point-like* γ-ray sources, the ability to accurately determine the celestial origin of a detected γ-ray-like event significantly enhances the background rejection capabilities of a Cherenkov telescope. Figure 1.10 illustrates the air-shower parameter θ, which is defined as the angular distance between the reconstructed direction of the incident γ-ray and the direction of a putative γ-ray source. In combination with knowledge of the instrumental point-spread func-

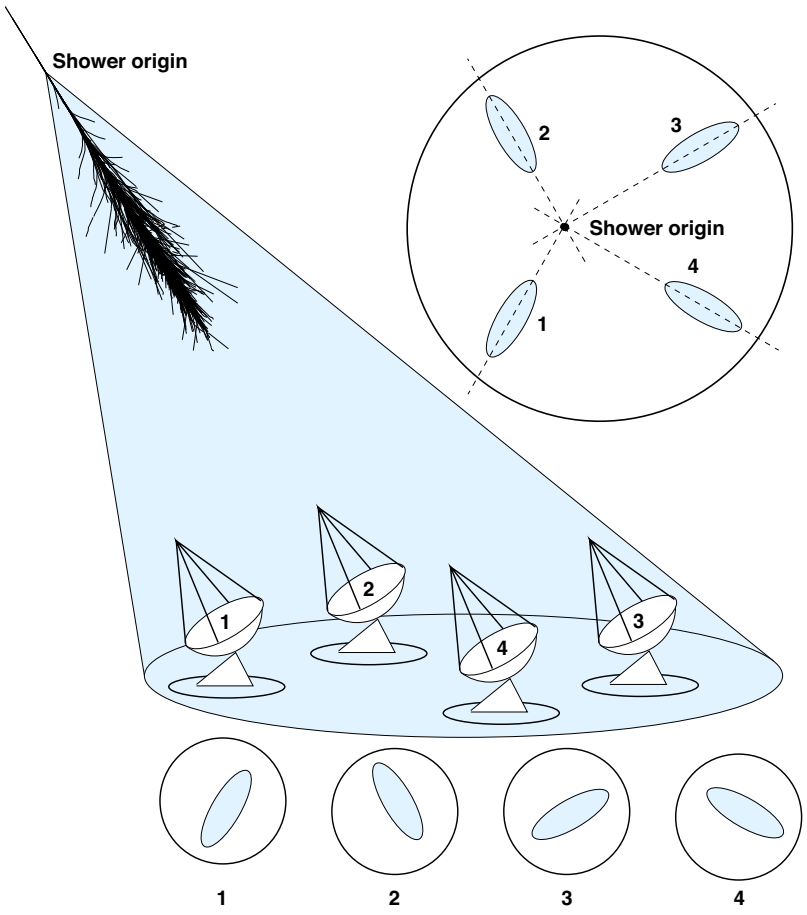

Figure 1.9: The stereoscopic IACT. The long axis of each shower image points to the source of the air shower on the sky.

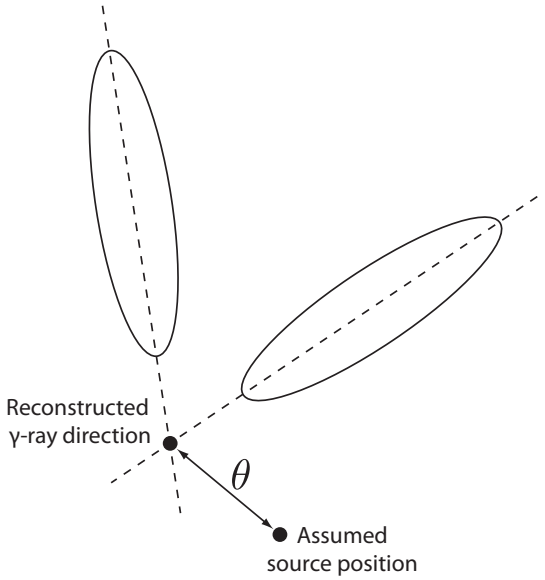

Figure 1.10: Illustration of the parameter shower parameter θ which is defined as the angular distance between the γ-ray's reconstructed celestial origin and the assumed source position.

tion, the square of this distance (θ^2) may be used to reject events whose incident directions are inconsistent with the assumed source position (see e.g. §3.5). For spatially resolvable or *extended* sources the background rejection power of θ^2 is significantly reduced because the expected angular distribution of γ-ray events is not known *a priori*.

Determining of the energy of the progenitor of a particular air shower relies on a form of electromagnetic calorimetry. Under good observing conditions, the amount of Cherenkov light emitted by an EAS scales approximately linearly with the energy of its progenitor. Using the reconstructed distance between the triggered telescope and the impact point of the air-shower, the summed pixel amplitudes of a Cherenkov image (the *image amplitude* or *size*) may be used to infer the light yield of the incident shower, and thus estimate the energy of the primary particle.

1.3.7 Mean Scaled Parameters

For a given image parameter p, Monte Carlo simulations may be used to derive an expected parameter value $\langle p \rangle$ together with an associated spread σ_p which correspond to a γ-ray-like air-shower. In fact, $\langle p \rangle$ and σ_p are functions of the image amplitude and reconstructed shower impact

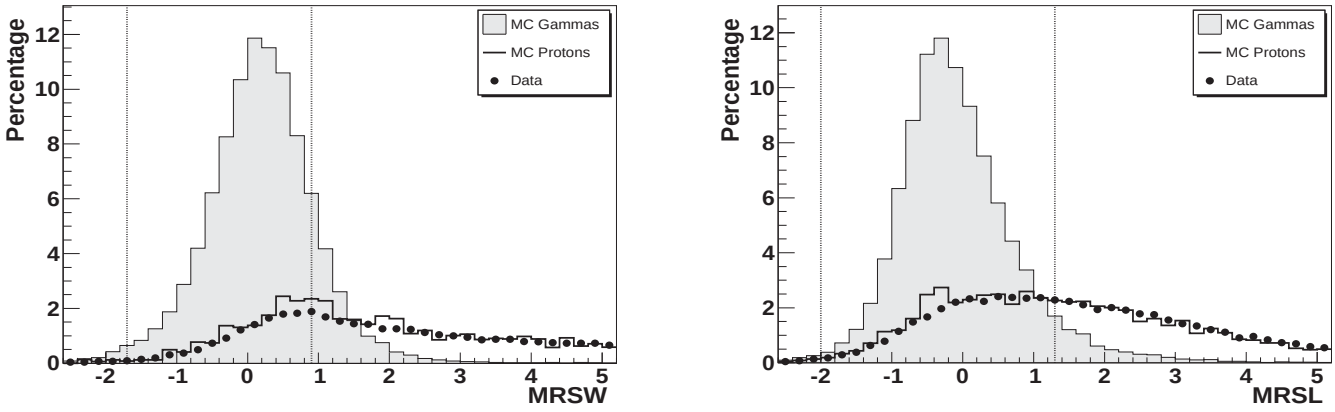

Figure 1.11: The simulated distributions of mean reduced scaled width and mean reduced scaled length for protons and γ-rays [36].

distance, and must be obtained from lookup tables on an event-by-event basis [11]. Using the Cherenkov image from a single telescope, the three values p, $\langle p \rangle$ and σ_p may then be used to define a corresponding *mean reduced scaled* parameter:

$$p_{\mathrm{rsc}} = \frac{p - \langle p \rangle}{\sigma_p} \tag{1.9}$$

When Cherenkov images from several telescopes are available, their individual characteristics may be used in combination to improve the background-rejection efficiency of the telescope system. For a specific air shower event, the average value of p_{rsc} may be derived from the images of all n triggered telescopes:

$$\bar{p}_{\mathrm{rsc}} = \sum_{n} \frac{p_{\mathrm{sc}}}{n} \tag{1.10}$$

Figure 1.11 compares the distributions the mean reduced scaled width (MRSW) and the mean reduced scaled length (MRSL) for simulated populations of protons and γ-rays with those obtained from real data. As expected, the parameter values derived from the background dominated data closely resemble the simulated proton events.

Event selection using the mean reduced scaled parameters relies on the fact that γ-ray events are localised within specific regions of the relevant parameter spaces, while cosmic ray events exhibit a much broader distribution. Events yielding parameters which fall outside the nominally γ-ray-like

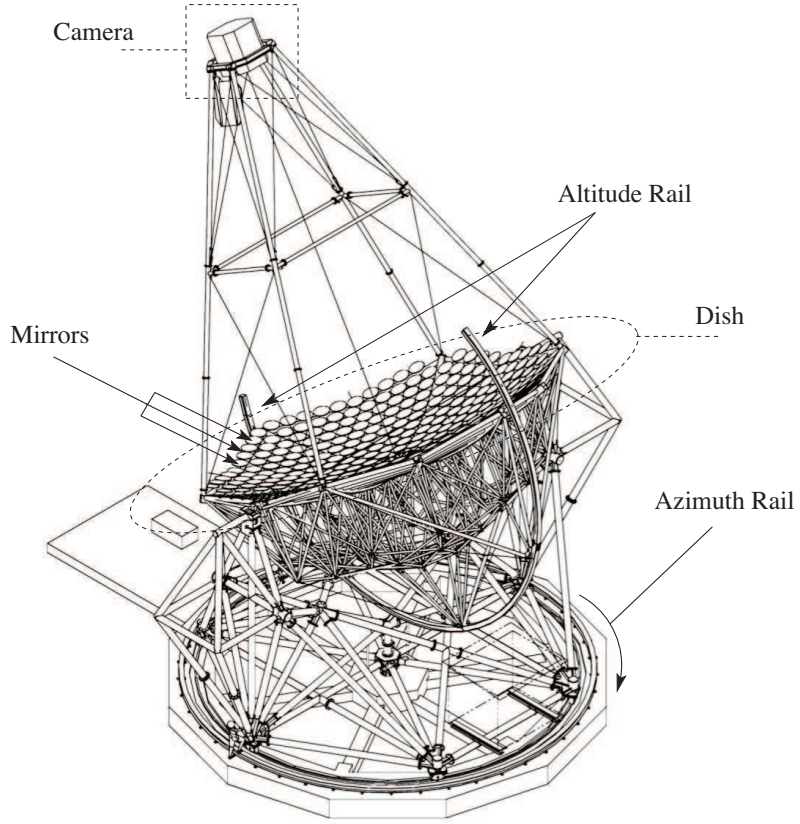

Figure 1.12: Schematic of one of the H.E.S.S. telescopes (Courtesy of the H.E.S.S. Collaboration).

regions are rejected, and the proportion of true γ-rays in the remaining sample is enhanced.

1.4 H.E.S.S.

The High Energy Stereoscopic System (H.E.S.S.) is an array of four IACT telescopes situated in the Khomas Highlands, Namibia. It represents the current state of the art in IACT design and employs all of the analysis techniques discussed in previous sections.

The individual H.E.S.S. telescopes are built around the Davies-Cotton design (See Figure 1.12). The reflecting component is a 13m tessellated mirror consisting of 380 round facets. The facets are mounted onto a spherical dish structure with a radius of curvature of 15 m, and have themselves a focal length of 15 m. This configuration is optimised to give good on-axis performance, and a large field of view [39].

The H.E.S.S. cameras consist of 960 photomultiplier tube (PMT) pixels subtending 0.16° each and combining to give a total field of view of $\sim 5°$. The photomultiplier tubes are fitted with *Winston Cones* which are effectively reflective funnels that channel the light which would fall between the individual PMTs, allowing it to be detected [11]. The typical extent of an on-axis Cherenkov shower image, at $\sim 2 - 3°$ is therefore easily encompassed by each camera. Readout of the camera systems is accomplished using a fast electronic system with a dead time of 446 μs for each successful trigger of the entire array. Such a trigger requires that two or more individual telescopes register an event within a fixed time window of 80 ns. The detection condition for each camera requires that at least 3 out of 64 adjacent pixels register a value greater than 5.7 photoelectrons within a window of ∼1.3 ns [101].

The effective collecting area of the H.E.S.S. array varies as a function of photon energy. At the low end of the detectable frequency range ($\sim$ 100 GeV), targets must be near the zenith for their Cherenkov light to be detected. This produces a smaller footprint on the ground and the effective area is a correspondingly small $\sim 10^4 \mathrm{m}^2$. At higher zenith angles the effective area increases at the expense of the low energy threshold to around $10^6 \mathrm{m}^2$ [36]. The large effective areas of Cherenkov telescopes arise from the fact that the atmosphere of the Earth acts as a calorimeter, producing the Cherenkov radiation and allowing us to sample a region far larger than the footprint of the telescope array.

Unfortunately, the presence of the atmosphere as a key component of the detector introduces significant systematic problems which must be appropriately corrected for. Factors such as humidity, temperature, cloud cover, and the presence of aerosols and dust in the atmosphere strongly affect the development of air-showers and consequently the intensity of the Cherenkov light detected. It is therefore necessary to monitor the condition of the atmosphere at all times and combine the data obtained with air-shower computer simulations in order to calibrate the observations.

The H.E.S.S. array has proven itself to be the most effective instrument of its type in the world. Situated in the southern hemisphere it is ideally positioned to observe the dense environments of the galactic center, as well as observing other galactic and extragalactic sources.

1.5 X-ray Binaries

X-ray binaries (XRBs) are galactic binary systems comprising a stellar-mass compact object (either a neutron star or black hole) and a stellar companion. As the name suggests, these systems are characterised by strong and often variable X-ray emission, which is believed to be powered by disc accretion of matter from the companion star (or *donor*) onto the compact object (or *primary*).

X-ray binaries are interesting astrophysical objects because they represent a nearby population of compact, accreting systems, and may be miniature analogues of the active galactic nuclei (AGN). Like AGN, they promise new insights regarding the interaction of matter, radiation and magnetic fields in and around regions of strongly curved space-time [82]. Moreover, while their supermassive, extra-galactic counterparts appear to require many thousands of years to manifest significant behavioural changes (e.g. the transition from radio-loud to radio-quiet behaviour), the comparatively miniature X-ray binaries exhibit evolution on time scales of years or less. Whereas for AGN, large population studies are required to infer global characteristics, a single X-ray binary may be studied in isolation, often facilitating a more complete and consistent physical interpretation.

The relative proximity of X-ray binaries is an additional advantage, particularly in the context of VHE γ-ray astronomy. An obvious advantage of studying galactic objects is that the source luminosity required for detection is correspondingly reduced. VHE γ-ray production is an extreme process, requiring particle acceleration to multi-TeV energies. Extra-galactic sources must produce large photon fluxes in order to overcome flux dilution effects and still be detected. Clearly, increasing the proximity of a γ-ray source relaxes the requirements for particle acceleration efficiency and lowers the overall energy budget, potentially resulting in more detectable sources in the VHE γ-ray regime. Furthermore, VHE γ-rays are susceptible to attenuation by pair production interactions with the extra galactic radiation field [e.g. 174], leading to spectral modification at low redshifts and increasing γ-ray flux suppression as the source distance increases. The resultant preferential detection of nearby AGN at TeV energies implies unavoidable selection effects and population studies may well yield biased results.

Notwithstanding the apparently advantageous properties of XRBs, the observed population of

VHE γ-ray emitting binary systems is frustratingly limited, with only three confirmed examples (see §1.5.3). In contrast, consultation of the TeVCat[1] online γ-ray source catalogue yields 31 AGN that exhibit significant GeV/TeV emission. Obscuration of XRBs due to their concentration in the galactic plane may inhibit the identification of multi-wavelength counterparts, but is unlikely to explain the small number of detectable γ-ray binaries. Indeed, the dense interstellar material which strongly attenuates low energy radiation is practically transparent to VHE γ-ray photons propagating on galactic distance scales [221]. A more likely explanation relates to the number of potentially observable AGN, which greatly exceeds the number of known X-ray binary systems. Despite uncertainties regarding the fraction of each source class for which γ-ray detection is possible, it seems reasonable that the large number of AGN detected in the TeV/GeV band is at least partially attributable to their comparative abundance. From the preceding discussion, it seems clear that parallel exploitation of the observational opportunities offered by γ-ray binaries and γ-ray-luminous AGN is necessary if the processes occurring in these objects are to be fully understood.

Evidently, the general definition of what constitutes an X-ray binary encompasses a broad range of morphologically distinct systems. Indeed, current catalogues [160, 161] list 301 potential X-ray binaries, which exhibit a broad range of spectral, and temporal characteristics. For this reason XRBs are typically characterised on the basis of a number of physical characteristics which often correspond to distinctive radiative behaviour. The following subsections outline the various categories of XRB and highlight the associated physical properties which may be important for VHE γ-ray production.

1.5.1 High Mass or Low Mass

It is common to categorise X-ray binary systems based on the spectral type of the companion star. In *high mass* X-ray binaries (HMXBs) the donor is a hot, early-type supergiant, and is expected to produce strong stellar winds in addition to a dense ultraviolet radiation field. In contrast,

[1] http://tevcat.uchicago.edu

low mass X-ray binaries (LMXBs) harbour a cool, late type star with a spectrum peaking in the near-infrared.

Accretion in high mass systems may either be *wind fed* whereby material is gravitationally captured from the stellar wind of the massive companion, or driven by *Roche lobe overflow* whereby matter flows through the inner Lagrangian point of the binary systems. In general, HMXBs which are powered by wind accretion are several orders of magnitude fainter in the X-ray band than those for which the primary mass transfer mechanism is Roche lobe overflow [41]. Some high mass systems, including the candidate γ-ray source Cygnus X-1 [26], have donor stars which almost fill their Roche lobes, and therefore exhibit hybrid characteristics of wind and Roche lobe accretion [e.g. 105, 42].

The donor star in low mass systems cannot drive a stellar wind which is powerful enough to fuel a bright X-ray source and therefore accretion in LMXBs is thought to occur exclusively by Roche lobe overflow.

In the context of VHE γ-ray emission, the most important differences between high and low mass X-ray binary systems involve the temperature and density of the ambient stellar radiation field. The absorption of γ-rays via pair production interactions (see §2.5) is likely to be far more prevalent for sources that are embedded in the intense ultraviolet radiation field of a high-mass companion. Moreover , the stellar radiation field provides a source of photons which could be inverse-Compton (IC) scattered to γ-ray energies (See §2.4). The early type stars in HMXBs are characterised by intense ultra-violet radiation, implying dense photon fields which may be scattered to γ-ray energies [75]. In contrast the stellar radiation from low-mass companions is relatively faint and soft, which decreases the importance of IC scattering for γ-ray production.

The relative strength of the stellar winds in high- and low-mass X-ray binaries is also relevant to VHE γ-ray emission. Interactions between the stellar wind and relativistic outflows produced by the compact object could lead to hadronic production of VHE γ-rays via the production and decay of neutral pions [208] (See §2.1). Furthermore, shocks resulting from the confinement of relativistic outflows by dense stellar winds facilitate the acceleration of particles to the multi-TeV

energies required for VHE γ-ray production [e.g. 86].

1.5.2 Black hole or Neutron Star

As noted by [82], the observable gravitational potentials of neutron stars and black holes are not markedly different. This is because the typical radii of neutron stars are comparable to the radii of the last stable orbit around black holes. Indeed, the only fundamental difference between neutron stars and black holes is that the former possess a solid surface while the matter simply falls through the event horizon of the latter. This critical distinction produces several observable differences which are discussed in detail by [154]. Most notably, all accreting neutron star spectra show evidence for non-thermal emission from a *boundary layer* between the accretion flow and the neutron star surface, which is absent in black hole binary spectra.

In the X-ray band, many black hole binaries (BHBs) are observed to exhibit spectrally distinct *canonical* states which are believed to be related to the mass accretion rate ($\dot{M}$) of the system. Moreover, simultaneous radio observations appear to indicate a clear correlation between the state of a given BHB and the production of synchrotron-emitting outflows within the system [97]. The canonical *low/hard* state is characterised by a non-thermally dominated X-ray spectrum and a relatively faint 2-10 keV X-ray flux [e.g. 82]. This state is believed to indicate low mass accretion rates and often corresponds the production of a mildly relativistic, collimated radio jet. In contrast the *high/soft* state exhibits a bright 2-10 keV flux, thought to imply a higher value of $\dot{M}$. The corresponding X-ray spectrum is dominated by thermal emission from an optically thick accretion flow, and jet formation appears to be suppressed. Transitions between the low/hard and high/soft states are often spectacular and exhibit a transient *very high/intermediate* state which is characterised by strong disk emission *and* a non-thermal tail extending to high energies. Occurrences of the very high/intermediate state often correspond to episodes of optically thin radio flaring. These flares have been interpreted as radiation from shocks which are produced by discrete, highly relativistic clouds of plasma propagating in the mildly relativistic remnants of the low/hard state jet.

Low magnetic field ($B \lesssim 10^{11}G$) neutron star binaries are generally segregated into two sub-categories which are named for the shapes traced out by their spectral evolution in a colour-colour diagram. *Z* sources typically have X-ray luminosities exceeding half the Eddington luminosity ($L_{\rm Edd}$), while *atoll* sources can be much fainter with $10^{-3}L_{\rm Edd} \lesssim L_{\rm atoll} \lesssim L_{\rm Edd}$. Like BHBs, the atoll sources exhibit spectrally distinct states which appear to be linked to the mass accretion rate. The *island* state is approximately analogous to the low/hard in black hole systems, while the *banana* state appears to correspond to the high/soft state [82]. Furthermore, there is some evidence that atoll sources also exhibit a correlation between X-ray and radio emission which is similar to that observed in black hole systems [241]. Z sources are neutron star binaries with consistently high accretion rates and consequently do not exhibit a counterpart to the low/hard state of BHBs. Although Z sources do produce relativistic outflows, a definitive correlation between the observed X-ray and radio phenomenology is yet to be established. Indeed, the processes which lead to jet formation in Z sources may be very different from those operating in BHBs and atoll sources [82, 61].

The presence of relativistic outflows in X-ray binary systems has particular relevance with regard to VHE γ-ray production. Indeed, a fundamental requirement for the emission of GeV/TeV photons is a population of particles with multi-TeV energies [246]. Shocks within collimated jets provide an obvious mechanism for the acceleration of these particles and for this reason microquasars (see Chapter 4) have often been considered as likely sources of transient γ-ray emission [e.g. 20]. If the compact object is a highly magnetised, rapidly rotating neutron star (i.e. a *pulsar*), then it can produce a relativistic wind of particles which may interact with the stellar wind of the companion star, forming shocks where particle acceleration can occur [167]. Recently, this mechanism was proposed as an alternative to the microquasar scenario for explaining the observed VHE γ-ray emission from the high-mass X-ray binaries LS 5039 and LS I +61°303 [86].

1.5.3 γ-ray Binaries

Remarkably, of the 301 X-ray binary systems identified by [160, 161] only three have been unambiguously identified as VHE γ-ray sources. These are the Be star/pulsar binary PSR B1259-63 [7], and the ambiguous high-mass binary systems LS I $+61°303$ [25] and LS 5039 [6]. Additionally, transient, marginally significant VHE γ-ray emission was detected during a broadband flare of the high-mass black hole binary Cygnus X-1 [26], although the nature of the emission means that the detection cannot be independently verified.

First detected using the H.E.S.S. telescope [7], PSR B1259-63 is a periodic transient VHE γ-ray source which becomes detectable every ~ 3.4 years , around the time of periastron passage. VHE γ-rays are thought to be produced by the interaction of a relativistic pulsar wind with the intense matter and radiation fields associated with the equatorial disc of the Be star companion.

The radio emitting HMXB LS I $+61°303$ was initially identified at GeV photon energies using the COS-B satellite [121, 113] and later associated with the EGRET source 3EG J0241+6103. Recent observations using the MAGIC [25, 24] and VERITAS [2] ground-based Cherenkov telescopes firmly establish the system as a VHE γ-ray source. LS I $+61°303$ comprises a B0Ve star orbiting an unidentified compact object with a period of ~ 26.5 days [53]. Orbital modulation of the observed γ-ray flux has been identified by [24]. VHE γ-ray spectra extracted at phase intervals corresponding to the maximum γ-ray flux are well described by power laws in energy and exhibit photon indices of $\Gamma \sim 2.4 - 2.6$ [2, 24].

LS 5039 is a HMXB containing an O6.5V((f)) star and an unidentified compact object which orbit each other every 3.9 days [54]. At VHE γ-ray wavelengths, it was serendipitously detected as part of the H.E.S.S. galactic plane survey [12, 6] and is by far the best studied of the three known γ-ray binaries. An overview of the observational properties of LS 5039 together with a detailed analysis of the associated VHE γ-ray emission is presented in Chapter 3.

Chapter 2

Radiative Emission

This chapter discusses several radiative emission mechanisms which can give rise to VHE γ-ray emission with particular emphasis given to synchrotron and inverse-Compton processes. In addition, the absorption of γ-rays by electron-positron pair production in low energy photon fields is described and effects of relativistic bulk motion on the observed spectrum of a radiation source are briefly summarised. Finally, two computerised implementations of previously published numerical models describing γ-ray emission and absorption are introduced. The first simulates the synchrotron self-Compton emission from a bulk relativistic electron gas, while the second models the attenuation of γ-rays in a binary system by pair production in the radiation field of the stellar companion.

2.1 Neutral pion decay

VHE γ-ray production via the decay of neutral π mesons (or *pions*) is an example of an hadronic radiative emission process. Relativistic protons (p) with kinetic energies in excess of 290 MeV may produce π^0 particles in interactions with a stationary hydrogen gas [246]. The most common interaction scheme is described by:

$$p + p \rightarrow N + N + n_1(\pi^+ + \pi^-) + n_2\pi^0 \tag{2.1}$$

where N is a nucleon, $\pi^{\pm,0}$ are charged and neutral pions, and n_1 and n_2 are integer multiplicities which account for the production of multiple $\pi^{\pm}$ or π^0 particles by protons with energies above 1 GeV.

The rest-frame lifetime of π^0 is 10^{-16} s after which it decays to produce two γ-rays:

$$\pi^0 \rightarrow \gamma + \gamma \tag{2.2}$$

Each γ-ray has an energy of ≈ 70 MeV in the rest frame of the decaying π^0. At energies above ≈ 70 MeV, and assuming a parent proton population with a power-law energy distribution with slope Γ_p, the spectrum of γ-rays produced by π^0 decay is also a power-law with photon index $\Gamma_\gamma = 4(\Gamma_p - 1/2)/3$ [246]. At lower photon energies the spectrum turns over, producing a characteristic peak at 70 MeV which is the spectral signature for hadronic $p-p$ interactions within an astrophysical source.

2.2 Bremsstrahlung

Bremsstrahlung (German for *braking radiation*) is emitted whenever an electron is accelerated via interaction with the electric field of an atomic nucleus. In an astrophysical context, bremsstrahlung becomes important when relativistic electrons propagate though dense molecular or atomic gases, such as those found in supernova remnants or the equatorial disks of Be stars. The γ-rays which are produced via bremsstrahlung have energies which are similar to those of the parent electrons which implies that the spectrum of emitted photons is similar in shape to the energy spectrum of the emitting electron population [246]. An in-depth discussion which presents the properties of bremsstrahlung emission from relativistic and non-relativistic electron populations in an astrophysical context is given by [43].

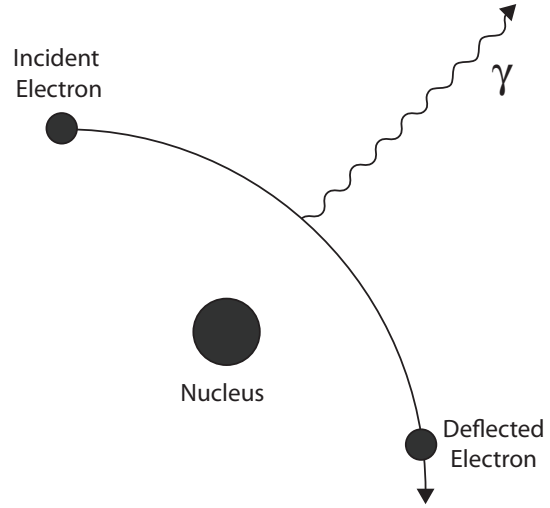

Figure 2.1: Illustration of the bremsstrahlung emission mechanism.

2.3 Synchrotron Radiation

Synchrotron radiation is emitted by relativistic and ultra-relativistic charged particles spiralling in a magnetic field. It produces a distinctive power-law spectrum spanning several decades in photon energy. Indeed, synchrotron emission from X-ray binaries has been observed at radio [e.g. 181], infra-red [99], optical [177] and possibly even X-ray [69] wavelengths. The observation of synchrotron radiation associated with an astrophysical object provides an unambiguous indicator of intrinsic, non-thermal particle acceleration [163].

2.3.1 Energy Loss Rate for a Single Electron

In the non-relativistic limit, the observed power radiated by an accelerated electron with charge e is described by Larmor's formula:

$$\frac{dW}{dt} = \frac{2e^2a^2}{3c^3} \tag{2.3}$$

where a is the magnitude of the electron's instantaneous acceleration. For a relativistic electron this expression becomes [218]:

$$\frac{dW}{dt} = \frac{2e^2}{3c^3}\gamma^4(a_\perp^2 + \gamma^2 a_\parallel^2) \tag{2.4}$$

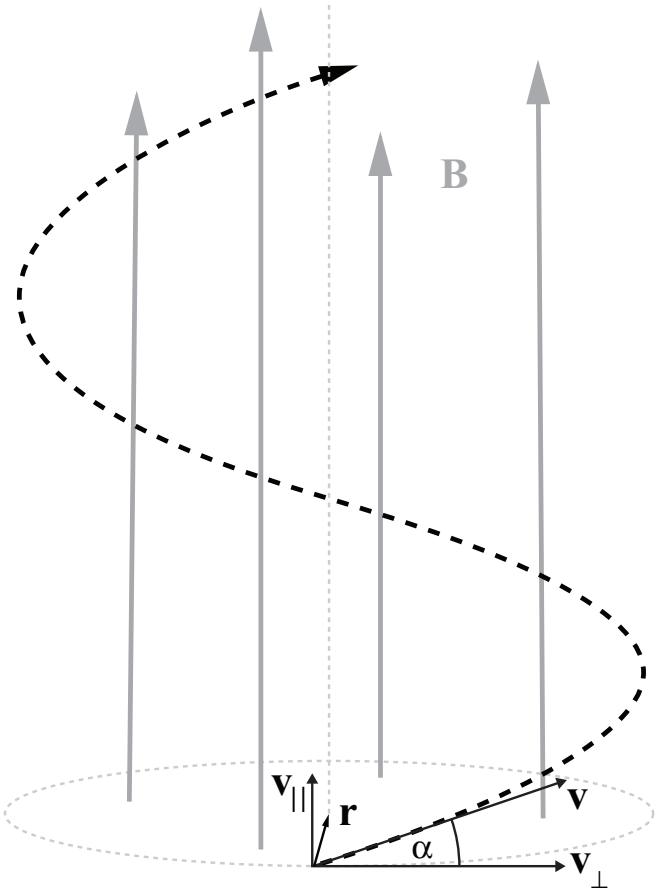

Figure 2.2: Schematic representation of the synchrotron emission process.

where $a_\perp$ and $a_\parallel$ denote the perpendicular and parallel components of acceleration with respect to the electron's velocity vector. As illustrated in Figure 2.2, a relativistic electron moving with constant speed in a uniform magnetic field follows a helical trajectory described by relativistic equations of motion:

$$\frac{d}{dt}(\gamma m\mathbf{v}) = \frac{e}{c}\mathbf{v} \times \mathbf{B} \tag{2.5}$$

$$\frac{d}{dt}(\gamma mc^2) = e\mathbf{v} \cdot \mathbf{E} = 0 \tag{2.6}$$

The logical implication of (2.6) is that γ (or alternatively $|\mathbf{v}|$) is constant and therefore:

$$m\gamma\frac{d\mathbf{v}}{dt} = \frac{e}{c}\mathbf{v} \times \mathbf{B} \tag{2.7}$$

Resolving the electron velocity into components parallel ($\mathbf{v}_\parallel$) and perpendicular ($\mathbf{v}_\perp$) to the magnetic field yields:

$$\frac{d\mathbf{v}_\parallel}{dt} = 0 \tag{2.8}$$

$$\frac{d\mathbf{v}_\perp}{dt} = \frac{e}{\gamma mc}\mathbf{v}_\perp \times \mathbf{B} = \frac{e|\mathbf{B}||\mathbf{v}_\perp|}{\gamma mc}\hat{\mathbf{r}} \tag{2.9}$$

where $\hat{\mathbf{r}}$ is the unit vector in the direction of the radial vector, $\mathbf{r}$ (See Figure 2.2). The resultant helical trajectory is a combination of uniform circular motion with frequency $\omega_B = e|\mathbf{B}|/\gamma mc$ in the plane perpendicular to $\mathbf{B}$ and uniform linear motion in all planes parallel to $\mathbf{B}$.

In this case $a_\perp$ and $a_\parallel$ as defined in (2.4) are precisely equivalent to $|d\mathbf{v}_\perp/dt|$ and $|d\mathbf{v}_\parallel/dt|$, allowing the total emitted power to be expressed as:

$$\frac{dW}{dt} = \frac{2e^2}{3c^3}\gamma^4\left(\frac{e|\mathbf{B}||\mathbf{v}_\perp|}{\gamma mc}\right)^2 = \frac{2}{3}r_0^2 c\beta_\perp^2\gamma^2 B^2 \tag{2.10}$$

where $\beta_\perp = |\mathbf{v}_\perp|/c$ and $r_0 = e^2/mc^2$ is the classical electron radius.

For an ensemble of electrons with isotropically distributed velocities, the average energy loss rate is obtained by integrating over all possible pitch angles α yielding:

$$\left\langle \frac{dW}{dt} \right\rangle = \left(\frac{2}{3}\right)^2 r_0^2 c\beta^2\gamma^2 B^2 \tag{2.11}$$

where β is the magnitude of the electrons' velocities in units of c.

Finally, using (2.11), the *characteristic cooling time* due to synchrotron radiation for an electron of specified energy $E_e = \gamma mc^2$, subject to a magnetic field with magnitude $B \equiv |\mathbf{B}|$ may be derived [e.g. 148]:

$$t_{\rm cool}^{\rm sync} = \frac{E_e}{dW/dt} = \frac{9\gamma mc^2}{4r_0^2 c\beta^2\gamma^2 B^2} \approx \frac{9mc}{4r_0^2}\gamma^{-1}B^{-2} \approx 4\times 10^2 B_{\rm G}^{-2}E_{e,\rm TeV}^{-1}\ \text{s} \tag{2.12}$$

where $B_{\rm G}$ is the magnetic field intensity in Gauss, and $E_{e,\rm TeV}$ is the electron energy in TeV.

2.3.2 Synchrotron Spectrum for a Single Electron

The measured radiation spectrum from a moving charge is dictated by the corresponding time variation of the electric field ($E(t)$) at the observation coordinates [218]. More specifically, the spectrum of radiation passing through a surface element dA is described by:

$$\frac{dW}{dAd\epsilon dt} = \frac{c}{T\hbar}\left|\mathcal{F}(E(t))\right|^2 \tag{2.13}$$

where $\mathcal{F}(E(t))$ denotes the Fourier transform of $E(t)$ during the observational interval T.

In the non-relativistic limit ($\beta \ll 1$), the electron's gyration produces a sinusoidal variation in the observed electric field and the resultant spectrum is monochromatic with frequency $\nu_B = \omega_B/2\pi$. In contrast, for $\beta \sim 1$ the radiated power is relativistically beamed into a narrow cone with opening angle $\sim 1/\gamma$ about the electron's velocity vector. The helical motion now produces a series of narrow peaks in the measured electric field as the beam sweeps across the observer's line-of-sight. The departure of $E(t)$ from a simple sinusoid complicates the emergent spectrum, with the narrow pulses introducing higher Fourier harmonics and often producing significant power at frequencies far in excess of ν_B.

The spectrum of synchrotron radiation due to a single electron, integrated over all solid angles is reported by many authors [e.g. 218, 163, 43] and is given by:

$$j_{\rm sync}(\epsilon;\gamma,\alpha,B) \equiv \frac{dW}{d\epsilon dt} = \frac{\sqrt{3}e^3 B\sin\alpha}{hmc^2}F(x) \tag{2.14}$$

where ϵ is the synchrotron photon energy. The form of $F(x)$ is shown in Figure 2.3 and is defined as:

$$F(x) = x\int_x^\infty d\xi K_{\frac{5}{3}}(\xi) \quad \text{where} \quad x = \frac{4\pi mc\epsilon}{3eh\sin\alpha}\gamma^{-2}B^{-1} = \frac{\epsilon}{\epsilon_c} \tag{2.15}$$

where $K_{\frac{5}{3}}(\xi)$ is the modified Bessel function of the second kind, of order 5/3. The single electron spectrum is strongly peaked at $\epsilon \approx \epsilon_c$ and falls off exponentially towards higher energies, implying that almost all the synchrotron photons from a specific electron with energy γmc^2 have $\epsilon \approx \epsilon_c \approx$

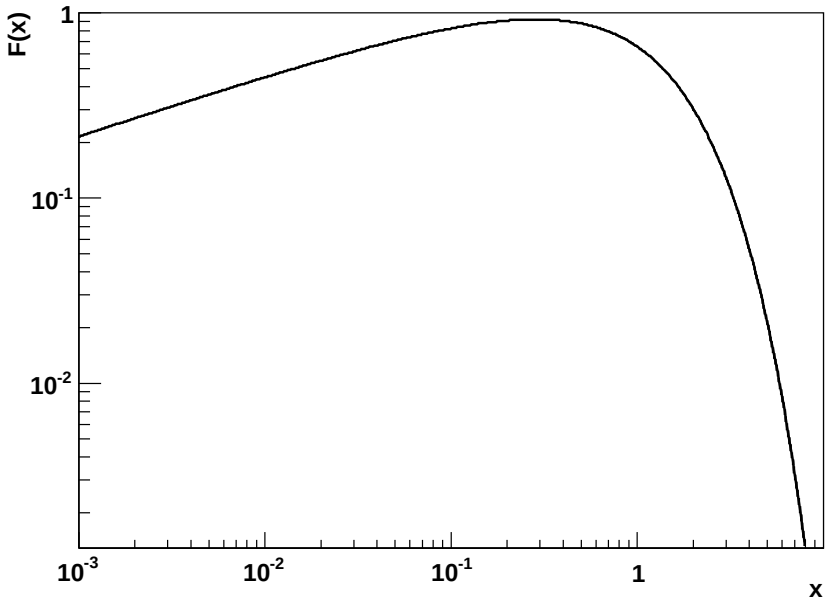

Figure 2.3: The form of $F(x)$.

$\gamma^3\hbar\omega_B$. A corollary of this fact is that, for a fixed magnetic field intensity B, all synchrotron photons at a specific energy were produced by electrons with approximately the same Lorentz factor.

2.3.3 The Synchrotron Spectrum for Many Electrons

Astrophysical synchrotron sources comprise poly-energetic populations of relativistic electrons, often radiating in non-uniform physical environments. A general formula for the synchrotron *volume emissivity* of such a source may be expressed as the superposition of individual electron spectra [e.g. 43]:

$$J_{\rm sync}(\epsilon;\gamma,\alpha,B,\mathbf{r},t) = \int d\Omega_\alpha \int d\gamma j_{\rm sync}(\epsilon;\gamma,\alpha,B) N(\gamma,\alpha,\mathbf{r},t) \tag{2.16}$$

where $N(\gamma,\alpha,\mathbf{r},t)d\gamma d\Omega_\alpha$ specifies the number density of electrons having Lorentz factor within $d\gamma$ and pitch angle within $d\Omega_\alpha$ at a specified position $\mathbf{r}$ within the source at time t. When performing

practical computations of $J_{\rm sync}$, it is common to make a number of assumptions which simplify the parametric dependencies. Accordingly, subsequent calculations constrain N to be spatially and temporally homogeneous throughout the synchrotron source. Furthermore, the conventional assumptions of an isotropic electron velocity distribution and a tangled magnetic field with constant average intensity will also be adopted. In combination, these simplifications reduce (2.16) to a more manageable form [e.g. 100]:

$$\begin{aligned} J_{\rm sync}(\epsilon;\gamma,\alpha,B) &= \int d\Omega_\alpha \frac{N(\alpha)}{4\pi} \int d\gamma N(\gamma) j(\epsilon;\gamma,\alpha,B) \\ &= \frac{\sqrt{3}e^3 B}{hmc^2} \cdot \frac{1}{2} \int d\alpha \sin^2\alpha \int d\gamma N(\gamma) x \int_x^\infty d\xi K_{\frac{5}{3}}(\xi) \\ &= \frac{\sqrt{3}e^3 B}{2hmc^2} \int d\gamma N(\gamma) \tilde{x} \int d\alpha \sin\alpha \int_x^\infty d\xi K_{\frac{5}{3}}(\xi) \end{aligned} \tag{2.17}$$

where $N(\alpha)$ is the fraction of electrons with pitch angles within $d\Omega_\alpha$ and $\tilde{x} = x \sin\alpha$.

Derivation of the overall photon spectrum requires the integration of (2.17) over the radiating volume $V_{\rm S}$. For simplicity, all subsequent calculations assume a spherical source geometry for which the specific synchrotron luminosity is simply:

$$L_{\rm sync}(\epsilon) = V_{\rm S} J_{\rm sync}(\epsilon) = \frac{4\pi R_{\rm S}^3}{3} J_{\rm sync}(\epsilon) \tag{2.18}$$

where $R_{\rm S}$ is the source radius. Figure 2.4 plots $\epsilon L_{\rm sync}$[1] for a typical set of source parameters, assuming a truncated power-law distribution of electron Lorentz factors ($N(\gamma) = N_0 \gamma^{-p}$) between $\gamma_{\rm min} = 100$ and $\gamma_{\rm max} = 1000$. The finite range of γ, combined with the close correspondence between the energies of the synchrotron photons and their parent electrons (See §2.3.2), leads to three distinct emission regimes in the emergent spectrum. In the energy range $\sim 10^{-18} - 10^{-16}$ ergs, electrons of all energies contribute to the observed emission and the photon index takes the

[1] All original model spectra presented in this thesis were generated using custom implemented computer simulations. The source code of these simulations is presented in Appendix E.2.

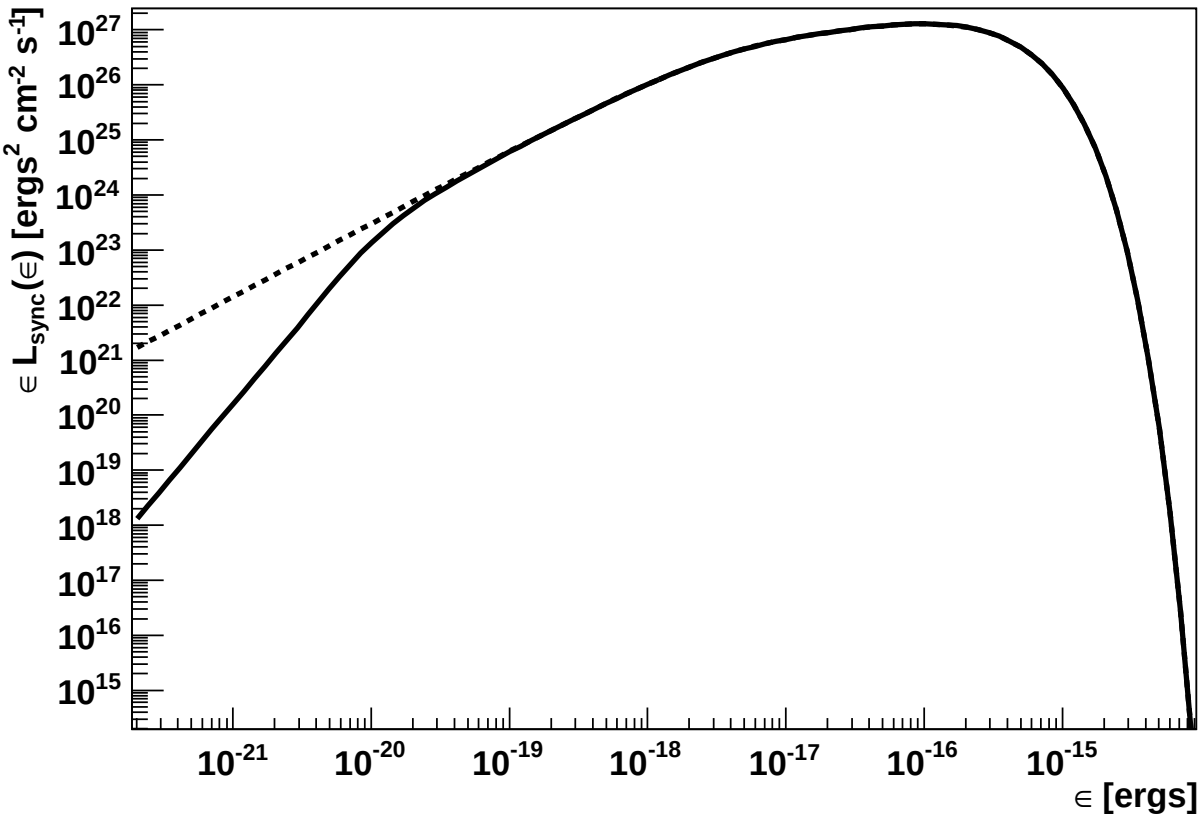

Figure 2.4: The specific synchrotron luminosity for a model of a spherical region containing a homogeneous magnetised electron gas. The solid line illustrates the attenuating effects of synchrotron self-absorption on low energy photons while the dotted line plots the unabsorbed spectrum.

familiar value for a power-law electron spectrum for which $\gamma_{\rm max} \rightarrow \infty$ [e.g. 43]:

$$L_{\rm sync}(\epsilon) \propto \epsilon^{-\alpha} \ : \alpha = \frac{(p-1)}{2} \tag{2.19}$$

At lower energies, only electrons with Lorentz factors such that $\gamma \lesssim (\epsilon/\hbar\omega_B)^{1/3}$ contribute and the photon index becomes harder with $\alpha \rightarrow p/2$. Finally, above 10^{-16} ergs, the lowest energy electrons cease to contribute to the spectrum and the observed luminosity falls off exponentially.

2.3.4 Synchrotron Self-Absorption

The attenuation of synchrotron photons by their parent electron population is known as *synchrotron self-absorption* (SSA). In fact, two opposing processes contribute to an overall modification of the emergent synchrotron spectrum. Genuine photoelectric absorption arises from the interaction of photons and electrons embedded in an ambient magnetic field. The photons are absorbed and their energy is returned to the electron population. Conversely, synchrotron photons may interact with excited atomic electrons, precipitating *stimulated emission* and replenishing the ambient radiation field. Consideration of the detailed balance between these two processes leads to a general expression for the coefficient for synchrotron self-absorption [218]:

$$\chi_\epsilon = -\frac{h^3 c^2}{8\pi\epsilon^2} \int d\gamma j(\epsilon,\gamma)\gamma^2 \frac{\partial}{\partial\gamma}\left[\frac{N(\gamma)}{\gamma^2}\right] \tag{2.20}$$

for the spherical, homogenous source described in §2.3.3, the optical depth for the SSA process may be expressed as:

$$\tau_{\rm SSA}(\epsilon) = \int_{s_0}^{s} \chi(\epsilon, s')ds' = \chi(\epsilon)R_S \tag{2.21}$$

If $\tau_{\rm SSA}(\epsilon) \gg 1$ then photons with energy ϵ will be strongly attenuated by SSA and the source is said to be *optically thick*. Conversely, if the source is *optically thin* ($\tau_{\rm SSA}(\epsilon) \ll 1$), then most synchrotron photons will escape. An interesting result noted by many authors [e.g. 43, 218, 106] is that for a power-law distribution of electron Lorentz factors, the optically thick region of the photon spectrum is described by:

$$L_{\rm sync}^{\rm thick}(\epsilon) \propto \epsilon^{\frac{5}{2}} \tag{2.22}$$

irrespective of the spectral indices of the unabsorbed synchrotron spectrum or the electron energy distribution.

Figure 2.4 illustrates the effect SSA on the spherical single-zone model spectrum developed in §2.3.3. The simulated source becomes optically thick for low energy photons and the expected $\alpha = 5/2$ photon index is reproduced below $\epsilon \sim 10^{-20}$ ergs. In fact, this behaviour is representative

of most real astrophysical sources, for which SSA only attenuates the lowest energy photons. As a consequence the direct effect of SSA on the production of VHE γ-rays, either via the synchrotron self-Compton process (see §2.7.1) or by re-energising the ambient electron population, is negligible.

2.4 Inverse Compton Scattering

Inverse Compton (IC) scattering is the process whereby relativistic electrons up-scatter soft photons to higher energies. As discussed in subsequent sections, the photon energy gain is approximately proportional to γ^2, where γ is the Lorentz factor of the scattering electron. For ultra-relativistic electrons ($\gamma \gg 1$), the potential energy gains are enormous, making IC scattering an extremely important process for the leptonic production of VHE γ-rays.

2.4.1 Energy Loss Rate for a Single Electron

The derivation of the total energy loss rate for a single electron proceeds in two stages. First the energy lost during a single scattering event is computed, then the total loss rate is obtained from multiplication by the expected rate of scattering events.

The process of inverse-Compton scattering appears particularly simple when viewed from the rest-frame (K') of the scattering electron. Indeed, in K' the observed process is simply Compton scattering and in the limit that the rest frame photon energy $\epsilon' \ll mc^2$, no energy is transferred at all! Consider the electron shown in Figure 2.5 which moves with speed βc along the x axis in the observer frame K. Suppose that in K a soft photon with energy ϵ is incident at an angle θ to the x-axis. The relativistic aberration formula:

$$\tan\theta' = \frac{\sin\theta}{\gamma(\cos\theta - \beta)} \tag{2.23}$$

may be used to calculate the photon's apparent angle of incidence θ', while the expression for the relativistic Doppler shift:

$$\epsilon' = \gamma\epsilon(1 - \beta\cos\theta) \tag{2.24}$$

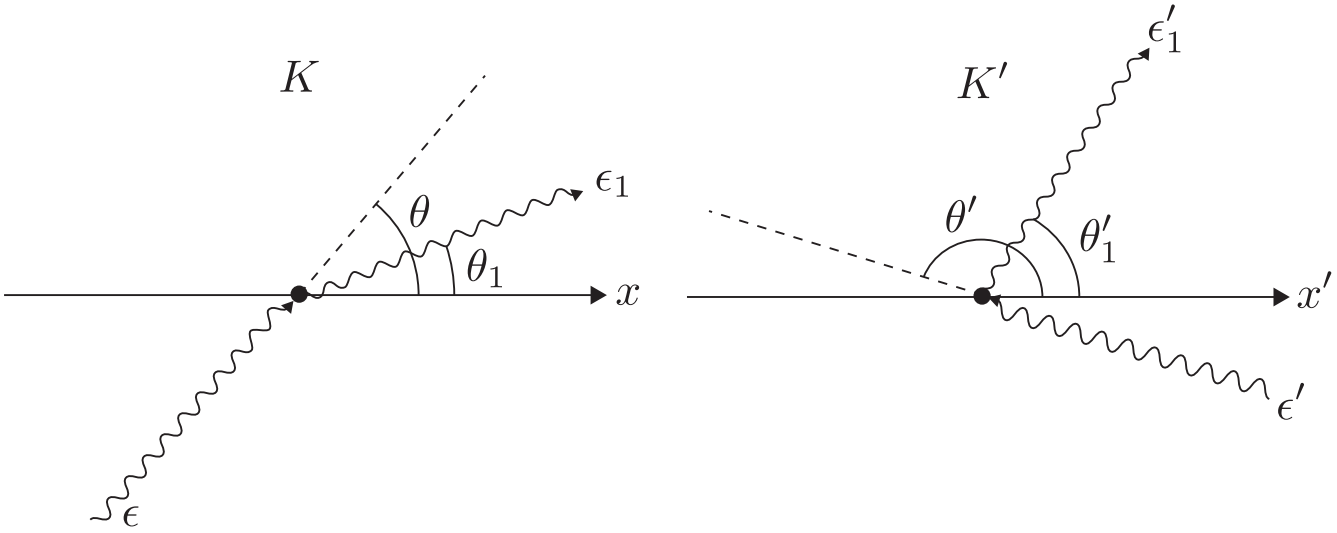

Figure 2.5: Illustration of the IC scattering process in the observer frame (K) at the rest frame of the scattering electron (K').

yields the photon energy in K'. The energy ϵ'_1 of the scattered photon in K' may be expressed using the general equation for Compton scattering:

$$\epsilon'_1 = \frac{\epsilon'}{1 + (\epsilon'/mc^2)(1 - \cos\Theta)} \tag{2.25}$$

where Θ is the rest frame photon scattering angle. In general, the value of Θ may be calculated using:

$$\cos\Theta = \cos\theta' \cos\theta'_1 + \sin\theta' \sin\theta'_1 \cos(\phi' - \phi'_1) \tag{2.26}$$

where ϕ' and ϕ'_1 are the azimuthal angles of the photon in K' before and after scattering (See Appendix D). This rather complicated angular dependence can be usefully simplified for ultra-relativistic electrons using the commonly applied *head-on* approximation for IC scattering, whereby $\theta' = \pi$ is assumed for all incident photons [e.g. 140, 77, 76]. To motivate this assumption, consider Figure 2.6, which illustrates the relationship between θ and θ' for various electron Lorentz factors. As $\beta \to 1$ the incidence angles of almost all photons in K' are concentrated into a narrow cone with opening angle $\sim 1/\gamma$ about $\theta' = \pi$. Indeed, the approximation $\theta' = \pi$ only breaks down for those photons having momenta almost parallel to the electron velocity in K. Moreover, Figure

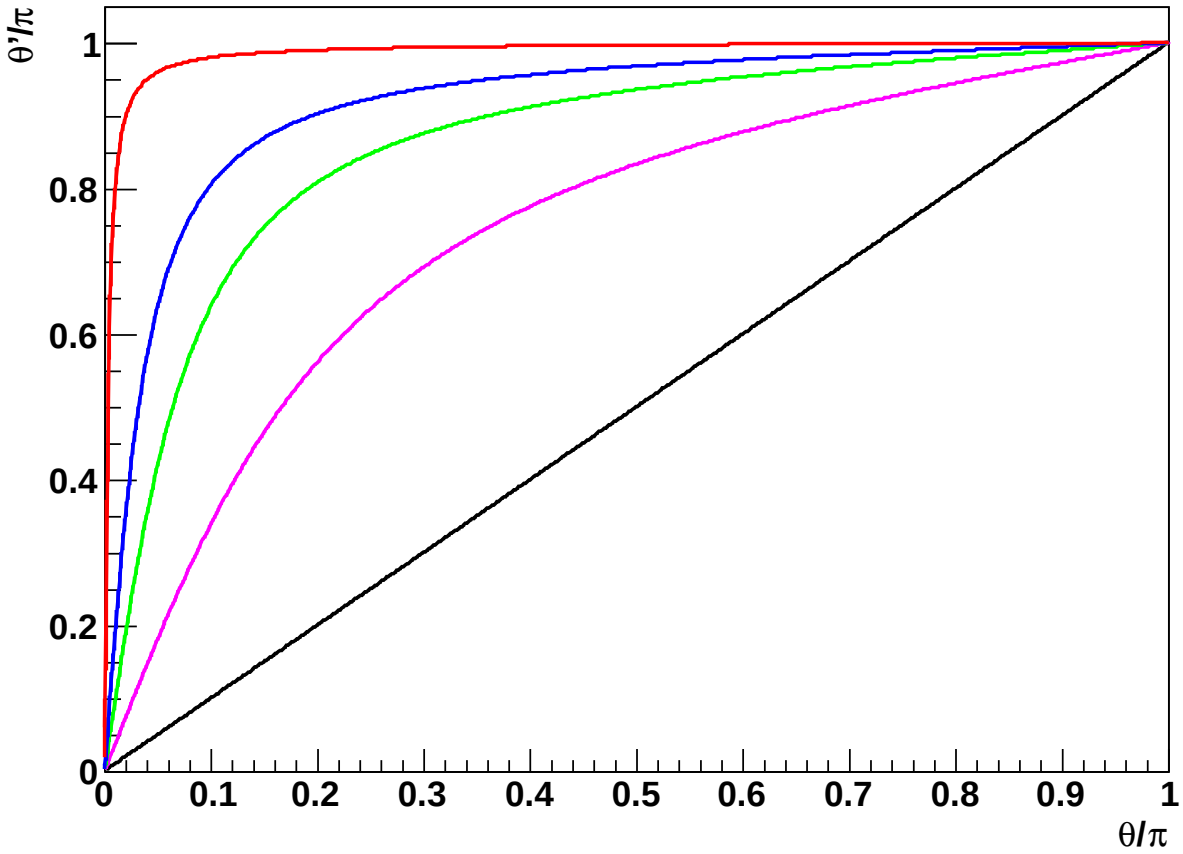

Figure 2.6: Illustration of the relationship between θ and θ' for various electron Lorentz factors. The individual curves correspond to $\gamma = 1$ (black), $\gamma = 2$ (magenta), $\gamma = 5$ (green), $\gamma = 10$ (blue) and $\gamma = 100$ (red).

2.7 reveals that photons for which $\theta \approx 0$ in K are Doppler de-boosted in K' and have a negligible effect on the electron energy [43]. Adopting the head-on approximation, $\Theta \rightarrow \theta_1$ and transforming back into K yields the observed energy of the scattered photon:

$$\epsilon_1 = \gamma\epsilon_1' \left[1 + \beta\cos(\pi - \theta_1')\right] \approx \gamma\epsilon_1'(1 - \cos\theta_1') \tag{2.27}$$

In the *Thomson Limit* ($\epsilon' \ll mc^2$) $\epsilon_1' \approx \epsilon'$ and combining (2.24) and (2.27) yields the familiar

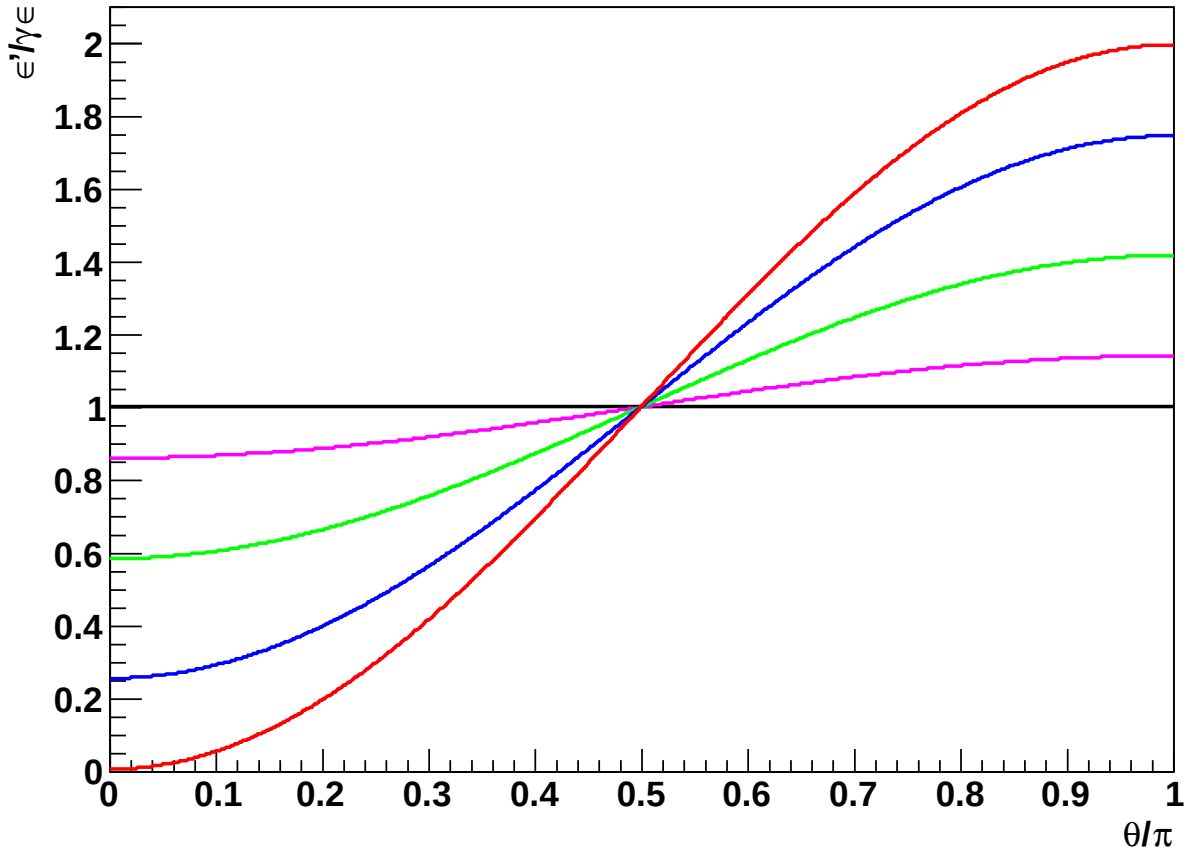

Figure 2.7: Graphical representation of the relativistic Doppler effect for various electron Lorentz factors. The individual curves correspond to $\gamma = 1$ (black), $\gamma = 1.01$ (magenta), $\gamma = 1.1$ (green), $\gamma = 1.5$ (blue) and $\gamma = 10$ (red).

expression for the maximum energy gain of the scattered photon:

$$\epsilon_1^{\max} \approx 2\gamma\epsilon_1^{\max\prime} \approx 4\gamma^2\epsilon \tag{2.28}$$

Clearly, for $\gamma \gg 1$, enormous boosts in photon energy are possible and IC scattering provides an excellent mechanism for the production of VHE γ-rays from a much softer photon population.

Maintaining the head-on approximation, the expected scattering rate is most easily computed in the electron rest frame and may be expressed in terms of the differential Compton cross-section

$d\sigma$ as:

$$\frac{dN'}{dt'} = c \iint \frac{d\sigma}{d\epsilon_1' d\Omega_1'} n'(\epsilon_1', \Omega_1') d\epsilon_1' d\Omega_1' = c \int \frac{d\sigma}{d\epsilon_1' d\Omega_1'} dn' \tag{2.29}$$

where $dn' = n'(\epsilon_1', \Omega_1') d\epsilon' d\Omega_1'$ is the number of photons per unit volume in K', which are scattered with energies within $d\epsilon_1'$ into the the solid angle element $d\Omega_1'$ about θ_1', and $d\sigma/d\epsilon' d\Omega_1'$ is given by the Klein-Nishina formula [e.g. 43]:

$$\frac{d\sigma}{d\Omega_1' d\epsilon_1'} = \frac{r_0^2}{2} \left(\frac{\epsilon_1'}{\epsilon'}\right)^2 \left(\frac{\epsilon'}{\epsilon_1'} + \frac{\epsilon_1'}{\epsilon'} - \sin^2\theta_1'\right) \delta\left(\epsilon_1' - \frac{\epsilon'}{1 + (\epsilon'/mc^2)(1 - \cos\theta_1')}\right) \tag{2.30}$$

In the observer frame, the energy lost by the electron as a result of each scattering event is simply $\epsilon_1 - \epsilon$. In almost all cases of interest, ϵ is much smaller than ϵ_1 and can be neglected [43]. Furthermore, if $\epsilon' \ll mc^2$, then the scattering in K' is effectively elastic and $\epsilon_1' = \epsilon'$. Consequently, equating the electron's energy loss rate (dE_e/dt) to the Lorentz invariant radiated power yields:

$$-\frac{dE_e}{dt} = \frac{dW'}{dt'} = c \int \frac{d\sigma}{d\epsilon_1' d\Omega_1'} \epsilon' dn' \tag{2.31}$$

Using the Lorentz invariance of the quantity [43]:

$$\frac{dn}{\epsilon} = \frac{dn'}{\epsilon'} \tag{2.32}$$

together with (2.24), yields:

$$-\frac{dE_e}{dt} = c\gamma^2 \int \frac{d\sigma}{d\Omega_1' d\epsilon_1'} \epsilon (1 - \beta\cos\theta)^2 dn \tag{2.33}$$

In the Thomson limit where $\epsilon' \ll mc^2$ and assuming an isotropic distribution of photon momenta in K, (2.33) reduces to [43]:

$$-\frac{dE_e}{dt} = \frac{4}{3} \sigma_T c \gamma^2 U_{\rm iso} \tag{2.34}$$

where σ_T is the Thomson cross-section and $U_{\rm iso}$ ambient radiation density in K. The corresponding

expression in the extreme Klein-Nishina regime $\epsilon' \gg mc^2$ is [43]:

$$-\frac{dE_e}{dt} = \pi r_0 m^2 c^5 \int \frac{n(\epsilon)}{\epsilon} \left(\ln \frac{4\epsilon\gamma}{mc^2} - \frac{11}{6} \right) d\epsilon \tag{2.35}$$

The characteristic cooling time for IC scattering in the Thomson limit is therefore defined as:

$$t_{\rm cool}^{\rm IC} = \frac{E_e}{dW/dt} = \frac{3m^2c^3}{4\sigma_T E_e U_{\rm iso}} \tag{2.36}$$

If scattering takes place deep in the Klein-Nishina regime, the electron may lose a significant proportion of its energy during each scattering event. The characteristic cooling time is therefore somewhat more difficult to predict, but can be approximated with good accuracy by [148]:

$$t_{\rm cool}^{\rm IC,KN} \approx 1.7 \times 10^2 U_{\rm iso}^{-1} E_{e,\rm TeV}^{0.7} \text{ s} \tag{2.37}$$

where as before, $E_{e,\rm TeV}$ is the electron energy in TeV.

2.4.2 Inverse-Compton Spectrum for a Single Electron

To derive the IC spectrum for a single electron with energy $E_e = \gamma mc^2$, [43] consider the spectrum of photons from a mono-directional beam of photons having energies ϵ within $d\epsilon$. The final spectrum is then obtained by integration of the individual beam spectra over all possible photon energies and incidence angles.

The full derivation is straightforward but extended and for simplicity only the final result is reiterated here. For an isotropic population of target photons, the general expression for the rate at which photons with initial energy ϵ which are scattered by an ultra-relativistic electron having Lorentz factor $\gamma \gg 1$ and emerge with energy $\epsilon_1 \equiv E_1/\gamma mc^2$ is [e.g. 140, 43]:

$$\frac{dN_{\gamma,\epsilon}}{dtdE_1} = \frac{2\pi r_0^2 mc^3}{\gamma} \frac{n(\epsilon)d\epsilon}{\epsilon} G(q) \tag{2.38}$$

where:

$$G(q,\Gamma_e) = \left[2q\ln q + (1+2q)(1-q) + \frac{1}{2}\frac{(\Gamma_e q)^2}{1+\Gamma_e q}(1-q)\right] \tag{2.39}$$

and:

$$\Gamma_e = \frac{4\epsilon\gamma}{mc^2}, \qquad q = \frac{E_1}{\Gamma_e(1-E_1)} \tag{2.40}$$

Kinematically, the absolute upper limit to ϵ_1 is achieved when *all* of the electron's kinetic energy is transferred to the scattered photon:

$$\epsilon_1^{\max} = \epsilon + (\gamma mc^2 - mc^2) \tag{2.41}$$

In reality, this limit is almost never reached because it requires that the incident photon momentum be comparable to or greater than that of the scattering electron. In the more feasible scenario, where the momentum of the electron dominates, the allowed range of E_1 is given by [140, 43]:

$$1 \gg \frac{\epsilon}{\gamma mc^2} \leq E_1 \leq \frac{\Gamma_e}{1+\Gamma_e} \tag{2.42}$$

where the lower limit obviously corresponds to no energy transfer.

2.4.3 Inverse-Compton Spectrum for many Electrons

Employing the head-on approximation, the otherwise general expression for the IC spectrum produced by an ensemble of electrons is obtained by integration over the initial electron and photon distributions:

$$\frac{dN_{tot}}{dtd\epsilon_1} = \int_0^{4\pi} d\Omega_e \int_{\epsilon_1}^{\epsilon_2} d\epsilon \int_{\gamma_{\min}}^{\gamma_{\max}} d\gamma \frac{dN_{\gamma,\epsilon}}{dtdE_1}\frac{dE_1}{d\epsilon_1} \tag{2.43}$$

where the limits on the energy integral follow from (2.40).

It is evident that in the general case, the spectrum of IC scattered radiation depends critically upon energy spectra of the incident electron and photon populations. Moreover, the angular dependencies of the photon energies in the electron rest frame and IC scattering cross-section,

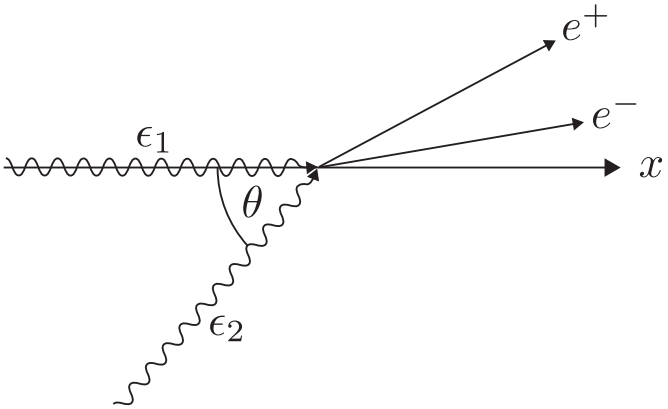

Figure 2.8: Illustration of the process $\gamma + \gamma \rightarrow e^- + e^+$.

render the *observed* γ-ray flux sensitive to anisotropies in the angular distributions of the scattering particles.

2.5 Absorption of VHE γ-rays

A VHE γ-ray propagating through a soft radiation field may interact with a low energy photon and produce an electron positron pair [111]:

$$\gamma + \gamma \rightarrow e^- + e^+ \tag{2.44}$$

Figure 2.8 illustrates the general scenario whereby a high energy photon propagating in the positive x direction interacts with a low energy photon which is incident at an angle θ to the x-axis. Clearly, pair production can only occur if the combined photon energies in the centre-of-momentum frame exceed twice the electron rest mass energy:

$$s = \frac{\epsilon_1 \epsilon_2 (1 - \cos\theta)}{2m^2c^4} > 1 \tag{2.45}$$

Above this threshold, the total cross-section for unpolarised photons is given by [137]:

$$\sigma_{\gamma\gamma} = \frac{\pi r_0^2(1-\beta^2)}{2}\left[(3-\beta^4)\ln\frac{1+\beta}{1-\beta} - 2\beta(2-\beta^2)\right] \tag{2.46}$$

where:

$$\beta = \sqrt{1-\frac{1}{s}} \tag{2.47}$$

In fact, the maximum interaction cross section occurs for $s \approx 1$ [111], so that 1 TeV γ-rays interact optimally with visible and ultraviolet photons having energies of a few electron-volts. The differential optical depth $d\tau_{\gamma\gamma}$ per unit path length dl, due to soft photons with number density $n(\epsilon_2)$, having energies within $d\epsilon_2$ and incident from the solid angle element $d\Omega_\theta$ is simply [85]:

$$d\tau_{\gamma\gamma} = n(\epsilon_2)\sigma_{\gamma\gamma}(1-\cos\theta)d\epsilon_2 d\Omega_\theta dl \tag{2.48}$$

The total optical depth for a γ-ray traversing a soft radiation field is then obtained by integrating (2.48) over all solid angles and soft photon energies along the path from its source to infinity:

$$\tau_{\gamma\gamma} = \int_0^\infty dl \int_0^{4\pi} d\Omega_\theta \int_{\epsilon_{2,\min}}^{\epsilon_{2,\max}} d\epsilon_2 \frac{d\tau_{\gamma\gamma}}{d\epsilon_2 d\Omega_\theta dl} \tag{2.49}$$

The absorption of VHE γ-rays by pair production can significantly affect the observed GeV-TeV spectra of X-ray binaries. In particular, the dense ultraviolet radiation fields produced by the companion stars in high-mass systems should strongly suppress the emitted VHE γ-ray flux. However, the angular dependence of $\sigma_{\gamma\gamma}$ implies a strong dependence of $\tau_{\gamma\gamma}$ on the relative orientation of the γ-ray and soft photon sources with respect to the observer's line-of-sight [e.g. 85]. Indeed, the effect is sufficiently pronounced that for a TeV photon propagating directly away from a luminous source of optical and ultraviolet photons ($\cos\theta \approx 1$), the optical depth for pair production is effectively zero.

The effect of e^+e^- pair production on the observed γ-ray spectrum depends primarily on the dominant cooling mechanism for relativistic electrons within the source. If $t_{\rm cool}^{\rm sync} \ll t_{\rm cool}^{\rm IC}$, then the

secondary $e^{\pm}$ pairs produced in the absorption process will radiate the bulk of their energy as low energy photons, and the VHE γ-ray emission is strongly attenuated. In contrast, if the ambient magnetic field is low enough that inverse-Compton losses dominate, then efficient *electromagnetic cascades* may be initiated, whereby repeated cycles of pair production and IC scattering can replenish the absorbed γ-ray spectrum.

2.6 Bulk Relativistic Sources

The formulae presented in the preceding sections define the spectral properties which would be measured by an observer who is stationary with respect to the radiation source. In reality, the radiating material in many astrophysical γ-ray sources exhibits large and often relativistic bulk motion. This section discusses the transformations which must be applied to predict the observed spectral characteristics in a rest frame which moves relativistically with respect to a radiation source.

2.6.1 Doppler Boosting

The phenomenon of *Doppler boosting* describes the effect of a bulk relativistic source's motion on the observed flux or luminosity at a specific photon energy. For an optically thin source, writing the observed flux S_ϵ in terms of the volume emissivity in the observer's rest frame, j_ϵ yields [1]:

$$S_\epsilon = \frac{\int j_\epsilon dV}{d^2} \tag{2.50}$$

where dV is an element of the observed source volume and d is the source distance. The volume emissivity can be expressed in terms of the number density of radiating particles n moving within the solid angle element $d\Omega$ and having energies within $d\epsilon$:

$$j_\epsilon = n\frac{dW}{dtd\Omega d\epsilon} \tag{2.51}$$

where dW/dt is the single particle loss rate corresponding to the emission of photons having energies within $d\epsilon$. To derive the volume emissivity in the co-moving frame of the relativistic source, each of the terms in (2.51) must be appropriately transformed. The relevant expressions are simplified by first defining the Doppler factor for a radiating source moving with velocity $v = \beta c$ at an angle θ to the line-of-sight:

$$\delta = \frac{1}{\Gamma(1 - \beta \cos\theta)} \tag{2.52}$$

where $\Gamma = (1 - \beta^2)^{-1/2}$ is the source's bulk Lorentz factor. The observer frame (unprimed) and source frame (primed) quantities are then related by [e.g. 1, 218]:

$$d\epsilon' = \delta^{-1} d\epsilon \tag{2.53}$$

$$dW' = \delta^{-1} dW \tag{2.54}$$

$$dt' = \delta^{-1} dt \tag{2.55}$$

$$n' = \Gamma^{-1} n \tag{2.56}$$

$$d\Omega' = \delta^2 d\Omega \tag{2.57}$$

$$dV' = \Gamma dV \tag{2.58}$$

where it should be noted that dt refers to the time interval during which the emitted radiation is *received* by in the observer's rest frame and therefore $dt' \neq \Gamma^{-1} dt$, as one might expected. In combination, these transformations imply:

$$j'_{\epsilon'} dV' = \delta^{-3} j_\epsilon dV \tag{2.59}$$

Combining 2.50 and 2.59 yields an expression for the observed flux in terms of the radiative quantities in the source rest frame:

$$S_\epsilon(\epsilon) = \delta^3 \frac{\int j'_{\epsilon'}(\epsilon') dV'}{d^2} \tag{2.60}$$

so that for a source with a power law photon spectrum $j'_{\epsilon'}(\epsilon') \propto (\epsilon')^{-\alpha}$, the observed flux at a specific frequency may be written as:

$$S_\epsilon(\epsilon) = \delta^{3+\alpha} \frac{\int j'_{\epsilon'}(\epsilon) dV'}{d^2} \tag{2.61}$$

where it should be noted that $j'_{\epsilon'}$ is now evaluated at the *observed* photon frequency. If the source is spherical, then the transformation between the observed and intrinsic luminosities may be obtained by integrating over energy and volume to give [1]:

$$L = \delta^4 L' \tag{2.62}$$

which indicates that L can be strongly affected if the radiation source moves at relativistic velocities.

As noted by [173], the angular dependence of the Doppler factor implies that for sources moving close to the line-of-sight with $\theta < 1/\Gamma$, $\delta \approx \Gamma$ and strong enhancements of the observed flux are expected. Conversely, if $\theta \gtrsim 1$ then $\delta \lesssim \Gamma^{-1}$ and the emitted radiation is Doppler *de-boosted* with the observed flux being reduced with respect to its intrinsic value.

2.6.2 Superluminal Motion

Superluminal motion is a geometrical phenomenon whereby bulk relativistic radiation sources exhibit apparent velocities in excess of c. Although it does not affect the spectral properties of the observed radiation, superluminal motion provides an unambiguous, quantitative indicator of bulk relativistic motion and may also constrain the angle of that motion with respect to the line-of-sight. As such, it provides an indirect indication of the expected levels of Doppler boosting affecting the observed spectrum.

Interestingly, the existence of this effect was predicted by [198] several years before its occurrence in nature was observationally verified [65]. Figure 2.9 illustrates the assumed geometry for the following derivation, which reveals the origin of the apparently superluminal bulk velocities.

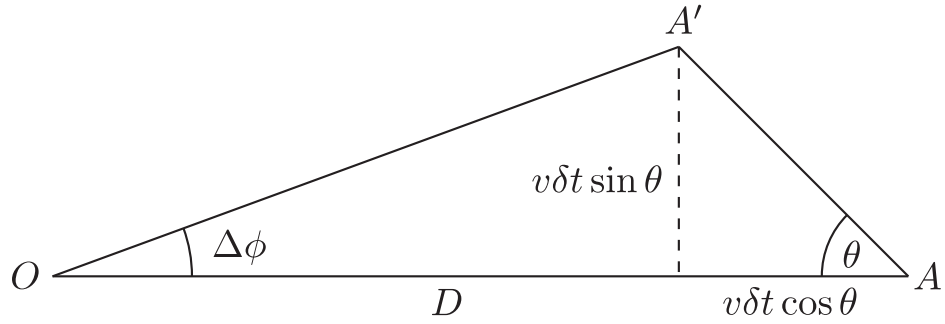

Figure 2.9: The geometry of superluminal motion.

Suppose that two radiation sources are ejected from A at some time t_1. This event is seen by an observer O at some later time t_1'. After some interval δt one of the emitters has travelled a distance $v\delta t$ and reaches A′ at time t_2. When the observer sees this happen at $t = t_2'$, the angular separation of the two objects on the sky is $\Delta\phi$, given by:

$$\Delta\phi = \frac{v\delta t \sin\theta}{D}. \tag{2.63}$$

Since the total distance from O to A is $D + v\delta t\cos\theta$, it follows that t_1 and t_1' are related via:

$$t_1' = t_1 + \frac{D + v\delta t\cos\theta}{c}. \tag{2.64}$$

If $\Delta\phi$ is small, implying motion close to the line-of-sight, then the distance from A' to O is approximately D and therefore:

$$t_2' = t_2 + \frac{D}{c}. \tag{2.65}$$

Subtracting (2.64) and (2.65) yields the interval $\Delta t = t_2' - t_1'$:

$$\begin{aligned}\Delta t &= t_2 - t_1 + \frac{D}{c} - \frac{D + v\delta t\cos\theta}{c} \\ &= t_2 - t_1 - \frac{v\delta t\cos\theta}{c} \\ &= \delta t(1 - \beta\cos\theta)\end{aligned} \tag{2.66}$$

where, as in §2.6.1, $\beta = v/c$. Consequently, the *observed* transverse velocity of the blob in moving from A to A' may be expressed as:

$$\begin{aligned}\beta_T &= \frac{v_T}{c} = \frac{D}{c}\frac{\Delta\phi}{\Delta t} \\ &= \frac{v\sin\theta}{c(1-\beta\cos\theta)} = \frac{\beta\sin\theta}{1-\beta\cos\theta}.\end{aligned} \tag{2.67}$$

Observing that the apparent transverse velocity is a function of the viewing angle and maximising (2.67) with respect to θ yields:

$$\beta_T^{\max} = \beta\Gamma. \tag{2.68}$$

when $\theta_{\max} = \cos^{-1}\beta$. In the limit as $\beta \to 1$ then $\beta_T^{\max} \to \Gamma$ implying that apparent transverse velocities in excess of c can be achieved for mildly relativistic ($v \gtrsim 0.7c$) motions close to the line of sight.

Finally, by rearranging (2.67), and noting that $\beta < 1$, the magnitude of the observed transverse velocity may also be used to constrain the possible range of θ [173]:

$$\frac{\beta_T - 1}{\beta_T + 1} < \cos\theta < 1 \tag{2.69}$$

2.7 Computer Models

This section briefly introduces two computer simulations describing radiative emission and absorption which are based on previously published numerical models. The predictions of these simulations are compared with the observed VHE γ-ray flux of the known γ-ray binary LS 5039 in Chapter 3. The source code for both model implementations can be found in Appendix E.2.

2.7.1 Synchrotron Self-Compton Model

Fundamentally, synchroton self-Compton (SSC) emission entails the inverse-Compton up-scattering of synchrotron photons by their parent electron population. Given a sufficiently energetic electron

population, perhaps in combination with relativistic bulk motion, large fluxes of high energy photons can be produced. Indeed, SSC emission in relativistic outflows is considered to be one of the most likely mechanisms for the leptonic production of VHE γ-rays in blazar type AGN.

Following the approach of [100], a simple model for the SSC emission from a spherical, homogeneous and bulk relativistic electron gas has been implemented. The model assumes all of the simplifications discussed in Sections 2.3 and 2.4. Namely, the source is assumed to be embedded in a tangled magnetic field with uniform intensity, and to contain a population of electrons with isotropic velocities and a time independent distribution of Lorentz factors. Expressions for the *observed* synchrotron and SSC fluxes are presented by [100] and follow from the derivations in Sections 2.3 and 2.4. Denoting quantities defined in the source rest frame with primes, and using the definition of $J_{\rm sync}$ from (2.17), the specific synchrotron flux $S_\epsilon^{\rm sync}(\epsilon)$ which is seen by a stationary observer may be calculated using:

$$S_\epsilon^{\rm sync} = \frac{\delta^4 \epsilon'}{4\pi d^2} J'_{\rm sync}(\epsilon') \tag{2.70}$$

where δ is the Doppler factor corresponding to the bulk motion of the source, d is the source distance. An expression for the observed SSC flux $S_\epsilon^{\rm SSC}$ at a specific photon energy ϵ is given in terms of quantities in the source rest frame by [100]:

$$S_\epsilon^{\rm SSC} = \frac{9\sigma_T \epsilon'^2 mc^2}{16\pi R'^2} \int_0^\infty d\tilde{\epsilon}' \frac{S_{\tilde{\epsilon}'}^{\rm sync}}{\tilde{\epsilon}'^3} \int_{\gamma'_{\rm min}}^{\gamma'_{\rm max}} d\gamma' \frac{N'(\gamma')}{\gamma'^2} G'(q, \Gamma_e) H\left(q; \frac{1}{4\gamma^2}, 1\right) \tag{2.71}$$

where σ_T is the Thomson cross section, R' is the source radius, $N'(\gamma')$ is the distribution of electron Lorentz factors $G'(q, \Gamma_e)$ is as defined in (2.39) and the Heaviside function:

$$H(x, x_1, x2) = \begin{cases} 1 \text{ if } x_1 \leq x \leq x_2 \\ 0 \text{ otherwise} \end{cases} \tag{2.72}$$

A complete derivation of (2.70) and (2.71) is given in [100].

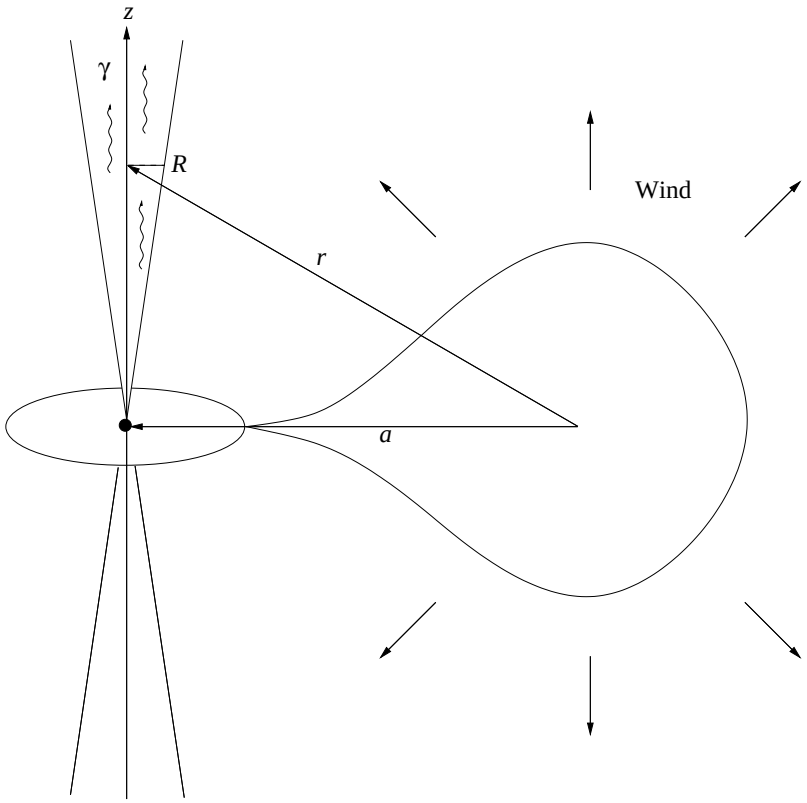

Figure 2.10: Schematic of the morphological assumptions of the model due to [209]

2.7.2 A Neutral Pion Decay Model

This section describes the adapted implementation of a model originally proposed by [209], which predicts the radiative emission resulting from the decay of neutral pions produced by the interaction of a relativistic jet and a stellar wind in a HMXB. Although the following derivation closely follows that presented by [209], several typographical errors in the originally published formulae have been corrected.

Figure 2.10 illustrates the physical scenario which this model is designed to simulate. The jet has a bulk Lorentz factor Γ and is launched some distance z_0 above the event horizon of the black hole. The cross-sectional radius R parameterised in terms of z the height above the black hole.

$$R(z) = \xi z^{\epsilon} \tag{2.73}$$

such that $\epsilon = 1$ corresponds to a conical jet. The energy distribution of the entrained proton

population in the jet rest frame is in the form of a power law,

$$N'_p(E) = K_p E'^{-\beta} \tag{2.74}$$

where K_p is the proton spectrum normalisation. Since the jet expands, the value of K_p must be a function of z.

$$K_p(z) = K_0 \left(\frac{z_0}{z}\right)^{\epsilon n}. \tag{2.75}$$

Combining (2.73) and (2.74), the flux of protons in the jet as a function of z can be obtained.

$$J'_p(E) = \frac{c}{4\pi} K_0 \left(\frac{z_0}{z}\right)^{\epsilon n} E'^{-\beta}_p. \tag{2.76}$$

This is the flux in the co-moving jet frame. Transforming into the observer frame yields

$$J_p(E) = \frac{c}{4\pi} K_0 \left(\frac{z_0}{z}\right)^{\epsilon n} \frac{\Gamma^{1-\beta}(E_p - \beta_b \sqrt{E_p^2 - m_p^2 c^4}\cos\theta)}{\left[\sin^2\theta + \Gamma^2 \left(\cos\theta - \frac{\beta_b E_p}{\sqrt{E_p^2 - m_p^2 c^4}}\right)^2\right]^{\frac{1}{2}}}, \tag{2.77}$$

where $\beta_b = \sqrt{1 - \Gamma^{-1}}$. Note that this expression is dependent upon θ, the viewing angle of the observer in relation to the jet axis. This is a result of the angular dependence of the relativistic Doppler boost.

K_0 is the normalisation of the proton spectrum at z_0 and can either be defined arbitrarily as a spectral fitting parameter or more consistently related to the mass accretion rate. Defining the jet power as

$$Q_j = q_j \dot{M}_{\rm disk} c^2, \tag{2.78}$$

where q_j quantifies the fraction of accretion power recycled into the jet, with typical values $10^{-3} \lesssim q_j \lesssim 10^{-1}$ [e.g. 88, 89]. Consequently, the integrated number density of particles flowing in the jet

at $R_0 = R(z_0)$, n'_0, can be defined via

$$c\pi R_0^2 n'_0 = \frac{Q_j}{m_p c^2}. \tag{2.79}$$

Using the alternative definition of n'_0,

$$n'_0 = \int_{E'^{\min}_p}^{E'^{\max}_p} N'_p(E'_p, z_0) dE'_p = \int_{E'^{\min}_p}^{E'^{\max}_p} K_0 E'^{-\beta} dE'_p, \tag{2.80}$$

the definition of K_0 becomes

$$K_0 = n'_0(\beta - 1)(E'^{\min}_p)^{\beta-1} = \frac{q_j \dot{M}_{\rm disk}}{m_p c \pi R_0^2}(\beta - 1)(E'^{\min}_p)^{\beta-1} \tag{2.81}$$

The stellar wind is modelled as a supersonic and spherical outflow of matter from the companion star. The velocity of the wind as a function of radial distance from the star is defined by

$$v(r) = v_\infty \left(1 - \frac{r_\star}{r}\right)^\delta = \frac{\dot{M}_\star}{4\pi r^2 \rho(r)}, \tag{2.82}$$

where v_∞ is the terminal velocity of the wind, $\dot{M}_\star$ is the stellar mass loss rate, $\rho(r)$ is the density of the wind, and $\delta \sim 1$ for massive O-type stars.

Assuming a wind dominated by protons, the particle density in the region of the jet at some height z is given by

$$n(z) = \frac{\dot{M}_\star}{4\pi m_p v_\infty (a^2 + z^2)} \left(1 - \frac{r_\star}{\sqrt{a^2 + z^2}}\right)^{-\delta}, \tag{2.83}$$

The interaction cross section for the inelastic proton-proton scattering process can be defined above $E_p \approx 10$ GeV as

$$\sigma_{pp}(E_p) \approx 30 \times [0.95 + 0.6 \log(E_p/\text{GeV})] \,\text{mb}. \tag{2.84}$$

β value	$Z^{(\beta)}_{p\to\pi^0}$
2	0.17
2.2	0.092
2.4	0.066
2.6	0.048
2.8	0.036

Table 2.1: Values of $Z^{(\beta)}_{p\to\pi^0}$ corresponding to different values of β. Note that an approximate value for all β may be obtained via $Z^{(\beta)}_{p\to\pi^0} \approx \frac{\beta+1}{2}10^{(1.49-2.73\beta+0.53\beta^2)}$ [84].

where $E_p \approx 10E_\gamma$. The differential γ-ray emissivity from π^0 decays is then given by

$$q_\gamma(E_\gamma) = 4\pi\sigma_{pp}(E_p)\frac{2Z^{(\beta)}_{p\to\pi^0}}{\beta}J_p(E_\gamma,\theta)\eta_A, \tag{2.85}$$

where η_A is a weighting factor which compensates for the abundance of heavy nuclei in the stellar wind (typically $\eta_A = 1.4-1.5$) and $Z^{(\beta)}_{p\to\pi^0}$ is the spectrum weighted moment of the inclusive cross section. Values of $Z^{(\beta)}_{p\to\pi^0}$ corresponding to various values of β are shown in Table 2.1. The γ-ray intensity due to some volume V of interacting protons is found by integrating the product of the wind proton number density and the differential emissivity over that volume.

$$I_\gamma(E_\gamma,\theta) = \int_V n(\mathbf{r}')q_\gamma(\mathbf{r}')d^3\mathbf{r}' \tag{2.86}$$

Finally, an expression is obtained for the γ-ray luminosity above 10 GeV due to π^0 decay in a given direction θ i.e. $L^{\pi^0}_\gamma(E_\gamma,\theta) = E^2_\gamma I_\gamma(E_\gamma,\theta)$. Substituting yields

$$\begin{aligned} L^{\pi^0}_\gamma(E_\gamma,\theta) = E^2_\gamma &\frac{q_j z_0^{\epsilon(n-2)} Z^{(\beta)}_{p\to\pi^0}\eta_A}{2\pi m_p^2 v_\infty}\frac{\beta-1}{\beta}(0.1E_p'^{\min})^{\beta-1} \\ &\times \dot{M}_\star\dot{M}_{\rm disk}\sigma_{pp}(10E_\gamma)\frac{\Gamma^{1-\beta}(E_\gamma-\beta_b\sqrt{E_\gamma^2-m_p^2c^4}\cos\theta)}{\left[\sin^2\theta+\Gamma^2\left(\cos\theta-\frac{\beta_b E_\gamma}{\sqrt{E_\gamma^2-m_p^2c^4}}\right)^2\right]^{\frac{1}{2}}} \\ &\times \int_{z_0}^{\infty}\frac{z^{\epsilon(n-2)}}{z^2+a^2}\left(1-\frac{r_\star}{\sqrt{a^2+z^2}}\right)^{-\delta}dz \end{aligned} \tag{2.87}$$

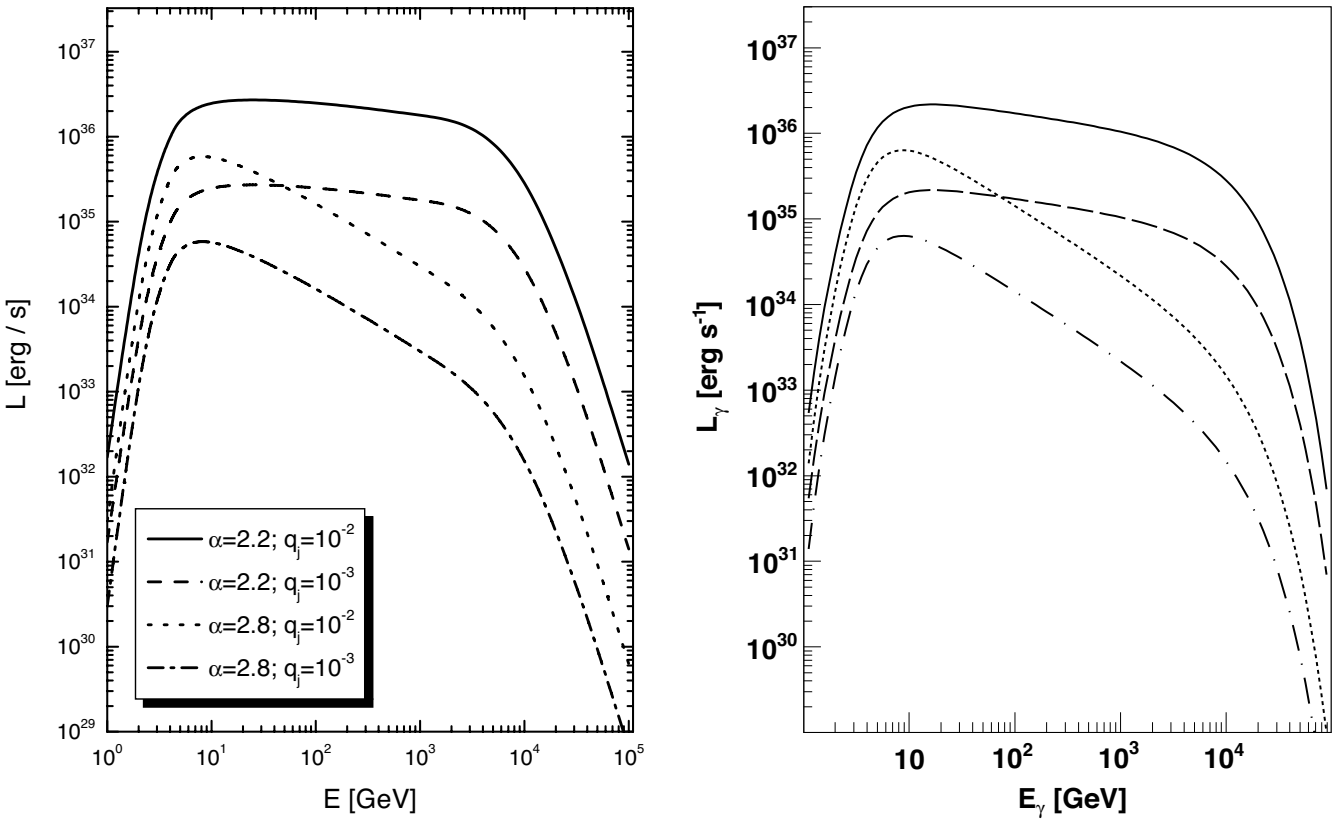

Figure 2.11: A comparison between the simulated γ-ray spectra presented by [209] (*left panel*) and those produced by the model implementation presented in this thesis (*right panel*).

Constructing a reliable simulation of this model was problematic because the model spectra presented by [209] correspond to the correct formulae and not to the erroneous expressions which were originally published. Nonetheless, the simulated γ-ray spectra illustrated in Figure 2.11 demonstrate that the final implementation accurately reproduces the results of [209] and can therefore be confidently compared with the H.E.S.S. observations of γ-ray binaries presented in later chapters.

2.7.3 γ-γ Absorption Model

An implementation of the γ-ray absorption model developed by [85] has been created. This model simulates the γ-ray absorption in X-ray binary systems due to electron-positron pair production in the radiation field of the stellar companion. The γ-ray source is assumed to be point-like and

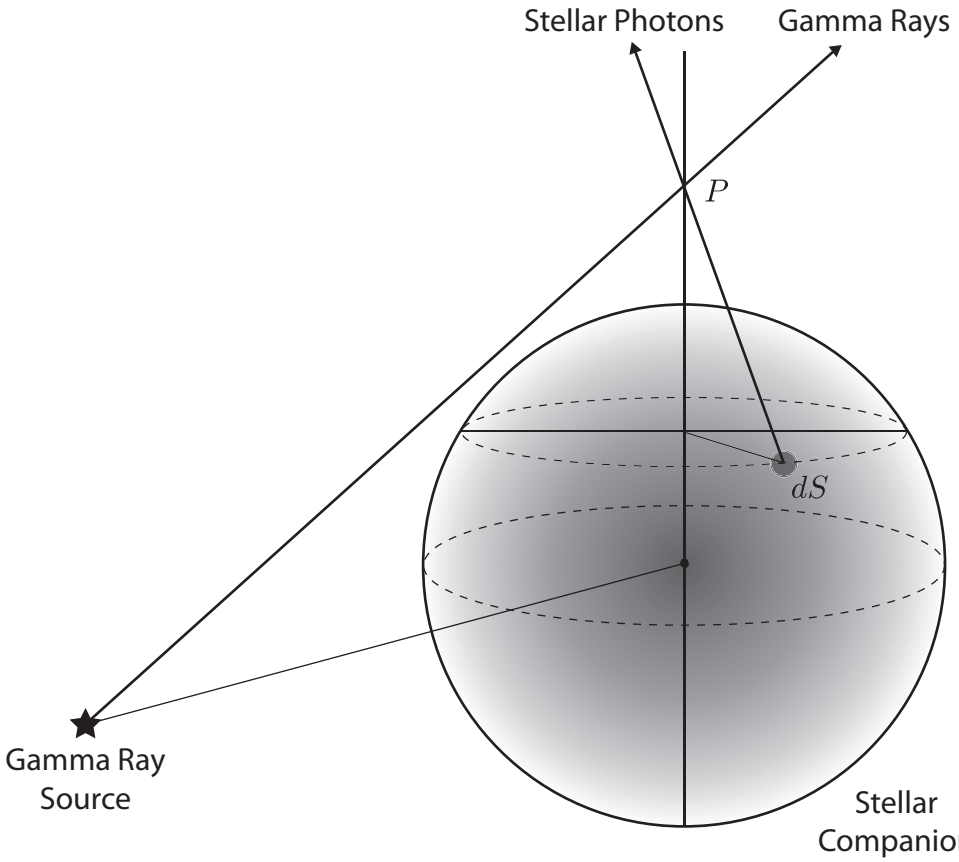

Figure 2.12: The geometry for the γ-ray absorption model developed by [85].

close to the compact object while the companion star is treated as a spherical blackbody with an assumed temperature and radius. Figure 2.12 provides a simple illustration of the assumed geometry. At a specific point P along the γ-ray trajectory, the specific number density $n(\epsilon)$ of stellar photons is obtained by integrating the contributions from all visible elements dS of the stellar surface. The value of n may then be used in conjunction with the angular distribution of the stellar photons and (2.48) to calculate the differential optical depth $d\tau_{\gamma\gamma}$ for pair production at P. The overall optical depth $\tau_{\gamma\gamma}$ is then obtained by integrating along the γ-ray trajectory to infinity.

The magnitude of $\tau_{\gamma\gamma}$ for a given stellar spectrum depends strongly on the relative orientation of the γ-ray source and the companion star with respect to the line of sight and also the energy of the γ-rays being absorbed. The simulation is able to predict the level of absorption as a function

of γ-ray energy at a given orbital phase *or* as a function of orbital phase for a given γ-ray energy. A detailed derivation of the model is presented by [85] and, since the implemented approach is essentially identical, it will not be repeated here.

Chapter 3

LS 5039

This chapter presents an extensive analysis of the VHE γ-ray emission from the high-mass binary system LS 5039 (RX J1826.2-1450). Simultaneously, it serves as an introduction to the analytical techniques that underpin the scientific results presented in this and succeeding chapters. Many of the methods and analyses described in this chapter are implemented as components of a standard *Heidelberg* software suite. This software is subject to continuous, collaborative development and is freely available for use by all members of the H.E.S.S. collaboration. Unless otherwise stated, results presented in this thesis were derived using this toolset.

3.1 Background and Observational History

At a distance of $\sim 2.5 - 3$ kpc [54, 204], LS 5039 is the optical counterpart of a high-mass, radio emitting X-ray binary system. It was associated with the faint X-ray source RX J1826.2-1450 by [184] following a cross-correlation of hot-spots in the ROSAT all-sky survey with the positions of known OB stars. Subsequent optical and near-infrared observations by [63] revealed a stable optical flux and permitted classification of the companion as an early type O6.5V((f)) star. Furthermore, the profiles of broad H_α absorption lines in the optical spectrum are indicative of a powerful stellar wind within the system [176].

Classification of the compact primary is somewhat problematic and remains a matter of some

debate. The masses of the binary components are related by the *mass function* [112]:

$$f(M) = \frac{M_{\rm co}^3 \sin^3 i}{(M_{\rm co} + M_\star)^2} \tag{3.1}$$

where $M_{\rm co}$ is the mass of the compact object, $M_\star$ is the mass of the companion, and i is the system inclination. The mass of the companion may be approximated spectroscopically using the derived surface gravity of the star in combination with an estimate of the stellar radius. For LS 5039, [54] derived $M_\star \sim 23 M_\odot$. Subsequent determination of the compact object mass relies upon an accurate estimate of the system inclination. The absence of eclipses in the X-ray lightcurve [199] constrains the system inclination to be $i \lesssim 64.6°$, while a strict lower limit follows from the breakup rotation velocity of the star, yielding $i \gtrsim 13°$ [54]. Presupposing pseudo-synchronisation between the rotational and orbital angular velocities of the companion star at periastron, [54] constrain the inclination to be $i = 24.9 \pm 2.8°$, corresponding to $M_c = 3.7^{+1.3}_{-1.0} {\rm M}_\odot$ and suggestive of a black hole. However, the assumption of pseudo-synchronicity is somewhat contrived and without this additional constraint the allowed range of M_c extends from 1.5 $\rm M_\odot$ to 8 $\rm M_\odot$. It follows that optical spectroscopy alone is unable to distinguish between a neutron star or a black hole.

Observations with the *Very Large Array* resulted in the detection of a persistent unresolved radio source within $0.1''$ of the nominal optical position of LS 5039 [171]. Follow-up observations with the *Very Long Baseline Array* succeeded in resolving milliarcsecond radio structures which were interpreted as mildly relativistic ($v \lesssim 0.4c$) bipolar jets by [194, 193], who categorised the system as a possible microquasar. The radio spectrum of LS 5039 exhibits a relatively steep photon index ($S_\nu \propto \nu^{-0.5}$), indicative of optically thin synchrotron emission [171, 206]. In contrast, the persistent radio spectra of most XRBs are characterised by flat or inverted radio spectra which only become steeper during transient outburst events [e.g 97, 93].

Various observations of LS 5039/RX J1826.2-1450 in the X-ray band indicate long term flux variations spanning a range $F_{3-30{\rm keV}} \sim 5 - 50 \times 10^{-12}$ ergs cm^{-2}s^{-1} [e.g. 199, 206, 45, 172]. In conjunction with the ephemeris of [54] (See Table 3.1), RXTE data presented by [45] indicate orbital modulation of the X-ray flux with the maximum emission observed close to periastron at

orbital phase $\phi \sim 0.8$. The X-ray spectrum is characterised by an absorbed power-law with a hard but variable photon index $1.3 \lesssim \Gamma \lesssim 1.8$ [e.g. 45, 172, 206] which is superficially reminiscent of the canonical low/hard state spectra of low mass X-ray binaries. However, there is no evidence of the rapid flux variation associated with the X-ray emission of LMXBs [206]. Accordingly, [45] suggested that the observed X-ray flux is dominated by synchrotron or inverse-Compton emission from the postulated radio jets. Furthermore, [45] found strong evidence for anti-correlation between Γ and the 3-30 keV flux. In the jet emission scenario, this behaviour would imply a variation in the efficiency of particle acceleration throughout the orbit.

The faintness of LS 5039 in the X-ray band, combined with an absence of ellipsoidal variability in the optical lightcurve [63], and a relatively large orbital separation [54] appear to preclude the possibility of Roche lobe overflow in the LS 5039 system. Instead it is likely that mass transfer is dominated by gravitational accretion from the stellar wind of the massive companion star [172]. This scenario is in contention with the predictions of appropriate *spherical* accretion models, which over-estimate the observed range of flux modulation by a factor of $\gtrsim 4$ [45]. Disc accretion could resolve the apparent discrepancy by buffering the accretion rate of the compact object, although an absence of emission features in the observed optical and X-ray spectra presents problems for this solution.

At MeV/GeV energies, [193] proposed an association between LS 5039 and the unidentified EGRET source 3EG J1824-1514 [118], attributing the γ-ray flux to inverse-Compton scattering in relativistic jets. The subsequent detection of a coincident VHE γ-ray source (HESS J1826-148) [6] exhibiting clear modulation of the GeV/TeV flux in phase with the optically determined period of LS 5039 [14] effectively confirmed this association. In contrast with the observed X-ray behaviour, the peak VHE γ-ray flux is observed close to inferior conjunction of the compact object at $\phi \approx 0.7$, while the minimum coincides with superior conjunction at $\phi \approx 0.06$. The apparent correlation of the observed γ-ray emission with epochs related to the observer's line-of-sight strongly indicates that the GeV/TeV flux is modulated by absorption within the system [e.g. 85](See §2.5).

The detection of VHE γ-rays from LS 5039 clearly implies an intrinsic population of particles

with multi-TeV energies (See Chapter 2). However, the processes which actually accelerate these particles remain somewhat uncertain, with two likely hypotheses competing in the literature. As mentioned previously, early models proposed a microquasar scenario [e.g. 193, 44], in which particle acceleration occurs at shocks in a relativistic outflow. Bipolar jets provide a natural explanation for the observed radio structure of LS 5039, while also implying a morphological parallel with VHE γ-ray emitting AGN. However, the absence of disc accretion signatures in the observed optical and X-ray spectra is difficult to reconcile with current theories of jet production. Alternatively, the observed emission may be driven by the spindown power of a young pulsar, with particle acceleration occurring at a termination shock, resulting from confinement of a relativistic pulsar wind by the stellar wind of the O-type companion [e.g. 167, 86]. This *binary plerion* scenario attributes the observed radio structure to cooling electrons in a cometary tail formed downwind of the shock. The proposed scenarios appear to be mutually exclusive, since the accepted paradigm for relativistic jet formation relies on disc accretion, which would be effectively inhibited by a powerful pulsar wind. Accordingly, an application was submitted for X-ray observations of LS 5039 using the *XMM Newton* satellite. The observations were designed to coincide with a newly revised estimate of the periastron passage of the compact primary, with the aim of diagnosing the presence of an accretion flow using the X-ray spectrum. If accretion were taking place, then enhanced mass transfer close to periastron should have maximised the chances of detecting its observational signatures. Observation of such signatures using an imaging X-ray telescope like *XMM Newton* would have effectively contradicted the binary plerion scenario. Unfortunately, the application was not successful. This was primarily due to the fact that previous observations with *XMM Newton* (albeit at markedly different orbital phases) had been unable to identify any evidence for accretion in the system.

Table 3.1 lists the orbital parameters and stellar properties for the LS 5039 system. These values will be assumed for all calculations in this chapter.

Table 3.1: The derived parameters of the LS 5039 system using the adopted orbital ephemeris of [54].

System Parameter	Value
$P_{\rm orb}$ (days)	3.90603 ± 0.00017
T_0 (HJD−2 451 000)	943.09 ± 0.10
e	0.35 ± 0.04
w (°)	225.8 ± 3.3
$f(M)$ ($M_\odot$)	0.0053 ± 0.0009
$M_\star$ ($M_\odot$)	23
$T_\star$ (K)	39000
$R_\star$ ($R_\odot$)	9.3

3.2 Data Quality and Run Selection

The validity of conclusions inferred from any scientific analysis is fundamentally dependent upon obtaining reliable, well calibrated data. Cherenkov telescope data are vulnerable to a number of electronic, mechanical and atmospheric factors which affect their quality, potentially rendering them unusable. This section discusses a number of metrics which are used to assess data quality, and outlines strategies for the exclusion of unreliable observations from scientific analyses.

3.2.1 Observing Strategy

For a data selection strategy to function effectively while simultaneously retaining a high data collection efficiency, an appropriate observing strategy is essential. Detecting the faint, transient Cherenkov light emitted by γ-ray-initiated air showers requires highly sensitive photodetectors with rapid response times, and a low level of background light. Consequently, IACTs can only operate during the hours of darkness and it is H.E.S.S. policy to observe exclusively during periods when the moon is below the horizon. This facilitates maximum suppression of unwanted noise due to background light sources and produces data of the highest possible quality.

The duty cycle of Cherenkov telescopes is also subject to seasonal variations in local weather. Although H.E.S.S. is located in a highly arid region of Namibia and rain is extremely rare for most of the year, atmospheric humidity can reach $> 90\%$ as air cools during the night. The high voltages required for operation of PMTs can lead to electrical arcing within the camera under such

conditions, rendering observations inadvisable or impossible. Furthermore, observational efficiency is often poor during the months of December and January which correspond to the Namibian rainy season.

Cherenkov telescopes are pointed instruments with a limited field-of-view. Consequently, identification of likely γ-ray sources and subsequent observational scheduling is required to maximise the operation efficiency of the instrument. Broadly speaking, the sensitivity of IACT arrays is maximised for targets near the zenith because this minimises the energy threshold and the typical spectra of VHE γ-ray sources are falling power laws in energy. Accordingly, the scheduling strategy dictates that non-time-critical observations are performed at highest possible elevation. Dedicated observations are typically performed using a *wobble mode* technique originally developed by the HEGRA collaboration [3, e.g.]. In normal wobble mode, the telescope pointing is offset by a small angle $0.5^\circ - 0.7^\circ$ in declination from the target position. The direction of the offset alternates between observations of a specific target within a single night, and the initial offset direction is alternated between subsequent nights of observation. Properly executed wobble mode observations permit the background of γ-raylike events to be estimated using the reflected background model described in §3.5.2 without the need for dedicated off-source runs. This effectively doubles the operational efficiency of the instrument.

H.E.S.S. observations are normally separated into individual *runs* lasting $\sim$ 28 minutes and the data are filtered on a run-wise basis. Complete runs are either rejected or retained depending on the values of the data quality metrics relative to a set of predefined thresholds. This somewhat conservative approach ensures that all data surviving run selection were obtained under near-optimal conditions, but may discard useful data from partially corrupted runs. In situations where the data are subject to transient periods of degradation, real-time monitoring of the data selection criteria facilitates judicious truncation of the affected runs at observation time. In this way, only data collected prior to the interruption of observation are lost, improving the overall data collection efficiency. Evidently, the filtering of observations on a run-wise basis results in the loss of high quality data from runs which are affected by sporadic episodes of degradation. Appendix B

describes an experimental approach which is currently in development and may effectively eliminate improve observational efficiency by filtering observational data on an event-wise basis.

3.2.2 Dead Camera Pixels

Reliable determination of the properties of an incident γ-ray is fundamentally dependent upon accurate imaging of the Cherenkov light pool. Deactivation or malfunction of PMTs in the telescope cameras may inhibit or corrupt derivation of the image shape parameters, introducing an unpredictable systematic effect into the event selection and reconstruction processes.

Active PMTs are vulnerable to damage if exposed to excessive illumination, and are therefore automatically deactivated when the anode current exceeds a threshold level of $120\mu A$. Once this *over-current* protection is in place, the affected pixel remains inactive for the remainder of the observation run. To minimise the instantaneous number of inactive PMTs, pixels corresponding to the positions of bright stars in the field-of-view are automatically deactivated and reactivated as the stellar images move across the camera. Failure to do this would result in lengthening arcs of dead pixels caused by field rotation as the telescope tracks. Furthermore, some PMTs may be voluntarily deactivated because of electronic malfunction as described by [9].

Deactivation of PMTs following illumination by unpredictable celestial (e.g. meteorites, satellites) and atmospheric (e.g. aircraft, lightning) phenomena cannot be compensated for and may result in large numbers of dead camera pixels.

To ensure accurate imaging of the detected Cherenkov flashes, data from an individual telescope are rejected if $> 10\%$ of its camera pixels are inactive at any point during a run [11].

3.2.3 Tracking Accuracy

Nominally, the pointing of the H.E.S.S. array is accurate to $\sim 2.5''$, allowing source location to within a few arc-seconds [128]. Malfunctions of the array tracking system shift the reconstructed directions of incident γ-rays with respect to the assumed pointing coordinates, potentially affecting subsequent flux estimates. Electro-mechanical monitoring of deviations in altitude and azimuth

from the nominal array pointing direction allows tracking failures to be easily identified. Runs exhibiting rms deviations in excess of $10''$ in either direction are rejected.

As a useful cross-check, the individual PMT currents are used to build a map of the sky brightness throughout each run. Correlating the brightest areas of this map with the positions of known stars provides a further verification of the pointing accuracy which is independent of the telescope tracking systems. Using this somewhat less precise metric, runs for which the derived pointing deviation exceeds 0.1° fail selection.

3.2.4 Atmospheric Conditions

A critical component of any atmospheric Cherenkov telescope is of course the atmosphere, which enables the conversion of the incident γ-ray's energy into Cherenkov radiation. Indeed, the quality of data obtained by Cherenkov telescopes is predominantly dependent upon the atmospheric conditions at the time of observation. Variations in the atmospheric density profile at high altitudes directly affect the development of EASs, modifying the altitude of maximum Cherenkov light yield (the *height of shower maximum*), and consequently the observed Cherenkov intensity at ground level [e.g. 38]. Sporadic obscuration by low-altitude clouds and aerosols in the telescope field-of-view leads to variable absorption or attenuation of Cherenkov radiation with consequent fluctuations in the overall telescope trigger rate [189]. Furthermore, attenuated Cherenkov pulses which are nonetheless detected as valid γ-ray events will likely yield reconstructed γ-ray energies which are systematically low. Data which are corrupted by adverse atmospheric conditions will probably contain spurious indications of variability in the observed flux and energy spectrum, making their exclusion mandatory for robust scientific analyses. This is particularly true for studies of γ-ray binary systems, for which reliable identification of *genuine* variability in an observed γ-ray signal is a key aspect of the analysis procedure.

The primary diagnostics of atmospheric quality are the true trigger rates of the individual telescopes and the complete array ($R^i_{\rm true}, i = 0, 1, \ldots, 4$, where i denotes the telescope number with $i = 0$ indicating the full array). Individual runs are retained or rejected based upon the values of

three statistics constructed using the time binned trigger rates $R^i_{\rm true}(t_j), j = 0, 1, \ldots, n_{\rm bins}$. The expected array and individual telescope trigger rates ($R^i_{\rm exp}(\theta_{\rm zen}(t))$) for a particular observation zenith angle may be derived either by modelling the telescope response to simulated cosmic ray events, or obtained directly from observations of a γ-ray-dark region of the sky [101]. The first statistic is, S_1 is the ratio of the mean array trigger rate to its mean expected value.

$$S_1 = \frac{\bar{R}^0_{\rm true}}{\bar{R}^0_{\rm exp}} \tag{3.2}$$

S_1 is primarily sensitive to global suppression of the cosmic-ray trigger rate with small values likely implying the presence of clouds or aerosols in the telescope field-of-view. Figure 3.1 (top row) plots the trigger rate characteristics corresponding to an observation of LS 5039 for which $S_1 \approx 0.6$, indicating heavy atmospheric absorption. Data collected under such conditions are evidently unreliable and therefore a conservative threshold of $S_1 > 0.8$ is required for a run to survive data selection.

The definition of S_1 implies an inherent insensitivity to progressive or transient episodes of atmospheric degradation, particularly if the resultant fluctuations in trigger rate do not significantly suppress $\bar{R}^0_{\rm true}$. Data obtained under such conditions are liable to yield spurious indications of variability and further filtering is required to ensure that they are identified and discarded. Defining Δt as the run duration, and $P^{i>0}_1(t)$ as the linear polynomials which best describe the observed trigger rate of each individual telescope as a function of time, the selection statistic S_2 is simply:

$$S_2 = \frac{\Delta t}{4} \sum_{i=1}^{4} \frac{1}{\bar{R}^i_{\rm true}} \frac{dP^i_1}{dt}. \tag{3.3}$$

S_2 identifies overall gradients in the observed trigger rate, perhaps indicating the gradual onset or diminution of adverse atmospheric conditions during a run. Ordinarily, runs for which $-0.3 < S_2 < 0.3$ are rejected, however there may be circumstances when values of S_2 outside this range are acceptable. For instance, robust data obtained at large zenith angles invariably exhibit significant evolution of $R^0_{\rm true}$ caused by varying atmospheric depth along the line of sight. However, in

practice there are no H.E.S.S. observations of LS 5039 which fail selection solely of the basis of S_2. As a representative example, Figure 3.1 (middle row) illustrates the trigger rate characteristics corresponding to a high zenith angle ($\theta_{\rm zenith} \approx 58^{\circ}$) observation of LS 5039 for which $S_2 \approx -0.5$ and $S_1 \approx 0.7$.

Trigger rate fluctuations on time scales significantly shorter than the run duration are identified using the statistic:

$$S_3 = \frac{1}{4}\sum_{i=1}^{4}\frac{1}{\bar{R}^i_{\rm true}}\sqrt{\frac{1}{n_{\rm bins}}\sum_{j=1}^{n_{\rm bins}}\delta_j^2} \tag{3.4}$$

formed from the polynomial fit residuals $\delta_j = P_1^{i>0}(t_j) - R_{\rm true}^{i>0}(t_j)$. Large, frequent deviations from the $P_1^{i>0}(t)$ likely correspond to intermittent obscuration by small clouds drifting through the telescope field-of-view and therefore runs for which $S_3 > 0.1$ are rejected. Figure 3.1 (bottom row) illustrates the trigger rate characteristics corresponding to an observation of LS 5039 for which $S_3 \approx 0.2$.

Independent, real-time measurements of atmospheric quality are obtained during each run using four telescope-mounted radiometers to monitor variations in the night sky luminosity temperature [58]. An increase in the observed temperature indicates the presence of obscuring material in the radiometer field-of-view. Indeed the individual radiometer temperatures are observed to be inversely correlated with the corresponding telescope trigger rates. Practically, the utility of radiometers as absolute calibrators of atmospheric quality is limited by unpredictable variations in sky temperature throughout the year. Nonetheless, radiometer data provide a useful confirmation of the atmospheric origin of an observed trigger rate fluctuation.

3.2.5 The LS 5039 Data Set

Although the nominal telescope field-of-view is $\sim 5^{\circ}$, in practice the system acceptance is somewhat uncertain beyond $\sim 2^{\circ}$, due to camera edge effects (See § 3.4.2). Conservatively, only runs with a pointing offset $< 1.5^{\circ}$ from the nominal position of LS 5039 were considered for analysis. Application of the various data selection criteria yields 183 good quality runs contributing to a total

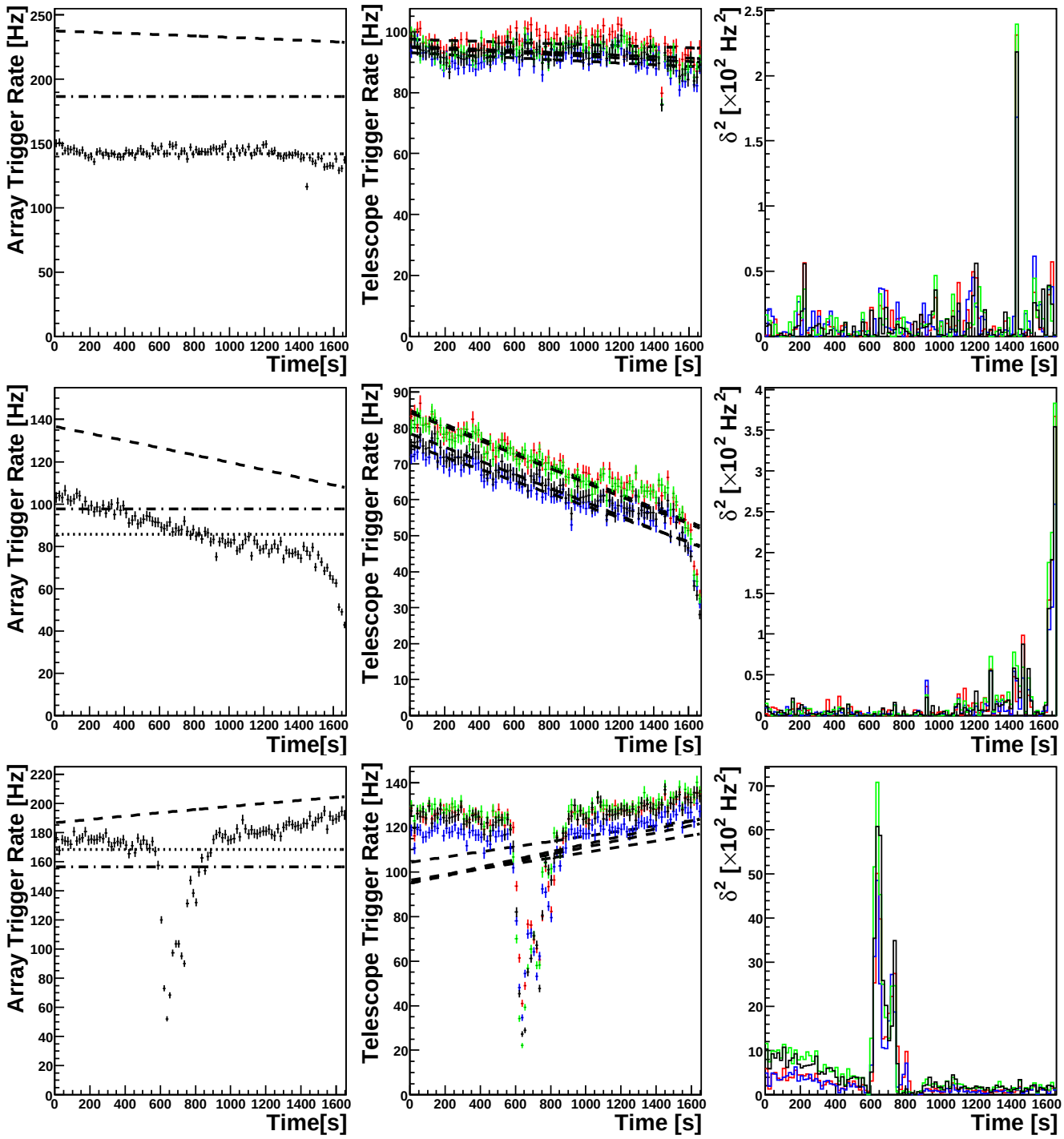

Figure 3.1: Illustration of the atmospheric quality selection criteria: The left hand column illustrates the role of S_1 in the data selection process. The overlaid lines correspond to the expected trigger rate $R^0_{\rm exp}$ (dashed lines), the threshold level for run selection $0.8\bar{R}^0_{\rm exp}$ (dot-dashed lines) and the mean observed trigger rate $\bar{R}^i_{\rm true}$ dotted lines. The middle column illustrates the role of S_2 with the dashed overlays indicating the best fitting linear polynomials $P_1^{i>0}(t)$. The right hand column shows the value of δ^2 used in the calculation of S_3.

livetime of 80.678 hours, with a mean zenith angle and target offset of $\bar{Z} \approx 22.5°$ and $\bar{\theta}^{\text{off}} \approx 0.6°$ respectively. The run list comprises 159 dedicated observations of LS 5039 with the remainder drawn from observations of the nearby PWN candidate HESS J1825-137 [22], and elements of the H.E.S.S. galactic plane scan [12].

3.3 Detector Calibration

Even under optimal conditions, the raw air-shower images captured by the individual H.E.S.S. cameras incorporate a number of systematic biases that directly affect the measured brightness distribution of detected Cherenkov light. Fortunately, careful measurement and calibration of these effects permits accurate extraction of the true shower parameters from the affected Cherenkov images.

3.3.1 Flat-fielding

Variations in optical response between individual pixels in each camera require calibration in order to achieve accurate reconstruction of the corresponding air-shower properties. During dedicated *flat-fielding* runs, a pulsing LED mounted at the centre of each telescope dish is used to provide uniform illumination across the camera aperture. The resulting images are used to derive an estimate of the combined relative optical and quantum efficiency of the individual Winston cones and PMTs constituting each pixel [9].

3.3.2 Single Photoelectron Response

The digital signal produced by each PMT in response to the generation of a single photo electron varies strongly as a function of the applied detector voltage. Understanding the correspondence between this measured *pixel amplitude* and the level of illumination is essential for accurate derivation of the incident γ-ray energy. During dedicated *single photoelectron* runs, the telescope trigger is synchronised to a faint pulsing LED which produces an average of approximately one photo-

electron in each PMT for every third trigger. The run-wise distribution of measured amplitudes for each pixel is then used to quantify the electrical response of the PMT and its associated analogue-to-digital conversion system [9].

3.3.3 Muon Correction

Inevitable degradation of the telescopes' optical surfaces and of the absolute quantum efficiency of the PMTs produce long term variations in the overall performance of the detector. In addition, shadowing of the telescope dish by elements of the mechanical support structure may affect the observed Cherenkov intensities. Such effects are monitored using the ring-like Cherenkov images of individual muons passing close to the individual telescopes [210]. The intrinsic faintness of the Cherenkov light from individual muons requires close proximity between point of emission and the telescope in order to achieve a detection. This affords a degree of immunity from the atmospheric degradation suffered by the Cherenkov light from extensive air showers. Furthermore, the precise details of the muon image can be used in conjunction with Monte-Carlo simulations to estimate the absolute Cherenkov yield [210]. In principle, this permits absolute calibration of the overall optical response. In practice, the measured muon intensities are used to derive a relative correction to an accurately calibrated optical response obtained at the telescope's inception.

3.4 Event Selection

The Cherenkov data which survive run selection are invariably dominated by the overwhelming background produced by cosmic ray air showers. The purpose of event selection is to reject a high proportion of these hadronic triggers, while simultaneously retaining a large fraction of genuine γ-ray events. Once the subset of γ-ray-like events has been identified, the properties of the corresponding air shower, and subsequently the incident γ-ray must also be derived. This section outlines the methods of γ-hadron separation which were applied to the data presented in this thesis.

3.4.1 Image Cleaning

Although the extreme sensitivity of the H.E.S.S. cameras is essential for effective detection of the faint Cherenkov pulses produced by γ-ray air showers, it inevitably results in Cherenkov images which are somewhat noisy. Each image is subjected to a two stage cleaning process designed to eliminate contamination by photons from the night sky background. Image pixels are retained only if their amplitude corresponds to a signal of 5 photoelectrons *and* at least one neighbouring pixel contains a signal of at least 10 photoelectrons, or vice-versa. The effect of this filtering is to isolate the contiguous clusters of bright pixels which correspond to the air shower image.

3.4.2 γ-Hadron Separation

Segregation of true γ-ray events from the hadronic background utilises the image moment and scaled parameter analyses outlined in §1.3.5 and §1.3.7 respectively. In order to partially ameliorate the computational cost of stereoscopically reconstructing the shower properties for all events, the event selection proceeds in two phases. Initially, the Hillas parameters and the sum of pixel amplitudes (the *image amplitude* or *size*) is calculated for each cleaned Cherenkov image. Images that are not well contained within the camera field-of-view are unlikely to yield reliable shower parameters, and consequently events with a calculated *distance* $> 2^\circ$ are discarded. Furthermore, events with image amplitudes below a certain analysis-dependent threshold are also discarded at this stage (See §3.4.3).

Air shower parameters are now derived for the remaining events, allowing calculation of mean reduced scaled parameters. Table 3.2 lists the ranges of each selection parameter which are considered γ-ray-like. Events which do not satisfy these criteria are rejected.

3.4.3 Cut Optimisation

The regions of shower parameter space which correspond to γ-ray-like events are identified using repeated analyses of simulated γ-ray sources in the presence of real background events. Depending

Table 3.2: Optimal event selection cuts for different assumed source properties.

Cuts	MRSL (min.)	MRSL (max.)	MRSW (min.)	MRSW (max.)	θ^2_{cut} (max.) [$\circ^2$]	Size (min.) [p.e.]	Distance (max.) [$\circ$]
Standard	-2.0	2.0	-2.0	0.9	0.0125	80	2.0
Hard	-2.0	2.0	-2.0	0.7	0.01	200	2.0

on the expected spectrum and flux level of a putative γ-ray source, event selection cuts may be specified which maximise the detection significance for a simulated source with comparable properties. Table 3.2 lists the parameter ranges corresponding to two distinct categories of point like γ-ray source. The *standard* cuts assume a source flux of ~ 0.1 Crab units with a spectral index $\Gamma \sim -2.6$. In contrast, the *hard* cuts are optimised for a weaker flux of 0.01 Crab units and a hard spectrum with $\Gamma \sim -2.0$ [11].

In fact, the small number of confirmed γ-ray binaries renders the expected observational characteristics of as yet undetected systems correspondingly uncertain. Furthermore, the systems which have been detected are highly variable, with LS 5039 exhibiting phase correlated evolution of the observed flux *and* spectrum [14]. Accordingly, where appropriate, target analyses will be presented which correspond to both the *standard* and *hard* selection cuts.

3.5 Background estimation

All known γ-ray binary systems are compact astrophysical objects, and consequently appear point-like under the modest angular resolution of current IACTs [7, 18, 25]. For this reason, and to preserve clarity of explanation, the subsequent discussion is restricted to the background estimation techniques employed in the analysis of point-like γ-ray sources. In the case of LS 5039 this specialisation is justified by the discussion in §3.6.

Following event selection and shower reconstruction (see §3.4), the raw *on-source* signal ($N_{\rm on}$) is defined as the accumulation of γ-ray-like events with incident directions that are reconstructed close to the nominal target position. More specifically, the union of permitted shower directions forms a circular *ON* region with squared angular radius $\theta^2_{\rm cut} \sim 0.1^{\circ^2}$, centred on the target coordinates.

Despite the excellent background rejection capabilities of modern IACTs, the small proportion of hadronic events which survive event selection nonetheless constitute a significant and often dominant fraction of the observed on-source signal [37, 11]. Robust quantification and elimination of this unwanted background component is a fundamental requirement for reliable source detection and subsequent flux determination.

The on-source *excess* of true γ-ray events (Δ) is defined as

$$\Delta = N_{\mathrm{ON}} - \alpha N_{\mathrm{OFF}}. \tag{3.5}$$

The expected number of background events falling within the ON region (αN_{off}) is estimated using the accumulation of γ-ray-like events detected within one or more distinct *OFF* regions, defined within the observation field-of-view. The parameter α is a normalisation factor which compensates for any differences in the detector efficiency between the ON and OFF regions. Formally, α is defined as the ratio of the integrated *acceptance*-weighted exposures of the ON and OFF regions [37]. The detector acceptance $A^{\gamma}(E, \psi_x, \psi_y, Z, T_{\mathrm{live}})$ defines the probability that a detected cosmic-ray with a certain reconstructed energy (E) and incident at specific coordinates (ψ_x, ψ_y) in the telescope field-of-view will appear sufficiently γ-ray-like to satisfy the event selection criteria. The additional dependencies of A^{γ} on the observation zenith angle (Z) and live time (T_{live}) become important for absolute flux calibration when combining data from several observations (See §3.8 and §3.9).

A detailed description of the derivation and implications of Cherenkov telescope acceptance is presented by [37]. For practical analyses, the acceptance is extracted from a lookup table of acceptance models. For fixed E and θ_{zenith}, these models are well described by a radially decreasing, azimuthally symmetric function of the reconstructed offset from the pointing coordinates, i.e. $A^{\gamma}(\psi_x, \psi_y) \approx \tilde{A}^{\gamma}(\theta_{\mathrm{offset}})$. The strong dependence of the acceptance function upon the reconstructed primary energy is manifested as a marked decrease in the radial falloff rate as E increases. This effect implies a particular sensitivity of spectral analyses to uncertainties in the acceptance model.

The precise choice of shape and configuration for the off-source region used to derive αN_{off} is

described by a *background model*. Several such models have been developed for use in VHE γ-ray astronomy and each has particular benefits and drawbacks depending upon the desired analysis outcome [see e.g. 37, 211, 3]. The following sections outline the two alternative approaches to background estimation employed in this thesis.

3.5.1 The Ring Background Model

The *ring* background model defines an annular OFF region surrounding the target coordinates. The angular radii of the annulus must be sufficiently large that contamination from the ON region is avoided, and are usually chosen such that $\alpha \sim 1/7$ [37]. Consequently, the ring background model is best suited for point source analyses. Indeed, for small ring radii, α is approximately equal to the ratio of the solid angles of the on and off-source regions ($\alpha \approx \Omega_{ON}/\Omega_{OFF}$) since *locally* linear gradients in the radial acceptance function are averaged by integration around the ring. For extended sources with correspondingly large ring radii, the validity of this approximation is diminished and the method becomes dependent on the accuracy of the acceptance model.

The ring background model is disfavoured for spectral analyses, since the energy dependence of the system acceptance introduces a further source of uncertainty into the calculation of α in each spectral energy band [37]. In contrast, generating γ-ray excess skymaps using the ring background model is relatively straightforward, since a background estimate may be generated for the majority of points in the field-of-view. Accordingly, both skymaps in Figure 3.2 and indeed all skymaps presented in this thesis were generated using the ring background model.

3.5.2 The Reflected Background Model

The *reflected* background model was developed by the HEGRA collaboration in conjunction with the *wobble* mode observational technique [3]. As illustrated in Figure 3.2b, this approach defines n_{OFF} off-source regions within the camera field-of-view which surround the nominal source position. These regions are identical in size and shape to the target region and have the same radial distance from the camera centre. During dedicated wobble mode observations, the telescope point-

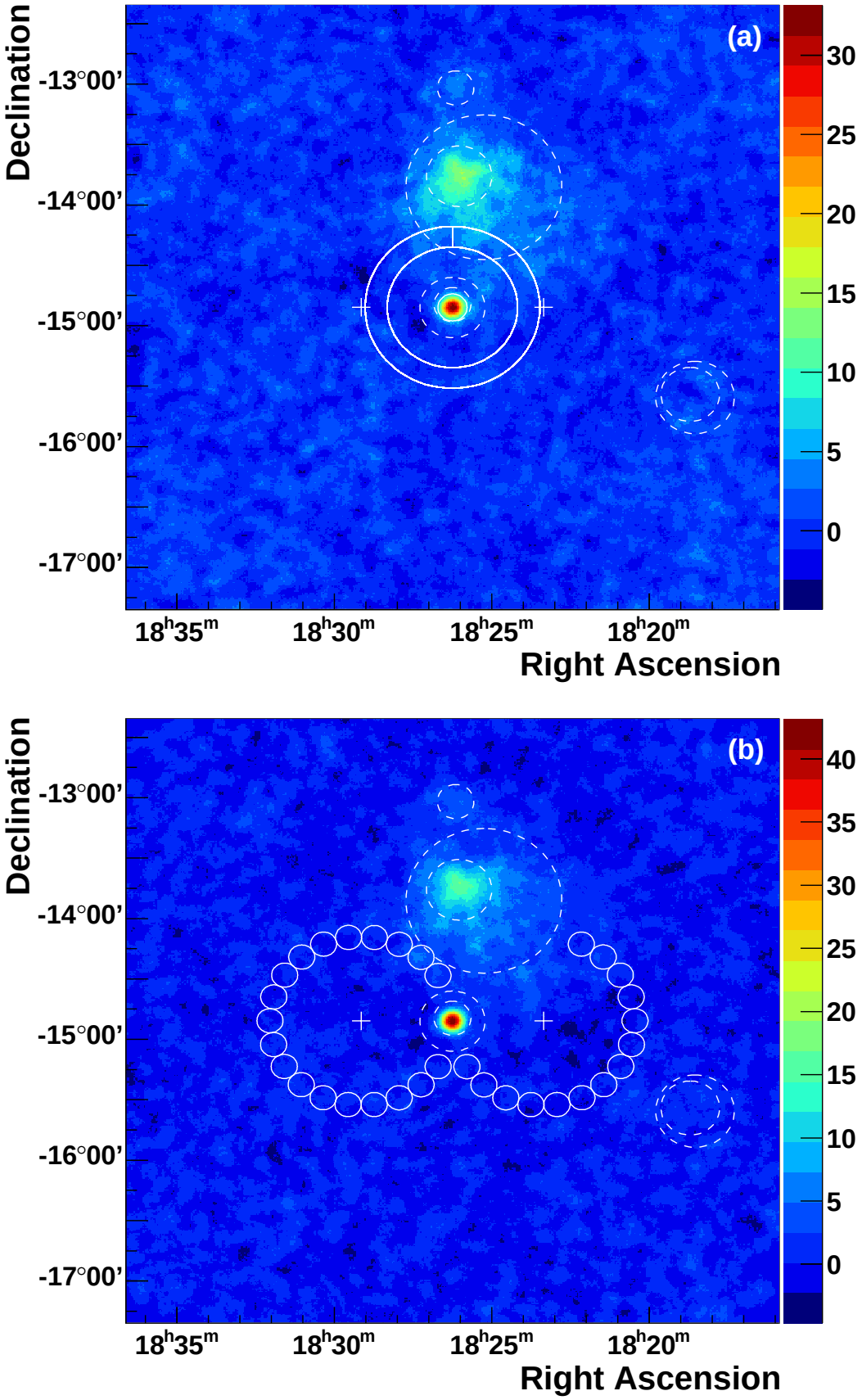

Figure 3.2: *Panel a:* Significance skymap centred on the nominal position of LS 5039 using standard cuts. The annular background region for the *ring* model (solid lines) and the excluded regions corresponding to HESS J1825-137 (North), HESS J1818-155 (East) and LS 5039 itself are overlaid as dashed lines. The white crosses illustrate typical observation positions for the LS 5039 data set. *Panel b:* Same as *(a)* but using hard cuts and the reflected background model.

ing is offset by a small amount ($\sim 0.5 - 0.7^{\circ}$) from the assumed target position. This offset is sufficient to ensure that the background events are not contaminated by any putative emission from the ON region. Crucially, the identical camera offsets inherent to this configuration imply identical acceptance characteristics of the individual ON and OFF regions and α is simply $1/n_{\rm OFF}$. This makes the reflected background model particularly appealing for spectral analysis, since it eliminates the requirement for an energy dependent acceptance correction in the calculation of α.

The lack of flexibility in the placement of the off-source regions can render the reflected background model unsuitable if the field-of-view is crowded with γ-ray sources. In such cases it may prove impossible to define a sufficient number of OFF regions with the required offset and the background estimate becomes vulnerable to a number of systematic effects. In particular the influence of gradients in the night sky background light or the presence of dead camera pixels is enhanced when the number of OFF regions is small [37].

3.5.3 Exclusion regions

When deriving the γ-ray excess for a nominal on-source region it is essential to avoid contamination of $N_{\rm OFF}$ by emission from known VHE γ-ray sources. For this reason, the background estimation utilises a set of *exclusion regions* which define the spatial extension of known γ-ray sources. Furthermore, the image calibration procedures discussed in §3.3 may fail to adequately compensate for the presence of bright ($M_V \geq 5$) stars in the field-of-view. Accordingly, regions falling within 0.2° of a bright star are also excluded from the derivation of background estimates. Several exclusion regions are defined in the LS 5039 field-of-view and are shown in Figure 3.2 using dashed lines. For the reflected background model, the exclusion regions are applied when the OFF regions are defined, as illustrated by the truncated ring of OFF regions to the right of Figure 3.2. In contrast, the ring background model accounts the presence of known γ-ray sources by zeroing those pixels of accumulated γ-ray-like event event map which fall within the defined exclusion regions.

Table 3.3: Parameters of the H.E.S.S. PSF corresponding to the mean observational zenith angle ($\bar{Z} \approx 22.5^\circ$) and target offset ($\bar{\theta}^{\rm off} \approx 0.6^\circ$) of the LS 5039 data set.

Parameter	Standard Cuts	Hard Cuts
$N_{\rm rel}$	0.08	0.014
σ_1 [°]	0.046	0.039
σ_2 [°]	0.11	0.11

3.5.4 Results

Table 3.4 lists the values $N_{\rm ON}$, $N_{\rm OFF}$, α and Δ for the nominal position of LS 5039. The results were derived using both the ring and reflected background models and employing both the standard and hard event selection cuts. For each cut regime, the choice of background model appears to have little effect on the derived excess, which inspires confidence that any systematic effects have been adequately accounted for.

3.6 Source Extension

A VHE γ-ray source is considered point-like if the observed angular distribution of detected γ-rays matches the telescope's *point spread function* (PSF). In fact, the H.E.S.S. PSF varies according to the event selection cuts employed, the observational zenith angle and the target offset within the field-of-view. In general, its functional form is well described by the superposition of two gaussian components [11]:

$$\mathrm{PSF} = N \left[\exp\left(-\frac{\theta^2}{2\sigma_1^2}\right) + N_{\rm rel} \exp\left(-\frac{\theta^2}{2\sigma_2^2}\right) \right] \tag{3.6}$$

where N is a normalisation factor which varies in proportion to the detected excess and Table 3.3 lists the remaining parameter values which correspond to the mean zenith angle and offset of the LS 5039 data set. Figure 3.3 reveals a close correspondence ($\chi^2_\nu = 0.88$ and $\chi^2_\nu = 1.1$ for standard and hard cuts respectively) between the observed γ-ray extension of LS 5039 and the calculated PSFs, confirming the point-like nature of the source. The noticeably narrower PSF which results from applying hard cuts is due to the removal of faint events which generally yield poorer directional information.

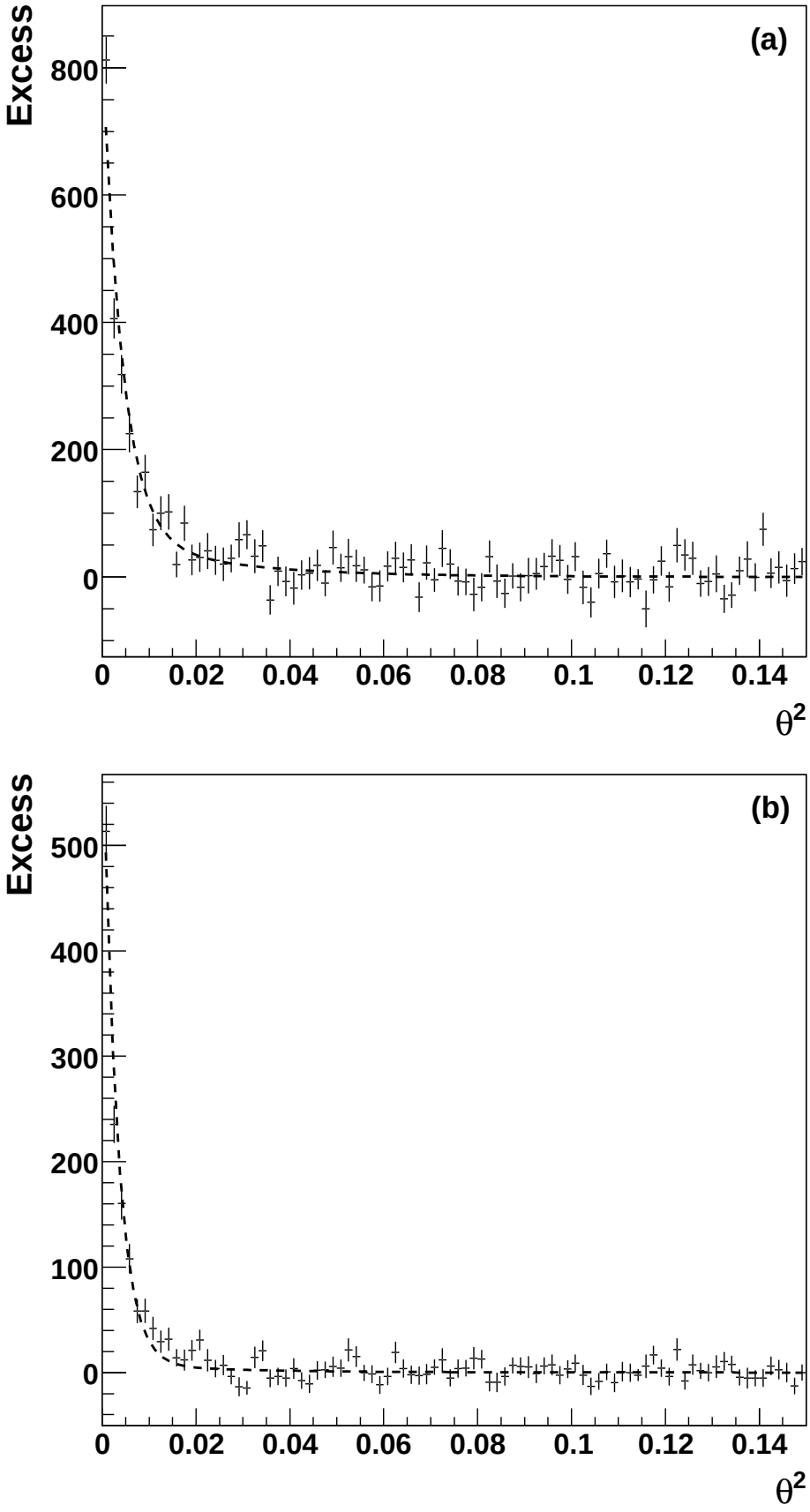

Figure 3.3: *Panel a:* The distribution of excess events in the LS 5039 field-of-view as a function of θ^2 using the ring background model and standard cuts. The dashed line indicates the expected distribution for a point-like source given by (3.6). *Panel b:* Same as *(a)* but using hard cuts.

Table 3.4: Measured event statistics and significances for LS 5039 using the four possible combinations of background model and cut optimisation regime.

Background	Cuts	N_{ON}	N_{OFF}	α	Δ	Significance $[\sigma]$
Ring	Standard	6538	54803	0.079	2209.15	29.8629
	Hard	1591	7151	0.063	1144.14	39.8527
Reflected	Standard	6538	47489	0.091	2236.8	30.1092
	Hard	1591	5640	0.077	1159.14	40.2828

3.7 Detection significance

Given N_{ON}, N_{OFF} and α as defined in §3.5.2, the statistical significance of a measured excess may be calculated using the likelihood ratio prescription of [156]:

$$S = \sqrt{2}\left\{ N_{\mathrm{ON}} \ln\left[\left(\frac{1+\alpha}{\alpha}\right)\frac{N_{\mathrm{ON}}}{N_{\mathrm{ON}}+N_{\mathrm{OFF}}}\right]^{N_{\mathrm{ON}}} + N_{\mathrm{OFF}} \ln\left[(1+\alpha)\frac{N_{\mathrm{OFF}}}{N_{\mathrm{ON}}+N_{\mathrm{OFF}}}\right]^{N_{\mathrm{ON}}}\right\}^{\frac{1}{2}} \tag{3.7}$$

In the absence of a genuine γ-ray signal, the expected distribution of S is the unit Gaussian $\mathcal{N}(S;0,1)$ and deviations from this distribution indicate the presence of a genuine γ-ray signal. More formally, the *significance level* $p(S') = \mathcal{N}(S';0,1)$ of the observed significance S' is simply the probability of a similar or greater value of S arising purely from background fluctuations. The detection confidence ξ is then defined as the complement of p:

$$\xi = 1 - p = 1 - \mathcal{N}(S';0,1) \tag{3.8}$$

Figure 3.4 illustrates the bin-wise significance distributions for the significance skymaps plotted in Figure 3.2, using both standard and hard cuts. The values of S drawn from the off-source regions of the maps correspond well to the expected unit Gaussian (thick dashed lines). There is also an obvious excess of positive significance values with contributions from both the excluded off-source regions (red lines) and LS 5039 itself (black lines).

Table 3.4 lists various values of S, derived at the nominal position of LS 5039 using the four possible combinations of background model and cut optimisation regime. The choice of event selection criteria has a profound effect. Indeed, the application of hard cuts enhances the detection significance by $\sim 10\sigma$ with respect to the standard event selection, strongly suggesting an energy spectrum which is significantly harder than that of the Crab Nebula. In fact, even the $\sim 30\sigma$ significances derived using standard cuts correspond to a confidence level $\xi \approx 1$ and the source is emphatically detected.

3.8 Effective Area and the Energy Threshold

Conceptually, the *effective area* (A_{eff}) is defined as the union of all impact distances at which a given air shower will trigger the telescope *and* survive event selection. Practically, A_{eff} is a function of the primary particle energy (E), the target offset from the pointing direction (θ^{off}) and the instantaneous pointing zenith angle (Z) that provides an absolute normalisation for the system acceptance. Monte Carlo modelling of the telescope response to simulated air showers is used to populate lookup tables of the effective area corresponding to various discrete values of E, θ^{off}, and Z. During flux calculation, the appropriate value of A_{eff} is extrapolated from the lookup tables by linear interpolation in θ^{off}, $\log E$, and $\cos Z$ [11].

For computational purposes, two variants of the effective area may be used which correspond to different definitions of the primary particle energy. The *true* effective area ($A_{\text{eff}}^{\text{true}}$) is defined as a function of the Monte Carlo energy of the simulated air shower. In contrast, values of the *reconstructed* effective area ($A_{\text{eff}}^{\text{reco}}$) correspond to the energy which would be derived by analysis of the captured Cherenkov images. While it is valid to use $A_{\text{eff}}^{\text{true}}$ to estimate the effective area over the full energy range, the reconstructed effective area should be used for all analyses which bin or select events on the basis of their reconstructed energy [11].

A quantity which is related to the effective area is the *energy threshold* which is used to derive a γ-ray flux (See §3.9). The threshold may be defined as that energy which corresponds to the peak in

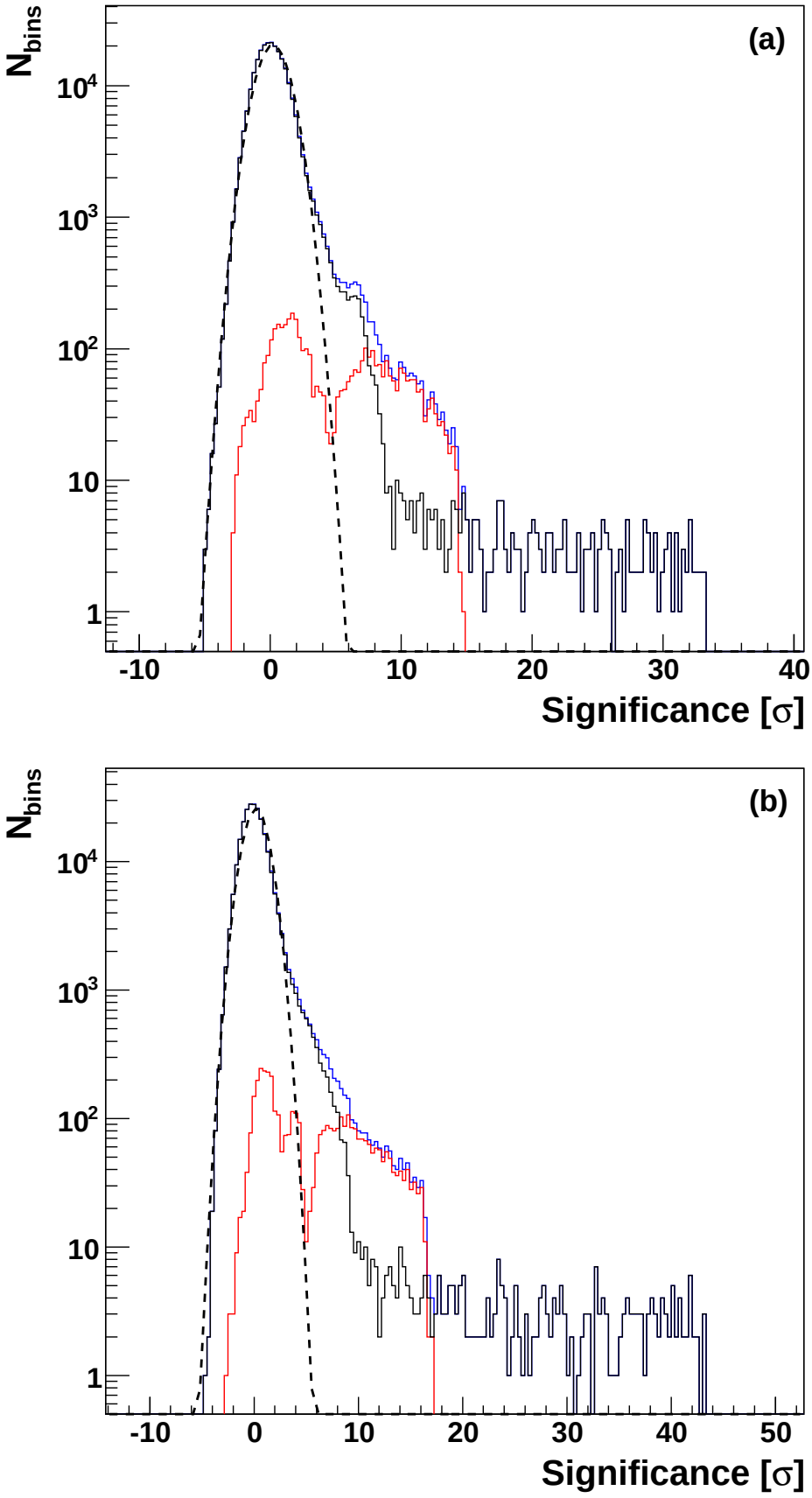

Figure 3.4: *Panel a:* The distribution of bin-wise significances in the LS 5039 field-of-view using the ring background model and standard cuts. The various lines correspond to the total field-of-view (blue), the exclusion regions (red), and the field-of-view with the exclusion regions removed (black). *Panel b:* Same as *(a)* but using hard cuts.

the distribution of the expected detection rate versus energy. This distribution is formed by folding the expected γ-ray spectrum with the simulated effective area curve. Below the peak, the effective area falls off rapidly and becomes increasingly uncertain with decreasing energy, potentially biasing flux calculations.

An alternative definition of the energy threshold which is often applied during spectral analyses involves the energy resolution of the telescope. Specifically, the threshold is defined as the energy below which the average difference between the true and reconstructed energies exceeds 10%.

Like the effective area, both variants of the energy threshold depend on θ^{off} and Z. Thresholds derived using the energy resolution are generally more conservative (i.e. higher), but are not strictly necessary for energy independent analyses such as the derivation of an integral flux.

3.9 Flux determination

Although calculation of the statistical significance is essential for conclusive source detection, most subsequent scientific analyses require the derivation of the observed γ-ray flux. In the field of γ-ray astronomy it is common to report the integral photon flux (I) above the analysis-specific threshold energy E_t. This quantity is expressed as:

$$I = \int_{E_t}^{E_{\max}} \frac{dN}{dE} dE \tag{3.9}$$

where dN/dE is the differential γ-ray flux and $E_{\max}$ is a nominal cutoff energy[1]. Derivation of I requires the specification of a functional form for dN/dE. A common convention, arising from the prevalence of conforming VHE γ-ray sources, is to assume a decreasing power law spectrum:

$$\frac{dN}{dE} = I_0 \left(\frac{E}{E_0} \right)^{-\Gamma} \tag{3.10}$$

[1]Usually dictated by the range of the effective area lookup tables.

where Γ is an assumed spectral index and I_0 is the unknown flux normalisation at energy E_0. The value of I_0 is derived using the following expression for the measured γ-ray excess in terms of the true effective area [e.g. 35]:

$$\begin{aligned}\Delta &= \int_0^{E_{\max}} \int_{t_{\rm start}}^{t_{\rm stop}} \frac{dN}{dE} A_{\rm eff}^{\rm true}(E, Z(t), \theta^{\rm off}(t))\, dt dE \\ &= \int_0^{E_{\max}} \int_{t_{\rm start}}^{t_{\rm stop}} I_0 \left(\frac{E}{E_0}\right)^{-\Gamma} A_{\rm eff}^{\rm true}(E, Z(t), \theta^{\rm off}(t))\, dt dE \end{aligned} \tag{3.11}$$

The computation of I_0 proceeds by discretising the ranges of t, E, Z and $\theta^{\rm off}$ such that $A_{\rm eff}$ is approximately independent of the relevant parameter within each resultant sub-interval. In this way the nested integrals in (3.11) are reduced to sums over E, Z and $\theta^{\rm off}$:

$$\Delta = \frac{I_0 E_0}{(1-\Gamma)} \sum_{i=0}^{N_Z} \sum_{j=0}^{N_\theta} \Delta t_{ij} \sum_{k=0}^{N_E} A_{\rm eff}(E_k, Z_i, \theta_j^{\rm off}) \left[\left(\frac{E_k^{\max}}{E_0}\right)^{1-\Gamma} - \left(\frac{E_k^{\min}}{E_0}\right)^{1-\Gamma} \right] \tag{3.12}$$

where Δt_{ij} is union of live time intervals during which $Z \approx Z_i$ and $\theta^{\rm off} \approx \theta_j^{\rm off}$, $E_k^{\min}$ and $E_k^{\max}$ are respectively the upper and lower bounds of the energy interval E_k and $N_{\rm Z,\theta,E}$ are the number of subdivisions in Z, $\theta^{\rm off}$ and E. Finally, rearranging (3.12) to obtain the differential flux normalisation allows the integral flux to be derived [2]:

$$I = \int_{E_t}^{E_{\max}} I_0 \left(\frac{E}{E_0}\right)^{-\Gamma} dE = \frac{I_0 E_0}{(1-\Gamma)} \left[\left(\frac{E_{\max}}{E_0}\right)^{1-\Gamma} - \left(\frac{E_t}{E_0}\right)^{1-\Gamma} \right] \tag{3.13}$$

Using the measured γ-ray excess at the nominal position of LS 5039, in conjunction with an assumed spectral slope $\Gamma = 2.24$ (which is consistent by the spectral analysis presented in §3.11), four estimates of the integral flux above 1 TeV were calculated. The seperate results are listed in Table 3.5 and correspond to the various combinations of background model and event selection critera. All four values are compatible at the 3σ level and correspond on average to $\sim 5\%$ of the Crab Nebula flux above the same threshold. Strictly, it is not correct to quote an integral flux above a threshold which is lower than the actual threshold of any observation in the dataset, since

[2] This method of flux derivation is employed by the standard *Heidelberg* analysis which was introduced in §3

Table 3.5: Derived values of the average integral flux of photons with $E > 1$ TeV corresponding to the entire H.E.S.S. exposure at the nominal position of LS 5039. The fluxes were derived assuming a spectral index $\Gamma = 2.24$. The errors correspond to the 68% confidence interval ($\approx 1\sigma$).

Background	Cuts	$I(>1\text{TeV})$ [ph cm^{-2}s^{-1}]
Ring	Standard	$(1.228 \pm 0.05) \times 10^{-12}$
	Hard	$(1.343 \pm 0.05) \times 10^{-12}$
Reflected	Standard	$(1.230 \pm 0.05) \times 10^{-12}$
	Hard	$(1.360 \pm 0.05) \times 10^{-12}$

the associated effective area estimate may be incorrect. Accordingly, three runs with $Z > 50°$ and $E_t > 1$ TeV were discarded from the LS 5039 data set for the purposes of the flux calculation.

3.10 Temporal analysis

Temporal variation of the observed broadband flux appears to be a common characteristic of X-ray binaries. Indeed, given the dynamic nature of these systems it would be surprising if some imprint of the rapidly evolving radiative environment was not detected. The temporal characteristics of astrophysical objects often encode a wealth of information regarding the physical processes taking place in and around them.

At X-ray wavelengths the observed variability of compact binary systems has afforded powerful insights regarding the process of accretion in strong gravitational fields [e.g. 200, 243, 82]. Observations of radio variability have revealed rapid fluctuations in flux density some of which correspond to the production of ultra-relativistic ejecta, expanding with apparently superluminal velocities [93, 181].

In combination with the high mass X-ray binary LS I +61°303 [25], the Be-pulsar system PSR B1259-63 [7] and the black hole binary Cyg X-1 [26], LS 5039 is one of four binary systems which exhibit variable VHE γ-ray emission. Whether due to evolution of the underlying emission mechanisms [e.g. 44], modulation of the intrinsic optical depth for TeV photons [e.g. 85], or a likely combination of both these effects [e.g. 148], such variability undoubtedly offers new insights into the most energetic processes occuring in X-ray binary systems.

The discussion in this section centres on the application of time series analysis methods for the detection, classification and analysis of potential variability in a VHE γ-ray signal. Many of the methods presented emulate those applied by [14] to a smaller sample of the H.E.S.S. LS 5039 data set, and comparison will be made with those results where appropriate. In order to maximise the available γ-ray statistics, all analyses presented in this section use data which were extracted using standard event selection cuts.

From an abstract perspective, a *time series* $\{Y(t_i), i = 1, 2, \ldots, n\}$ is simply a discrete set of n measurements of a physical variable Y, sampled at times t_i. The run-wise integral flux lightcurve of LS 5039 plotted in Figure 3.5 represents a concrete realisation of a time series ($\{I_i \equiv I(t_i), i = 1, 2, \ldots, n = 180\}$) which will be used as input data for the techniques outlined in this section[3].

3.10.1 Secular variability

Secular variability refers to the presence of measurable long term gradients in the temporal evolution of the source flux. A straightforward approach for the identification of such trends is outlined by [71] and involves χ^2 fitting of two simple models to the observed flux points. A constant flux model ($I_i = c$) represents the null hypothesis (i.e. that there is no long term trend), while a linear polynomial ($I_i = at_i + b$) provides a coarse simulation for secular variation. The detection of secular variability hinges on the value of the linear coefficient a, and whether it is significantly non-zero. Since the constant model is nested within the linear model, the F-Test can be used to compare the calculated χ^2 values for each fit. Under the null hypothesis the F statistic:

$$F_{\text{obs}} = (n-2)\frac{\chi^2_{n-1} - \chi^2_{n-2}}{\chi^2_{n-2}} \tag{3.14}$$

where χ^2_{n-1} and χ^2_{n-2} are the χ^2 values for the constant and linear models respectively, follows Fisher's F distribution with 1 and $n-2$ degrees of freedom [e.g. 40]. By comparison with $F_{1,n-2}$

[3] All original VHE γ-ray lightcurves presented in this thesis were generated using a custom implemented analysis tool. The source code for this tool is presented in Appendix E.1

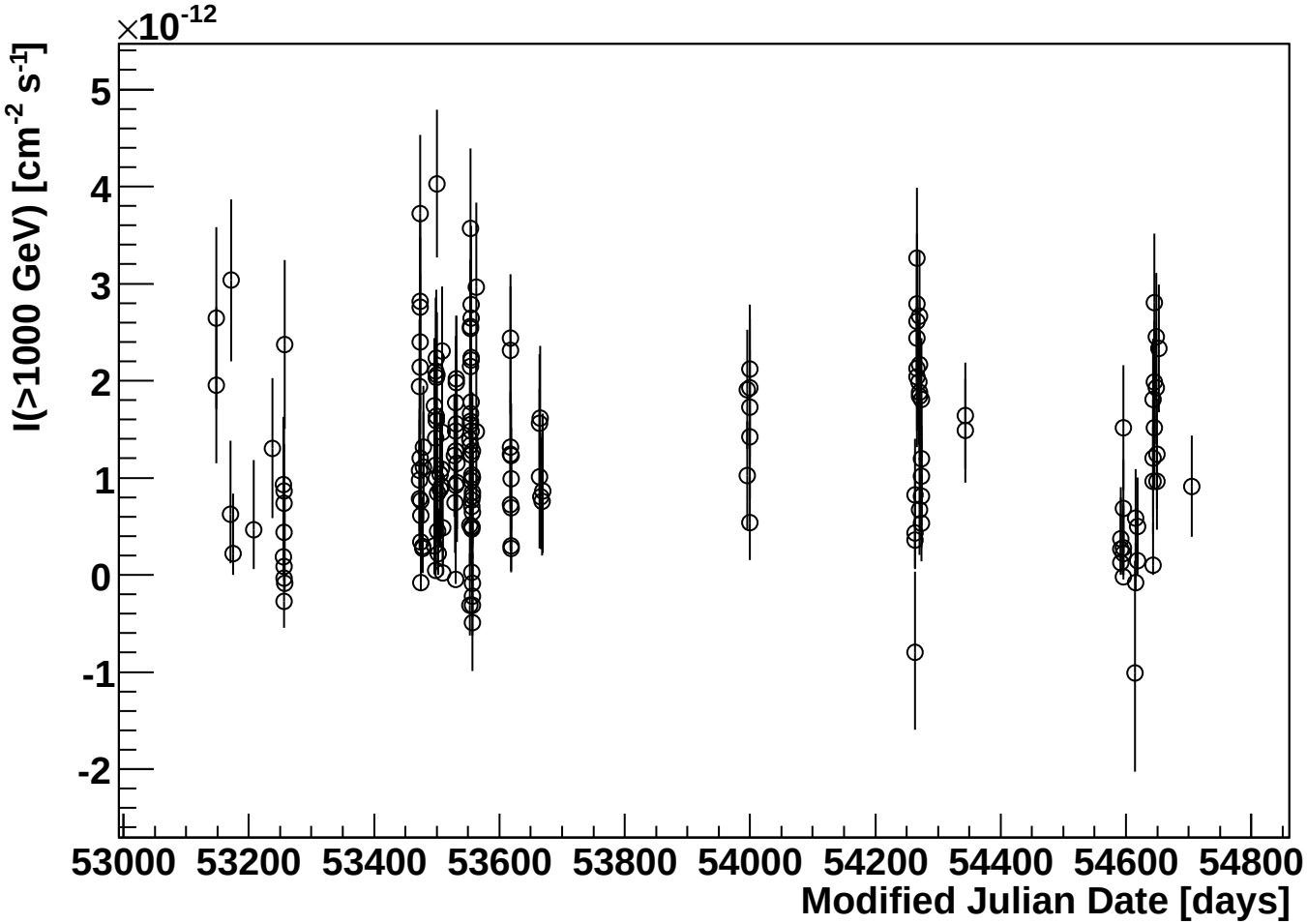

Figure 3.5: Run-wise lightcurve for LS 5039 showing the integral flux of photons with $E > 1$ TeV. The fluxes were derived assuming a spectral index of $\Gamma = 2.24$. The error bars correspond to the 68% confidence interval ($\approx 1\sigma$).

the probability of observing the value of $F_{\rm obs}$ may be derived. The *false alarm probability* is the probability of a value of *at least* $F_{\rm obs}$ being observed purely by chance and is defined as:

$$P_{\rm fa}^{\rm sec} = 1 - \int_0^{F_{\rm obs}} F_{1,n-2}(x)dx. \tag{3.15}$$

Small values of $P_{\rm fa}^{\rm sec}$ imply a positive detection of secular variability.

Applying this test to the LS 5039 lightcurve yields $P_{\rm fa}^{\rm LS5039} = 0.74$, strongly disfavouring secular variability of the observed γ-ray flux.

3.10.2 Additional variability

The next logical step is the identification of additional short term variations, which cannot be accounted for by a long term trend. In the absence of genuine variability, the observed flux points are independent and normally distributed about the datum supplied by the preferred secular variability model. Comparing the value of χ^2_{n-1} (or χ^2_{n-2} if secular variation was identified) obtained from the fit with the *expected* χ^2 distribution for the appropriate number of degrees of freedom yields the probability of observing $\chi^2_{n-1,2}$ purely as a result of statistical fluctuations.

Using χ^2_{n-1} for the LS 5039 lightcurve, a false alarm probability $P_{\rm fa}^{\rm add} = 2 \times 10^{-17}$ is derived. As before, this probability defines the chance of the best fit model yielding *at least* χ^2_{n-1} and indicates strong evidence for excess variability around the mean flux value.

3.10.3 Periodic variability

All binary systems possess an inherent periodicity associated with their orbital motion. Assuming that γ-ray production is localised to a region within the system that undergoes regular environmental changes as a result of the binary orbit, then one might reasonably expect detectable periodic modulation of an observed γ-ray flux [e.g. 85, 47, 46].

Indeed, accurate measurement of a periodic γ-ray signal can be an effective discriminator for the identification of multi-wavelength counterparts. If the frequency of modulation is consistent

with previously established periodicities at shorter wavelengths, then potential source confusion is effectively eliminated.

3.10.3.1 The Lomb-Scargle Periodogram

To facilitate the search for periodic signals in the LS 5039 data set, a computerised analysis based on the Lomb-Scargle periodogram [162, 219] was developed[4]. The Lomb-Scargle periodogram identifies periodicities in the input lightcurve $\{I_i\}$ by examining a large number of pre-selected trial frequencies, $f = \omega/2\pi$. At each frequency a linear least-squares fit of a sinusoidal model:

$$P_i \equiv P(t_i) = a\cos\omega t_i + b\sin\omega t_i \tag{3.16}$$

to the I_i is performed. The fit quality at a particular ω is quantified by comparative reduction in the sum of the squared fit residuals with respect to the sum of squared residuals about the mean flux value (ΔR). In practice the data are usually mean subtracted before application of the Lomb-Scargle algorithm, and the statistic may be expressed as:

$$\Delta R = \sum_{i=1}^{n} \tilde{I}_i^2 - \sum_{i=1}^{n} (\tilde{I}_i - P_i^{\rm best}(\omega))^2 \tag{3.17}$$

where $\tilde{I}_i$ is the mean-subtracted counterpart of I_i and $P_i^{\rm best}(\omega) \equiv P^{\rm best}(t_i, \omega)$ are the values of the best fitting model with frequency ω.

The following derivation of the Lomb-Scargle periodogram considers the process of least squares fitting in the context of abstract vector spaces. While this approach may appear unnecessarily complex, formulating the periodogram in this way will facilitate the straightforward introduction of improvements to the classical definition in subsequent sections.

Fundamentally, fitting a linear model with least-squares is precisely equivalent to finding the

[4]The source code for this implementation is presented in Appendix E.1.

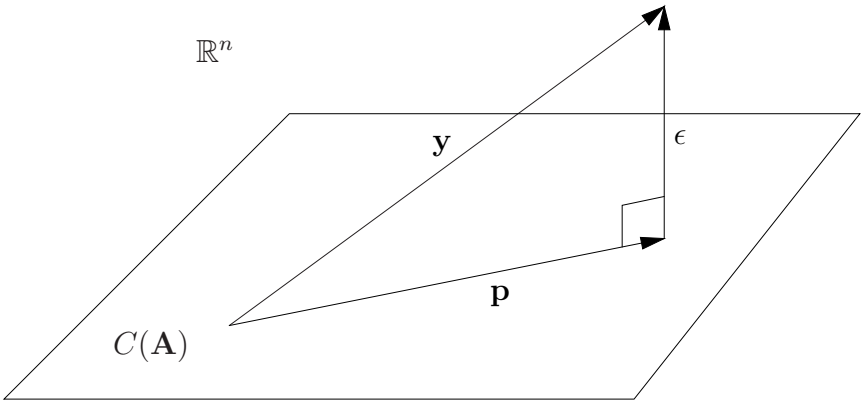

Figure 3.6: A geometrical representation of the data vector $\mathbf{y}$, its orthogonal projection $\mathbf{p}$ into the column space $C(\mathbf{A})$ of the model matrix $\mathbf{A}$, and the orthogonal residual vector $\epsilon = \mathbf{y} - \mathbf{p}$.

vector $\mathbf{x}_{\text{best}}$ which most closely satisfies the matrix equation:

$$\mathbf{A}\mathbf{x} \approx \mathbf{y} \tag{3.18}$$

Writing this explicitly for the sinusoidal model (3.16):

$$\begin{pmatrix} \cos\omega t_1 & \sin\omega t_1 \\ \cos\omega t_2 & \sin\omega t_2 \\ \vdots & \vdots \\ \cos\omega t_n & \sin\omega t_n \end{pmatrix} \begin{pmatrix} a \\ b \end{pmatrix} \approx \begin{pmatrix} \tilde{I}_1 \\ \tilde{I}_2 \\ \vdots \\ \tilde{I}_n \end{pmatrix} \tag{3.19}$$

reveals that the columns of the matrix $\mathbf{A}$ contain the components of the model function (3.16) for every t_i, the vector $\mathbf{x}$ contains the unknown model coefficients, and the elements of the data vector $\mathbf{y}$ are the $\tilde{I}_i$).

Figure 3.6 illustrates a geometrical interpretation of the components of equation (3.18). For a real-valued time series $\{I_i \in \mathbb{R}, \forall\, t_i \in \mathbb{R}\}$, it is clear that $\mathbf{y} \in \mathbb{R}^n$, and also that the set of vectors formed by all possible linear combinations of the columns of $\mathbf{A}$ form an n-dimensional subspace of $\mathbb{R}^n$. This subspace is the *column space* of $\mathbf{A}$ which is denoted $C(\mathbf{A})$. In the special case that the model (3.16) is a perfect description of the data, $\mathbf{y} \in C(\mathbf{A})$ and equation (3.18) reduces to an

exactly solvable system of linear equations, allowing $\mathbf{x}$ to be evaluated directly. In reality, there will usually remain some residual discrepancy between the data and the model function values (in general $\mathbf{y} \notin C(\mathbf{A})$), in which case equation (3.18) has no exact solution. Instead, the *best possible* solution $\mathbf{x}_{\text{best}}$ must be obtained by finding the vector $\mathbf{p} \in C(\mathbf{A})$ that most closely approximates $\mathbf{y}$. As illustrated in Figure 3.6, $\mathbf{p}$ is that vector which minimises the length of the *residual vector*:

$$\epsilon = \mathbf{y} - \mathbf{p} \tag{3.20}$$

Clearly, the minimum ($|\epsilon|_{\text{min}}$) is obtained when $\mathbf{p}$ is the orthogonal projection of $\mathbf{y}$ into $C(\mathbf{A})$, implying orthogonality between ϵ and all vectors in $C(\mathbf{A})$. As a consequence, the scalar products of ϵ with all vectors $\mathbf{a} \in C(\mathbf{A})$ vanish:

$$\epsilon \cdot \mathbf{a} = \epsilon^{\mathrm{T}}\mathbf{a} = 0, \forall\, \mathbf{a} \in C(\mathbf{A}) \Leftrightarrow \mathbf{A}^{\mathrm{T}}\epsilon = 0 \tag{3.21}$$

where $\mathbf{A}^{\mathrm{T}}$ is the transpose of $\mathbf{A}$. Combining equations (3.20) and (3.21) yields the *normal equations*:

$$\mathbf{A}^{\mathrm{T}}\epsilon = \mathbf{A}^{\mathrm{T}}\mathbf{p} - \mathbf{A}^{\mathrm{T}}\mathbf{y} = 0 \tag{3.22}$$

Solving for $\mathbf{p}$ and noting from the definition of $C(\mathbf{A})$ that $\mathbf{p}$ is a linear combination of the columns of $\mathbf{A}$ with coefficients given by $\mathbf{x}_{\text{best}}$:

$$\mathbf{p} = \mathbf{A}(\mathbf{A}^{\mathrm{T}}\mathbf{A})^{-1}\mathbf{A}^{\mathrm{T}}\mathbf{y} \tag{3.23}$$

$$\Rightarrow \mathbf{x}_{\text{best}} = (\mathbf{A}^{\mathrm{T}}\mathbf{A})^{-1}\mathbf{A}^{\mathrm{T}}\mathbf{y} \tag{3.24}$$

It is now straightforward to show that the *reduction in the sum of squares* is simply the scalar

product of $\mathbf{y}$ and $\mathbf{p}$:

$$\begin{aligned}
\Delta R &= \sum_{i=1}^{n} \tilde{I}_i^2 - \sum_{i=1}^{n} (\tilde{I}_i - P_i^{\text{best}}(\omega))^2 \\
&= \mathbf{y}^{\mathrm{T}}\mathbf{y} - (\mathbf{y}-\mathbf{p})^{\mathrm{T}}(\mathbf{y}-\mathbf{p}) \\
&= 2\mathbf{y}^{\mathrm{T}}\mathbf{p} - \mathbf{p}^{\mathrm{T}}\mathbf{p} \\
&= \mathbf{y}^{\mathrm{T}}\mathbf{p} + \epsilon^{\mathrm{T}}\mathbf{p} \\
&= \mathbf{y}^{\mathrm{T}}\mathbf{p} = \mathbf{y}\cdot\mathbf{p} \;\; \because \epsilon \perp \mathbf{p} \Rightarrow \epsilon^{\mathrm{T}}\mathbf{p} = 0 \\
&= \mathbf{y}^{\mathrm{T}}\mathbf{A}\mathbf{x}_{\text{best}} = (\mathbf{A}^{\mathrm{T}}\mathbf{y})^{\mathrm{T}}(\mathbf{A}^{\mathrm{T}}\mathbf{A})^{-1}\mathbf{A}^{\mathrm{T}}\mathbf{y}
\end{aligned} \tag{3.25}$$

which is maximised as $\mathbf{y} \to \mathbf{p}$ and the fit residuals approach zero. Following [162] and defining the notation:

$$\begin{aligned}
CC &= \sum_{i=1}^{n} \cos^2 \omega t_i, \qquad & SS &= \sum_{i=1}^{n} \sin^2 \omega t_i, \\
CS &= \sum_{i=1}^{n} \cos \omega t_i \sin \omega t_i, & & \\
YC &= \sum_{i=1}^{n} \tilde{I}_i \cos \omega t_i, \qquad & YS &= \sum_{i=1}^{n} \tilde{I}_i \sin \omega t_i
\end{aligned} \tag{3.26}$$

equation (3.25) may be written explicitly as:

$$\Delta R = \begin{pmatrix} YC & YS \end{pmatrix} \begin{pmatrix} CC & CS \\ CS & SS \end{pmatrix}^{-1} \begin{pmatrix} YC \\ YS \end{pmatrix}. \tag{3.27}$$

Although equation (3.27) may be used directly to calculate the value of ΔR, [162] further simplified the expression by introducing a frequency dependent phase offset $\tau(\omega)$ into the time dependence of the model function such that the cross-term CS vanishes. Formulating the new model function explicitly gives

$$P_i \equiv P(t_i) = a \cos \omega(t_i - \tau) + b \sin \omega(t_i - \tau). \tag{3.28}$$

Later, [219] showed that this approach renders the periodogram invariant under translation of the

time origin of the data, and is equivalent to orthogonalising the model basis functions *at each frequency*. The value of τ is derived using the condition that $CS = 0$, and may be expressed as [162, 219, 251]:

$$\tan 2\omega\tau = \frac{2CS}{CC - SS} = \frac{\sum_{i=1}^{n} \sin 2\omega t_i}{\sum_{i=1}^{n} \cos 2\omega t_i} \tag{3.29}$$

With this modification in place, (3.27) may be expanded to yield the usual expression for the classical *normalised* Lomb-Scargle *power*:

$$z = \frac{1}{s^2}\frac{YC^2}{CC} + \frac{YS^2}{SS} = \frac{1}{2s^2}\left\{ \frac{\left[\sum_{i=1}^{n} \tilde{I}_i \cos\omega(t_i - \tau)\right]^2}{\sum_{i=1}^{n} \cos^2\omega(t_i - \tau)} + \frac{\left[\sum_{i=1}^{n} \tilde{I}_i \sin\omega(t_i - \tau)\right]^2}{\sum_{i=1}^{n} \sin^2\omega(t_i - \tau)} \right\} \tag{3.30}$$

where the classical normalisation factor s^2 corresponds to the *sample variance* of the data. Figure 3.7 (top panel) shows the classical normalised Lomb-Scargle periodogram derived using the integral flux lightcurve for LS 5039 illustrated in Figure 3.5. An obvious peak is visible at $f = 0.255998$ days^{-1} corresponding to an orbital period of 3.90628 days. This is consistent with with the optical ephemeris of [54] who derive an orbital period of 3.90603 ± 0.00017 days from measurements of Doppler shifted emission lines. The likely origin of several subsidiary peaks which are also apparent in the periodogram is discussed in §3.10.3.6.

3.10.3.2 The Inclusion of Measurement Errors

The classical periodogram (3.30) takes no account of the relative uncertainties associated with individual measurements comprising the integral flux lightcurve. From an experimental standpoint, flux points with large statistical errors are likely to misrepresent the temporal evolution of the γ-ray signal and should be accounted for by an appropriate point-wise weighting of the input data. A simple prescription, implemented by [71], involves multiplying the data points and model functions by a factor $\epsilon_i = 1/\sigma_i$ where σ_i is the statistical error associated with I_i. This approach is

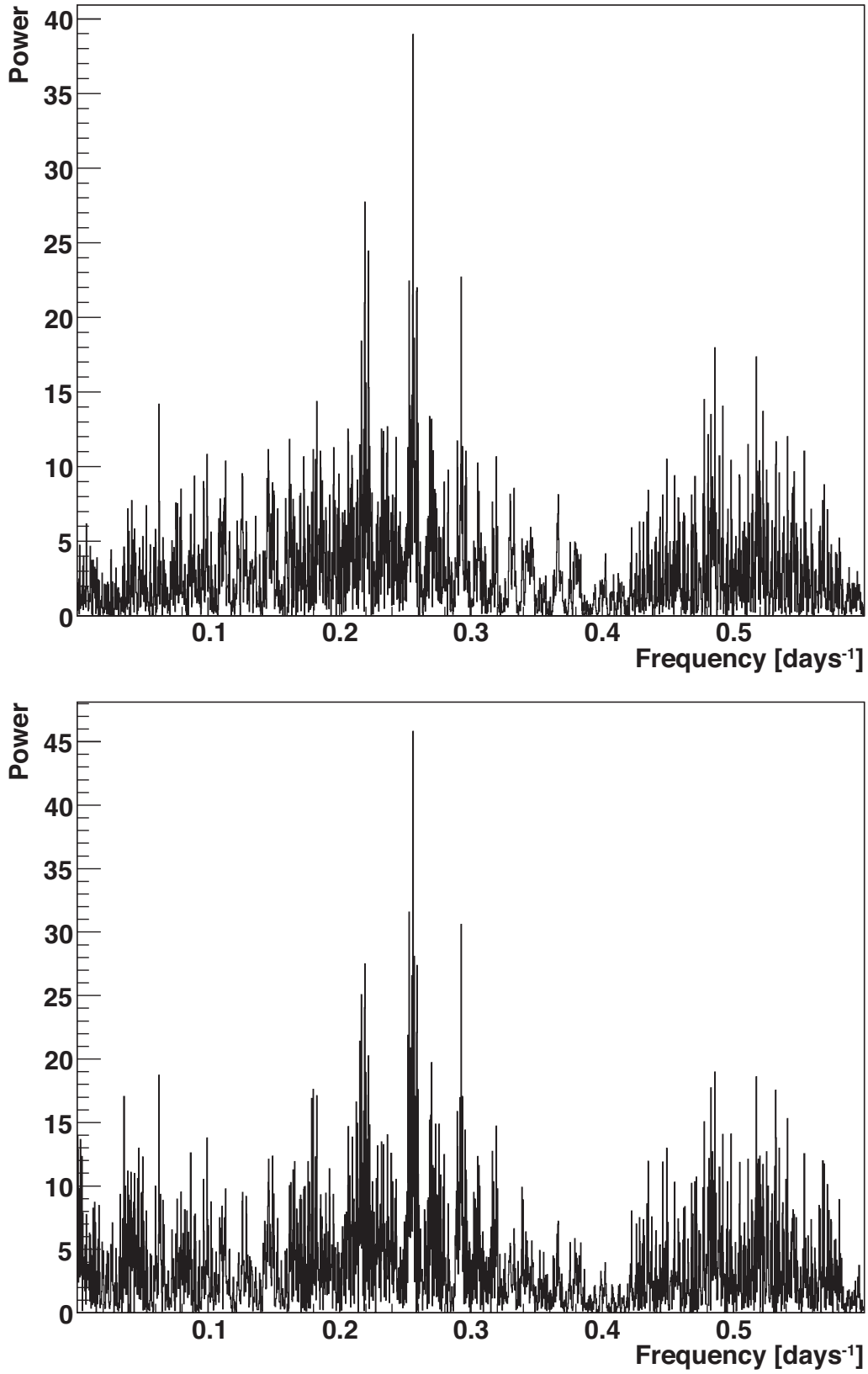

Figure 3.7: *Top panel:* The classically normalised Lomb-Scargle periodogram for LS 5039. *Bottom panel:* The classically normalised Lomb-Scargle periodogram for LS 5039 with treatment of experimental uncertainties included.

functionally equivalent to replacing the least squares fit with a χ^2 fit in the Lomb-Scargle algorithm i.e. $\Delta R \rightarrow \Delta\chi^2$. With the appropriate adaptations, (3.19) becomes:

$$\begin{pmatrix} \epsilon_1 \cos\omega(t_1-\tau) & \epsilon_1 \sin\omega(t_1-\tau) \\ \epsilon_2 \cos\omega(t_2-\tau) & \epsilon_2 \sin\omega(t_2-\tau) \\ \vdots & \vdots \\ \epsilon_n \cos\omega(t_n-\tau) & \epsilon_n \sin\omega(t_n-\tau) \end{pmatrix} \begin{pmatrix} a \\ b \end{pmatrix} \approx \begin{pmatrix} \epsilon_1 \tilde{I}_1 \\ \epsilon_2 \tilde{I}_2 \\ \vdots \\ \epsilon_n \tilde{I}_n \end{pmatrix} \tag{3.31}$$

The corresponding expression for the periodogram is then derived precisely as before, yielding:

$$z' = \frac{1}{2s^2} \left\{ \frac{\left[\sum_{i=1}^{n} \epsilon_i^2 \tilde{I}_i \cos\omega(t_i-\tau)\right]^2}{\sum_{i=1}^{n} \epsilon_i^2 \cos^2\omega(t_i-\tau)} + \frac{\left[\sum_{i=1}^{n} \epsilon_i^2 \tilde{I}_i \sin\omega(t_i-\tau)\right]^2}{\sum_{i=1}^{n} \epsilon_i^2 \sin^2\omega(t_i-\tau)} \right\} \tag{3.32}$$

Figure 3.7 (bottom panel) shows the error weighted periodogram for LS 5039. Comparison with the classical periodogram shown in Figure 3.7 (top panel) reveals a significant enhancement of the main signal peak with respect to the background noise level. The increased signal detection power which is afforded by the inclusion of measurement errors in the periodogram calculation may prove invaluable for the detection of weaker periodic signals (See Chapter 5).

3.10.3.3 The Floating Mean Periodogram

A second shortcoming of the classical periodogram arises from its inherent assumption that the mean of the data is a good approximation for the mean of the putative sinusoidal signal. In fact, there are several reasons why this may not be the case. Indeed, sparse and uneven sampling of the input lightcurve, the combined statistical fluctuations of the individual data points, or a true signal period which is longer than the overall observation interval may all result in a biased estimate of the true mean.

The obvious solution is to modify the sinusoidal model to include a constant offset [e.g. 71, 251]:

$$P_i = a\cos\omega t_i + b\sin\omega t_i + c \tag{3.33}$$

Retaining the point-wise weights from the previous section, the matrix representation of this new model becomes:

$$\begin{pmatrix} \epsilon_1\cos\omega(t_1-\tau) & \epsilon_1\sin\omega(t_1-\tau) & \epsilon_1 \\ \epsilon_2\cos\omega(t_2-\tau) & \epsilon_2\sin\omega(t_2-\tau) & \epsilon_2 \\ \vdots & \vdots & \vdots \\ \epsilon_n\cos\omega(t_n-\tau) & \epsilon_n\sin\omega(t_n-\tau) & \epsilon_n \end{pmatrix} \begin{pmatrix} a \\ b \\ c \end{pmatrix} \approx \begin{pmatrix} \epsilon_1 I_1 \\ \epsilon_2 I_2 \\ \vdots \\ \epsilon_n I_n \end{pmatrix} \tag{3.34}$$

Notice that the I_i are no longer mean-subtracted, since the mean is now a free parameter of the model. Redefining (3.26):

$$\begin{aligned} CC &= \sum_{i=1}^{n} \epsilon_i^2 \cos^2\omega(t_i-\tau), & SS &= \sum_{i=1}^{n} \epsilon^2 \sin^2\omega(t_i-\tau), \\ CS &= \sum_{i=1}^{n} \epsilon_i^2 \cos\omega(t_i-\tau)\sin\omega(t_i-\tau), & & \\ YC &= \sum_{i=1}^{n} \epsilon_i^2 I_i \cos\omega(t_i-\tau), & YS &= \sum_{i=1}^{n} \epsilon_i^2 I_i \sin\omega(t_i-\tau) \end{aligned} \tag{3.35}$$

and introducing the additional notation:

$$\begin{aligned} C &= \sum_{i=1}^{n} \epsilon_i^2 \cos\omega(t_i-\tau), & S &= \sum_{i=1}^{n} \epsilon^2 \sin\omega(t_i-\tau), \\ Y &= \sum_{i=1}^{n} \epsilon^2 I_i & YY &= \sum_{i=1}^{n} \epsilon^2 I_i^2 \end{aligned} \tag{3.36}$$

the normal equations may be expressed as:

$$\begin{pmatrix} CC & CS & C \\ CS & SS & S \\ C & S & 1 \end{pmatrix} \begin{pmatrix} a \\ b \\ c \end{pmatrix} = \begin{pmatrix} YC \\ YS \\ Y \end{pmatrix} \tag{3.37}$$

Eliminating the bottom row of (3.34) by subtraction yields a simplified expression which has the same form as an expanded version of (3.22):

$$\begin{pmatrix} CC - C \cdot C & CS - C \cdot S \\ CS - C \cdot S & SS - S \cdot S \end{pmatrix} \begin{pmatrix} a \\ b \end{pmatrix} = \begin{pmatrix} YC - Y \cdot C \\ YS - Y \cdot S \end{pmatrix} \tag{3.38}$$

or equivalently, using a more compact notation:

$$\begin{pmatrix} \widehat{CC} & \widehat{CS} \\ \widehat{CS} & \widehat{SS} \end{pmatrix} \begin{pmatrix} a \\ b \end{pmatrix} = \begin{pmatrix} \widehat{YC} \\ \widehat{YS} \end{pmatrix} \tag{3.39}$$

The corresponding classically normalised periodogram expression is therefore defined as [251]:

$$z'' = \frac{1}{\widehat{YY}} \left[\frac{\widehat{YC}^2}{\widehat{CC}} + \frac{\widehat{YS}^2}{\widehat{SS}} \right] \tag{3.40}$$

where $\widehat{YY} = YY - Y \cdot Y$. The phase offset $\hat{\tau}$ must also be redefined as:

$$\hat{\tau} = \frac{2\widehat{CS}}{\widehat{CS} - \widehat{SS}} \tag{3.41}$$

Figure 3.8 (top panel) plots the floating mean periodogram of the LS 5039 lightcurve. The improvements over the error weighted periodogram are minimal, and the period corresponding to the maximum Lomb-scargle power is unchanged. This is expected because the LS 5039 lightcurve is exceptionally well sampled and spans many orbital periods, making it essentially immune to the effects which motivated the implementation of the floating mean periodogram. Nonetheless, there is

some suppression of noise peaks at low frequencies, where the corresponding period approaches the overall sampling interval. Furthermore, this approach often yields significantly improved results for more sparsely sampled lightcurves [e.g 71], and may also be useful when the signal-to-noise ratio is low or the sampling interval is short (See Chapter 5). Unless otherwise stated, the discussions in the following subsections relate to the floating mean periodogram.

3.10.3.4 Normalising the Periodogram

All variants of the periodogram require normalisation in order that the resultant Lomb-Scargle powers ($z(\omega)$) have a simple statistical distribution when the data are pure gaussian noise [71]. If this can be achieved, robust estimates for the false-alarm probability (See §3.10.3.5) of an observed peak power are possible. Although there are several common normalisation strategies in use, [224] was able to show that all these approaches are *statistically* equivalent. Accordingly, while the calculated powers and overall appearance of the periodogram may be markedly dissimilar for different normalisation prescriptions, the peak significances derived using the appropriate probability distributions will be identical.

As shown by [219], if the data are white noise with *true* variance σ_0^2, then the classical unnormalised periodogram ($\hat{z}(\omega)$) is the sum of the squares of two random gaussian variables and has an exponential (χ_2^2) distribution [e.g. 130]:

$$f(\hat{z})d\hat{z} = \frac{1}{\sigma_0^2}\exp\left(-\frac{\hat{z}}{\sigma_0^2}\right)d\hat{z} \tag{3.42}$$

If true variance is known, then the periodogram may be normalised by σ_0^2 yielding:

$$f(z)dz = \exp(-z)dz \tag{3.43}$$

with the corresponding *single trial* probability of observing $z > z_0$ given by:

$$\text{Prob}(z > z_0) = \exp(-z_0) \tag{3.44}$$

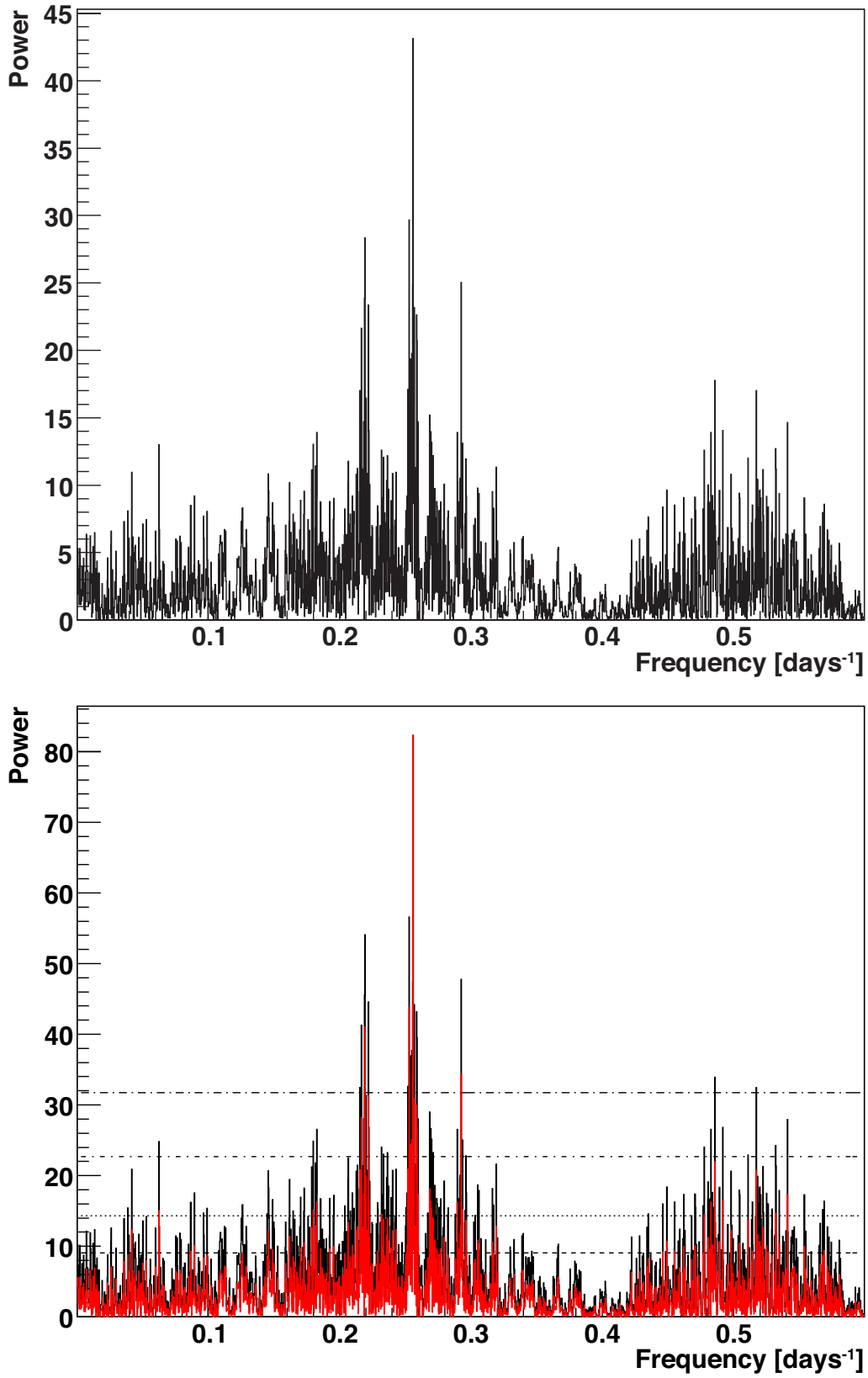

Figure 3.8: *Top panel:* The classically normalised floating mean periodogram of the LS 5039 lightcurve. *Bottom panel:* The floating mean periodogram normalised by the residual variance corresponding to the best fitting sinusoid (black), and by the best fitting sinusoid at each individual frequency (red). The overlaid lines indicate powers which correspond to false alarm probabilities (see §3.10.3.5) of 10^{-1} (dashed), 10^{-3} (dotted), 10^{-6} (dot-dashed), and 10^{-9} (dot-long dashed).

The more common situation in observational sciences such as astronomy is that the sample variance s^2 must be used to estimate σ_0^2. When normalising by the sample variance, the corresponding probability distribution for $z > z_0$ may be expressed in terms of the incomplete beta function, I [71]:

$$\text{Prob}(z > z_0) = 1 - I_{2z_0/(n-1)}\left(1, \frac{n-3}{2}\right) = \left(1 - \frac{2z_0}{n-1}\right)^{(n-3)/2} \tag{3.45}$$

Another alternative is to normalise using s_n^2, the variance of the residuals between the data points and the best-fitting sinusoid. Using this *residual variance* normalisation, the relevant probability distribution is [71]:

$$\text{Prob}(z > z_0) = \int_{z_0}^{\infty} dz\, F_{2,n-3}(z) = \left(1 + \frac{2z_0}{n-3}\right)^{-(n-3)/2} \tag{3.46}$$

where F is the Fischer-Snedecor distribution.

If only the *highest* peak (i.e. the most likely period) is important, then it is valid to normalise each power independently, using the residual variance of the best fitting model at the appropriate frequency [e.g. 71]. Figure 3.8 (bottom panel) compares this frequency-wise residual normalisation strategy with the standard residual normalisation. By definition, the probability distribution of the highest peak is unchanged, but this approach enhances the contrast of significant peaks with respect to the background noise. Finally, it should be noted that the frequency-wise residual normalisation method was used to generate the Lomb-Scargle periodogram presented by [14] (Mathieu de Naurois, by private communication).

3.10.3.5 The False Alarm Probability

Some care is required when interpreting the periodogram. Indeed, as noted by [219], aperiodic but noisy data may still produce unexpectedly high Lomb-Scargle powers in the calculated spectrum. Calculation of the false alarm probability provides a way to confidently distinguish between spurious peaks and those which indicate a genuine periodic signal.

The false alarm probability $P_{\text{fa}}^{\text{LS}}$ associated with an observed Lomb-Scargle power z_0 is defined

as the probability of a similar or greater power arising if the input time series is pure Gaussian noise. For a single trial frequency, the relevant expressions for $\text{Prob}(z > z_0)$ have already been given in §3.10.3.4. However, the construction of the periodogram entails calculation of z for many trial frequencies, with the overall false alarm probability given by [219] as:

$$P_{\text{fa}}^{\text{LS}}(z_0) = 1 - [1 - \text{Prob}(z > z_0)]^N \tag{3.47}$$

where N is the effective number of *independent* trial frequencies. Estimation of N is complicated by the fact that values in the Lomb-Scargle periodogram may be correlated due to the uneven sampling of the input lightcurve [224]. A common Monte Carlo approach involves calculating the maximum Lomb-Scargle power for a large number of lightcurves containing Gaussian noise [e.g. 130]. The response of the periodogram, including the level of correlation between frequencies, is mainly determined by the window function of the input time series, which in turn depends upon the details of the lightcurve sampling [219]. For this reason, it is important that the simulated lightcurves emulate the sampling intervals of the time series under test. Figure 3.9 plots the complement of the cumulative distribution (or *survival function*) of z which describes the fraction of simulated lightcurves for which the maximum Lomb-Scargle power exceeds z and, for a given $z = z_0$, corresponds to the false alarm probability defined by (3.47). To generate this distribution, 10^4 lightcurves were simulated by randomly shuffling the flux points of the input lightcurve *after* subtraction of the best fitting sinusoid while maintaining the same observation times. The number of independent frequencies may then be estimated from the best fit of (3.47) to the simulated survival function. For the periodograms shown in this chapter, the number of independent frequencies was found to be ~ 585. For illustration, Lomb-Scargle power levels corresponding to various values of the false alarm probability are overlaid in Figure 3.8 (bottom panel). Using the floating mean periodogram, with measurement errors included, the false alarm probability corresponding to the peak Lomb-Scargle power is 5.42×10^{-26} corresponding to the emphatic detection of a periodic signal in the VHE γ-ray flux.

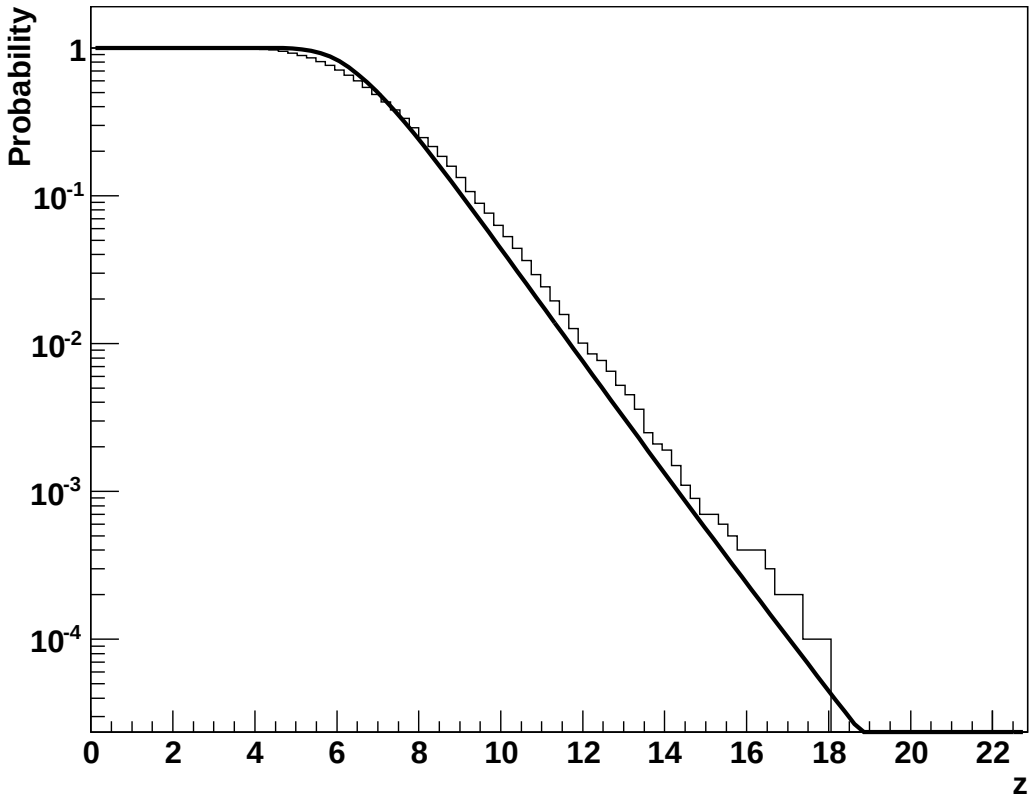

Figure 3.9: The complement of the cumulative distribution of maximum Lomb-Scargle powers corresponding to 10^4 simulated lightcurves. The fitted survival function, corresponding to the false alarm probability at each z is overlaid.

3.10.3.6 Period Subtraction

In all variants of the Lomb-Scargle periodogram, the main peak exhibits prominent *side-lobes* which appear to indicate additional periodic signals in the data. In fact, these satellite peaks result from interference between the true signal and any systematic periodicities arising from sampling restrictions inherent to the mode of observation. In the case of Cherenkov telescope data, the requirement for absolute darkness at the time of observation almost inevitably results in some imprint of the diurnal, lunar and annual cycles on the sampling intervals. In order to verify the origin of these alias peaks it is necessary to subtract the best fitting Lomb-Scargle model:

$$P_i^{\text{best}} = a_{\text{best}} \cos \omega_{\text{best}} t_i + b_{\text{best}} \sin \omega_{\text{best}} t_i + c_{\text{best}} \tag{3.48}$$

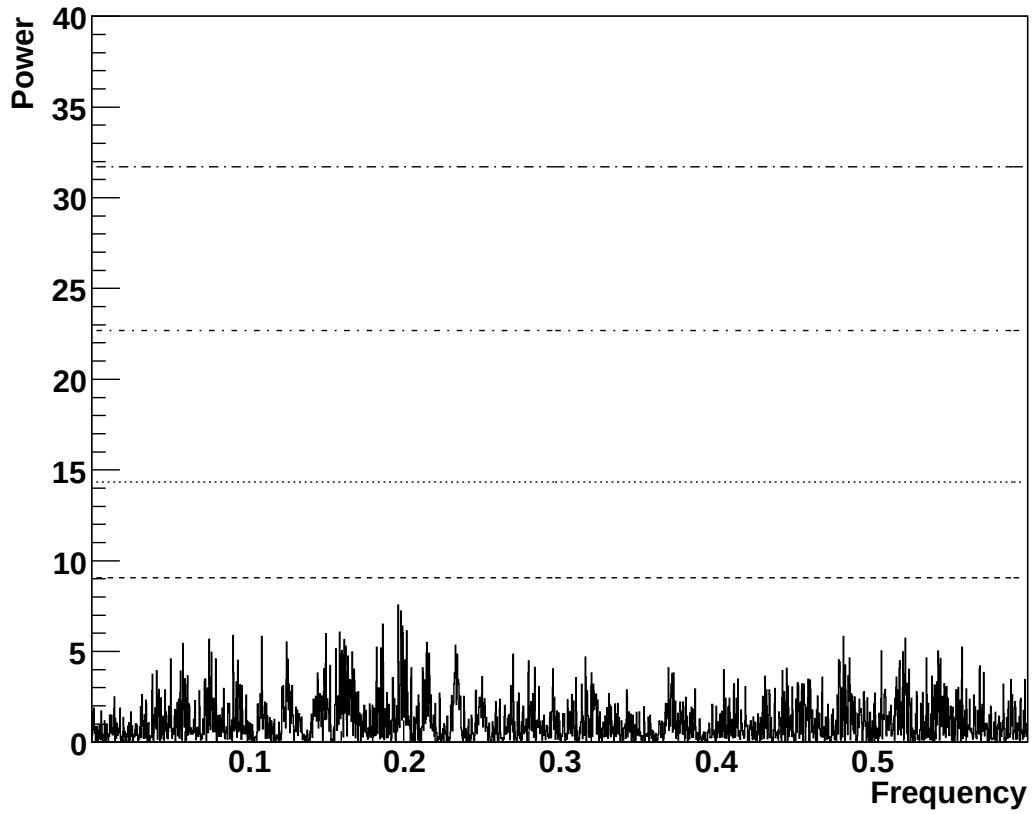

Figure 3.10: Floating mean periodogram of the LS 5039 lightcurve after subtraction of the best-fitting sinusoidal function. The overlaid lines indicate powers which correspond to false alarm probabilities of 10^{-1} (dashed), 10^{-3} (dotted), 10^{-6} (dot-dashed), and 10^{-9} (dot-long dashed).

from the lightcurve. Using (3.38) for the floating mean periodogram, the coefficients of the sine and cosine components of the Lomb-Scargle model (3.48) at the frequency $\omega_{\rm best}$ may be derived:

$$a_{\rm best} = \frac{\widehat{YC}\cdot\widehat{SS} - \widehat{YS}\cdot\widehat{CS}}{\widehat{CC}\cdot\widehat{SS} - \widehat{CS}^2} \tag{3.49}$$

$$b_{\rm best} = \frac{\widehat{YS}\cdot\widehat{CC} - \widehat{YC}\cdot\widehat{CS}}{\widehat{CC}\cdot\widehat{SS} - \widehat{CS}^2} \tag{3.50}$$

and the value of the constant term $c_{\rm best}$ may then be obtained directly using the bottom row of (3.37).

Figure 3.10 illustrates the result of subtracting $P^{\rm best}$ from the input lightcurve and re-evaluating the periodogram. The absence of statistically significant peaks in the resultant power spectrum confirms the origin of the alias peaks, and eliminates the possibility of additional genuine period-

Table 3.6: The phase-binned mean and RMS of the residuals between the folded LS 5039 lightcurve and the best fitting sinusoid.

Phase Interval	Residual Mean [$\mathrm{cm}^{-2}\ \mathrm{s}^{-1}$]	Residual RMS [$\mathrm{cm}^{-2}\ \mathrm{s}^{-1}$]	Number of Runs
$\mathbf{0.75 \leq \phi \leq 0.9}$	5.83×10^{-13}	7.35×10^{-13}	54
$0 \leq \phi \leq 0.3$	1.41×10^{-13}	5.51×10^{-13}	55
$0.3 \leq \phi \leq 0.6$	-6.85×10^{-15}	7.19×10^{-13}	45
$0.6 \leq \phi \leq 0.75$ $0.9 \leq \phi \leq 1.0$	-1.97×10^{-13}	5.45×10^{-13}	26

icities in the observed γ-ray signal.

3.10.3.7 Folded Lightcurve

In Figure 3.11 (top panel) the LS 5039 integral flux lightcurve has been epoch folded according to the most likely optical period derived by [54]. Inspection of the resulting phasogram reveals two distinct regimes of TeV emission. The bulk of the observed TeV flux is emitted during the phase interval $0.45 < \phi \leq 0.9$ (hereafter INFC) , which spans the *inferior conjunction* of the binary system. In contrast, the phase intervals $0.9 < \phi \leq 1$ and $1 < \phi \leq 0.45$ (hereafter SUPC) which encompass the epoch of *superior conjunction* are characterised by a relatively low average γ-ray flux. This result is in good agreement with the observations of [14] with the additional data giving no indication of a recent alteration in the source behaviour.

Figure 3.11 (bottom panel) plots the epoch-folded residuals between the data and the best fitting sinusoidal model P^{best}. The figure appears to indicate a narrow peak in the observed TeV flux during the phase interval $0.75 \leq \phi \leq 0.9$. It is interesting to note that the 3-30 keV X-ray phasogram presented by [45] exhibits a flux maximum at $\phi \sim 0.8$, which corresponds well with apparent excess of γ-ray emission. Table 3.6 lists the phase-resolved mean and RMS of the Lomb-Scargle residuals during the suspected peak interval and three other control intervals. Although the mean of the residuals for $0.75 \leq \phi \leq 0.9$ is noticeably larger than the corresponding values for the remaining phase bins, it is evident that the large RMS values do not support the existence of a significant peak.

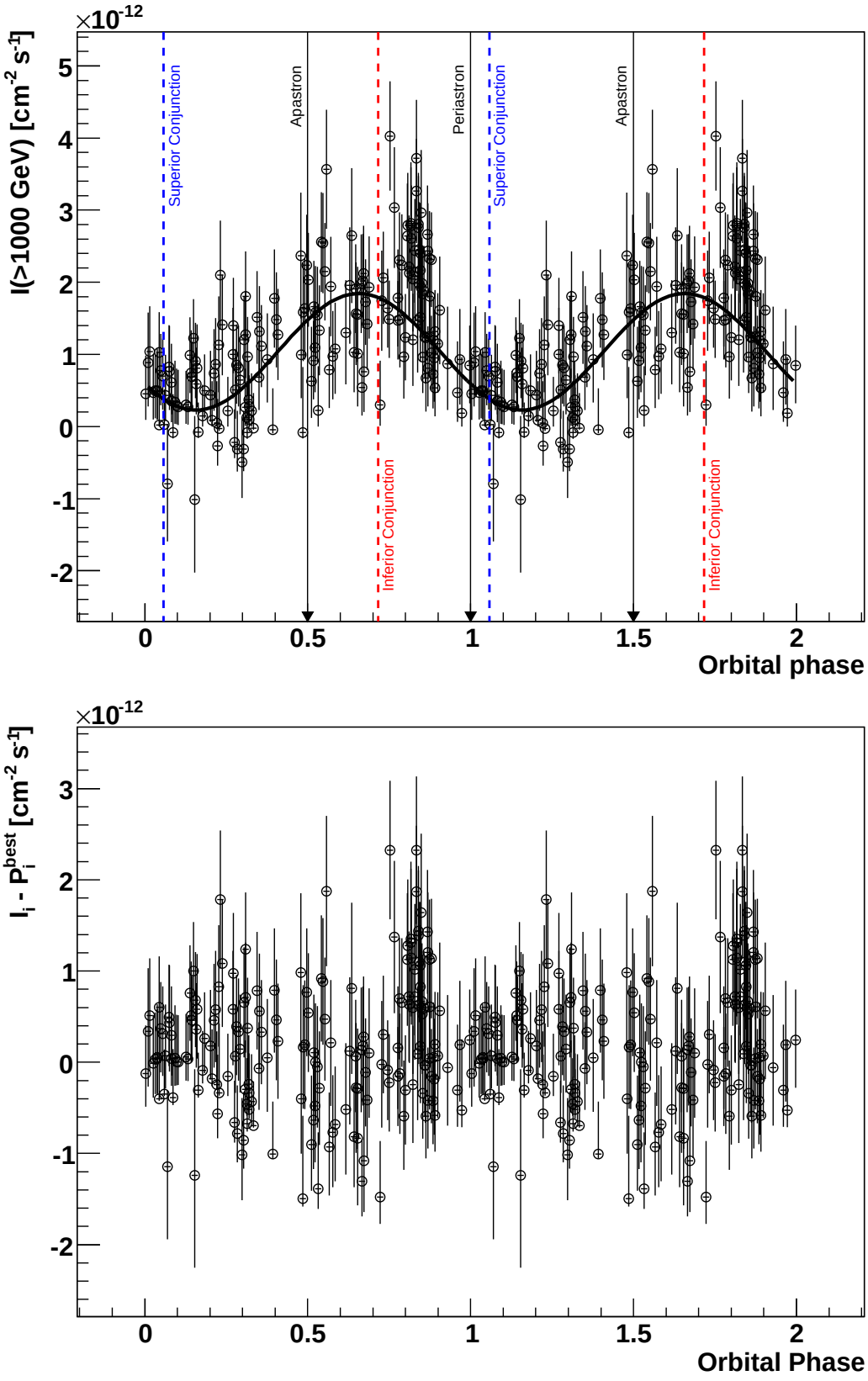

Figure 3.11: *Top Panel:* The LS 5039 integral flux lightcurve folded with the optical ephemeris of [54]. The thick black curve plots the sinusoidal function corresponding to the Lomb-Scargle coefficients at the best optical period. *Bottom Panel:* The residuals between the data and the best fitting sinusoid.

3.10.3.8 Frequency Resolution

In general, derivation of the frequency resolution of the Lomb-Scargle periodogram is not straightforward since it is dictated both by the details of the lightcurve sampling, and also by the level of the aperiodic background noise. For the usual case of noisy, unevenly sampled data the frequency resolution cannot be expressed analytically and Monte Carlo simulations must be used to obtain an estimate of its value.

The best estimate of the background noise level is contained in the period-subtracted integral flux lightcurve. By randomly shuffling the subtracted lightcurve fluxes and then re-inserting the periodic signal, 10^4 Monte-Carlo time series were generated with the same periodic and aperiodic variability properties as the LS 5039 data set. The Lomb-Scargle periodogram was then evaluated for each simulated time series and the frequency resolution of 0.0013 days was calculated as the RMS of the resultant distribution of best fitting periods.

3.10.4 Temporal Analysis Summary

The integral flux lightcurve for photon energies above 1 TeV has been used to perform a detailed analysis of the temporal variability of LS 5039. While no evidence was found for long term trends in the observed γ-ray signal, there was a strong indication for short term flux variation.

The Lomb-Scargle periodogram was used to search for periodicity in the LS 5039 lightcurve and identified a clear signal corresponding to a period of 3.90628 ± 0.0013 days. This is in good agreement with published VHE γ-ray results of [14] and with the optical period of 3.90603 ± 0.00017 days derived by [54]. The periodic behaviour was characterised by two distinct flux regimes with most of the observed TeV flux emitted around inferior conjunction, during the orbital phase interval $0.45 < \phi \leq 0.9$. Conversely, the remaining phase intervals spanning superior conjunction are characterised by low, but notably non-zero γ-ray fluxes.

After subtraction of the best-fitting Lomb-Scargle model function from the data, the period-folded lightcurve appeared to indicate a correlated excess in the residual γ-ray flux during the orbital phase interval $0.75 \leq \phi \leq 0.9$, perhaps corresponding to a similar excess in the 3-30 keV

X-ray phasogram [45]. The distribution of residual fluxes corresponding to the putative excess was compared with equivalent distributions from three other phase intervals. While the mean residual flux for $0.75 \leq \phi \leq 0.9$ was somewhat larger than for the control intervals, the spread of the period-subtracted data points was too large for a peak to be conclusively identified.

3.11 Spectral Analysis

The spectrum of radiation from X-ray binaries provides a crucial means of validating the predictions of radiative emission models. Indeed, high resolution spectral observations at non-γ-ray energies often yield powerful insights regarding the intrinsic processes of accretion, particle acceleration and radiative emission [e.g. 82, 81, 97]. The primarily non-thermal characteristics of VHE γ-ray spectra are likely representative of the most energetic processes taking place within X-ray binary systems. As such they may help to constrain critical parameters such as the maximum efficiency of particle acceleration, the density of ambient radiation fields, and the origin of intrinsic opacity to very high energy radiation.

The differential energy spectra of typical VHE γ-ray sources are well approximated as a falling power law in photon energy (c.f. (3.10)). Accordingly, useful spectral extraction requires a luminous γ-ray source or a long overall exposure in order to accumulate sufficient photon statistics at high energies. Fortunately, the extensive LS 5039 data set yields an event sample which is easily sufficient for spectral analysis and even permits consideration of spectral variability. This section introduces several spectral analysis techniques that are applicable to the VHE γ-ray emission from X-ray binary systems while also presenting the results of their application to the LS 5039 data set. Where possible the results will be compared to those of [14], although it should be noted that some discrepancies consistent with systematic uncertainties are expected. Indeed, while the results presented here utilised the image moment and scaled parameter analyses outlined in §1.3.5 and §1.3.7, [14] employed a combined semi-analytical shower model and Hillas parameterisation approach for event selection [74] which often yields superior background suppression and hence

Table 3.7: Spectral fit parameters for spectra corresponding to the INFC and SUPC phase intervals and also to the complete LS5039 data set.

Phase Interval	N_0 $\times 10^{-12}$ [cm^{-2} s^{-1}]	Γ	$1/E_c$ [TeV]	χ^2 (NDF)
$0.45 < \phi \leq 0.9$ (INFC)	2.99 ± 0.15	1.85 ± 0.07	0.13 ± 0.03	20.71 (10)
$0.9 < \phi \leq 1$, $1 < \phi \leq 0.45$ (SUPC)	0.68 ± 0.7	2.58 ± 0.13	-	2.31 (5)
All Phases	1.64 ± 0.05	2.24 ± 0.03	-	28.55 (9)
	1.89 ± 0.10	2.02 ± 0.08	0.09 ± 0.03	18.93 (8)

spectral sensitivity. Furthermore, the data set used for this study incorporates 23 additional observation runs which were not available when [14] performed their analysis. While these additional runs constitute a small fraction of the overall exposure, their incorporation may nonetheless affect the derived spectra.

3.11.1 Overall Spectrum

Spectra were generated using the method outlined by [11] with the differential flux in an energy bin of width ΔE calculated using:

$$\frac{dF}{dE} = \frac{1}{T\Delta E}\left(\sum_{i=0}^{N_{\rm on}} \frac{1}{A_{{\rm eff},i}^{\rm reco}} - \alpha \sum_{j=0}^{N_{\rm off}} \frac{1}{A_{{\rm eff},j}^{\rm reco}}\right) \tag{3.51}$$

where T is the overall livetime and $N_{\rm on}$ and $N_{\rm off}$ refer respectively to the number of ON and OFF events having reconstructed energies within ΔE. The *reconstructed* effective areas $A_{{\rm eff},ij}^{\rm reco}$ are interpolated from lookup tables for each ON or OFF event, whereas the acceptance normalisation α is calculated on a run-wise basis. The reconstructed effective areas are generated using Monte-Carlo γ-ray events with a spectral index of $\Gamma_{\rm MC} \approx 2.0$ in order to ensure sufficient statistics at high photon energies [11]. To calculate the differential flux for sources having $\Gamma \neq \Gamma_{\rm MC}$ it is strictly correct to iteratively modify the effective areas until convergence is achieved, taking into account the calculated spectral slope at each iteration as well as the energy resolution of the H.E.S.S. array [e.g. 182]. However, as noted by [11], the omission of this step biases the differential flux

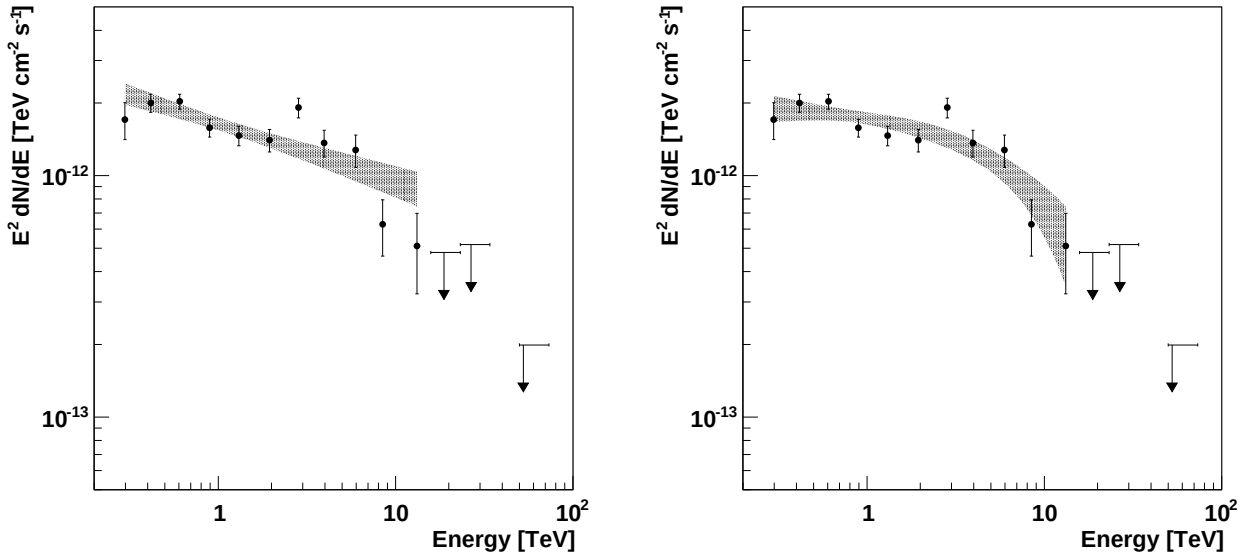

Figure 3.12: Fits to the overall spectrum of LS 5039 using a power law function (*left panel*) and a power law function with an exponential cutoff (*right panel*). The shaded areas plot the 68% confidence band for each fit.

calculation by $\lesssim 5\%$ at the threshold (and significantly less at higher energies) for true photon indices in the range $1.1 \leq \Gamma \leq 3.2$. Consequently, the unmodified reconstructed effective areas were used to calculate all the VHE γ-ray spectra presented in this section.

Figure 3.12 (left panel) plots the results of a power law fit to the overall LS 5039 spectrum, extracted from the full 183 run data set. The resultant function parameters are listed in Table 3.7 and include the value of the photon index $\Gamma = 2.24$ which was used for calculation of the integral flux in §3.9. The corresponding reduced χ^2 value of 3.17 indicates that the overall spectrum is not well described by a pure power law function. In order to obtain a better description of the overall spectral shape, and also to facilitate comparison with the results of [14], an additional fit (Figure 3.12 (right panel)) was made to the overall spectrum using a power law function with an exponential cutoff:

$$\frac{dN}{dE} = N_0 \frac{E}{E_0}^{-\Gamma} \exp\left(-\frac{E}{E_c}\right) \tag{3.52}$$

where N_0 is the differential photon flux at energy E_0 and E_c is the cutoff energy. The resultant fit parameters are listed in Table 3.7 and are broadly compatible with the previously published

values. In fact, the best fitting cutoff energy $E_c \sim 11$ TeV is ~ 2 TeV lower than that derived by [14], but the large uncertainties associated with this value preserve the compatibility of the two results. Although the reduced χ^2 remains somewhat high, the addition of the exponential cutoff results in a noticeable improvement to the overall fit quality, with an F-Test favouring the more complicated model at a confidence level of $\sim 94\%$. Integrating the best fitting exponentially cutoff power law function and assuming a distance of 2.5 kpc, the average 0.2-10 TeV luminosity of LS 5039 is calculated to be 6.61×10^{33} erg s^{-1}.

3.11.2 Spectral variability

Observation of spectral variability provides a valuable diagnostic for the temporal evolution of the γ-ray emission region. Following the approach of [14], separate spectra were extracted which correspond to the broad INFC and SUPC phase intervals. As illustrated in Figure 3.13 these *phase resolved* spectra exhibit markedly different characteristics. The spectrum corresponding to the INFC phase interval exhibits a hard ($\Gamma_{\rm INFC} = 1.85$) power law spectrum with evidence for an exponential cutoff with $E_c = 7.7^{+2.3}_{-0.9}$ TeV. In contrast, the spectrum extracted around superior conjunction is well described by a pure power law with a soft photon index $\Gamma_{\rm SUPC} = 2.58$. The fit parameters corresponding to each phase interval are listed in Table 3.7 and correspond well with the values derived by [14].

Assuming a source distance of 2.5 kpc and integrating the best fitting model functions for each phase interval indicates that the 0.2-10 TeV γ-ray luminosity of LS 5039 varies between $\sim 4 \times 10^{33}$ erg s^{-1} close to superior conjunction, up to $\sim 9 \times 10^{33}$ erg s^{-1} around inferior conjunction. These luminosity estimates are broadly compatible with the values of $L_{\rm SUPC} \sim 4 \times 10^{33}$ erg s^{-1} and $L_{\rm INFC} \sim 1.1 \times 10^{34}$ erg s^{-1} derived by [14], with the slight difference during INFC primarly due to the difference in fitted cutoff energies.

In order to explore the spectral variability on shorter time scales, spectra were extracted which correspond to narrow phase intervals of width $\Delta\phi = 0.1$. Fits were made to the individual spectra using a pure power law function in a restricted range of energies between 0.2 and 5 TeV,

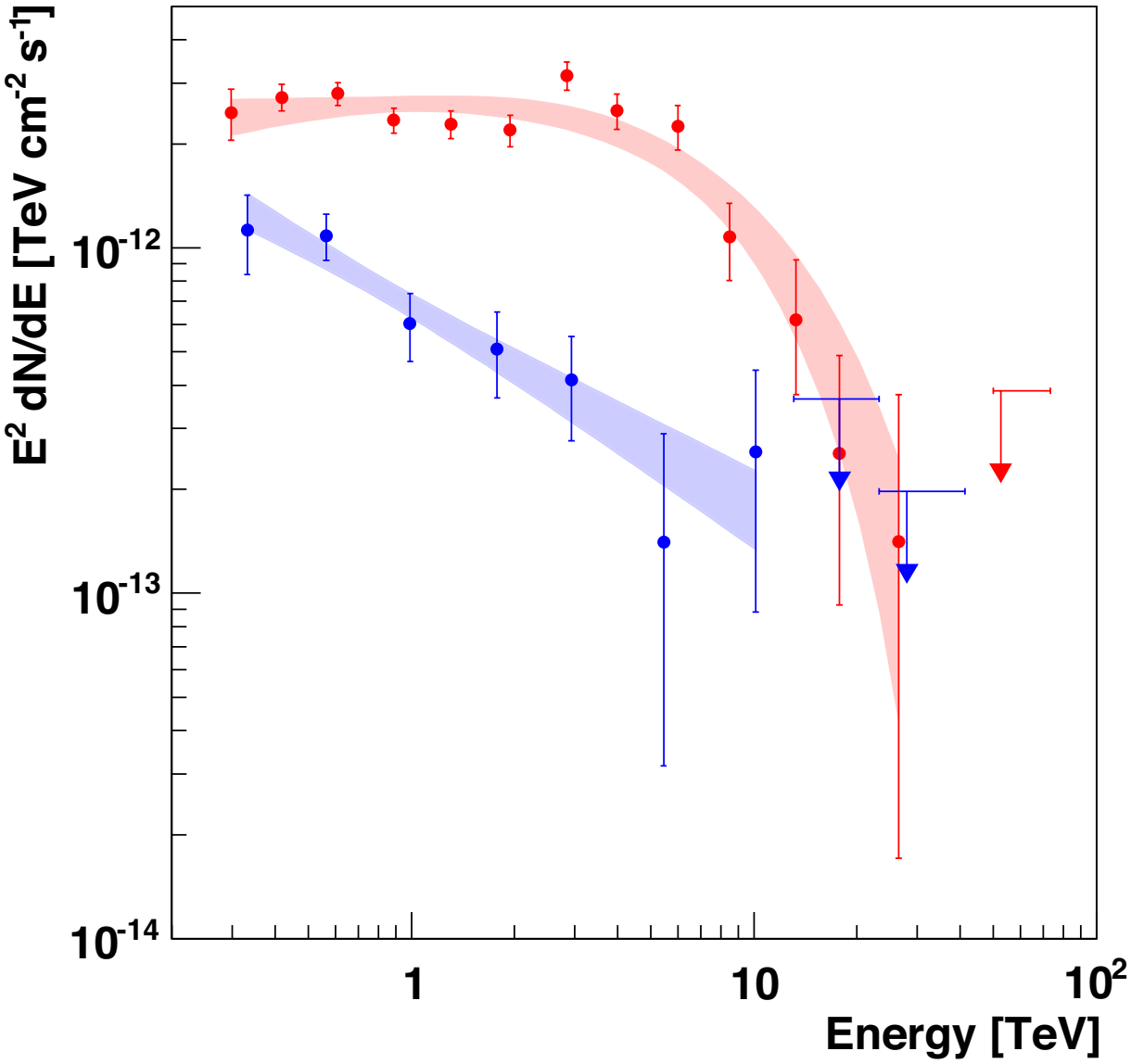

Figure 3.13: VHE γ-ray spectra corresponding to the broad phase intervals (INFC) (*Red*) and SUPC *blue*. The shaded bands indicate the 68% confidence bands for the best-fitting model functions. While the SUPC spectrum was well approximated by a pure power-law, the addition of an exponential cutoff provided a better fit to the INFC spectrum.

with the upper energy limit designed to ameliorate the effect of any spectral cutoffs close to inferior conjunction. Figure 3.14 plots the resultant fit parameters as a function of orbital phase. Although the results shown in Figure 3.14 are somewhat noisier than those presented by [14], they nonetheless appear to replicate the correlation between the 1 TeV differential flux and the 0.2-5 TeV photon index revealed by the earlier analysis with a calculated correlation coefficient of ~ -0.74. Interestingly, this spectral hardening with increasing TeV flux echoes a similar behaviour observed in the 3-30 keV X-ray lightcurve by [45] and may indicate that the same particle population is responsible for the emission in both energy regimes.

3.12 Phenomenological Modelling

The results which were derived in the previous sections reveal a rich phenomenology associated with the VHE γ-ray emission from LS 5039. In this section the simple models for γ-ray emission and absorption which were outlined in §2.7 are applied to determine whether they can adequately reproduce the observed spectral and temporal behaviour.

3.12.1 γ-ray Absorption

As noted by several authors [e.g. 85, 47, 14], the close temporal correspondence between the extrema of the VHE γ-ray phasogram and the epochs of superior and inferior conjunction implies that a significant proportion of the observed variability is due to intrinsic absorption of γ-ray photons. Indeed, the dense ultraviolet photon field of the O-type companion, combined with orbital variations of the system separation and orientation with respect to the line-of-sight should produce strong and variable modulation of the observed GeV/TeV flux [85].

Figure 3.15 illustrates the expected levels of intrinsic absorption as a function of orbital phase based on the system properties listed in Table 3.1. The predictions are derived using a custom implementation of the the model of [85], which assumes that VHE γ-rays are produced close to the compact object and suffer attenuation from electron-positron pair production with photons

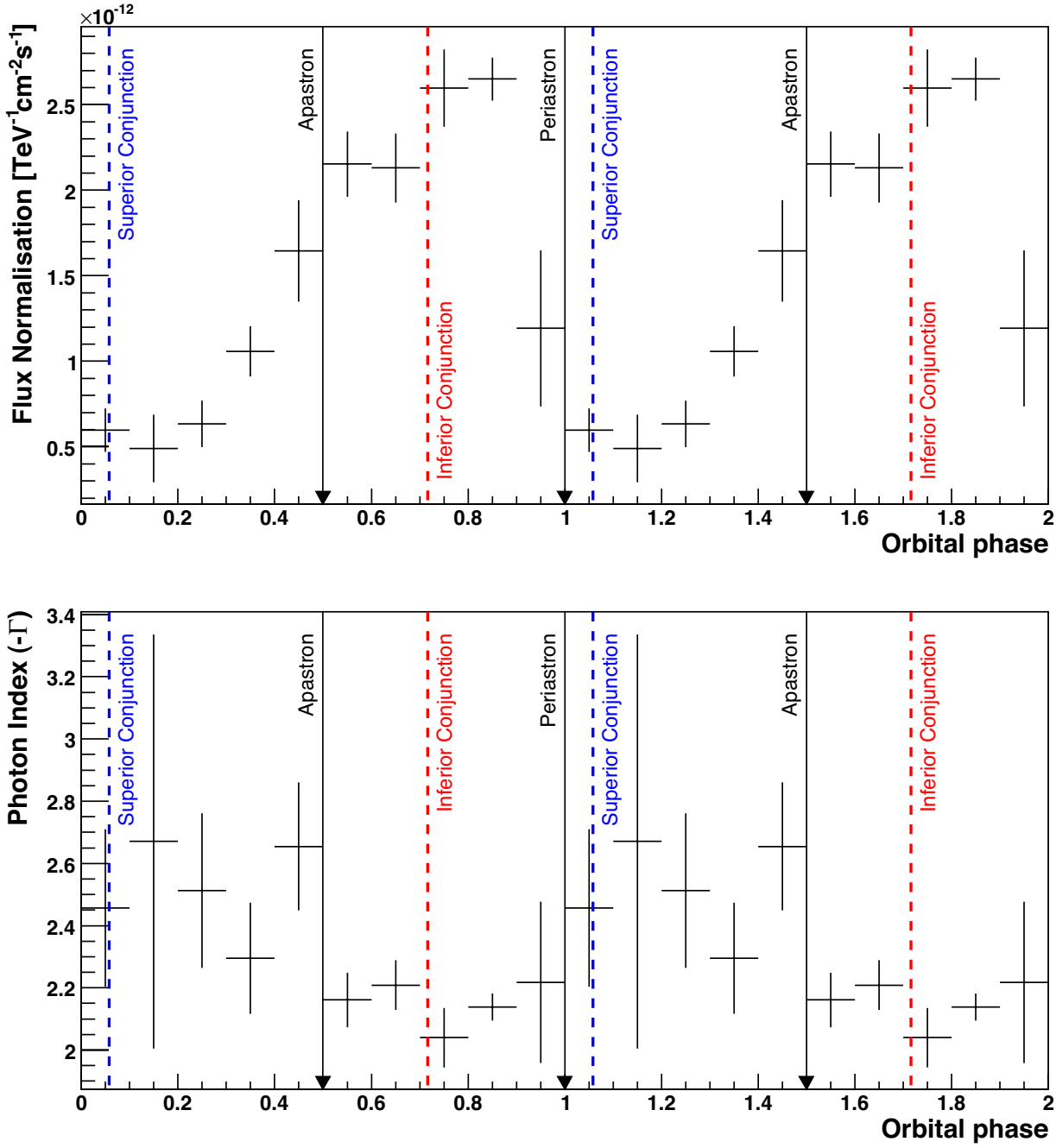

Figure 3.14: *Top panel:* Values of the differential flux normalisation at 1 TeV corresponding to pure power law fits between 0.2 and 5 TeV of spectra exctracted from narrow phase bins of width $\Delta\phi = 0.1$. *Bottom panel:* Values of the photon index Γ corresponding to pure power law fits between 0.2 and 5 TeV of spectra extracted the from same phase bins as in the top panel.

from the stellar radiation field. In view of the ambiguity regarding the compact object in the LS 5039 system (see §3.1), predicted absorption levels are shown which broadly correspond to regimes of the orbital inclination angle. The top panel of Figure 3.15 assumes an inclination of 60° which would imply a ~ 1.4 $M_\odot$ neutron star, while the bottom panel adopts a 20° inclination and would correspond to a ~ 4.5 $M_\odot$ black hole. The modelled absorption characteristics are broadly compatible with the observed γ-ray variability illustrated in Figure 3.14. More specifically, the maximum γ-ray transmission occurring close to inferior conjunction, and the predicted flux minimum at $\phi \sim 0.05$ around superior conjunction. Perhaps most noteworthy is the fact that for both inclination regimes, the model predicts *total* absorption of 1 TeV γ-rays close to superior conjunction. This is not consistent with the results illustrated in Figure 3.14 which clearly indicate a non-zero minimum in the differential γ-ray flux at 1 TeV.

The obvious implication of an unabsorbed flux component is that γ-ray emission takes place in an extended region which is not entirely co-spatial with the compact object. If parts of the γ-ray source extend into regions of lower γ-ray opacity, then the expected flux suppression at superior conjunction may be ameliorated. The observation of milliarcsecond radio structure associated with LS 5039 [193] implies the existence of extended regions where particle acceleration is taking place, and lends some credibility to this scenario.

The expected effects of pair production on the VHE γ-ray energy spectrum are illustrated in Figure 3.16 for several orbital phases. As before, two inclination regimes which correspond to the two possible compact object types are considered. The predicted absorption spans a wide range of energies for both assumed inclination angles. Considering the implied differential flux *variability* which would result from absorption by pair production, the predictions for a neutron star system appear to indicate that the maximum variation is expected for photon energies $\lesssim 1$ TeV. In contrast, the expectied variability in a black hole system would be maximised for γ-ray energies $2 \lesssim E_\gamma \lesssim 10$ TeV. Comparing these predictions with the broad spectral variability illustrated in Figure 3.13 under the assumption that the observed variability arises purely from intrinsic γ-ray absorption, would appear to favour a low inclination angle, implying that the LS 5039 system

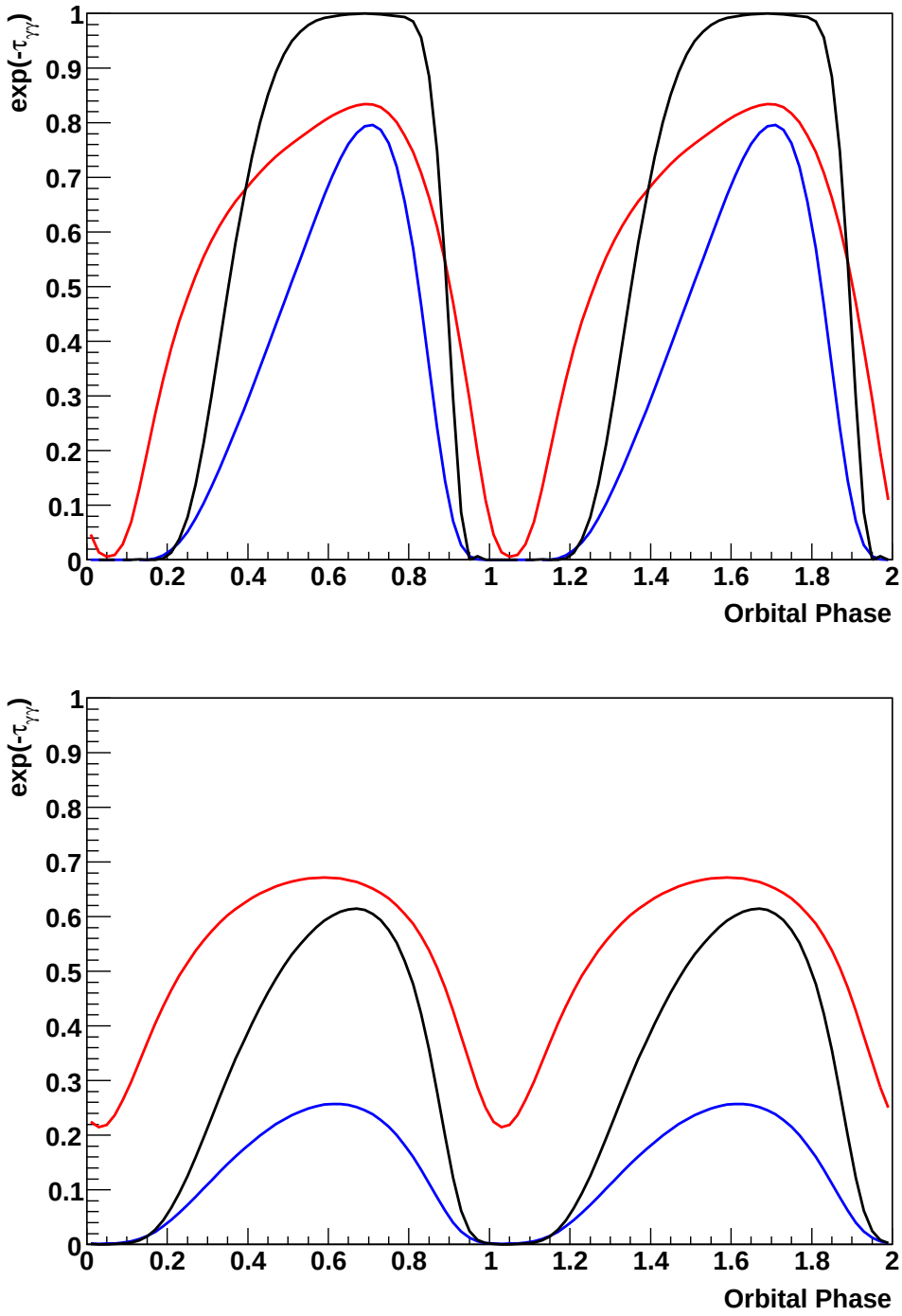

Figure 3.15: *Top panel:* Predicted levels of γ-ray transmission for the LS5039 system as a function of orbital phase assuming an inclination of $i = 60°$. The different curves correspond to photon energies of 100 GeV (*black*), 1 TeV (*blue*) and 10 TeV (*red*). *Bottom panel:* The same but assuming an inclination of $i = 20°$.

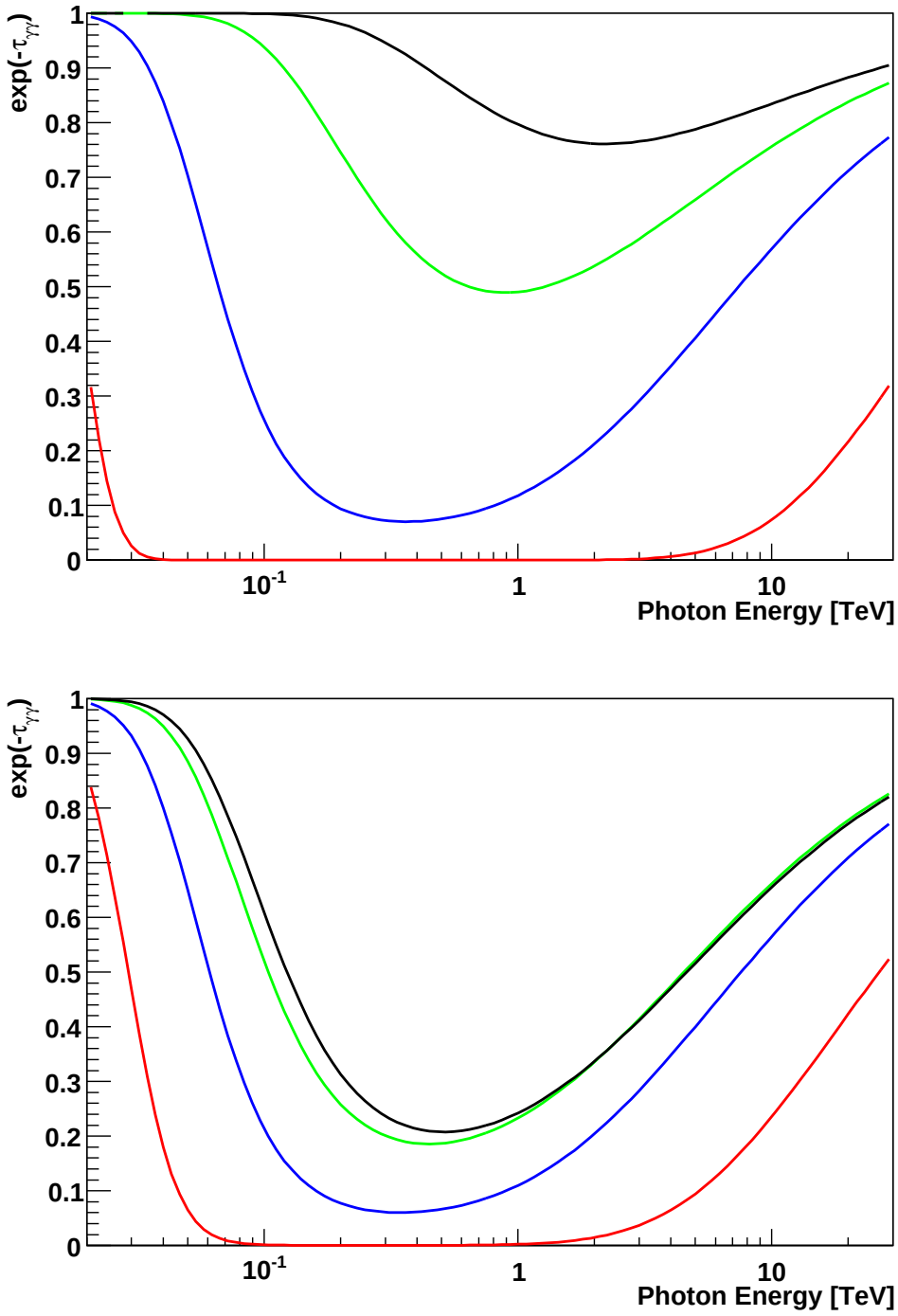

Figure 3.16: *Top panel:* Predicted γ-ray transmission levels for the LS5039 system as a function of photon energy assuming an inclination of $i = 60°$. The different curves correspond to orbital phases of $\phi = 0$ (*red*), $\phi = 0.3$ (*blue*), $\phi = 0.5$ (*green*) and $\phi = 0.7$ (*black*). *Bottom panel:* The same but assuming an inclination of $i = 20°$.

contains a black hole. While firm categorisation of the LS 5039 compact object as a black hole would effectively dismiss the pulsar wind scenarios for VHE γ-ray production in the system, the indications arising from the observed spectral variability are at best tentative and further detailed work would be required to properly address this issue.

Finally, the identical correspondence of Figures 3.15 and 3.16 with similar results presented by [85] illustrates the reliability of the model implementation used in this thesis, validating its further application in subsequent chapters.

3.12.2 γ-ray Emission

3.12.2.1 Synchrotron Self-Compton Emission

This section contains a brief assessment of the viability of VHE γ-ray emission in LS 5039 via the synchrotron self-Compton process. Using a few simple assumptions regarding the system's physical parameters the single zone, homogeneous SSC model developed in §2.7.1 is used to derive an expected VHE γ-ray spectrum. This model spectrum is then compared with the observational data to establish whether synchrotron self-Compton emission represents a plausible mechanism for γ-ray emission in LS 5039.

The spectrum of electron Lorentz factors in the source rest frame is assumed to take the form of a truncated power law $N(\gamma) = N_0\gamma^{-p}$ between $\gamma_{\rm min}$ and $\gamma_{\rm max}$. To estimate the maximum possible value of $\gamma_{\rm max}$, the approach of [75] is adopted, which assumes that the electron energy losses are dominated by synchrotron emission. In this scenario, the maximum electron Lorentz factor may be derived using the *radiation reaction limit* [116] which is obtained by equating the fractional synchrotron loss rate $\omega_{\rm syn} = |-\dot{\gamma}_{\rm syn}/\gamma|$ to the maximum particle acceleration rate $\omega_{\rm acc}$. For Fermi acceleration processes, $\omega_{\rm acc}$ cannot exceed the electron gyration frequency since the electron cannot gain more than a fraction of its energy for every gyration in either the first or second order Fermi processes. Using this approach, [75] derive an expression for the maximum possible value of γ:

$$\gamma_{\rm max} \approx \frac{1.2 \times 10^8}{\sqrt{B}} \tag{3.53}$$

Table 3.8: Assumed parameters for the SSC model.

Model Parameter	Value
d [kpc]	2.5
i [°]	20
$\Gamma_{\rm bulk}$	1.09
B [G]	0.26
$R_{\rm source}$ [cm]	1.0×10^{11}
W'_e [ergs]	2.0×10^{38}
p	2.55
$\gamma_{\rm min}$	100
$\gamma_{\rm max}$	4.0×10^{7}

where B is the magnetic field in Gauss. Accordingly, while $\gamma_{\rm max}$ remains a variable model parameter, its value is constrained to be below that given by (3.53). Again following [75], the normalisation N_0 of the electron spectrum is derived using:

$$W'_e \approx m_e c^2 \int_1^{\infty} \gamma N(\gamma) d\gamma \approx m_e c^2 \int_{\gamma_{\rm min}}^{\gamma_{\rm max}} \gamma N_0 \gamma^{-p} d\gamma \tag{3.54}$$

where m_e is the electron rest mass and W'_e is the total co-moving energy of electrons in the source. For continuous injection of monoenergetic particles with dominant synchrotron cooling and in the absence of particle escape, the expected electron spectral index is $p = 2$ [e.g. 146]. If additional cooling mechanisms are important or particle escape cannot be ignored, then the electron spectrum will soften. Consequently values of the electron index $p > 2$ are considered here.

Associating the orbital periodicity of the observed γ-ray flux with absorption due to pair production implies that the size of the γ-ray emission region ($R_{\rm source}$) is significantly smaller than the mean orbital separation ($\bar{r}_{\rm orb} = 2.5 \times 10^{12}$ cm) of the LS 5039 system [14]. A value of 10^{11} cm adopted by [75] seems appropriate. Although the magnetic field strength in and around the LS 5039 system is not well known, consideration of the electron Lorentz factors required to produce TeV photons, in combination with the assumption of particle acceleration close to the radiation reaction limit allowed [75] to derive a range of possible values $0.06 \lesssim B({\rm G}) \lesssim 0.6$ which is adopted here. The inclination angle i describes the direction of the bulk motion of the γ-ray emission region with respect to the line-of-sight. For simplicity, it is assumed that the emission region

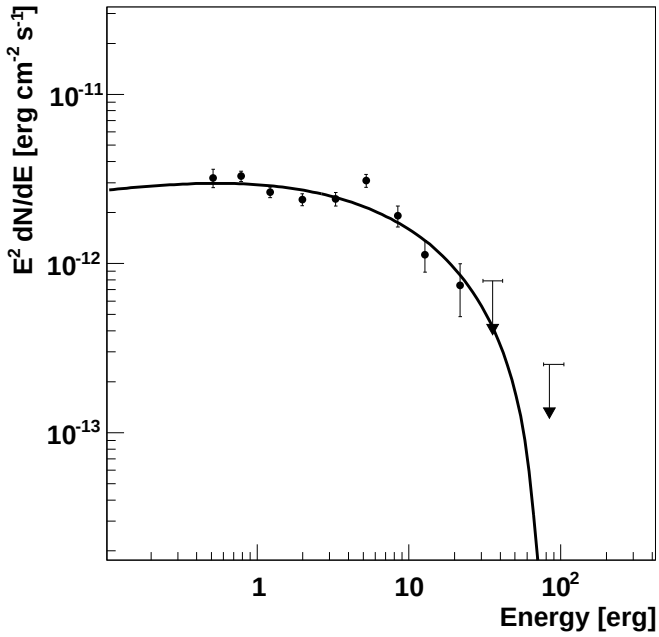

Figure 3.17: Illustration of the plausibility of the synchrotron self-Compton mechanism for the production of VHE γ-rays in LS5039. The spectral points correspond to the average over all orbital phases. The solid line illustrates the results of the SSC model calculation assuming the parameters listed in Table 3.8.

moves perpendicular to the orbital plane and therefore i is equivalent to the orbital inclination. Using the tentative indication from §3.12.1 that the observed differential flux variability favours low inclination angles, a value of $i = 20°$ is adopted here. Finally, the bulk lorentz factor of the γ-ray emitting region is assumed to be $\Gamma_{\rm bulk} = 1.09$ which corresponds to the $\sim 0.4c$ outflow velocity estimated from radio observations by [193].

Figure 3.17 compares the results of the SSC model calculation using the parameters listed in Table 3.8 to the phase averaged energy spectrum of LS 5039 and illustrates a reasonable correspondence between the simulated and observed spectral shapes. Although the simplicity of the applied model, combined with the limited temporal and spectral resolution prohibits detailed interpretation, it seems clear that the synchrotron self-Compton process is capable of producing the required photon fluxes at energies > 0.2 GeV, given a plausible range of system properties. Perhaps the most serious shortcoming of the pure SSC model is that it ignores the photon field

of the stellar companion. Indeed, as shown by [75], inverse-Compton scattering of stellar photons by an energetic electron population can produce significant γ-ray emission. Moreover, at orbital phases close to superior conjunction, spectral modification due to γ-ray absorption is likely to be important and this is not treated by the model. Lastly, the SSC model assumes a time-independent electron distribution and as such makes no predictions regarding possible temporal variations of the emitted γ-ray flux.

3.12.2.2 Neutral Pion Decay

This section briefly compares the predictions the neutral pion decay model for γ-ray emission developed in §2.7.2 with observed spectral and temporal characteristics of LS 5039. Figures 3.18 and 3.19 overlay the observed and simulated γ-ray spectra for several plausible values of the proton spectral index β and the fraction of accreted power recycled into the jet q_j. The system parameters are assumed to be as listed in Tables 3.1 and 3.8 and a stellar wind terminal velocity $v_\infty \approx 2440 \mathrm{kms}^{-1}$ is adopted [66]. In view of the substantial uncertainty surrounding the nature of the compact object in LS 5039, two separate scenarios are simulated independently. Figure 3.18 corresponds to a system inclination of 20° and is consistent with a ~ 4.5 $\mathrm{M}_\odot$ black hole, while in Figure 3.19 a ~ 1.4 $\mathrm{M}_\odot$ neutron star is assumed, implying an inclination of 60°.

In fact, the model predictions are remarkably similar for both compact object variants. The Doppler boost resulting from the smaller jet inclination in the black hole system is effectively counteracted by the lower z_0 and orbital separation associated with a the neutron star primary. The observed spectra apparently indicate a hard proton spectrum ($\beta \approx 2$) and a rather low jet production efficiency ($q_j \approx 10^{-3}$). In Figure 3.20 the differential flux variability at 1 TeV has been predicted using values of β and q_j which closely reproduce the observed spectral characteristics. Although the pion decay model predicts flux variations which are similar in amplitude to those observed by H.E.S.S. it conspicuously fails to reproduce the characteristic extrema close to inferior and superior conjunction. Instead, the model flux is maximised at periastron when the ambient stellar wind density is highest, and reaches a minimum at apastron.

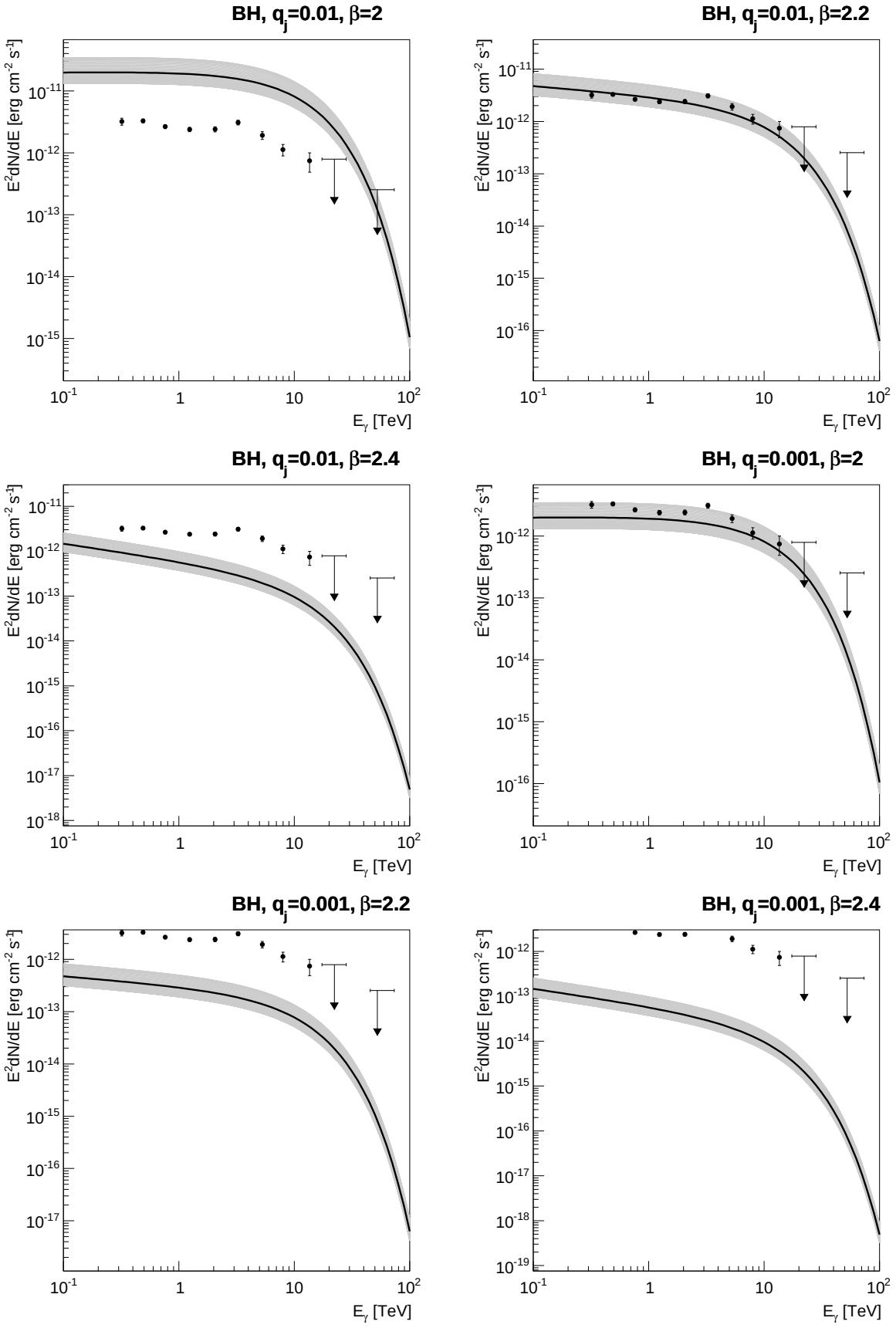

Figure 3.18: Spectral predictions of the neutral pion decay model assuming a $\sim$ 4.5 $M_\odot$ black hole primary. Simulated spectra are plotted for plausible values of β and q_j. The black curves illustrate the phase-averaged model predictions while the grey curves illustrate the range of spectral variation throughout the binary orbit. The overlaid spectral data-points correspond to the overall phase-averaged H.E.S.S. γ-ray spectrum.

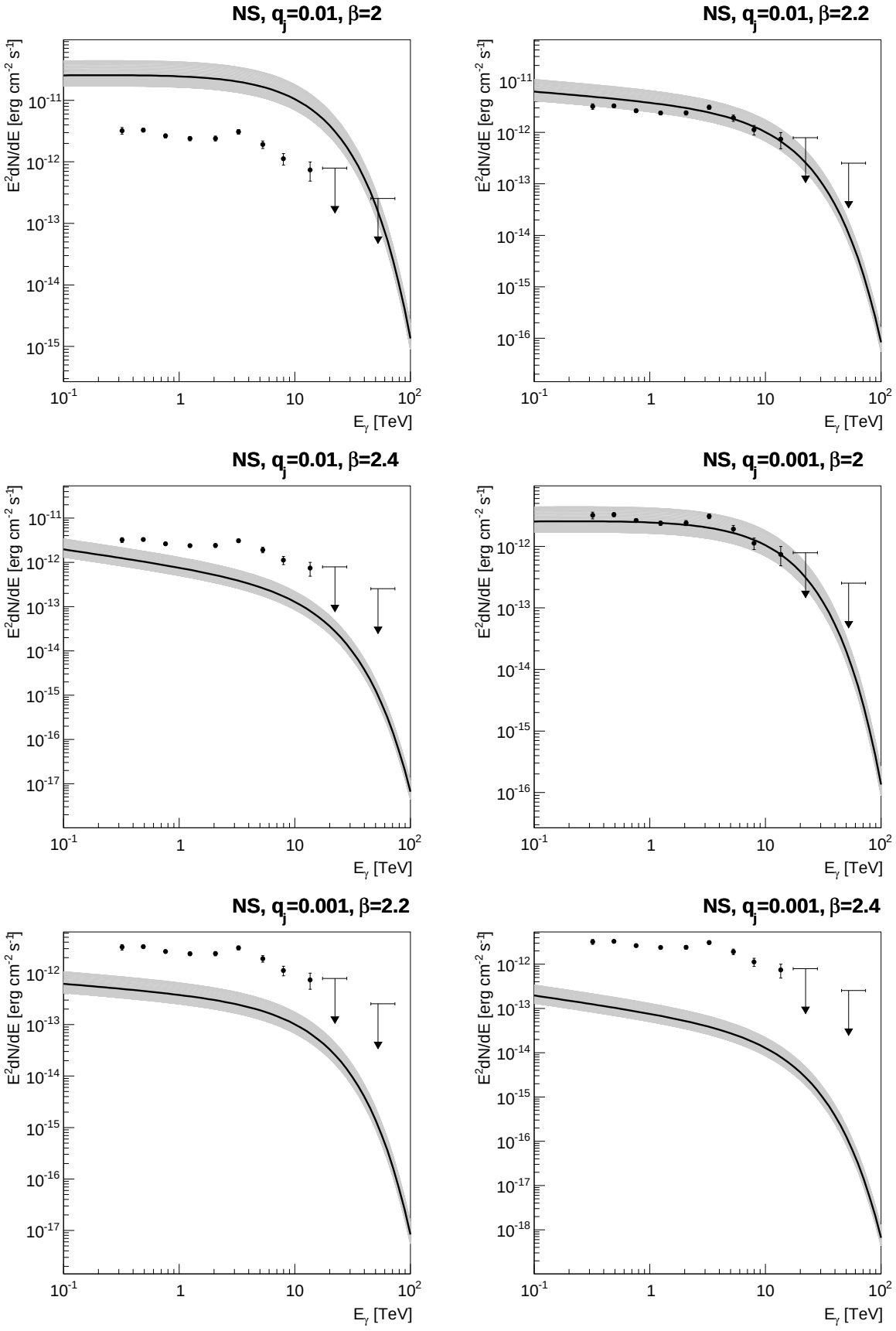

Figure 3.19: Spectral predictions of the neutral pion decay model assuming a ~ 1.4 $M_\odot$ neutron star primary. Simulated spectra are plotted for plausible values of β and q_j. The black curves illustrate the phase-averaged model predictions while the grey curves illustrate the range of spectral variation throughout the binary orbit. The overlaid spectral data-points correspond to the overall phase-averaged H.E.S.S. γ-ray spectrum.

The true nature of VHE γ-ray emission from LS 5039 is likely to be complex, with the possibility of several spatially disconnected regions of emission, perhaps involving different processes for particle acceleration and radiative emission. The literature contains numerous theoretical models which attempt to address these issues which often involve startlingly disparate, yet equally effective approaches [e.g. 148, 44, 47, 75]. Therefore, it seems likely that the improved sensitivity of next-generation γ-ray telescopes, combined with the overlapping low energy coverage provided by the *Fermi* satellite will be required to disentangle the various absorption and emission processes which occur in LS 5039.

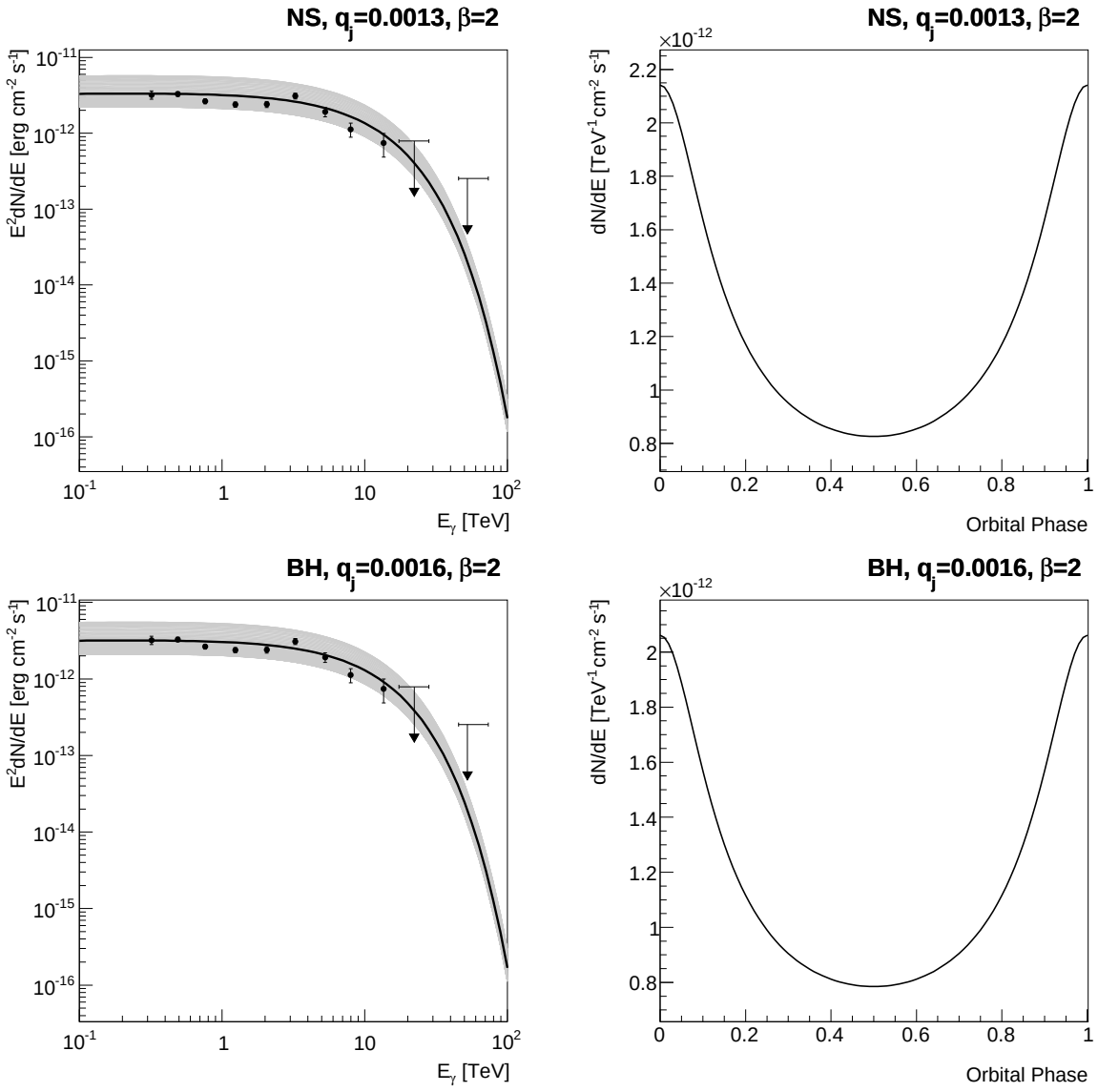

Figure 3.20: Differential flux variability predictions of the neutral pion decay model assuming a ~ 1.4 $M_\odot$ neutron star primary (*top panel*) and a ~ 4.5 $M_\odot$ black hole primary (*bottom panel*). As illustrated by the *left-hand* plots, values of β and qj which closely reproduce the phase-averaged spectral characteristics have been chosen. Corresponding predictions of the differential flux variability at 1 TeV are shown in the *right-hand* plots.

Chapter 4

Microquasars: A multi-wavelength case study

This chapter presents the results of contemporaneous VHE γ-ray and X-ray observations of the galactic *microquasars* GRS 1915+105, Circinus X-1 and V4641 Sgr using H.E.S.S. and the *Rossi X-ray Timing Explorer* (RXTE). The data presented in this chapter were obtained by Dr Paula Chadwick, who was the principle investigator for the internal H.E.S.S. observation proposal as well as the RXTE proposals 90108[1] and 90124[2]. These data also formed the basis of a conference proceeding which I authored and which was presented by Dr Sam Nolan at the 29th International Cosmic Ray Conference [57].

The proven value of multiwavelength data as a diagnostic of possible radiative mechanisms in variable sources is evident from previous VHE γ-ray observations of variable AGN. A notable example is the observation of VHE γ-ray flaring in Mkn 501 using the HEGRA IACT in conjunction with contemporaneous X-ray coverage provided by the RXTE satellite [10, 21]. More recently the H.E.S.S. collaboration obtained simultaneous radio, optical, X-ray and VHE γ-ray observations of the BL Lac object PKS 2155-304 [13]. The existence or otherwise of temporal inter-band correlations in flux, spectral index, or both can often eliminate potential models, narrowing avenues

[1] http://heasarc.gsfc.nasa.gov/FTP/xte/abstracts/abstracts/90108.txt
[2] http://heasarc.gsfc.nasa.gov/FTP/xte/abstracts/abstracts/90124.txt

of investigation and placing constraints on the physical environment in the emission region.

4.1 The RXTE Satellite

The *Rossi X-ray Timing Explorer* is a satellite based X-ray observatory which was launched on December 30th, 1995. As the name suggests, its primary mission is to provide astrophysical X-ray data with high timing resolution. It occupies a circular low-earth orbit with an orbital period of ~ 90 minutes and carries three separate X-ray telescopes.

The *Proportional Counter Array* (PCA) comprises five co-pointing xenon and propane *Proportional Counter Units* (PCUs) which are nominally sensitive in the energy range $\sim 2 - 60$ keV with an energy resolution of $< 18\%$ at 6 keV [252]. The flux sensitivity of the PCA for a source with a Crab-like spectrum spans a dynamic range of ~ 4.5 orders of magnitude, extending from a confusion limited lower limit of $\sim 4 \times 10^{-12}$ ergs cm^{-2} s^{-1} up to a dead-time limited maximum of $\sim 2 \times 10^{-7}$ ergs cm^{-2} s^{-1} [136]. For studies of rapidly varying sources like X-ray binaries, the PCA timing resolution of ~ 1 μs can prove invaluable. However, rapid timing measurements also require a bright source to provide sufficient counting statistics within such short time bins. The PCA is not an imaging detector and therefore attains a rather modest angular resolution of $\sim 1^\circ$ FWHM by mechanical collimation of the incident X-rays [136].

The *High Energy X-ray-Timing Experiment* (HEXTE) comprises two independent clusters of four *phoswitch* scintillation detectors which are sensitive to photons in the $\sim 12 - 250$ keV energy range and have an energy resolution of ~ 9 keV at 60 keV. During observations, only one cluster observes the target, while the other provides a simultaneous background estimate from an off-source region. At 100 keV, the HEXTE yields a 3σ detection within 10^5 seconds for a source with a photon flux of 10^6 ph. cm^{-2} s^{-1} keV^{-1}. Like the PCA, the HEXTE relies on mechanical collimation to achieve its nominal angular resolution of $\sim 1^\circ$ (FWHM) and has a timing resolution of ~ 8 μs.

The *All-Sky Monitor* (ASM) is a wide field-of-view instrument which monitors $\sim 80\%$ of the sky

over the course of each ~ 90 minute orbit. It consists of three identical *Scanning Shadow Cameras* which use the X-ray shadows cast by a set of irregular masks across the telescope aperture to reconstruct the positions of X-ray sources. The ASM is designed to provide pseudo-continuous monitoring of bright X-ray sources, and can be used to alert observers to the appearance of transients or to other time-variable phenomena which can then be observed with the pointed instruments. Nominally, the ASM is sensitive in the energy range from 2-10 keV and has a rectangular field of view spanning $110 \times 12^{\circ}$.

Detailed information regarding the instruments carried by RXTE can be found in the *RXTE Technical Appendix* which is available from the *RXTE Guest Observers Facility* web site[3].

4.2 Microquasars

Microquasars are X-ray binaries which exhibit significant radio emission, usually associated with a collimated outflow or jet. The prototypical microquasar, SS433, was detected in 1979 [179] but it was the discovery of GRS 1915+105, later identified as a superluminal source [180], which completed the analogy with quasars and justified the nomenclature.

Structurally, microquasars closely resemble their super-massive cousins the radio-loud active galactic nuclei (AGN). Both classes of object are believed to contain a compact central engine, a source of material for accretion onto the central engine, and collimated outflows of matter known as jets. In the current paradigm, gravitational potential energy is liberated from matter as it falls onto the central object.

Partial dissipation of the converted energy occurs in a disc of material surrounding the compact primary, producing both thermal and non-thermal X-ray emission. Microquasars also exhibit non-thermal radio emission, indicative of synchrotron radiation, in a collimated outflow which carries away a sizeable fraction of the accretion luminosity [97]. In AGN, the jet structures are known to be regions of strong particle acceleration, and often display highly relativistic bulk motions. The resulting radiation spectrum can extend from radio wavelengths into the very high energy (VHE)

[3]http://heasarc.gsfc.nasa.gov/docs/xte/appendix_f.html

γ-ray regime [13].

Microquasars represent unique laboratories with which to study the behaviour of matter in strong gravitational fields. When compared with AGN (in which significant behavioural changes can take many years to manifest), the vastly smaller size scales of microquasars lead to evolutionary variation which occurs over humanly accessible timescales of a few years or less. It remains to be confirmed, however, whether microquasars really do behave like scaled down AGN. It may be that the scaling factor of $\sim 10^9$ between the engine masses in microquasars and AGN leads to significantly different physical processes in the two object classes.

VHE γ-ray emission has been observed from many AGN in the Blazar sub-class [e.g. 197, 10, 8, 13], where the jet axis is aligned close to the observer line-of-sight, and also from the superluminal radio galaxies M87 [4] and Centaurus A [5]. The argument for phenomenological parity between AGN and microquasars would be improved if, in addition to structural resemblance, spectral similarities were shown to exist in the TeV band for both object classes.

The definition of a microquasar encompasses a somewhat broad class of objects, with many possible permutations of primary mass and type; donor spectral type; accretion mode and rate [205]. Microquasar behaviour is exhibited by both high and low mass X-ray binaries, and where either a black hole or a neutron star constitutes the compact primary. The mode of accretion, whether wind fed or via Roche lobe overflow, also appears to be a poor predictor for the presence of outflows, although their nature and persistence may be affected. To date, only one *confirmed* microquasar has been observed to emit in the VHE γ-ray band. This is the galactic black hole Cygnus X-1 which was marginally detected by the MAGIC telescope in coincidence with a 2-50 keV X-ray flare observed by the *Swift* BAT and *RXTE* ASM [26].

4.3 γ-Ray Production and Absorption

Mechanisms for γ-ray production in microquasars have been widely investigated [see e.g. 29, 208, 46, 86]. This has resulted in two broad classes of models, describing the expected fluxes and spectra

of microquasars in the GeV-TeV band. *Hadronic* models are those in which the dominant emission processes involve hadrons, whereas *leptonic* models rely on leptons as the radiating particles. In both cases, a highly energetic population of the relevant particles is required, and consequently proposed emission scenarios generally localise the radiating region to within the jet structures of the microquasar.

Leptonic models rely upon synchrotron radiation and inverse-Compton (IC) scattering to produce photons in VHE regime. In this respect they closely resemble models of extragalactic jets [103, 151] but with additional emphasis on the role of external photon fields. Indeed, while the synchrotron self-Compton mechanism provides a good first order fit to the non-thermal spectra of many blazars [102], the emission regions of microquasars are likely embedded in the photon fields of the donor star and accretion disc, requiring a detailed treatment of external Comptonisation (EC) processes.

While direct production of GeV γ-rays via proton synchrotron emission in jet structures is perhaps possible [19, 185], the high magnetic fields (~ 100 G), extreme proton energies ($\sim 10^{19}$ eV), and almost maximal particle acceleration efficiency required make this process rather implausible in the context of galactic binaries. Consequently, models of VHE γ-ray production by hadronic particles generally invoke electromagnetic cascades initiated by both neutral and charged pion decays [208]. In this scenario, neutral pions created via interactions of energetic protons with ambient nucleons ($pN \rightarrow \pi^0 + X$) produce direct TeV γ-rays as they decay ($\pi^0 \rightarrow \gamma\gamma$) [23, 207].

Many blazar models rely upon relativistic beaming and Doppler boosting to achieve the observed γ-ray fluxes, requiring highly relativistic outflows moving at small angles ($\theta < 10^\circ$) to the observers line of sight. In contrast, the *steady* jets of microquasars are often only mildly relativistic ($\beta \sim 0.2 - 0.6$) with few having $\theta \lesssim 20^\circ$. On the other hand, the required degree of relativistic beaming in microquasars is mitigated somewhat by their proximity in comparison to AGN. Indeed, using the Eddington luminosity (L_{Edd}) as an indicator of the *potential* power output of each source class, the ratio L_{Edd}/d^2 (where d is the source distance) is typically 2-4 orders of magnitude larger for microquasars than for AGN [29]. Nonetheless, it may be that even microquasars with jets

aligned close to the line of sight may only become visible in the TeV band during powerful flaring events. These transient outbursts, characterised by the ejection of discrete superluminal *plasmons*, sometimes occur at the transition between low and high luminosity X-ray states [97]. Indeed, the tantalising detection of a marginally significant TeV signal from Cyg X-1 during a high flaring state would seem to support this hypothesis [26].

VHE γ-rays can be absorbed via electron-positron pair production , $\gamma\gamma \rightarrow e^+e^-$ (see §2.5). In the case of 1 TeV γ-rays, the cross section for this process is maximised for ultraviolet target photons ($E_{ph} \sim 3.5$ eV) where its value reaches $\sigma_{\gamma\gamma} \approx \sigma_T/5$ [e.g. 111]. In high mass systems, the companion star is expected to produce a dense field of target photons to interact with the γ-ray flux [e.g. 85]. This process can be very significant and probably contributes to the observed orbital modulation in the VHE γ-ray flux from LS 5039 [14]. In contrast, the ultraviolet spectrum of low mass microquasars is likely dominated by the reprocessing of X-ray emission in the cool outer accretion flow [244, 104], although reprocessing on the companion star surface and jet emission might also be significant [217]. Regardless of origin, the observed optical and ultraviolet luminosities of LMXBs are generally orders of magnitude lower than those of high-mass systems [217], with the likelihood of strong γ-ray absorption correspondingly reduced.

4.4 The Targets

This section reviews the observational characteristics of the target microquasars, GRS 1915+105, Circinus X-1, and V4641 Sgr. Focus is given to previous results which may constrain the likelihood of VHE γ-ray emission at the time of observation. To facilitate the comparison with AGN, the likely orientation of the jet axes to the line-of-sight are examined. The majority of AGN detected by IACTs have jets moving close to the line-of-sight, which enhances the observed GeV/TeV flux by Doppler boosting the intrinsically softer photons into the VHE γ-ray band. Previously identified correlations between each target's observed X-ray behaviour and the likelihood of relativistic or ultra-relativistic outflows are also discussed. As outlined in §4.3, the existence of powerful jets or

discrete ejecta is a prerequisite of most models for VHE γ-ray emission from microquasars. Finally, the nature of the companion star in each system is investigated. As discussed in §2.5, γ-γ pair production on the radiation field of a high-mass stellar companion in any of the target systems could have a profound effect on the observed VHE γ-ray flux.

4.4.1 GRS 1915+105

GRS 1915+105 is a well studied galactic black hole candidate (BHC) first identified by the WATCH all-sky monitor on board the *GRANAT* satellite [55]. A markedly unusual system, GRS 1915+105 gained a measure of celebrity as the prototype galactic superluminal source [180] and is the only BHC observed to radiate at super-Eddington X-ray luminosities for significant fractions of its duty cycle [83].

The distance to GRS 1915+105 is a subject open to some debate, with numerous estimates spanning $\sim 6-12.5$ kpc [79, 78, 143, 98]. Notwithstanding this rather large uncertainty, the source is undoubtedly subject to heavy optical extinction ($A_V \sim 19 - 26.5$ mag) and may be obscured behind the core of a molecular cloud [60, 59]. Nevertheless, VLT observations in the optical and near infra-red succeeded in identifying the stellar companion as a low-mass KM III giant [115]. Periodicity analysis of optically determined radial velocity measurements reveals a strong signal corresponding to $P = 35.5 \pm 1.5$ days, most likely indicating the orbital period of the system [114]. In combination with an inclination of $i = 70^\circ \pm 0.2^\circ$ derived from observations of the system's jet structures [180, 98] and a presumed donor mass $M_D = 0.81 \pm 0.53$ $M_\odot$, this period implies a compact primary mass $M_{BH} = 14.0 \pm 4.4$ $M_\odot$ which is clearly indicative of a black hole [117].

Accretion by Roche lobe overflow in such a wide binary system implies the formation of a gigantic accretion disc, not only capable of sustaining super-Eddington accretion rates for extended periods of time ($\gtrsim 10$ years) [245], but perhaps also responsible for the spectacular X-ray variability of GRS 1915+105 . Indeed, the unique *limit cycle* behaviour evident in GRS 1915+105 most likely arises through successive state changes in the inner accretion disc, and occurs exclusively when the source radiates at super-Eddington luminosities [83]. In a detailed study of the X-ray lightcurves

of GRS 1915+105, [32] succeeded in identifying twelve distinct variability *classes*, internally characterised by the duration and juxtaposition of three separate *states*. Remarkably, there is a clear correlation between the prevalence of each state and the observed radio loudness of the source [94, 239]. More specifically, it appears that protracted, contiguous occurrences of the spectrally hard, low-luminosity state C (designated as class χ) often manifest steady, spectrally flat radio emission, indicative of the self-absorbed synchrotron emission often associated with continuous relativistic jets [150].

Episodes of class χ behaviour lasting several days are known as *plateaux* and are invariably terminated by flaring activity in the radio, infra-red, and X-ray bands [94]. In contrast with the evidence for self-absorption seen in state C, radio spectra obtained during these end-plateau flaring episodes indicate optically thin synchrotron emission which may also contribute significantly to the observed infra-red flux [99, 87]. Occasionally, these flaring episodes are linked to powerful discrete plasma ejections with instantaneous power output reaching $\gtrsim 10^{40}$ erg s^{-1} [180, 108, 79]. Modelling the emission from these discrete relativistic ejecta, [29] showed that inverse-Comptonisation of emitted synchrotron photons into the GeV/TeV regime could produce significant and persistent γ-ray fluxes which remain detectable for several days.

Radio imaging of GRS 1915+105 during the plateau state reveals clear elongation of the compact nucleus, indicative of conical, expanding AU-scale jets [79]. Relativistic ejecta resulting from end-plateau flares are resolved at core separations exceeding $\sim 500 - 1000$ AU and are observed to move ballistically thereafter [79]. In fact, it is somewhat unclear whether the observed emission originates in genuinely discrete *plasmons*, or is in fact produced by shocks propagating through a continuous jet medium. On extended scales, [143] propose the association of two infra-red sources (IRAS 19124+1106 and 19132+1035) with bow-shocks driven into the interstellar medium at the jet termination point of GRS 1915+105. The detection of a non-thermal radio feature, associated with 19132+1035 and elongated in the direction of GRS 1915+105, may indicate the ongoing injection of relativistic particles into the shock region. Assuming a genuine relationship between the IRAS sources and the GRS 1915+105 jet impact sites, the absence of a symmetric non-thermal

feature associated with IRAS 19124+1106 implies that the injection is a transient process, perhaps linked to the arrival of discrete plasma clouds.

4.4.2 Circinus X-1

First identified by [168], Circinus X-1 (hereafter Cir X-1) is a highly ambiguous binary system. Indeed, despite extensive observations with numerous satellites and ground-based telescopes, spanning over thirty years, many of the system's fundamental physical characteristics remain unconfirmed. A ~ 16.6 day period in the X-ray lightcurve was first reported by [145] and has since been confirmed in multiple ephemerides based on regular dips [64] and flares [195] in the X-ray band. Replication of the observed X-ray periodicity in the radio [188], infra-red [107] and optical [183] bands suggests an association of the 16.6 day cycle with the orbital period of the system.

Despite an initial identification as a black hole candidate due to rapid X-ray variability reminiscent of Cygnus X-1 [238], the observation of type I X-ray bursts during a low flux state implies that the compact primary in Cir X-1 is almost certainly a low magnetic field ($B \lesssim 10^{11}$G) neutron star [237, 236]. This scenario was reinforced by the detection of twin kHz QPOs in the power density spectrum of Cir X-1, despite their frequencies being rather low compared to other neutron star binaries [48]. Further sub-classification as a Z or atoll source is not possible since Cir X-1 exhibits a confusing array of spectral and timing properties, subsets of which are characteristic of both source types [see e.g. 227, 191].

Definitive classification of the donor star in Cir X-1 is rather more problematic. An initial identification of an early-type companion [248] was superseded when the proposed optical counterpart was resolved into three separate stars, with the true counterpart to Cir X-1 being the southernmost of these [27, 183]. Optical measurements are complicated by a high, yet rather uncertain degree of interstellar extinction ($5 \lesssim A_V \lesssim 12$) [183, 139] and furthermore, spectral analysis is likely to be dominated by emission from the accretion disc, giving few clues as to the nature of the donor [139, 138]. The low apparent magnitude of the optical counterpart implies a de-reddened luminosity consistent with a low-mass or sub-giant companion and indeed, the current consensus appears

to be that Cir X-1 is a low-mass X-ray binary [e.g. 138]. Nonetheless, recent near infra-red [62] and I-band optical [142] observations reveal emission features consistent with a mid-B supergiant. While these measurements may well be subject to contamination by emission from the accretion flow [62], the observations obtained by [142] correspond to epochs of low X-ray luminosity, when the contribution of the accretion disc is presumably significantly reduced. Notwithstanding the spectral evidence, a B-type star would need to have been significantly altered through interaction with the compact primary in order to reproduce the low apparent magnitude, even with very high extinction $A_V \sim 12$ [142].

In common with the donor classification, estimates of the distance to Cir X-1 have been subject to repeated revision. Early, HI absorption measurements [110] implied a distance in the range 8-10 kpc, similar to distance estimates derived from X-ray burst observations [141] . However, more recent X-ray measurements suggest values as low as 4.1 kpc [134], while comparison of the systemic radial velocity with local standards of rest in the direction of Cir X-1 yields an upper limit of ~ 11.8 kpc [142].

Observations of Cir X-1 in the X-ray band reveal a long term secular evolution of the average source brightness. Fluxes rose monotonically from near-undetectable in the early 1970s to a peak value of $\sim 1.5 - 2$ Crab (1.5-10 keV) at the turn of the millennium, before returning over a period of ~ 4 years to their pre-rise levels [195]. Various X-ray spectra, obtained during epochs of both high and low flux, display evidence of complex and variable absorption and emission processes.

Measurements with the *Rossi X-ray Timing Explorer* (*RXTE*) indicate that the observed continuum emission comprises two separate elements: a bright but heavily absorbed component and a much fainter component which becomes apparent during periodic X-ray dips and appears only weakly attenuated [229]. One explanation is that the bright component corresponds to emission from an obscured central source, while the faint component results from Thomson scattering of the intrinsic X-ray spectrum in a mildly ionised medium surrounding the source. The repeated detection, by various instruments, of a prominent Fe Kα line at ~ 6.5 keV with a flux that appears largely unaffected by dipping activity is also indicative of an extended scattering region which

reprocesses X-rays from the central source back into the line of sight [e.g. 229, 228, 131, 49].

The unmodified continuum itself is often adequately modelled as a blackbody or multicolour blackbody, as thermal Comptonisation or as a superposition of two of these components [e.g. 229, 227, 131]. In some cases, the appearance of a hard X-ray tail at higher energies ($E \gtrsim 10$ keV) requires the addition of a power law component to obtain an acceptable fit [131, 80]. This hard tail appears indicative of a non-thermal electron population and may constitute the signature of a relativistic outflow or jet in the system.

Recent low-flux spectra obtained using the *Chandra* satellite reveal numerous emission and absorption complexes, the strength and width of which appear to indicate the presence of at least two, if not more, emission regions with distinct temperatures, velocities and ionisation fractions [72, 223]. Earlier *Chandra* observations, when the average source flux was higher, showed broad ($\pm 2000 \mathrm{kms}^{-1}$) emission lines with distinctive P-Cygni profiles, characteristic of an absorption in an out-flowing wind [50, 222]. Moreover, spectral evidence for the survival of various heavy ions in the wind, in combination with the high X-ray luminosity of Cir X-1, imply ambient densities, temperatures and ionisation fractions consistent with the outer edge of the accretion disc. Consequently, the fact that we observe these spectral signatures imprinted on the bright continuum is consistent with wind originating from a disc which is being viewed relatively edge-on [50]. This is in agreement with [49] who propose a similar scenario based upon observations of spectral variability.

The jets of Cir X-1 have been identified at both radio and X-ray frequencies on angular scales ranging from arcseconds to arcminutes [232, 95, 240] extending from the source along a northeast to southwest alignment. Observations made with the ATCA radio telescope reveal significant southward curvature of the jets at distances beyond $\sim 30''$ from the source. Initially, this curvature was seen as evidence that Cir X-1 was a runaway binary associated with the nearby supernova remnant G 321.9-0.3 [232]. However, subsequent observations with the Hubble Space Telescope failed to detect any proper motion associated with the optical counterpart [178], invalidating this interpretation. At radio wavelengths, Cir X-1 also displays notable structure on arcsecond scales, appearing as a bright core with significant extension along the axial direction of the arcminute

jets [95]. In fact, the observed extension is rather asymmetric with a ratio of at least 2 between the observed fluxes of the two opposing jets. Interpreted as pure relativistic aberration, this asymmetry implies a jet velocity $\gtrsim 0.1c$, although any significant physical disparity between the jets would modify this result. Cir X-1 has also been observed to eject condensations of matter with apparently 'superluminal' velocities $\gtrsim 15c$ [96]. These observations imply a physical velocity for the ejecta $v > 0.998c$ with a maximum angle between the velocity vector and the line of sight $\theta < 5°$. If correct, these results identify Cir X-1 as a *microblazar* - a galactic, small-scale analogue of the blazar class of AGNs, several of which are known sources of VHE γ-rays. Assuming jet emission perpendicular to the accretion disc, this result seems to be in contention with the previously discussed body of evidence suggesting a system with a much larger inclination. An X-ray counterpart to the north-eastern radio jet has been identified which appears extended on arcminute scales and may indicate an interaction between the jet and the surrounding ISM [120]. Recently, [132] identified double-peaked emission features of several highly ionised elements in the energy spectrum of Cir X-1 near periastron, explaining these components as blue and red-shifted emission from a bipolar X-ray jet with velocity $0.08c$ moving at 92° to the line of sight. Reconciling this with the ultra-relativistic ejections observed by [96], they propose an inclination for Cir X-1 in the range $45° \leq i \leq 63°$ with precessing jet axes inclined at $\sim 45°$ to the accretion disc.

Wide field images of Cir X-1 show the source embedded in a synchrotron nebula [232, 240]. Before the association with G 321.9-0.3 was dismissed, this nebula was interpretted as a radio lobe formed by interaction of a low inclination jet with the ISM, reinforcing the argument for a blazar-like morphology. However, the dissociation of Cir X-1 and G 321.9-0.3 admits the possibility that the synchrotron nebula is the remnant of the event that created the neutron star in Cir X-1 and consequently the jet inclination of Cir X-1 remains rather uncertain.

4.4.3 V4641 Sgr

V4641 Sgr is the optical designation of the habitually weak X-ray source SAX J1819.3-2525 (= XTE J1819-254), independently identified using the *BeppoSAX* [135] and *RXTE* [170] satellites.

In marked contrast to both GRS 1915+105 and Cir X-1, the interstellar extinction in the direction of V4641 Sgr is rather low ($A_V \approx 1$) [192, 157] and consequently, the system parameters are somewhat better constrained. Indeed, by re-analysing archival photometric data [109], [192] derived an orbital period $P = 2.81730$ days, accurate to within ≈ 0.9 s. Optical spectroscopic measurements [192, 157] strongly suggest a late B-type/early A-type companion with an effective temperature $T_{\rm eff} \approx 10500$ K and mass $5.49 \leq M_2 \leq 8.14 M_{\odot}$, while a derived compact primary mass $8.73 \leq M_1 \leq 11.7 M_{\odot}$ [192] categorises V4641 Sgr as a firm black hole candidate. The absence of eclipses in the X-ray lightcurve, under the likely assumption of a compact X-ray emission region, constrains the orbital inclination $i_{\rm orb} \lesssim 70^{\circ}$. Conversely, a lower limit $i_{\rm orb} \gtrsim 60^{\circ}$ is implied by the large (~ 0.5 mag) amplitude of the ellipsoidal optical light curve [192]. Finally, using known relations between the radius, temperature and mass of the companion star, and assuming an extinction $E(B-V) = 0.32 \pm 0.1$, [192] used the apparent V-band luminosity of V4641 Sgr to derive a system distance of $7.4 \leq d \leq 12.31$ kpc.

V4641 Sgr is probably best known for its exhibition of rapid and violent outbursts. Perhaps the most spectacular of these events was the super-Eddington flare detected by the *RXTE All-Sky Monitor* in September 1999. The observed X-ray fluxes (2-12 keV) increased sharply, reaching ≈ 12.2 Crab within 8 hours before fading again to below 0.1 Crab in under two hours [202]. Powerful contemporaneous flares were also observed at hard X-ray [175], optical [233], and radio [127] wavelengths. In fact, *Very Large Array* (*VLA*) radio observations obtained within a day of the X-ray flare resolved a bright jet-like radio structure ≈ 0.25 arcsec in length [127]. Obtaining an estimate for the proper motion of the radio-emitting material observed by the *VLA* is complicated by considerable uncertainty regarding the time of its ejection. Nonetheless, assuming the most likely hypothesis i.e. that the ejection is coincident with some phase of the X-ray flare, proper motions in the range $0.22 \lesssim \mu_{\rm jet} \lesssim 1.1$ arcsec day^{-1} are derived. At the minimum distance $d = 7.4$ kpc, the implied lower limit to the apparent velocity of the ejecta is $9.47c \lesssim v_{\rm min} \lesssim 47.7c$, comparable with the extragalactic jets seen in blazars. Indeed, the remarkably high apparent velocities imply that V4641 Sgr may be a *microblazar* with a relativistic jet moving close to the

Table 4.1: Targets and contemporaneous observational epochs

Target	*RXTE* Observations (MJD)	H.E.S.S. Observations (MJD)
GRS 1915+105	53123.091 → 53123.109	53123.067 → 53123.150
	53124.074 → 53124.094	53124.079 → 53124.162
	53125.130 → 53125.149	53125.083 → 53125.148
	53126.114 → 53126.129	53126.109 → 53126.132
	53127.097 → 53127.114	53127.106 → 53127.165
	53128.150 → 53128.165	53128.149 → 53128.165
Cir X-1	53174.749 → 53174.761	53174.748 → 53174.832
	53175.768 → 53175.780	53175.735 → 53175.822
	53176.781 → 53176.793	53176.772 → 53176.858
V4641 Sgr	53193.904 → 53193.924	Not Observed
	53194.887 → 53194.908	53194.883 → 53194.926
	53195.871 → 53195.892	53195.890 → 53195.931

line of sight ($\theta_{\rm jet} \lesssim 12^{\circ}$). Subsequent, weaker broadband outbursts were observed in July 2000 [126], May 2002 [212, 169, 52], August 2003 [215, 213, 51, 30], and July 2004 [234, 216, 203, 149], suggesting recurrent activity on a timescale $\sim 1-2$ years.

During the 1999 flare, the X-ray spectrum of V4641 Sgr was observed to evolve rapidly, with markedly different spectral shapes corresponding to different stages of the outburst [202]. Preceding the outburst, the quiescent spectrum is rather soft, and roughly consistent with a thermal bremsstrahlung or a multicolour blackbody disc. The onset of quasi-periodic optical activity [147] approximately coincided with a significant hardening of the 3-20 keV photon index ($\alpha \sim 1$), in conjunction with the appearance of an emission line at ~ 7 keV. The 3-200 keV spectrum at the peak of the X-ray flare closely resembled that of a BHC in the low-hard state [202]. Earlier, at lower luminosities, a significantly harder spectrum, accompanied by stronger emission line, was suggestive of strong intrinsic absorption of the emitted X-rays. *RXTE* spectroscopy during the 2003 outburst also implied the presence of an optically thick cloud enshrouding V4641 Sgr [165], perhaps arising from substantial matter outflow around the time of flaring.

4.5 Analysis and Results

Contemporaneous X-ray (*RXTE*) and VHE γ-ray (H.E.S.S.) observations were performed at the epochs listed in Table 4.1. The observations were initiated at epochs which, on the basis of previous observational evidence, were thought likely to correspond to powerful outburst events. The precise trigger criteria for each target are discussed in subsequent sections. X-ray data reduction with the `FTOOLS 5.3.1` software suite employed the recommended data selection criteria regarding elevation, offset, electron contamination and proximity to the South Atlantic Anomaly. For each observation, the Proportional Counter Array (PCA) STANDARD2 data were extracted from all available Proportional Counting Units (PCUs) except PCU 1, which was ignored because a lost propane layer in the detector degrades the spectral resolution. HEXTE Archive mode data for both clusters were extracted for all observations following the recommended procedures for time filtering and background estimation. Spectral analysis was carried out using the `XSPEC 11.3.2` package [28]. Spectral fits for GRS 1915+105 use both PCA and HEXTE data, including an energy range of 3-200 keV. The remaining sources, Cir X-1 and V4641 Sgr, were not significantly detected by HEXTE and therefore only PCA data in the 3-20 keV range were considered to ensure good data quality. In the case of GRS 1915+105, power density spectra (PDS) were derived using the ftool `powspec`. A combination of 16μs resolution generic event data and binned mode data with a resolution of 8ms were used, with respective PCA channel ranges of 36-249 and 0-35 spanning an energy range $\sim 2 - 100$keV. For each *RXTE* pointing, individual PDS were extracted from 8s intervals comprising 1024 bins. The resulting spectra were then averaged to produce a PDS for the total lightcurve, with errors estimated using the the standard deviation of the average of the power in each frequency bin. The overall PDS were logarithmically rebinned and normalised to represent the squared fractional RMS in each frequency bin [see e.g. 155]. Corrections for instrument dead-time [see e.g. 201] were applied (although this was found to have a negligible effect in the frequency range under consideration) and the expected white noise level was subtracted [152]. Similar temporal analyses for the remaining targets proved unfeasible due to insufficient count statistics at all but the lowest frequencies.

Table 4.2: VHE γ-ray significances corresponding to both event selection regimes

Target	Cuts	N_{ON}	N_{OFF}	α	Excess	Significance [σ]
GRS 1915+105	Standard	445	6195	0.071	2.33	0.107
	Hard	32	545	0.062	-1.76	-0.297
Circinus X-1	Standard	368	3982	0.092	3.82	0.191
	Hard	42	450	0.079	6.46	1.012
V4641 Sgr	Standard	179	1902	0.091	6.36	0.461
	Hard	14	217	0.077	-2.62	-0.637

Table 4.3: VHE γ-ray integral flux upper limits above the telescope energy threshold corresponding to both event selection regimes. The upper limits are derived at the 99% confidence level, assuming a power law spectrum ($dN/dE \propto E^{-\Gamma}$) with the photon index $\Gamma_{\mathrm{std}} = 2.6$ for standard cuts and $\Gamma_{\mathrm{hard}} = 2.0$ for hard cuts. The rather high threshold energies derived for GRS 1915+105 and Circinus X-1 are the result of large maximum observational zenith angles.

Target	Cuts	T_{Live} [s]	E_{thresh} [GeV]	Z_{max} [°]	$I(> E_{\mathrm{thresh}})$ [ph cm^{-2}s^{-1}]
GRS 1915+105	Standard	24681	380	40.6	8.723×10^{-13}
	Hard	24681	709	40.6	2.186×10^{-13}
Circinus X-1	Standard	19433	423	43.6	1.115×10^{-12}
	Hard	19433	789	43.6	4.822×10^{-13}
V4641 Sgr	Standard	6335	179	8.4	5.529×10^{-12}
	Hard	6335	311	8.4	9.839×10^{-13}

H.E.S.S. observations were carried out using the full four-telescope array. The γ-ray analysis followed the standard point-source procedure described in Chapter 3. For all three binaries, no significant detection was obtained. Upper limits to the VHE γ-ray flux above the telescope threshold were therefore derived at the 99% confidence level using an approach based on the Unified Feldman-Cousins method [92]. The reflected background model was used to derive results for both the hard and standard image selection cuts

4.5.1 GRS 1915+105

Observations of GRS 1915+105 were initiated following a private communication from Guy Pooley, that the Ryle radio telescope had monitored an apparent decrease in the 15 GHz radio flux during a $\sim$ 50 day plateau state. On the basis of previously observed behaviour, it was thought likely that the observed radio behaviour signalled the end of the plateau state and therefore that flaring activity would begin within the subsequent 24 hours. The *RXTE* observations of GRS 1915+105

comprised six individual pointings, contributing to accumulated PCA and HEXTE livetimes of 7600s and 5176s respectively. As illustrated by the PCA and All Sky Monitor (ASM) lightcurves shown in Figure 4.1, the X-ray count rate was stable to within $\sim 10\%$ during each observation and varied by no more than $\sim 20\%$ between observations. Indeed, the long-term *RXTE* All Sky Monitor (ASM) lightcurve in Figure 4.1 clearly indicates that the H.E.S.S. observation epochs occur during an extended and relatively faint *plateau* in the 2-10 keV flux.

While numerous, extensive studies of the X-ray spectrum of GRS 1915+105 show it to be generally spectacular in its variability [e.g. 33, 94, 83], the plateaux are prominent exceptions to this rule. With a relatively stable characteristic X-ray flux, the C-type spectra of the plateau states are often modelled as the superposition of a dominant Comptonised power law component and a multicolour black body, both modified by interstellar absorption, and show little variation for the duration of the plateau. The 3-200 keV X-ray spectra shown in Figure 4.3 also exhibit remarkable stability between observations. The individual spectra are dominated by a hard non-thermal component, and strongly suggest class χ behaviour [e.g. 250, 239]. Broadly, χ class behaviour in the X-ray band is not sufficient to guarantee jet formation. Fortunately, segregation of χ class observations on the basis of radio loudness reveals that distinction is possible on the basis of X-ray energy spectra and PDS [239, 150]. Fast timing measurements of radio quiet (χ_2 [33] or Type I [239]) observations exhibit significant band limited white noise extending to high frequencies $f \sim 60 - 80$ Hz, while in radio loud (χ_1,χ_3 or Type II) observations such noise is either absent or exhibits an exponential cut-off at ~ 15 Hz [239]. The PDS shown in Figure 4.2 show no evidence for band limited noise at high frequencies. Following the approach of [34] and performing a Lorentzian decomposition[4] of the observed power spectra reveals two broad continuum components and several narrower quasi-periodic oscillation (QPO) peaks. Crucially, the characteristic frequency ($\nu_{max} = \sqrt{\nu_0^2 + \Delta^2}$ [see 34]) of the higher frequency continuum component never exceeds ~ 4 Hz, far less than would be expected for the radio quiet χ state.

In the energy domain, [239] found that radio loud observations exhibit a clear spectral break

[4]The decomposition was performed using a custom implemented compound function fitting tool based on the ROOT framework (See http://root.cern.ch). The source code for this tool is presented in Appendix E.1.

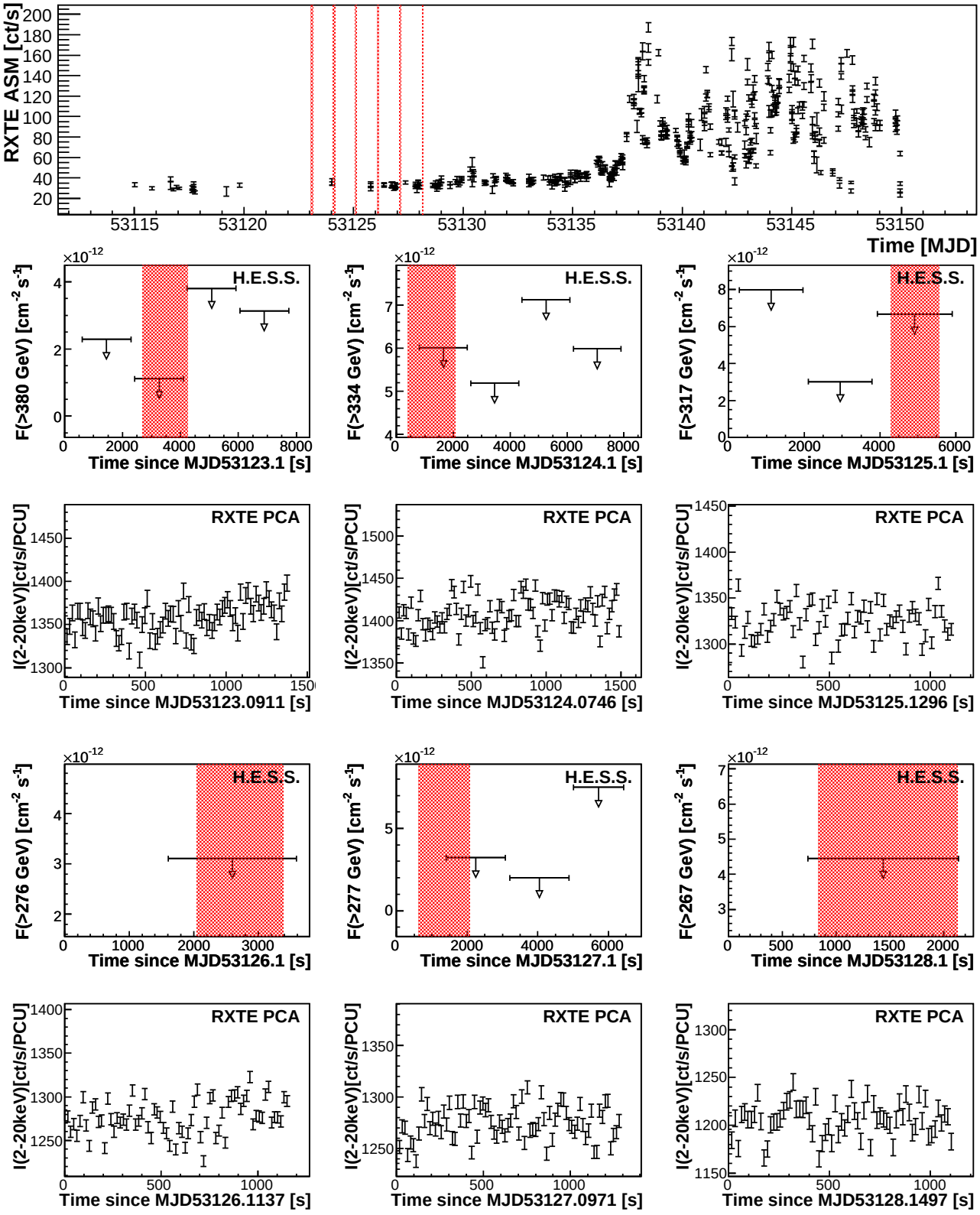

Figure 4.1: H.E.S.S. run-wise upper limits together with *RXTE* ASM and PCA lightcurves for GRS 1915+105. The red shaded bands on the ASM lightcurve indicate the extent of the H.E.S.S. observations, while on the H.E.S.S. upper limit plots they illustrate the duration of the contemporaneous PCA observations.

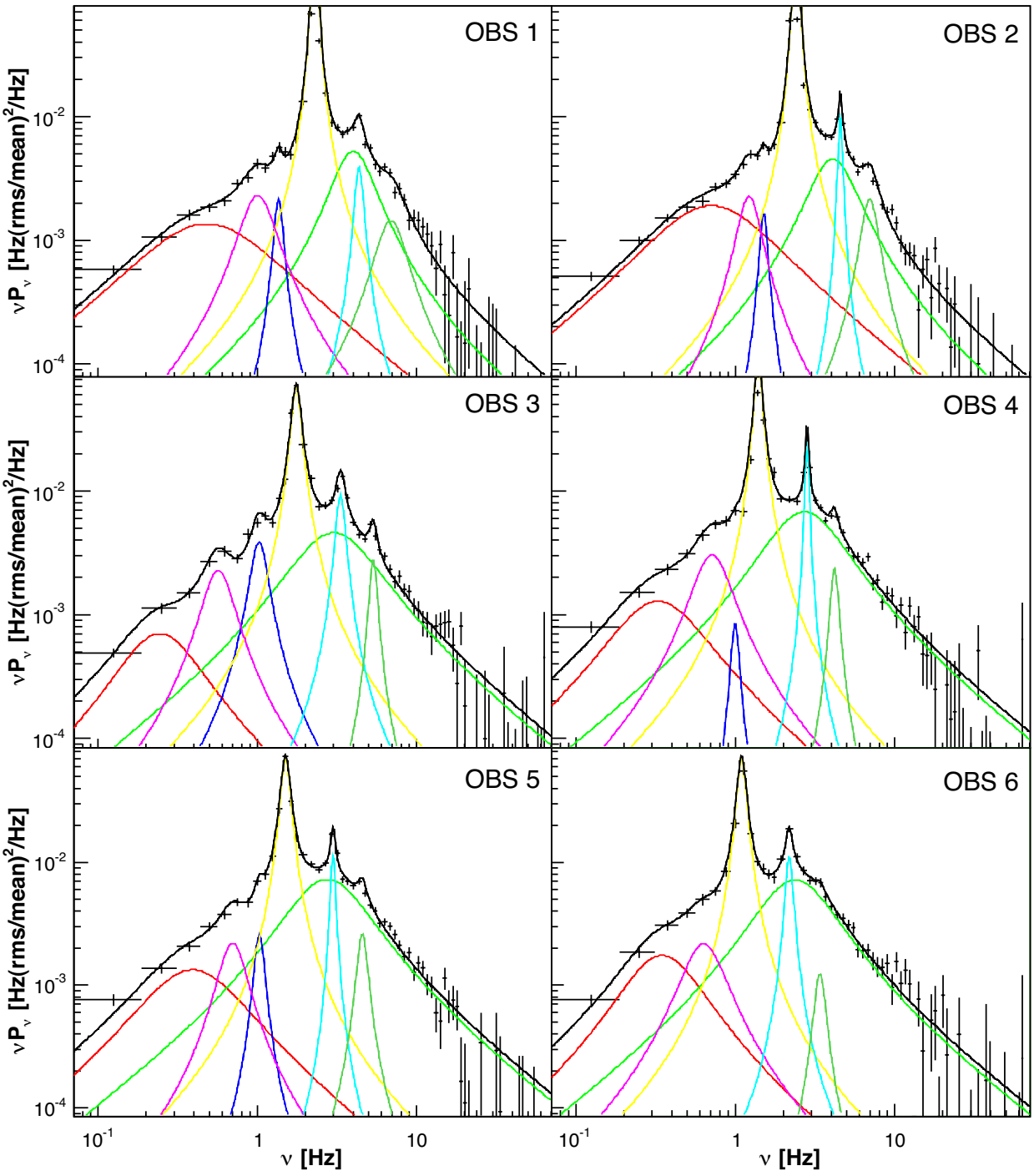

Figure 4.2: X-ray power density spectra (PDS) corresponding to the six RXTE observations of GRS 1915+105. The PDS have been fitted using a superposition of Lorentzian functions following the approach of [34].

between $\sim 12 - 20$ keV whereas radio quiet X-ray spectra extend unbroken to a quasi-exponential cut-off at $\sim 60 - 120$ keV. The X-ray spectra in Figure 4.3 exhibit a marked change in spectral index in the 15-20 keV range, reinforcing the association of the radio loud χ state with all contemporaneous observations. Modelling the dominant hard component as pure thermal comptonisation (using the `XSPEC` model COMPTT) reveals a significant hard excess at high energies ($E \gtrsim 100$ keV) and probably implies the existence of non-thermal Comptonisation processes within the source [250]. Following the approach of [249] the hybrid comptonisation model EQPAIR [68, 67] was used in combination with a multicolour blackbody component (DISKBB) at low energies to simulate the X-ray continuum. The input photon temperature of the EQPAIR model was tied to the disc inner temperature of the multicolour blackbody component, with the spectrum of input photons derived using the `XSPEC` model DISKBB. The ionised reflection model implemented by EQPAIR is extremely computationally expensive and since the precise ionisation levels of the accretion disk are not relevant for the current discussion it was disabled by fixing the REFL parameter at zero. Instead, the reflection signatures present in the spectra were approximated by a combination of a gaussian line (GAUSSIAN) and a smeared absorption edge (SMEDGE). For all observations, the best-fitting values of the free parameters in the emission model are listed in Table 4.6, while important fixed parameters are listed in Table 4.4. *Chandra* spectra obtained by [153] reveal significantly enhanced

Table 4.4: XSPEC model components and best-fitting free parameter values for GRS 1915+105.

COMPONENT	PARAMETER	
EQPAIR	l_{bb}	100
EQPAIR	kT_{bb}	DISKBB$\rightarrow T_{\rm in} \times 1000$
EQPAIR	radius (cm)	1.0×10^7
EQPAIR	$\gamma_{\rm min}$	1.3
EQPAIR	$\gamma_{\rm max}$	1000

column densities of Mg, Si, and Fe relative to the observed hydrogen column. Simulation of the spectral modifications introduced by these over-abundances is shown by [83] to be a significant requirement when modelling 3-20 keV *RXTE* spectra. Consequently, the combined intrinsic and interstellar absorption was simulated using the variable abundance photoelectric absorption model

VARABS with the elemental column densities listed in Table 4.5 and using Balucinska-Church and McCammon cross-sections. A constant multiplicative factor was introduced to account for the

Table 4.5: The equivalent hydrogen columns used for the VARABS component in the X-ray spectral model for GRS 1915+105. The values were taken from [153].

PARAMETER	N_H ($\times 10^{22}$cm^{-2})
$N_{\mathrm{H,He,C,N,O}}$	4.7
$N_{\mathrm{Ne,Na}}$	4.7
$N_{\mathrm{Mg,Al}}$	4.7
N_{Si}	16.4
$N_{\mathrm{S,Cl,Ar,Ca,Cr}}$	4.7
N_{Fe}	10.9
$N_{\mathrm{Co,Ni}}$	4.7

normalisation of HEXTE relative to the PCA. To achieve this, the reference normalisation of the PCA data was frozen at unity, while the normalisations of the two HEXTE clusters were allowed to vary independently. As demonstrated by the reduced χ^2 values listed in Table 4.6, the fitted model provides a formally excellent description of the RXTE data. While the physical implications of this largely phenomenological model should not be over-interpretted, the observed spectral shapes are entirely consistent with those observed by [249] and [239] during the radio loud χ state.

The combined spectral and temporal analyses allow a robust association of the contemporaneous H.E.S.S. observation with the *radio-loud* χ state and we may confidently infer the presence of steady, mildly relativistic jets at the time of observation. The contemporaneous H.E.S.S. observations represent an overall livetime of 6.86 hours and did not yield a significant VHE γ-ray detection. The signifcances corresponding to the total H.E.S.S. exposure are listed in Table 4.2. Figure 4.1 plots run-wise 99% confidence level upper limits to the integral VHE γ-ray flux above the telescope threshold energy and illustrates the overlap between the *RXTE* and H.E.S.S. observations. It is evident that almost all of the PCA exposure has corresponding, strictly simultaneous, VHE γ-ray data. Integral flux upper limits which correspond to the overall H.E.S.S. exposure are listed in Table 4.3.

An analysis of the entire H.E.S.S. data set for GRS 1915+105 was presented by [123] who derive an upper limit to the γ-ray flux above 1 TeV of 6.1×10^{-13} s^{-1}cm^{-2} corresponding to a

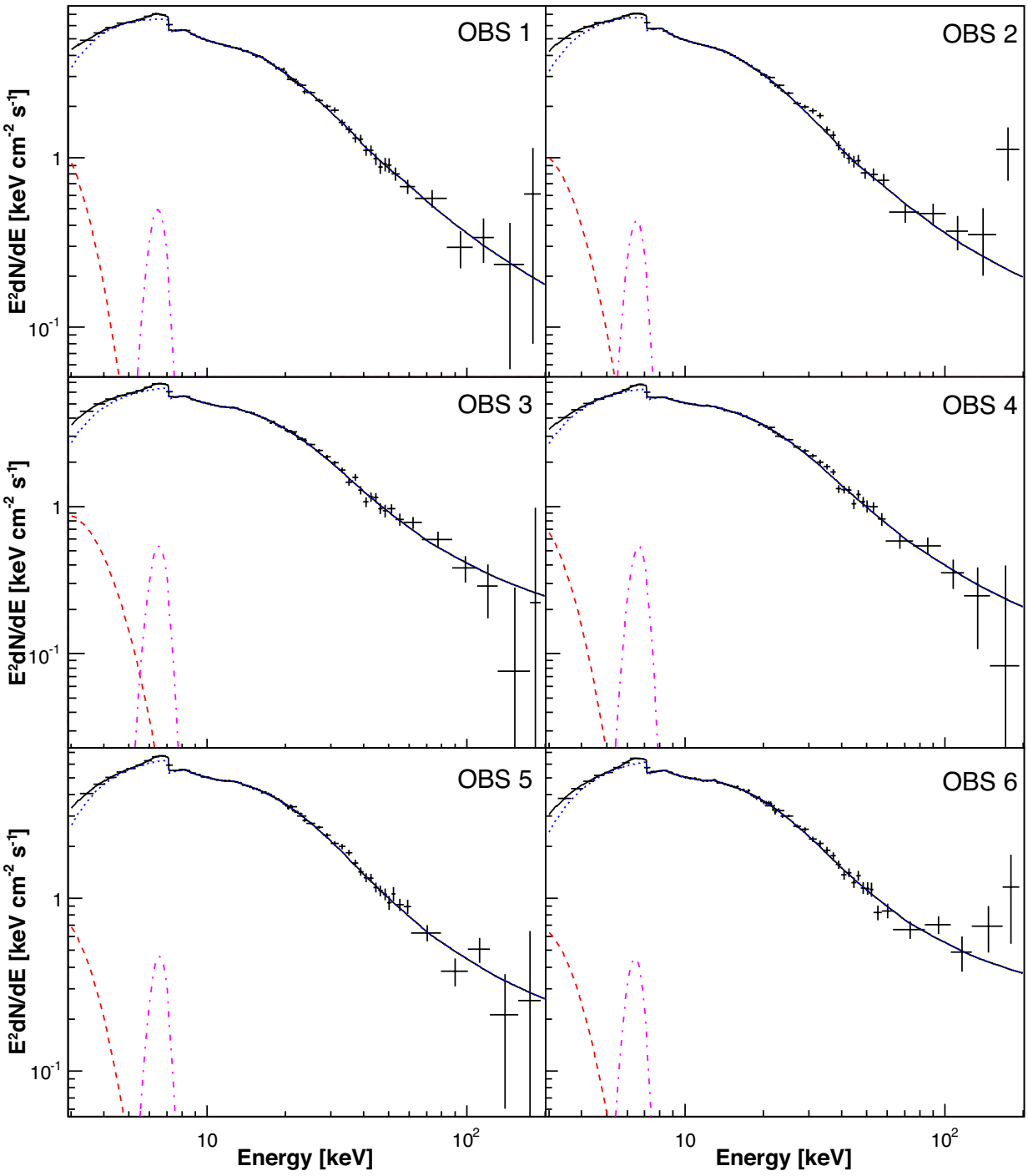

Figure 4.3: *RXTE* X-ray spectrum of GRS 1915+105 showing the individual XSPEC model components: DISKBB (red dashes), EQPAIR (blue dots), GAUSSIAN (magenta dot-dashed), and the total spectrum (black).

Table 4.6: XSPEC model components and best-fitting free parameter values for GRS 1915+105. The errors correspond to a $\Delta\chi^2$ of 2.71.

Component	Parameter	Pointing 1	Pointing 2	Pointing 3
Smedge	$E_{\rm Edge}$ (keV)	$8.302^{+0.12}_{-0.14}$	$8.158^{+0.13}_{-0.23}$	$8.273^{+0.27}_{-0.23}$
Smedge	$\tau_{\rm max}$	$(9.734^{+0.55}_{-0.89}) \times 10^{-1}$	$1.081^{+0.14}_{-0.12}$	$(8.503^{+0.94}_{-1.96}) \times 10^{-1}$
Diskbb	$T_{\rm in}$ (keV)	$(3.256^{+1.01}_{-0.83}) \times 10^{-1}$	$(4.335^{+1.50}_{-0.64}) \times 10^{-1}$	$(4.961^{+0.81}_{-0.76}) \times 10^{-1}$
Diskbb	Norm	$(9.329^{+1.70}_{-2.29}) \times 10^{5}$	$(7.130^{+1.24}_{-0.75}) \times 10^{4}$	$(2.174^{+2.47}_{-0.42}) \times 10^{4}$
Eqpair	l_h/l_s	$1.230^{+0.16}_{-0.13}$	$1.480^{+0.17}_{-0.10}$	$1.712^{+0.11}_{-0.14}$
Eqpair	l_{nt}/l_h	$(9.999^{+0.00}_{-1.13}) \times 10^{-1}$	$(9.331^{+0.44}_{-0.30}) \times 10^{-1}$	$(6.524^{+0.54}_{-0.09}) \times 10^{-1}$
Eqpair	τ_p	$7.703^{+0.83}_{-0.20}$	$8.751^{+0.31}_{-0.43}$	$7.679^{+0.24}_{-0.30}$
Eqpair	$G_{\rm inj}$	$3.955^{+0.15}_{-0.18}$	$3.663^{+0.20}_{-0.14}$	$3.212^{+0.29}_{-0.15}$
Eqpair	Norm	$(1.280^{+0.17}_{-0.20}) \times 10^{5}$	$(2.933^{+0.78}_{-1.03}) \times 10^{4}$	$(1.311^{+0.28}_{-0.26}) \times 10^{4}$
Gaussian	$E_{\rm Line}$ (keV)	$6.361^{+0.19}_{-0.19}$	$6.430^{+0.25}_{-0.23}$	$6.422^{+0.19}_{-0.18}$
Gaussian	σ (keV)	≤ 0.680	≤ 1.00	≤ 0.522
Gaussian	Norm	$(1.703^{+0.39}_{-0.54}) \times 10^{-2}$	$(1.437^{+0.79}_{-0.82}) \times 10^{-2}$	$(1.812^{+0.60}_{-0.85}) \times 10^{-2}$
Constant	factor	$1.025^{+0.02}_{-0.02}$	$1.027^{+0.02}_{-0.02}$	$1.007^{+0.02}_{-0.02}$
Constant	factor	$1.003^{+0.02}_{-0.02}$	$1.035^{+0.02}_{-0.02}$	$1.016^{+0.02}_{-0.02}$
χ^2_ν (NDF)		0.72 (125)	0.71 (125)	0.79 (125)

Component	Parameter	Pointing 4	Pointing 5	Pointing 6
Smedge	$E_{\rm Edge}$ (keV)	$8.346^{+0.34}_{-0.17}$	$8.268^{+0.31}_{-0.20}$	$8.404^{+0.24}_{-0.25}$
Smedge	$\tau_{\rm max}$	$(7.334^{+0.57}_{-1.71}) \times 10^{-1}$	$(8.314^{+1.04}_{-1.93}) \times 10^{-1}$	$(8.678^{+1.41}_{-0.68}) \times 10^{-1}$
Diskbb	$T_{\rm in}$ (keV)	$(3.496^{+1.46}_{-0.71}) \times 10^{-1}$	$(3.847^{+1.15}_{-1.16}) \times 10^{-1}$	$(4.293^{+2.09}_{-1.56}) \times 10^{-1}$
Diskbb	Norm	$(3.257^{+3.43}_{-0.86}) \times 10^{5}$	$(1.354^{+3.47}_{-0.35}) \times 10^{5}$	$(4.902^{+3.40}_{-1.85}) \times 10^{4}$
Eqpair	l_h/l_s	$1.837^{+0.27}_{-0.16}$	$1.881^{+0.17}_{-0.11}$	$2.128^{+0.21}_{-0.10}$
Eqpair	l_{nt}/l_h	$(7.073^{+0.91}_{-0.93}) \times 10^{-1}$	$(6.697^{+2.06}_{-0.29}) \times 10^{-1}$	$(7.242^{+0.48}_{-0.56}) \times 10^{-1}$
Eqpair	τ_p	$7.340^{+0.49}_{-0.37}$	$7.596^{+0.54}_{-0.13}$	$7.973^{+0.26}_{-0.26}$
Eqpair	$G_{\rm inj}$	$3.637^{+0.17}_{-0.36}$	$3.258^{+0.28}_{-0.16}$	$2.894^{+0.34}_{-0.22}$
Eqpair	Norm	$(5.680^{+0.80}_{-2.59}) \times 10^{4}$	$(3.658^{+0.58}_{-1.69}) \times 10^{4}$	$(1.997^{+0.34}_{-0.64}) \times 10^{4}$
Gaussian	$E_{\rm Line}$ (keV)	$6.555^{+0.26}_{-0.21}$	$6.459^{+0.33}_{-0.23}$	$6.334^{+0.28}_{-0.20}$
Gaussian	σ (keV)	≤ 1.11	≤ 1.03	≤ 0.633
Gaussian	Norm	$(1.728^{+0.68}_{-0.62}) \times 10^{-2}$	$(1.536^{+0.61}_{-0.51}) \times 10^{-2}$	$(1.570^{+0.61}_{-0.56}) \times 10^{-2}$
Constant	factor	$1.011^{+0.02}_{-0.02}$	$(9.810^{+0.21}_{-0.21}) \times 10^{-1}$	$1.027^{+0.02}_{-0.04}$
Constant	factor	$1.013^{+0.02}_{-0.02}$	$1.016^{+0.02}_{-0.02}$	$1.013^{+0.02}_{-0.02}$
χ^2_ν (NDF)		1.17 (125)	0.76 (125)	0.77 (125)

detector live time of 24.07 hours. None of the H.E.S.S. observations of GRS 1915+105 coincide with bright flaring episodes at longer wavelengths.

4.5.2 Circinus X-1

Observations of Circinus X-1 were scheduled to coincide with the periastron passage of the binary components. The previous observation of regular radio flares during this orbital interval were thought to provide a good chance of observing during a period of outburst, with the associated possibility that superluminal ejections might occur. The *RXTE* observations of Cir X-1 comprised three individual pointings, corresponding to orbital phase intervals $0.0486 \leq \phi \leq 0.0498$, $0.1104 \leq \phi \leq 0.1112$ and $0.1718 \leq \phi \leq 0.1725$ (using the radio flare ephemeris of [188]), and contributing to an accumulated PCA livetime of 2576s. It should be noted that the observations reported here were obtained during an extremely faint episode in the secular X-ray flux evolution of Cir X-1 [195]. Additionally, the ASM lightcurve shown in Figure 4.4, reveals that the H.E.S.S. observation epochs occur during an extended $\sim$ 4 day dip in the 2-10 keV X-ray flux. As a consequence, the measured X-ray fluxes are significantly lower than most others reported for this source. As illustrated in Figure 4.4, the individual PCA lightcurves obtained during the the first two pointings are characterised by a relatively low count rate which remains approximately constant throughout each observation. In marked contrast, the third observation exhibits clear variability with count rates doubling on timescales of $\sim$ 50s. Previous observations of Cir X-1 during periastron dips [e.g. 229, 223] reveal the evidence of strong, complex and variable intrinsic X-ray absorption. Consequently, diagnosis of the system behaviour during the third *RXTE* observation is critically dependent upon whether the observed variability represents a genuine change in the underlying continuum emission or is simply an artefact of varying absorption.

Inspection of the 3-20 keV PCA spectra shown in Figure 4.5 reveals that the observed flux variability is accompanied by marked variations in spectral shape. For the third observation, individual spectra were extracted from the four regions shown in Figure 4.4, segregated on the basis of average 2-20 keV count rates. Fitting of the spectral data from the third observation employed a

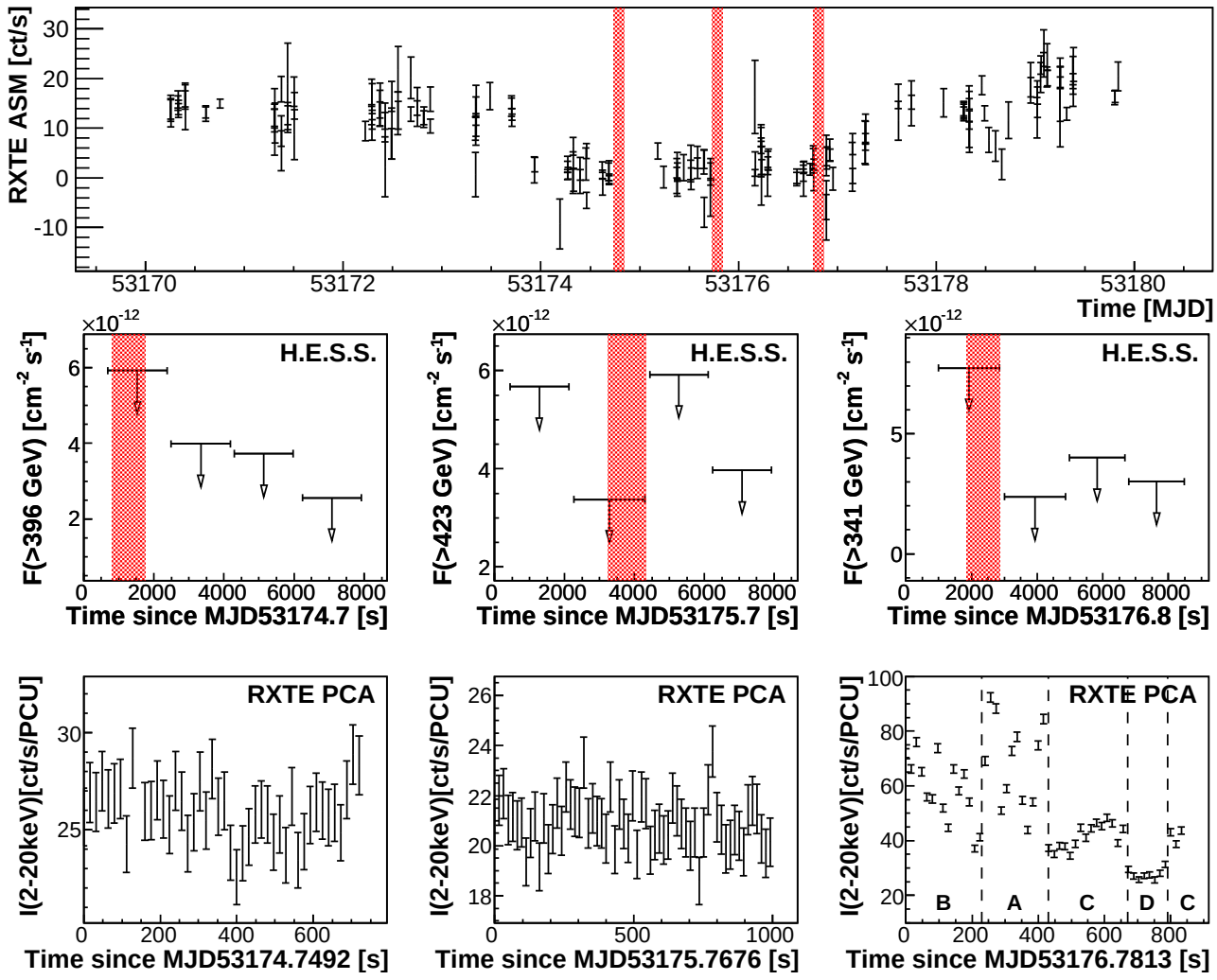

Figure 4.4: H.E.S.S. run-wise upper limits together with *RXTE* ASM and PCA lightcurves for Cir X-1. The red shaded bands on the ASM lightcurve indicate the extent of the H.E.S.S. observations, while on the H.E.S.S. upper limit plots they illustrate the duration of the contemporaneous PCA observations.

similar approach to that of [229], with the unabsorbed continuum modeled using a disc blackbody component (DISKBB in XSPEC) at low energies in combination with a single temperature blackbody (BBODY) that dominates above $\sim$ 15 keV. As mentioned in §4.4.2, previously reported *RXTE* measurements indicate that the observed continuum emission comprises two separate but spectrally similar elements: a bright but heavily absorbed component and a much fainter component which becomes apparent during periodic X-ray dips and appears only weakly attenuated. Accordingly,

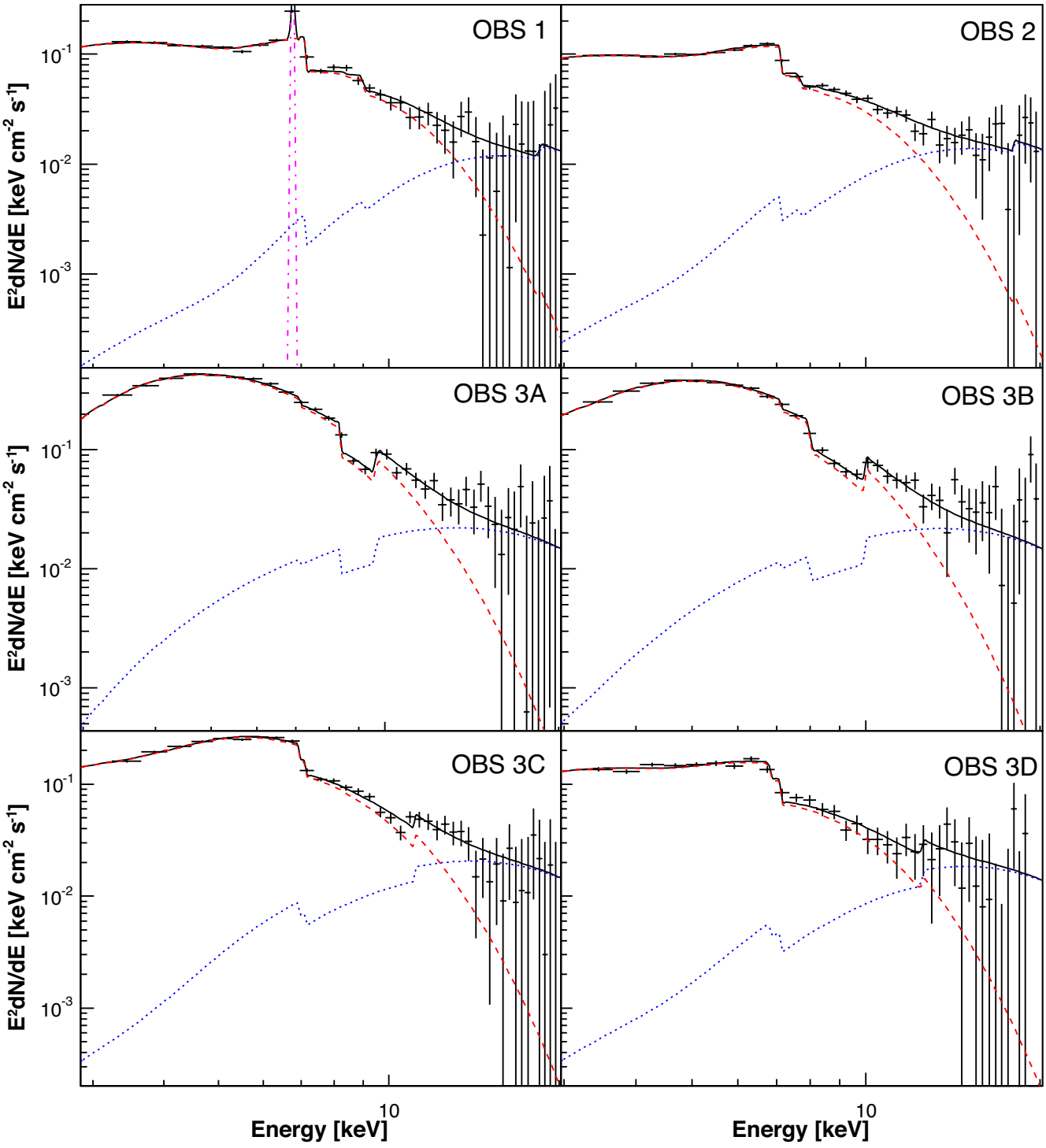

Figure 4.5: *RXTE* 3-20 keV X-ray spectra of Circinus X-1 for the first and second observations (top two panels), and the four sub-intervals of the third observation (bottom four panels). The solid black curves illustrate the total spectral model while the individual components are represented as follows: DISKBB (red dashed), BBODY (blue dotted), GAUSSIAN (pink dot-dashed dashes).

two components are used to separately simulate intrinsic and extrinsic X-ray absorption. The bipartite intrinsic absorption is treated using a partial covering model (PCFABS), while a simple photoelectric model (PHABS) simulates the absorbing effect of the interstellar medium. Adopting a weighted average of the neutral hydrogen data of [144] calculated using the `nH` ftool, a fixed effective hydrogen column with $N_H = 1.59 \times 10^{22}$ cm^{-2} was assumed for the PHABS component. Fits to the individual spectra from the third observation using this simple absorbed continuum model reveal large correlated residuals in the energy range from 6-15 keV, indicative of the superposition of complex absorption and emission features. This is consistent with the numerous emission and absorption complexes evident in the recent low-flux *Chandra* spectra discussed in §4.4.2. While the modest energy resolution of *RXTE* prohibits detailed modeling of these features, their combined effect must be approximated in order to obtain an acceptable fit to the observed spectrum. After testing `XSPEC`'s GAUSSIAN, EDGE, and SMEDGE components (all of which provided significant improvements), the best fit to the individual spectra was obtained by convolving with a NOTCH component centered at ~ 9 keV. In order to constrain the origin of the observed spectral variability, a joint fit was performed using the complete best-fitting model. The continuum and extrinsic absorption components (DISKBB, BBODY, PHABS) were constrained to be equal for all individual spectra, while the components related to intrinsic absorption (PCFABS, NOTCH) were allowed to vary independently. The parameters of the resulting fit are listed in Table 4.7. The formally excellent nature of the fit ($\chi^2_\nu = 0.88$) is entirely consistent with the observed spectral behaviour arising purely from variations in the intrinsic absorption, with no requirement for flaring of the underlying continuum.

Table 4.8 lists the parameters of the spectral fits obtained from the first and second observations. Remarkably, an identical continuum model to that obtained from the third observation also provides an excellent fit ($\chi^2_\nu = 0.82$) to the spectrum obtained during the second observation. In contrast, the spectrum obtained during the first observation is more appropriately described by a single, heavily absorbed disc blackbody component, with large correlated residuals around ~ 6.5 keV statistically favouring the addition of a GAUSSIAN line component. This continuum variabil-

Table 4.7: Spectral parameters for Cir X-1 during the orbital phase interval $0.1718 \leq \phi \leq 0.1725$ (according to the ephemeris of [188]). XSPEC model components, best fit parameters, and 3-20 keV model fluxes are shown for the four separate sub-intervals illustrated in Figure 4.4, in order of decreasing model flux. The errors correspond to a $\Delta\chi^2$ of 2.71.

Component	Parameter	Interval A	Interval B	Interval C	Interval D
Diskbb	$T_{\rm in}$ [keV]	$1.269^{+0.08}_{0.08}$	Joint fit		
	Norm	$(4.891^{+1.55}_{2.81}) \times 10^{1}$			
Bbody	kT [keV]	$3.276^{+0.94}_{2.00}$	Joint fit		
	Norm	$(6.052^{+1.47}_{3.33}) \times 10^{-4}$			
Notch	$E_{\rm Line}$ [keV]	$9.004^{+0.28}_{0.51}$	$8.971^{+0.22}_{0.29}$	$9.018^{+0.34}_{0.54}$	> 8.417
	Width [keV]	$1.260^{+0.95}_{1.68}$	$1.970^{+1.30}_{0.98}$	$4.171^{+0.68}_{1.12}$	$5.673^{+3.30}_{2.46}$
	CvrFract	$> (2.143) \times 10^{-1}$	$(3.954^{+0.95}_{4.83}) \times 10^{-1}$	$(2.531^{+0.59}_{0.57}) \times 10^{-1}$	$(2.754^{+0.89}_{1.74}) \times 10^{-1}$
Pcfabs	$N_{\rm H}$ ($\times 10^{22}$)	$(1.056^{+0.21}_{0.55}) \times 10^{1}$	$(1.819^{+0.35}_{0.50}) \times 10^{1}$	$(3.820^{+0.26}_{0.37}) \times 10^{1}$	$(8.008^{+0.87}_{1.66}) \times 10^{1}$
	CvrFract	$> (8.129) \times 10^{-1}$	$(7.618^{+0.53}_{0.50}) \times 10^{-1}$	$(7.843^{+0.34}_{0.40}) \times 10^{-1}$	$(8.075^{+0.27}_{0.33}) \times 10^{-1}$
χ^2_ν (NDF)		0.88 (136)	Joint fit		
Model Flux	[ergs cm^{-2}s^{-1}]	6.073×10^{-10}	5.4966×10^{-10}	3.8305×10^{-10}	2.5656×10^{-10}

ity is consistent with the results of [227] who found that significant variation of the continuum parameters could occur on timescales of a few hours.

Table 4.8: XSPEC model components, best fit parameters, and 3-20 keV model fluxes for Cir X-1 during the orbital phase intervals $0.0486 \leq \phi \leq 0.0498$ and $0.1104 \leq \phi \leq 0.1112$ (according to the ephemeris of [188]). Parameters marked by * are fixed to the best-fitting values from the third observation (See Table 4.7). The errors correspond to a $\Delta\chi^2$ of 2.71.

Component	Parameter	First Observation ($0.0486 \leq \phi \leq 0.0498$)	Second Observation ($0.1104 \leq \phi \leq 0.1112$)
Diskbb	$T_{\rm in}$ [keV]	$1.306^{+0.07}_{0.07}$	1.269*
	Norm	$(1.463^{+0.75}_{0.52}) \times 10^2$	$(4.891) \times 10^1$*
Bbody	kT [keV]	-	$3.276^{+0.94}_{2.00}$
	Norm	-	$(6.052^{+1.47}_{3.33}) \times 10^{-4}$
Notch	$E_{\rm Line}$ [keV]	$(1.106^{+0.03}_{0.06}) \times 10^1$	$(1.285^{+0.22}_{0.51}) \times 10^1$
	Width [keV]	$3.936^{+0.89}_{9.43}$	$(1.032^{+0.45}_{0.74}) \times 10^1$
	CvrFract	$(4.612^{+0.75}_{0.83}) \times 10^{-1}$	$(2.031^{+0.37}_{0.42}) \times 10^{-1}$
Pcfabs	$N_{\rm H}$ ($\times 10^{22}$)	$(1.815^{+0.30}_{0.11}) \times 10^2$	$(9.921^{+0.27}_{0.27}) \times 10^1$
	CvrFract	$(9.503^{+0.23}_{0.15}) \times 10^{-1}$	$(8.642^{+0.02}_{0.02}) \times 10^{-1}$
Gaussian	$E_{\rm Line}$ [keV]	$6.655^{+0.15}_{0.09}$	-
	σ [keV]	$< (3.056) \times 10^{-1}$	-
	Norm	$(8.204^{+4.22}_{4.06}) \times 10^{-3}$	-
χ^2_ν (NDF)		0.77 (32)	0.82 (35)
Model Flux	[ergs cm^{-2}s^{-1}]	2.337×10^{-10}	1.9255×10^{-10}

Overall, the *RXTE* data appear to reinforce the accepted paradigm of enhanced mass transfer during the periastron passage of the compact primary with the strong and variable intrinsic absorption attributed to obscuration by a turbulent accretion flow [see e.g. 191, 186, 133]. A marked disparity between best fitting model components and parameters of the first and second observations implies a dramatic evolution of the local radiative environment. A three-fold decrease in continuum luminosity accompanied by a halving of the intrinsic absorption column appears to suggest a significant decrease in the mass transfer rate. The continued reduction of the magnitude and then continuity of the inferred absorption column during the second and third observations is potentially indicative of dispersion or reorganisation of the recently accreted material.

The ephemeris of [188] predicts the onset of a radio flare $\sim 19 - 20$h before the first *RXTE*

observation. Unfortunately, despite the undoubted occurrence of pseudo-periodic radio flares from Cir X-1 near periastron, a robust correlation between the observed X-ray and radio behaviour is yet to be identified. Although rapid brightening of the X-ray continuum might indicate accompanying radio flares, evidence for a definitive association is far from clear [231, 242]. Recent radio observations of Cir X-1 [e.g. 96, 242] focus primarily on the ultra-relativistic ejection events that manifest as $\gtrsim$ 3 day episodes of flaring on timescales of a few hours. In principle, the lack of contemporaneous radio data admits the possibility of such persistent outbursts at the time of observation. However, the absence of any evidence for flaring in the X-ray band renders this a rather unlikely scenario, especially as the dramatic events reported by [96] were ubiquitously accompanied by a strong X-ray outburst. By analogy with canonical black hole binaries, it might be that the inferred variation in the mass accretion rate between the first and second *RXTE* observations also implies an evolution of the jet properties, but this is far from clear in such an unusual system. Finally, [242] report compelling evidence that prior to 2006, Cir X-1 underwent a $\sim$ 6 year episode of unusual radio quiescence, suggesting that jet formation was somewhat suppressed during the epochs of H.E.S.S. observation.

Contemporaneous H.E.S.S. observations with *RXTE* yield an overall livetime of 5.4 hours, with a resulting non-detection evident from the significances listed in Table 4.2. Figure 4.4 plots run-wise 99% confidence level upper limits to the integral VHE γ-ray flux above the telescope threshold energy and illustrates complete overlap between the *RXTE* and H.E.S.S. observations. Integral flux upper limits which correspond to the overall H.E.S.S. exposure are listed in Table 4.3.

An analysis of a larger H.E.S.S. data set for Circinus X-1 was presented by [187] who derive a preliminary upper limit to the γ-ray flux above 1 TeV of 1.9×10^{-13} s^{-1}cm^{-2} corresponding to a detector live time of 28 hours. Although some of the H.E.S.S. observations presented by [187] were obtained after Circinus X-1 resumed its periodic radio flares in 2006, poor weather and impractical scheduling requirements have prevented H.E.S.S. observations of this source from being obtained during a radio outburst.

4.5.3 V4641 Sgr

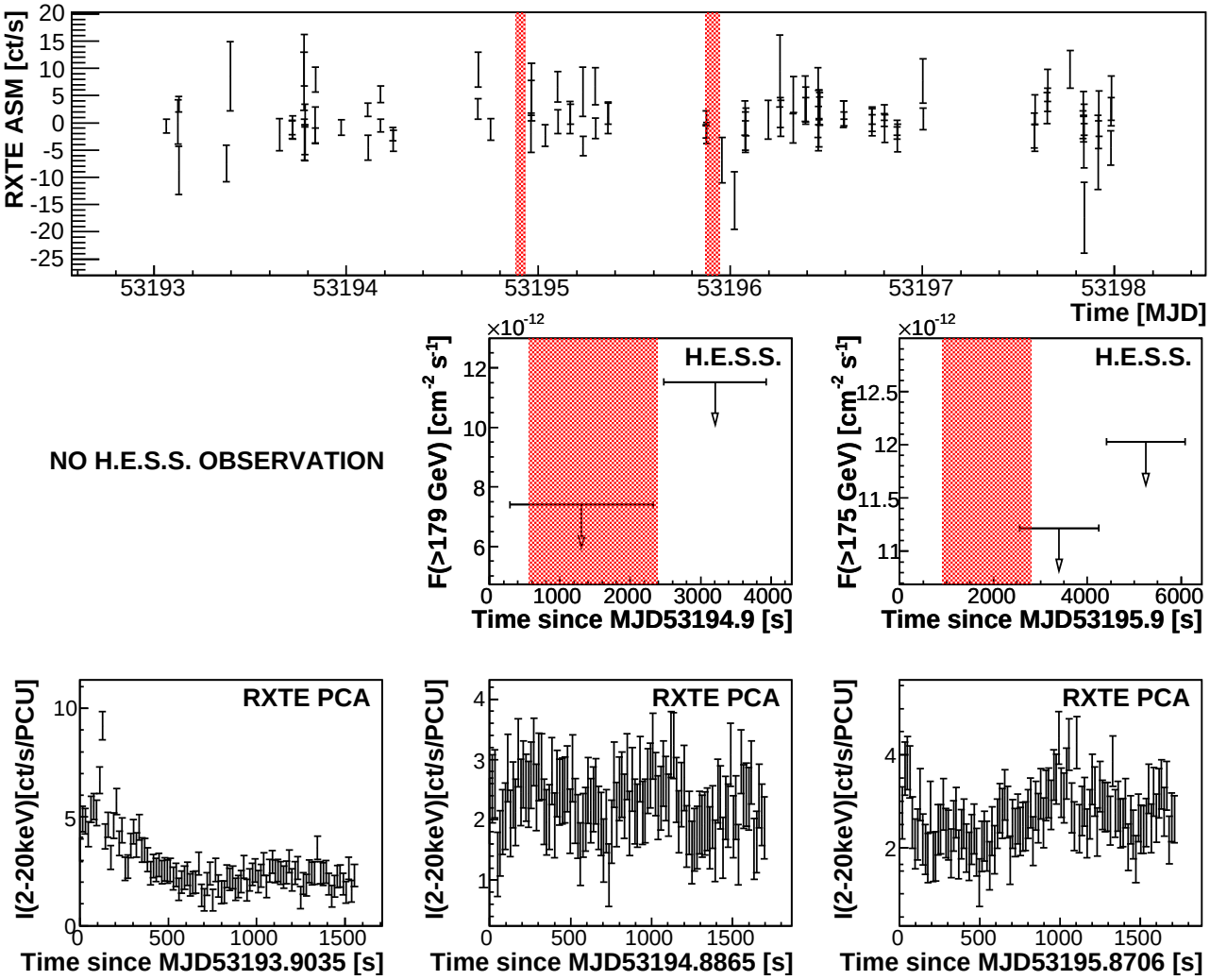

Figure 4.6: H.E.S.S. run-wise upper limits together with *RXTE* ASM and PCA lightcurves for V4641 Sgr. The red shaded bands on the ASM lightcurve indicate the extent of the H.E.S.S. observations, while on the H.E.S.S. upper limit plots they illustrate the duration of the contemporaneous PCA observations.

Observations of V4641 Sgr were initiated on on July 7th 2004 in response to the source brightening rapidly in the radio [216], optical [203] and X-ray [234] bands. Figure 4.6 shows *RXTE* PCA lightcurves derived from from the three resulting observations which contribute to an accumulated PCA livetime of 5008s. The individual lightcurves indicate various degrees of X-ray variability with the clearest evidence for flaring visible as a sharp $\sim$ 5-fold count rate fluctuation during the first

observation. In marked contrast, the second observation is uniformly faint with the χ^2 probability of constant count rate $P_{\rm const} = 0.97$, and hence consistent with a period of quiescent behaviour. Subsequently, the third observation reveals a reemergence of mild variability ($P_{\rm const} = 0.07$) with $\sim$ 2-fold count rate fluctuations occurring on timescales of $\sim$ 500s. At this point is should be noted that despite evidence for significant X-ray variability during two of the *RXTE* observations, the highest measured count rates are at least four orders of magnitude lower than those associated with the 12.2 Crab X-ray flare of V4641 Sgr in 1999 [202]. Radio data obtained using the VLA and the ATCA between MJD 53190 and MJD 53208 indicate rapid variability with peak flux densities of $\sim$ 30 mJy observed on MJD 53193 [216, 226, 214]. An optically thin radio spectrum ($S_\nu \propto \nu^{-0.7}$ observed on MJD 53191 was interpreted by [216] as the signature of a decaying radio flare.

The time averaged 3-20 keV PCA spectra for each observation are shown in Figure 4.5. Low event statistics resulting from a combination of short observations and an intrinsically weak source flux prohibit the fitting of complex models to the X-ray data. Instead, the continuum is modelled as a simple unabsorbed power law and the addition of a GAUSSIAN component at $\sim 6.4 - 6.7$ keV significantly improves the spectral fit. The resulting fit parameters are listed in Table 4.9.

While V4641 Sgr is evidently the most X-ray-faint binary in the studied sample, it simultaneously exhibits the hardest spectrum. In fact, the spectral shape closely resembles that which corresponded to the period of optical oscillation preceding the 1999 flare, albeit at much lower luminosity. Furthermore, in spite of the poor data quality, the spectral fits provide some evidence for evolution of the 3-20 keV spectral index between observations which is consistent with the observations of rapid flux evolution in the radio band. In view of the various multi-wavelength data, it seems likely that V4641 Sgr underwent a period of mild activity which spanned the H.E.S.S. observation epochs.

The H.E.S.S. dataset representing contemporaneous observations with *RXTE* constitutes an overall livetime of 1.76 hours yielding a non-detection with the corresponding γ-ray significances listed in Table 4.2. As illustrated by Figure 4.6 no γ-ray data were obtained which correspond to the first *RXTE* observation. This is unfortunate, since the first observation exhibits the best

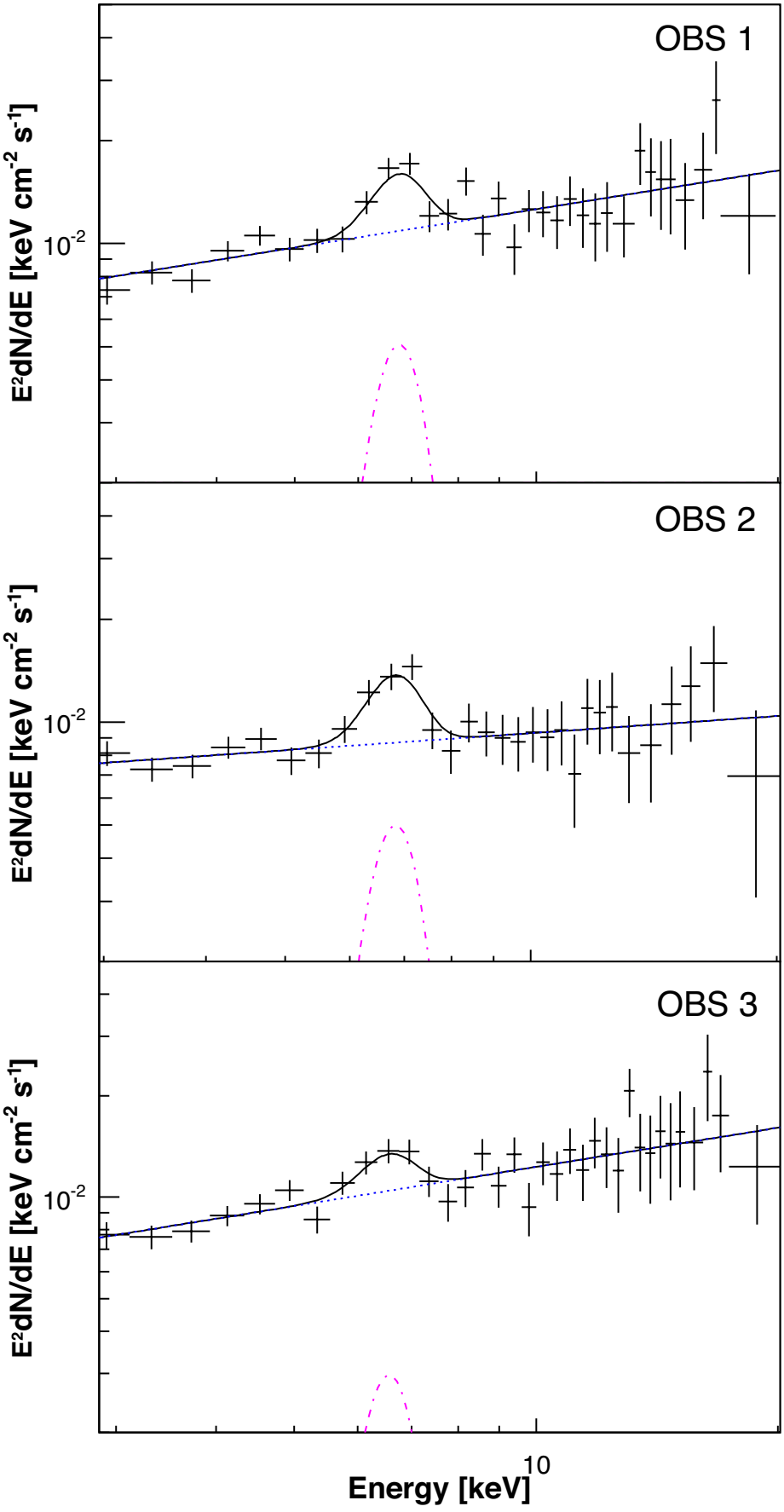

Figure 4.7: *RXTE* 3-20 keV X-ray spectra of V4641 Sgr for all three observations. The solid black curves illustrate the total spectral model while the individual components are represented as follows: Powerlaw (blue dotted), Gaussian (magenta dot-dashed).

Table 4.9: XSPEC model components and best fit parameters for V4641 Sgr. The errors correspond to a $\Delta\chi^2$ of 2.71.

Component	Parameter	Pointing 1	Pointing 2	Pointing 3
Powerlaw	$\Gamma_{\rm phot}$	$1.626^{+0.09}_{-0.07}$	$1.805^{+0.10}_{-0.05}$	$1.614^{+0.07}_{-0.09}$
Powerlaw	Norm	$(5.325^{+0.81}_{-0.72}) \times 10^{-3}$	$(5.991^{+1.24}_{-1.03}) \times 10^{-3}$	$(5.050^{+0.66}_{-0.80}) \times 10^{-3}$
Gaussian	$E_{\rm Line}$ (keV)	$6.679^{+0.29}_{-0.59}$	$6.745^{+0.24}_{-0.24}$	$6.487^{+0.33}_{-0.49}$
Gaussian	σ (keV)	≤ 1.181	≤ 0.723	≤ 0.896
Gaussian	Norm	$(1.412^{+2.47}_{-0.42}) \times 10^{-4}$	$(1.337^{+0.65}_{-0.43}) \times 10^{-4}$	$(8.742^{+6.42}_{-4.29}) \times 10^{-5}$
χ^2_ν (NDF)		0.81 (37)	0.45 (37)	0.63 (38)

evidence for flaring activity at X-ray wavelengths. Simultaneous γ-ray observations were obtained corresponding to the second *RXTE* exposure, which showed no indications of X-ray variability. Although the source began to show increased X-ray activity during the third *RXTE* observation, the degree of overlap with the corresponding H.E.S.S. observations was minimal. At non-γ-ray energies V4641 Sgr exhibits rapid variability on timescales of minutes or less. Consequently, despite the compelling evidence for mild broadband flaring close to the H.E.S.S. observation epochs, the failure to obtain strictly simultaneous X-ray and VHE γ-ray exposure probably restricts the utility of these data for inferring the detailed source properties which correspond to the γ-ray non-detection. Integral flux upper limits above the telescope threshold energy which correspond to the overall H.E.S.S. exposure at the position of V4641 Sgr are listed in Table 4.3.

4.6 The Results in Context

Currently, the high-mass black hole binary Cygnus X-1 remains the only confirmed microquasar to show any indication of VHE γ-ray emission [26]. A tentative $\sim 4\sigma$ detection was obtained using the MAGIC telescope during a 79 minute interval immediately preceding the peak of a hard X-ray flare observed by the *INTEGRAL* satellite [166], the *Swift* BAT and the *RXTE* ASM. Other observations bracketing the X-ray flare obtained no significant detections and yielded upper limits to the integral γ-ray flux above 150 GeV between 5 and 25 percent of the Crab nebula flux, indicating a highly transient episode of VHE γ-ray emission. The measured 0.1-1 TeV spectrum

Table 4.10: Estimated maximum VHE γ-ray luminosities of the target microquasars which would still be consistent with a non-detetction. Source distances correspond to the largest estimate that was found in the literature (see § 4.4).

Target	Maximum Distance Estimate [kpc]	$E_{\rm thresh}$ [GeV]	Luminosity above $E_{\rm thresh}$ [erg s^{-1}]
GRS 1915+105	12.5	380	2.05×10^{36}
Circinus X-1	11.8	423	2.33×10^{36}
V4641 Sgr	12.31	179	1.26×10^{37}

of Cyg X-1 is consistent with a soft power law ($dN/dE \propto E^{-\Gamma}$) with photon index $\Gamma \approx 3.2$ and the source was not detected above 1 TeV.

The principal aim of the study reported in this chapter was to obtain contemporaneous X-ray and VHE γ-ray observations of three known superluminal microquasars during major flaring events. Unfortunately, the results presented in §4.5 reveal no conclusive evidence that this goal was achieved and interpretation of the VHE γ-ray non-detections cannot proceed under the assumption of energetic flaring or bulk superluminal ejections at the time of observation. Nonetheless, upper limits to the VHE γ-ray flux have been derived and analysis of the contemporaneous *RXTE* observations has helped to reveal the X-ray behaviour corresponding to the H.E.S.S. observation epochs. A simple constraint permitted by the observational data relates to the γ-ray luminosity of the target binary systems. In Table 4.10 the calculated flux upper limits have been used to infer the *maximum* γ-ray luminosities above the telescope threshold energy for each target binary system by assuming the maximum source distance estimate discussed in §4.4.

Analysis of the contemporaneous X-ray observations conclusively places GRS 1915+105 in a radio loud plateau state at the time of observation. In contrast with the superluminal flaring episodes, this state is characterised by the production of continuous, mildly relativistic radio jets with an estimated power of $\sim 3 \times 10^{38}$ erg s^{-1} [150]. Theoretically, it seems unlikely that bright VHE γ-ray emission would be expected from the compact self-absorbed jets which are typical of the plateau state of GRS 1915+105. For example, a leptonic emission model developed by [46] to simulate the broadband emission of microquasar jets in the low/hard state predicts VHE γ-ray luminosities $\lesssim 10^{33}$ erg s^{-1} which are consistent with the H.E.S.S. non-detection. Notwithstanding

the plausibility of VHE γ-ray emission in the plateau state, comparison of the estimated jet power with the maximum γ-ray luminosity listed in Table 4.10, reveals that the jet power conversion efficiency is constrained to be $\lesssim 0.68\%$ for γ-ray production above 380 GeV.

Observations of Circinus X-1 were obtained during an extended dip in the X-ray flux, at phase intervals close to the periastron passage of the binary components. Spectral analysis of the *RXTE* data showed some evidence for a recent increase in mass transfer, producing strong signatures of X-ray absorption. It was hoped that H.E.S.S. observations would coincide with one of the pseudo-regular radio flares which often accompany periastron passage in Circinus X-1. Unfortunately, it seems likely that the H.E.S.S. observations were obtained during a period of unusually low flaring activity [242], and without strictly simultaneous radio data indicating otherwise, the most likely scenario is that no outflows were present. In this context the absence of a detectable γ-ray signal is not surprising. Indeed, the thermally dominated X-ray spectra give little indication for non-thermal acceleration which might produce the multi-TeV particle energies required for VHE γ-ray emission.

As a confirmed high-mass black hole candidate, V4641 Sgr is the studied target which most closely resembles Cygnus X-1. Moreover, the H.E.S.S. observations were obtained during a period of sporadic broadband flaring, and by analogy with the results of [26] VHE γ-ray emission might have been expected. However, no H.E.S.S. observations were obtained which unambiguously correspond to flaring episodes at other wavelengths. The MAGIC detection of Cyg X-1 appeared to coincide with the rising part of a strong X-ray flare. In contrast, radio spectra obtained close to the H.E.S.S. observational epochs are indicative of the *decay* following a flaring episode. Assuming that the γ-ray emission mechanisms operating in Cyg X-1 also occur in V4641 Sgr, the failure to obtain a significant H.E.S.S. detection might be viewed as evidence that production of GeV and TeV photons is a highly transient process. This would further suggest that γ-ray emission originates in a spatially compact region which is at most a few light hours in size.

Absorption of γ-rays by pair production is expected to be negligible in GRS 1915+105, since the donor star is too cool and faint to produce a strong ultraviolet photon field. The same is true of

Circinus X-1 if the conventional assumption of a low-mass companion is adopted. For completeness, Figure 4.8 plots the level of γ-ray absorption predicted by the numerical model outlined in §2.7.3, assuming that the companion star in Cir X-1 is indeed a mid-B supergiant as proposed by [142]. The separate curves are representative of the three orbital phase intervals corresponding to the H.E.S.S. observation epochs, and were derived using the system parameters derived by [142] in conjunction with typical values for the temperature ($T_{eff} \approx 20000$ K) and radius ($R \approx 9$ R$_{\odot}$) of a mid-B supergiant. It is evident that some non-negligible absorption is expected, particularly during the first observation interval. Nonetheless, it seems unlikely that the expected attenuation would suppress an otherwise detectable γ-ray flux sufficiently to yield the low significances listed in Table 4.2.

The situation with regard to γ-ray absorption is clearer in the case of V4641 Sgr, since the companion has been spectroscopically identified as a late B/early A-type star. Using the system parameters derived by [192] and assuming a circularised orbit, the numerical model described in §2.7.3 was used to predict the expected levels of γ-ray absorption as a function of orbital phase. As illustrated in Figure 4.8 (bottom panel), absorption might be an important effect during the first H.E.S.S. observation interval, although as with Circinus X-1 it is not likely that a bright γ-ray source would be attenuated so far below the detection threshold. During the second H.E.S.S. observation interval, when X-ray data show marginal indications of source activity, the predicted absorption due to pair production on the stellar radiation field is negligible.

X-ray binaries are dynamic systems and as such are likely to exhibit evolution of their radiative properties, both as a function of orbital phase and also in response to non-deterministic properties. It follows that the non-detections presented in this chapter do not indicate that the target binary systems do not emit detectable VHE γ-ray emission at phases other than those corresponding to the H.E.S.S. observations.

It should also be noted that all the confirmed γ-ray binaries lie at distances of $2 - 4$ kpc. In contrast, the targets studied in this chapter have maximum distances in the range $11 - 13$ kpc, resulting in flux dilution factors which are greater by factors of $\sim 10 - 30$. Obviously, this has

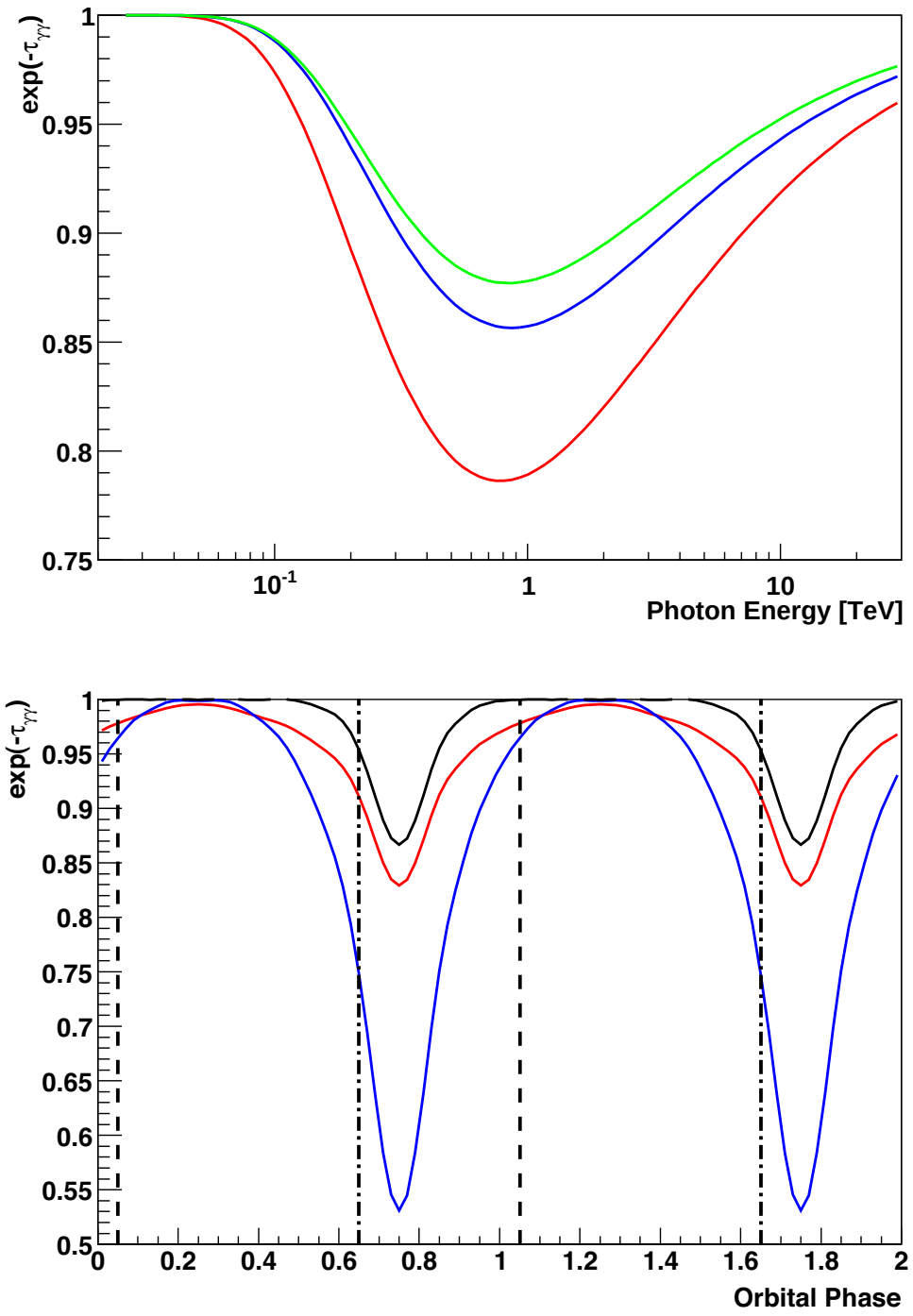

Figure 4.8: The levels of γ-ray absorption due to pair production with stellar photons as predicted by the numerical model described in §2.7.3. *Top panel:* Expected γ-ray transmission as a function of photon energy for Circinus X-1 assuming that the companion is a mid-B supergiant as proposed by [142]. The individual curves correspond to the orbital phases of the first (*red*), second (*blue*) and third (*green*) H.E.S.S. observation intervals. *Bottom panel:* Expected γ-ray transmission for V4641 Sgr as a function of orbital phase. The individual curves represent photon energies of 10 GeV (*black*), 1 TeV (*blue*) and 10 TeV (*red*). Vertical lines indicate the first (*dot-dashed*) and second (*dashed*) H.E.S.S. observation epochs.

strong implications for the detectability of any emitted γ-ray signal.

Finally, for future studies of this type it is worth commenting that X-ray data are not ideal discriminators of the outflow behaviour of microquasars. Unlike the blazar sub-class of AGN, for which both X-ray and VHE γ-ray emission likely originate in the relativistic jets [13, e.g.], the X-ray flux of microquasars is dominated by emission from the accretion flow and is therefore unlikely to correlate strongly with any GeV/TeV emission. Indeed, assuming that VHE γ-ray production is most likely to occur in relativistic outflows, then radio observations would offer an improved diagnostic of the relevant radiative environments. Radio measurements with high angular resolution are not essential, but would be useful to constrain the location of the radio (and presumably γ-ray) emitting material. Moreover, given the strongly variable behaviour exhibited by V4641 Sgr, it is not clear whether merely contemporaneous multi-wavelength observations are useful for constraining the radiative properties when the corresponding VHE γ-ray observations were obtained. It follows that wherever possible, strictly simultaneous observations should be obtained. Furthermore, there is circumstantial evidence from the results of [26] that VHE γ-ray emission from microquasars is highly transient and coincides with bright flares in observed broadband flux. Since prediction of violent flaring in microquasars is not normally possible, and serendipitous observation of an outburst during scheduled observations is unlikely, microquasars should be classified as targets of opportunity (ToOs) for IACTs, with observations triggered by flaring at longer wavelengths. Accordingly, pre-existing ToO agreements with the operators of optical, radio and X-ray observatories are likely to be essential if the desired simultaneity between multi-wavelength observations and the required rapid response times are to be achieved.

Chapter 5

A γ-ray Binary Survey

This chapter presents the results of a VHE γ-ray survey of known X-ray binaries. Fundamentally, the survey entailed point source γ-ray analysis of the nominal positions of all X-ray binary systems listed in the catalogues of [158] and [159] that fall within 1.5° of the pointing position of at least one H.E.S.S. observation. In total, this selection strategy yields a balanced working sample of 125 X-ray binaries comprising 64 HMXBs and 61 LMXBs. With the exception that no spectral analyses were performed, the techniques employed for each potential source position were identical to those discussed in Chapter 3.

5.1 Significances

The significance of the observed γ-ray signal was calculated for all targets and the results are presented in Table A.1. Results were derived using both of the background models and event selection strategies outlined in Chapter 3 and Figure 5.1 plots the significance distributions arising from the four possible combinations. At this point, it should be noted that in contrast with analyses presented in earlier chapters, none of the observations utilised for the survey were dedicated for the target in question. Instead, the runs are drawn from observations of known or suspected γ-ray sources, or from elements of the H.E.S.S. galactic plane scan [12]. A corollary of this fact is that many of the targeted binaries occupy fields-of-view which are subject to contamination by the

γ-ray sources which were being observed. As discussed in §3.5, crowded fields-of-view can present problems for both background models if exclusion regions limit the placement of OFF regions or overlap the ON region, leading to contamination of the on-source signal. In order to help identify results which may be affected in this way, targets which lie within a nominal exclusion region are marked in Tables A.1, A.2 and A.3 by a † symbol, while those within 0.5° of an exclusion region are identified by a ‡.

It is clear from Table A.1 and Figure 5.1, that the survey yielded no conclusive source detections. Indeed, any sources which appear to show a significant γ-ray signal are in fact subject to source confusion with known GeV/TeV emitters. When the contaminated targets are removed from the distributions in Figure 5.1, the histograms of the remaining target significances are reasonably well approximated by the $\mathcal{N}(0,1)$ Gaussian distribution expected from background fluctuations. A possible exception is the significance distribution which corresponds to the ring background model and hard cuts which appears to have a marginally significant bias towards positive significances. Indeed, both the distributions which correspond to the ring background model exhibit a higher mean and a larger spread towards positive significances than those derived using the reflected background model. As noted by [37], the ring background model is preferred for source searches since it is relatively unaffected by the position of the source within the field of view. Accordingly, the tendency towards higher significances indicated by the ring background may imply that the survey targets represent a population of weak γ-ray sources emitting below the detection threshold. In reality, the magnitude of the observed effect is not large enough to draw robust conclusions, especially given the small sample of non-confused targets and the observed bias is at best a tentative indication of underlying γ-ray emission.

5.2 Flux Upper Limits

Integral flux upper limits to the γ-ray flux above the telescope threshold E_{Thresh} are presented in Table A.2. As in Chapter 4, the upper limits were derived at the 99% confidence level using an

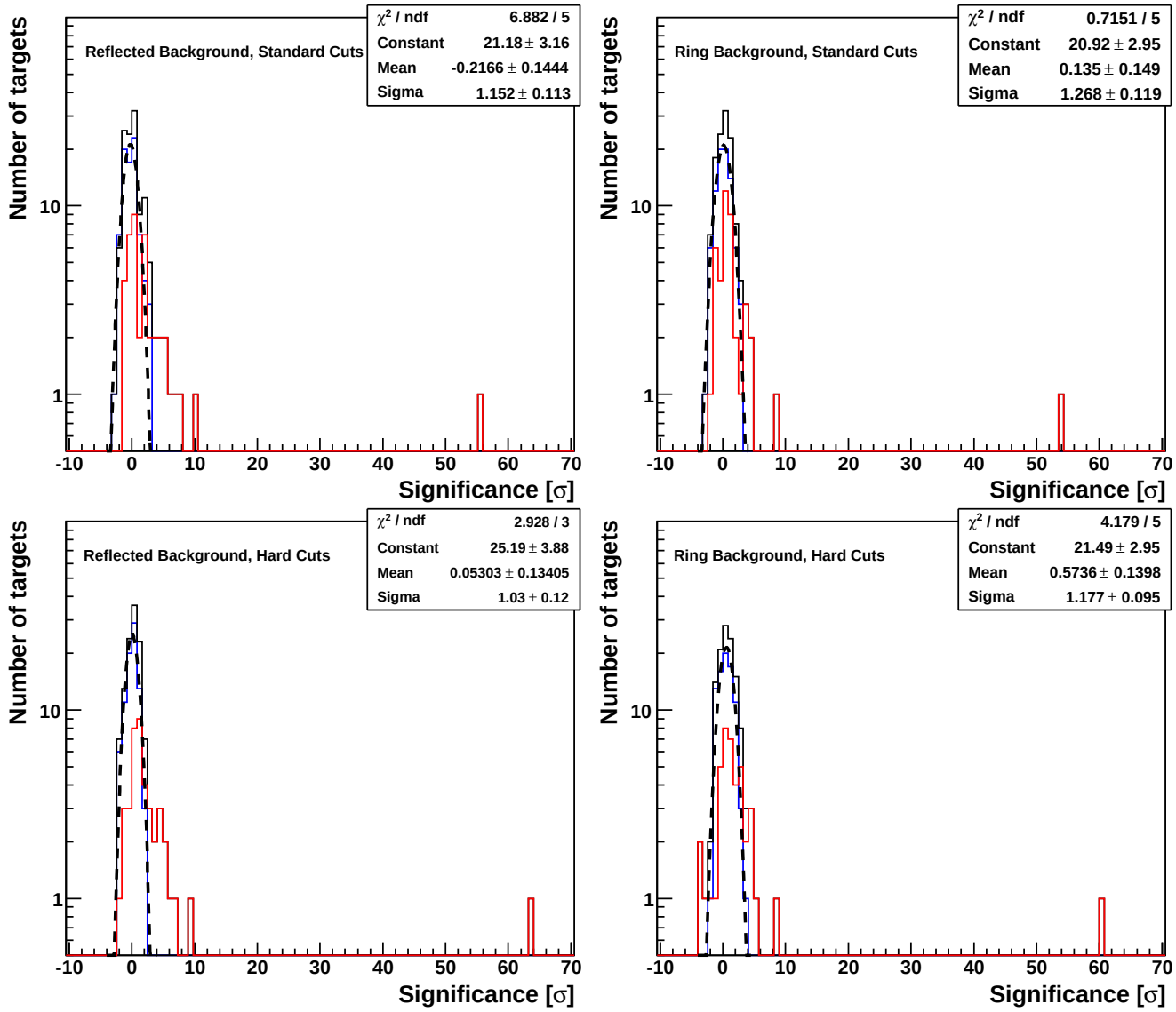

Figure 5.1: Distributions of the point source significance corresponding to the nominal position of all targets in the survey. Plots are shown which correspond to the four possible combinations of background model and event selection regime. The solid lines represent targets which are subject to source confusion (*red*), targets which are not subject to source confusion (*blue*) and all targets (*black*). The dashed line plots the Gaussian function which best describes the distribution of non-confused targets.

approach based on the Unified Feldman-Cousins method [92]. Where a target's on-source region is contaminated by a significant γ-ray signal, a flux with errors given by the 99% confidence interval is listed. Using a slightly more relaxed run selection criterion than was described in §3.9, only runs having $E_{\rm Thresh} \leq 2$ TeV were used in the upper limit calculations.

5.3 Temporal analyses

As outlined in §3.10, variability is a prominent characteristic of known γ-ray binaries. Indeed, even in the absence of a significant γ-ray signal, the presence of variability in excess of that expected due to background fluctuations can hint at the presence of a γ-ray source and further investigation using dedicated observations may then be recommended.

Where possible, the time series analysis techniques used to investigate the variability of LS 5039 in Chapter 3 were applied to the survey targets. Lightcurves were created using all runs having $E_{\rm thresh} < 1$ TeV and $1500 \leq T_{\rm live}[s] \leq 2400$. After this filtering, tests for secular and excess variability were carried out if the relevant lightcurves comprised more than three runs, and periodicity analysis using the error weighted, floating mean Lomb-Scargle periodogram (See §3.10.3) was applied for targets with more than 20 runs. If a target exhibits periodic behaviour at lower energies with frequency $f_{\rm known} = 1/P_{\rm known} > 2$ days^{-1}, then the periodogram was calculated for frequencies up to $2f_{\rm known}$. Otherwise frequencies up to 2 days^{-1} were tested. All resultant periodograms were visually inspected for obvious peaks and none were observed. As discussed in Chapter 3, proper statistical interpretation of the periodogram requires estimation of the effective number of trial frequencies N. In §3.10.3.5 computationally expensive Monte-Carlo simulations were used to derive an estimate for N. Clearly it is not practical to perform these simulations for all the targets with lightcurves containing more than 20 runs. Instead, N was estimated using the conservative prescription suggested by [225]:

$$N = \min(n_{\rm obs}, n_f, \Delta T \Delta f) \tag{5.1}$$

where $n_{\rm obs}$ and ΔT are respectively the number of data points and the overall sampling interval corresponding to the input lightcurve, n_f is the number of points in the Lomb-Scargle spectrum and Δf is the range of tested frequencies. Using values of N calculated in this manner, no peak false alarm probabilities less than 10^{-2} were derived, which is consistent with the absence of periodicities in the γ-ray signals associated with the survey targets.

The results of the temporal analyses are listed in Table A.3. No compelling evidence was found for secular or excess variability from any of the target binaries.

5.4 Stacking Analyses

A stacking analysis involves combining the observed γ-ray signal from a suspected population of individually undetected γ-ray sources. If the targets are genuinely emitting a γ-ray flux below the detection threshold, then by superposition their on-source fluxes will reinforce to produce a detectable signal. Conversely, if the observed counts are due to background fluctuations, then the calculated significance will average to zero over time yielding a non-detection for the postulated source population.

Table 5.4 lists the significances derived from a stacking analysis for all targets in the survey which are not subject to source confusion. As usual, results were derived for both the ring and reflected background models, and using both hard and standard event selection cuts. Furthermore, the survey sample is subdivided into populations of high and low mass X-ray binaries, allowing comparison between the two variants. It should be noted that although the stacking analysis involves the combination of data from several source positions, this does *not* increase the number of independent trials associated with the derived significances. Indeed, each of the significances listed in Table 5.4 effectively correspond to a *single* trial because for each source variant, the overall *ensemble* of tested source positions is fixed *a priori*.

Interestingly, the pattern observed in §5.1 appears to be replicated in the results of the stacking analysis. Namely, the stacked significances corresponding to the ring background model are no-

Table 5.1: The results of the stacking analysis performed for all non-confused targets in the survey. Targets were segregated into high- and low-mass binary systems and results are presented which correspond to the four possible combinations of background model and event selection regime.

Binary Variant	Background Model	Event Cuts	Nº of Targets	Stacked Significance [σ]
Low Mass	Reflected	Standard	37	-1.15
	Reflected	Hard	37	2.09
	Ring	Standard	37	0.80
	Ring	Hard	37	4.02
High Mass	Reflected	Standard	44	2.01
	Reflected	Hard	44	3.26
	Ring	Standard	44	1.82
	Ring	Hard	44	5.94

ticeably higher than those resulting from application of the reflected background model. Moreover, there is a clear indication that event selection using the hard cuts results in larger stacked significances relative to those obtained using the standard cuts. This might be interpreted as evidence for an underlying population of spectrally hard γ-ray sources, which is interesting in view of the fact that the known γ-ray binaries such as LS 5039 exhibit hard spectra in their high flux states.

The highest stacked significance of 5.94σ was obtained for the *high-mass* binary population using the ring background and hard cuts. Indeed, the stacked significances associated with the high-mass targets are generally larger than those which correspond to the low-mass systems. Although the evidence is purely circumstantial, this result fits well with the fact that all known γ-ray binary systems have high mass companions.

5.4.1 Reliability of the Stacking Analysis Results

Validation of the results listed in Table 5.4 first requires verification that that the stacking process yields significances which follow the expected $\mathcal{N}(0,1)$ distribution when observed signal level is due to background fluctuations. Emulating the approach of [156], the measured number OFF counts $N^j_{\mathrm{OFF,m}}$ was used in combination with the corresponding ON-OFF normalisation α^j_{m} to generate 10^5 paired Monte Carlo realisations of the number of ON and OFF counts for each of the N targets which were consistent with the null hypothesis. Specifically, each realisation was generated

according to

$$N^j_{\mathrm{OFF,s}} = \mathrm{Pois}(N^j_{\mathrm{OFF,m}}) \quad j = 1 \ldots N \tag{5.2}$$

$$N^j_{\mathrm{ON,s}} = \mathrm{Pois}(\alpha^j_{\mathrm{m}} N^j_{\mathrm{OFF,m}}) \quad j = 1 \ldots N \tag{5.3}$$

where $\mathrm{Pois}(\lambda)$ is a randomly sampled value from a Poisson distribution with expectation λ. Figures 5.2 and 5.3 plot the resultant distributions of the total numbers of ON and OFF counts:

$$N_{\mathrm{ON/OFF,s}} = \sum_{j=1}^{N} N^j_{\mathrm{ON/OFF,s}} \tag{5.4}$$

for the LMXB and HMXB populations respectively. Gaussian fits to each distribution yield the variances $\sigma_{N_{\mathrm{ON/OFF,s}}}$ listed in Table 5.2, which approximately equal the square root of the distribution means $\bar{N}_{\mathrm{ON/OFF,s}}$. This property of the generated distributions is consistent with the expectation for large random samples drawn from a Poisson-distributed population. Stacking analyses were performed for each Monte Carlo realisation of the ensemble datasets for both binary variants. The left-most columns of Figures 5.2 and 5.3 illustrate that histograms of resultant significances accurately reproduce the $\mathcal{N}(0,1)$ distribution. Accordingly, in the absence of systematic uncertainties, the results listed in Table 5.4 may be reliably interpreted within the framework of Gaussian statistics.

The results presented in Figures 5.2 and 5.3 were derived under the implicit assumption that the individual values of α_{m} are free from systematic biases. Moreover, approximate fulfilment of this condition by the values of α^j_{m} calculated *for each target* does not guarantee accuracy of the

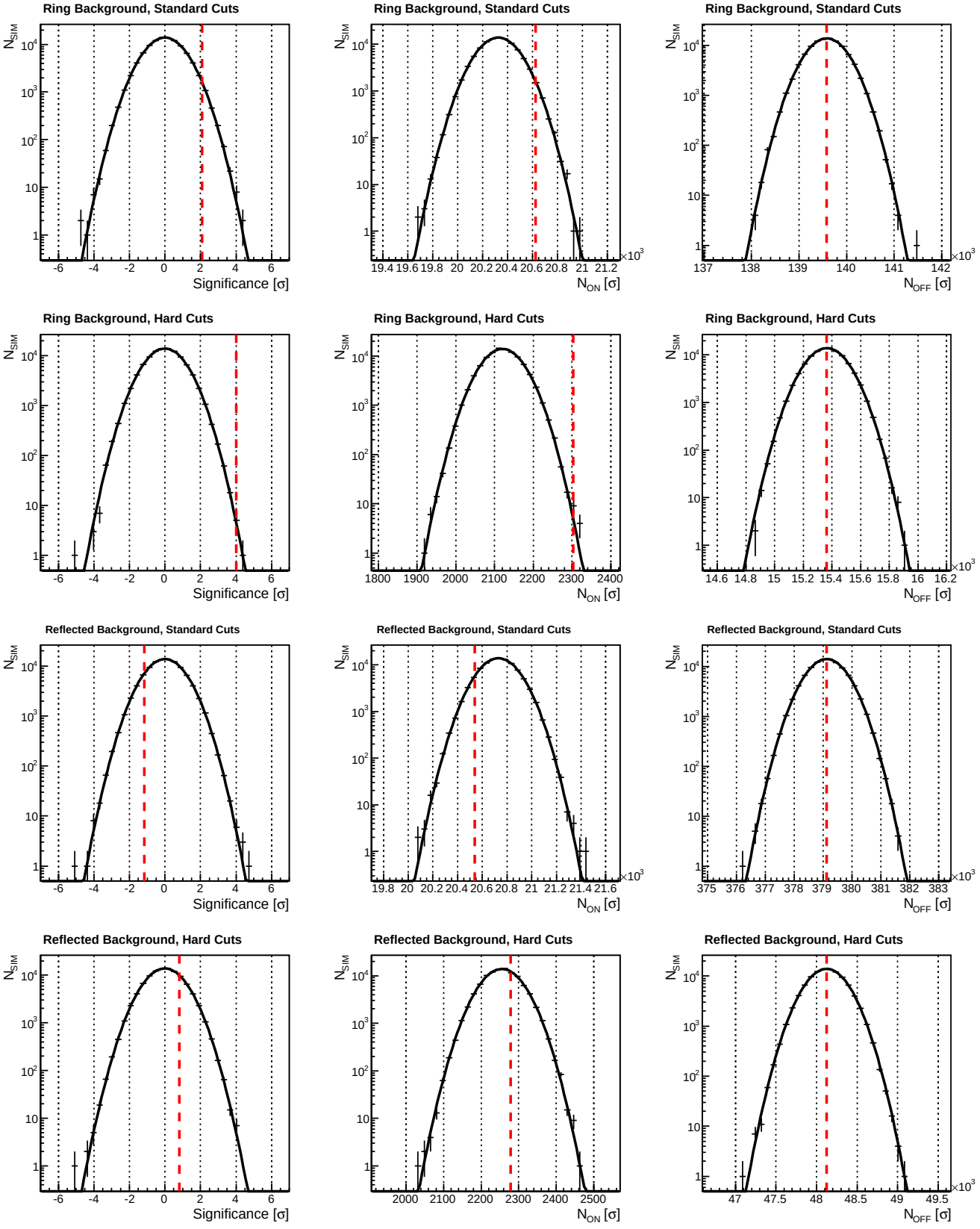

Figure 5.2: Monte Carlo distributions of $N_{\mathrm{ON,s}}$, $N_{\mathrm{OFF,s}}$ and simulated stacked significance for the LMXB sample. Distributions are shown which correspond to the four possible combinations of background model and event selection regime. The solid black curves are the Gaussian functions which best describe each distribution. The red dashed lines indicate the values of S, $N_{\mathrm{ON,m}}$ and $N_{\mathrm{OFF,m}}$ obtained from the actual observations.

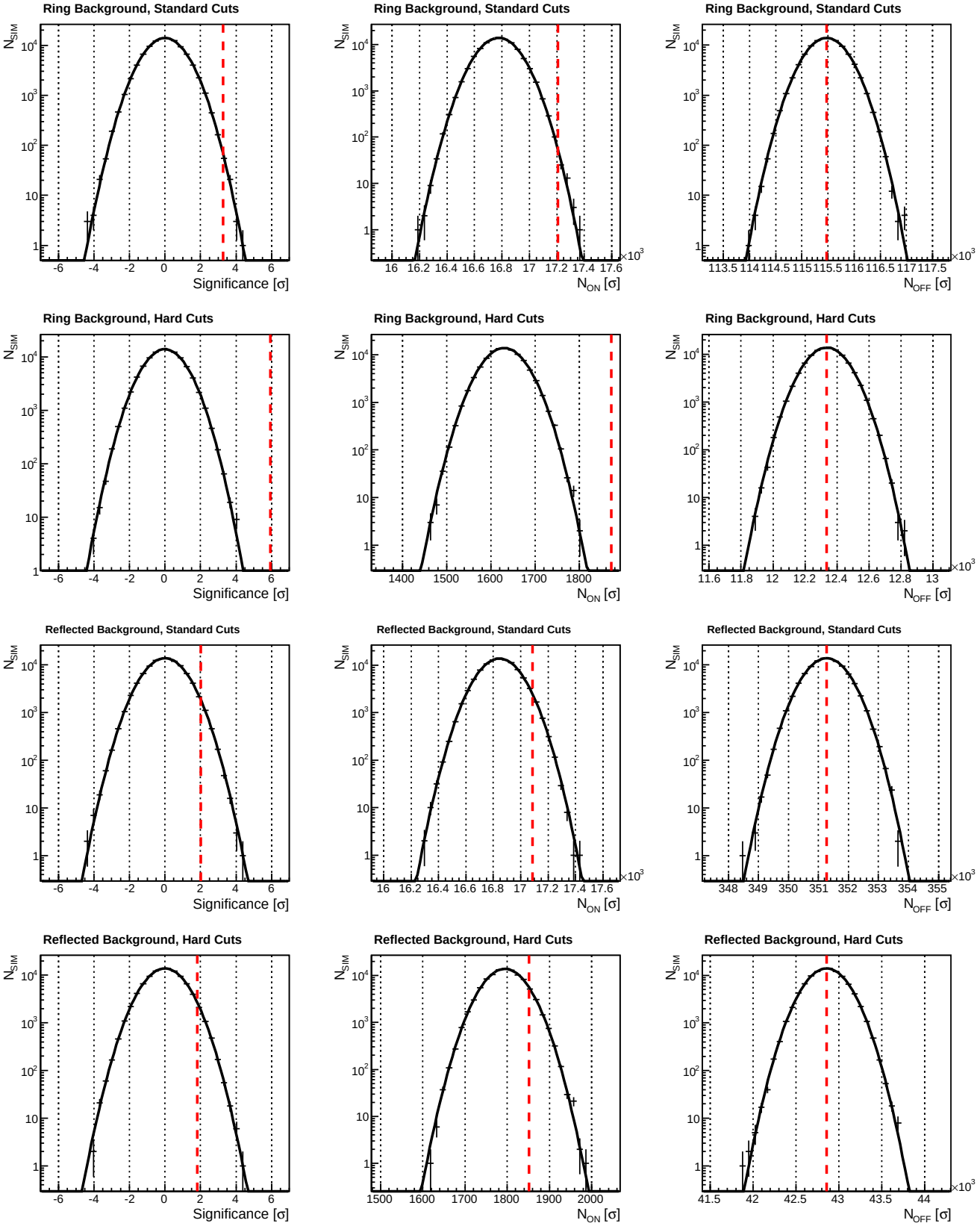

Figure 5.3: Monte Carlo distributions of $N_{\mathrm{ON,s}}$, $N_{\mathrm{OFF,s}}$ and simulated stacked significance for the HMXB sample. Distributions are shown which correspond to the four possible combinations of background model and event selection regime. The solid black curves are the Gaussian functions which best describe each distribution. The red dashed lines indicate the values of S, $N_{\mathrm{ON,m}}$ and $N_{\mathrm{OFF,m}}$ obtained from the actual observations.

Table 5.2: Statistical properties of Gaussian fits to the Monte Carlo distributions of S, $N_{\mathrm{ON,s}}$ and $N_{\mathrm{OFF,s}}$ for both the HMXB and LMXB samples.

Binary Variant	HMXB				LMXB			
Background	Reflected		Ring		Reflected		Ring	
Event Cuts	Hard	Standard	Hard	Standard	Hard	Standard	Hard	Standard
$\bar{S}$	-0.00428	-0.00257	-0.00459	0.00101	-0.000782	0.00193	0.000111	-0.00202
σ_S	1	1.01	1	1.01	1.01	1	1.01	1
$\chi^2_{\nu,S}$	0.52	1.12	1.16	1.4	1.66	0.906	0.961	0.814
$\bar{N}_{\mathrm{ON}}$	1794.5807	16844.24	1629.6686	16775.573	2255.5156	20731.026	2120.3796	20325.231
$\sqrt{\bar{N}_{\mathrm{ON}}}$	42.4	130	40.4	130	47.5	144	46	143
$\sigma_{N_{\mathrm{ON}}}$	42.5	130	40.4	130	47.6	144	46.1	143
$\chi^2_{\nu,N_{\mathrm{ON}}}$	5.22	1.94	4.04	1.62	4.87	1.72	4.34	1.1
$\bar{N}_{\mathrm{OFF}}$	42856.937	351269.33	12334.889	115473.97	48124.465	379123.59	15362.328	139580.66
$\sqrt{\bar{N}_{\mathrm{OFF}}}$	207	593	111	340	219	616	124	374
$\sigma_{N_{\mathrm{OFF}}}$	208	596	111	342	220	619	124	375
$\chi^2_{\nu,N_{\mathrm{OFF}}}$	1.1	0.743	1.35	1.08	1.75	0.757	1.19	1.21

effective $\alpha_{\rm m}$ of the entire ensemble. Using (3.5) and (5.4), the derivation of $\alpha_{\rm m}$ is straightforward.

$$\Delta = N_{\rm ON} - \alpha_{\rm m} N_{\rm OFF} = \sum_{j=1}^{N} N_{\rm ON}^{j} - \alpha_{\rm m} \sum_{j=1}^{N} N_{\rm OFF}^{j} = \sum_{j=1}^{N} N_{\rm ON}^{j} - \sum_{j=1}^{N} \alpha_{\rm m}^{j} N_{\rm OFF}^{j}$$

$$\Longrightarrow \alpha_{\rm m} = \frac{\sum_{j=1}^{N} \alpha_{\rm m}^{j} N_{\rm OFF}^{j}}{\sum_{j=1}^{N} N_{\rm OFF}^{j}} \tag{5.5}$$

It is evident from (5.5) that normally negligible systematic offsets associated with the values of $\alpha_{\rm m}^{j}$ are compounded by the summation and might significantly bias the calculated value of $\alpha_{\rm m}$ for the entire target ensemble.

Further simulations were employed to quantify the magnitude of a systematic offset associated with $\alpha_{\rm m}$ which would reproduce the observed stacked significances in the absence of a true γ-ray signal. Adopting the measured number of ON events for each target as a fixed datum, one may define $N_{\rm OFF,s}^{j}$ as a number of OFF counts which satisfies the null hypothesis given the number of *observed* ON counts and the calculated value of $\alpha_{\rm m}^{j}$ for each target.

$$\sum_{j=1}^{N} N_{\rm ON,m}^{j} = \alpha_{\rm m} \sum_{j=1}^{N} N_{\rm OFF,s}^{j} = \alpha_{\rm m} \sum_{j=1}^{N} {\rm Pois}\left(\frac{N_{\rm ON,m}^{j}}{\alpha_{\rm m}^{j}} \right) \tag{5.6}$$

Alternatively, one may define

$$\alpha_0 = \frac{\sum_{j=1}^{N} N_{\rm ON,m}^{j}}{\sum_{j=1}^{N} N_{\rm OFF,m}^{j}} \tag{5.7}$$

as the overall acceptance ratio which fulfils the null hypothesis for the entire target ensemble, given the total number of *observed* ON and OFF counts. Combining (5.6) by (5.7) yields the overall

systematic offset between $\alpha_{\rm m}$ and α_0

$$\Delta\alpha = \alpha_{\rm m} - \alpha_0 = \alpha_{\rm m}\left(1 - \frac{\alpha_0}{\alpha_{\rm m}}\right) = \alpha_{\rm m}\left(1 - \frac{\sum_{j=1}^{N} N^j_{\rm OFF,s}}{\sum_{j=1}^{N} N^j_{\rm OFF,m}}\right) = \alpha_{\rm m}\left(1 - \frac{N_{\rm OFF,s}}{N_{\rm OFF,m}}\right) \tag{5.8}$$

Figures 5.4 and 5.5 plot the distributions of $N_{\rm OFF,s}$, $\alpha_0/\alpha_{\rm m}$ and $\Delta\alpha/\alpha_m$ resulting from 10^5 independent Monte Carlo realisations for the LMXB and HMXB populations respectively. The left-hand panels compare the generated distributions of $N_{\rm OFF,s}$ with an analytical $\mathcal{N}(N_{\rm OFF,m}, \sqrt{N_{\rm OFF,m}})$ function which models the distribution of 10^5 samples drawn from a Poisson distribution with expectation $N_{\rm OFF,m}$. The degree of overlap between the Monte Carlo distributions and the model distribution of observed OFF counts indicates the likelihood that $N_{\rm OFF,m}$ is consistent with a statistical background fluctuation. Table 5.3 lists the salient statistical properties of the generated distributions. Once again, results which correspond to the ring background and hard cuts exhibit marked incompatibility with the absence of a true γ-ray signal. In particular, the measured number of OFF counts for the HMXB sample using the ring background and hard cuts is offset from the mean of the Monte Carlo distribution by over 15 standard deviations. Moreover, the stacking results for the HMXB and LMXB populations using the ring background model and hard event cuts require large overall normalisation offsets of $\Delta\alpha/\alpha_m \sim 10^{-1}$ to achieve compatibility with the null hypothesis. In contrast, the marginally significant (3.26σ) result obtained for the HMXB population using hard cuts and the reflected background model can be explained by a somewhat lower systematic bias of $\Delta\alpha/\alpha_m \sim 10^{-2}$.

In summary, the Monte Carlo results appear to disfavour a systematic origin for the high stacked significances, lending a measure of credibility to the apparent identification of X-ray binary systems as a population of faint VHE γ-ray sources. Nonetheless, further work is required before this result can be considered definitive. Indeed, all the results presented in this chapter should be subjected to independent cross-checks using alternative analysis chains. Moreover, improved quantification of systematic effects would be facilitated by repetition of the analysis using data which closely

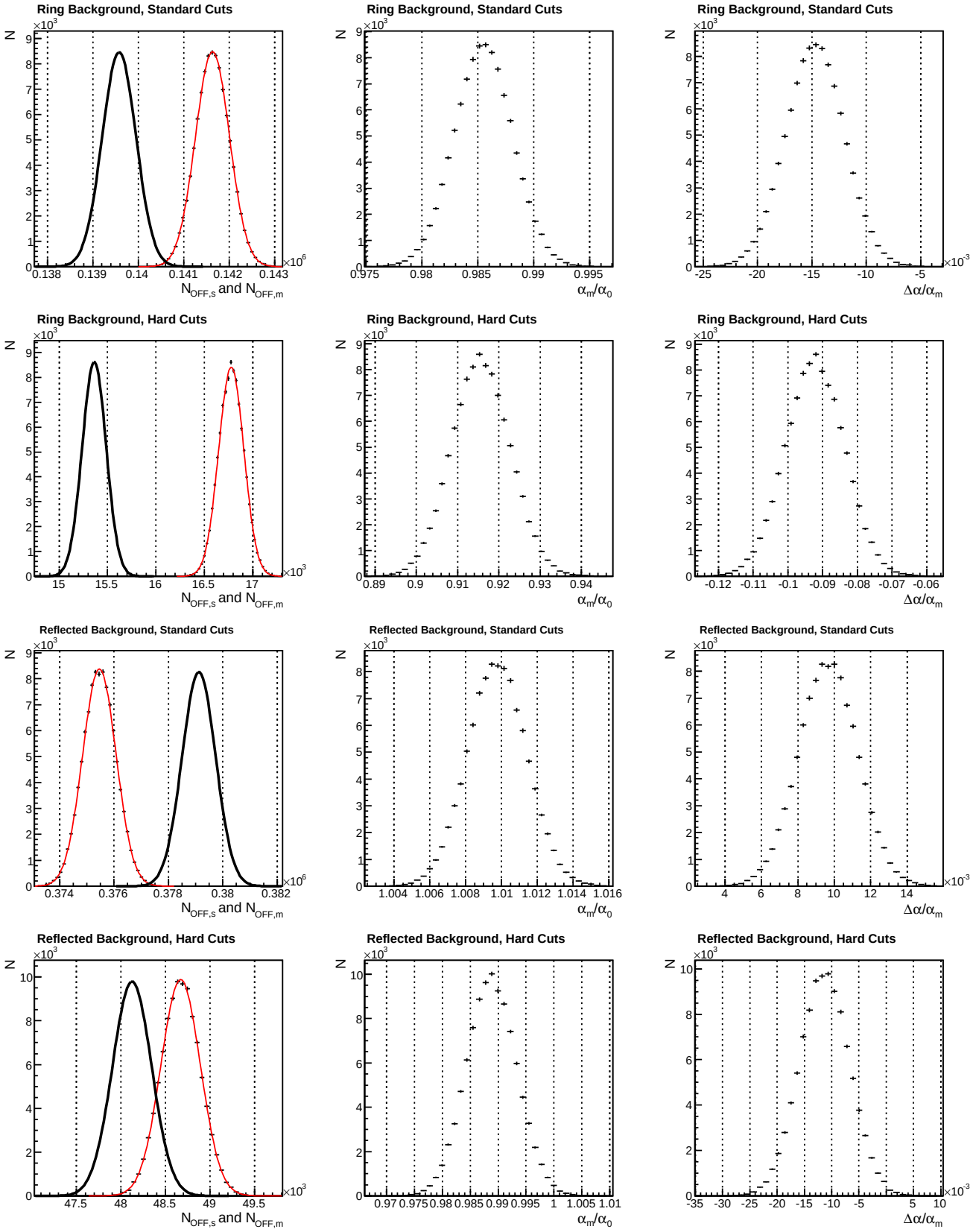

Figure 5.4: Monte Carlo distributions of $N_{\mathrm{OFF,s}}$ $\alpha_0/\alpha_{\mathrm{m}}$ and $\Delta\alpha/\alpha_{\mathrm{m}}$ for the LMXB sample which correspond to the four possible combinations of background model and event selection regime. The solid black curves are analytical $\mathcal{N}(N_{\mathrm{OFF,m}}, \sqrt{N_{\mathrm{OFF,m}}})$ functions which model the distribution of 10^5 samples drawn from a Poisson distribution with expectation $N_{\mathrm{OFF,m}}$. The red curves show the corresponding Monte Carlo distributions of $N_{\mathrm{OFF,s}}$.

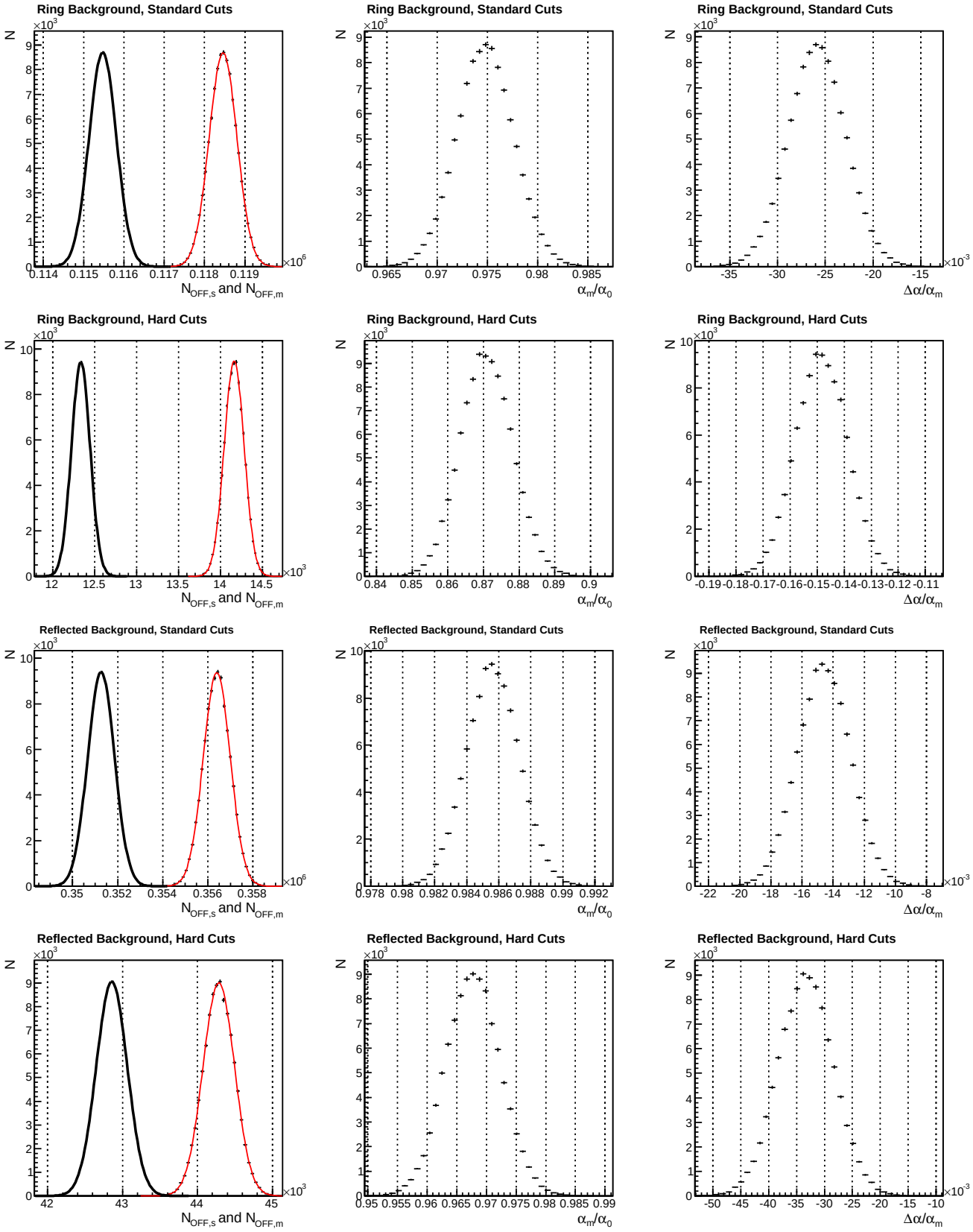

Figure 5.5: Monte Carlo distributions of $N_{\mathrm{OFF,s}}$ $\alpha_0/\alpha_\mathrm{m}$ and $\Delta\alpha/\alpha_\mathrm{m}$ for the HMXB sample which correspond to the four possible combinations of background model and event selection regime. The solid black curves are analytical $\mathcal{N}(N_{\mathrm{OFF,m}}, \sqrt{N_{\mathrm{OFF,m}}})$ functions which model the distribution of 10^5 samples drawn from a Poisson distribution with expectation $N_{\mathrm{OFF,m}}$. The red curves show the corresponding Monte Carlo distributions of $N_{\mathrm{OFF,s}}$.

Table 5.3: Statistical properties of Gaussian fits to the Monte Carlo distributions of $N_{\mathrm{OFF,s}}$ and $\Delta\alpha/\alpha_{\mathrm{m}}$ for both the HMXB and LMXB samples.

Binary Variant	HMXB				LMXB			
Background	Reflected		Ring		Reflected		Ring	
Event Cuts	Hard	Standard	Hard	Standard	Hard	Standard	Hard	Standard
$N_{\mathrm{OFF,s}}$	44285.4	356391	14165.6	118459	48669.1	375457	16779.4	141636
$\sqrt{\bar{N}_{\mathrm{OFF,s}}}$	210.441	596.985	119.019	344.178	220.611	612.746	129.535	376.345
$N_{\mathrm{OFF,m}}$	42857	351270	12335	115474	48124	379121	15362	139580
$\sqrt{N_{\mathrm{OFF,m}}}$	207.019	592.68	111.063	339.815	219.372	615.728	123.944	373.604
$\frac{\bar{N}_{\mathrm{OFF,s}}-N_{\mathrm{OFF,m}}}{\sqrt{\bar{N}_{\mathrm{OFF,s}}}}$	6.78754	8.57767	15.3803	8.67154	2.47074	-5.97884	10.9424	5.46194
$\frac{\bar{N}_{\mathrm{OFF,s}}-N_{\mathrm{OFF,m}}}{T_{\mathrm{live}}}$ [h^{-1}]	2.73845	9.58581	3.47419	5.55162	0.939132	-6.18314	2.41634	3.45475
$N_{\mathrm{OFF,m}}/T_{\mathrm{live}}$ [h^{-1}]	82.1645	657.563	23.4105	214.795	82.9152	639.867	26.1882	234.588
$\overline{\Delta\alpha}/\alpha_{\mathrm{m}}$	-0.0333	-0.0146	-0.1484	-0.0258	-0.0113	0.0096	-0.0922	-0.0147
T_{live} [h]	521.6	534.2	526.9	537.6	580.4	592.5	586.6	595

replicate the live times, zenith angles, offsets, and ambient night sky backgrounds of the XRB survey analysis, but using ON regions which contain no known or putative γ-ray sources. Such a sample should implicitly fulfil the null hypothesis, and if similar large stacked significances were derived, then this would be a clear indication of systematic effects dominating the results.

Evidently, some disparity exists between results obtained using different strategies for background estimation. The data set employed in the XRB survey consists exclusively of runs which were not dedicated observations of the target binaries, which has important implications for the reliability of each background model. As noted by [37] and outlined in §3.5.2, the reflected background model is specifically designed for the analysis of data obtained using the dedicated wobble-mode runs described in §3.2.1. However, if the target offset from the camera centre varies between runs, then linear gradients in the system acceptance along the direction of zenith angle are not properly accounted for and systematic biases may be introduced. In contrast, the ring background is well suited for non-spectral, point source analyses at arbitrary positions within the field of view, since it explicitly calculates the relative acceptance correction within a limited area surrounding the source position [37]. Accordingly, the nature of the survey data set implies that the ring background should yield the most reliable results, lending additional credence to the high stacked significances derived using this model.

Bright ($M_B > 7$) stars in the telescope field-of-view constitute another well known source of systematic error for IACT observations [37]. As mentioned in §3.2.2, camera pixels which correspond to the positions of bright stars are automatically deactivated during observations in order to prevent undue degradation of the PMTs. This leads to a measurable decrease in the detector acceptance close to the stellar position because the removal of pixels from faint or compact Cherenkov images can cause valid γ-raylike events to be discarded during the image cleaning process or to fail selection cuts. Accordingly bright stars which coincide with the *background* regions might artificially enhance the observed significance. As outlined in §3.5.3, the standard H.E.S.S. analysis defines background exclusion regions at the positions of bright stars, which should ameliorate this effect. Nonetheless, imperfections in this background exclusion strategy might

accumulate over many observation runs to produce a measurable systematic bias, and further investigation of this possibility is advisable.

Optical photons from the donor star might also bias the observed *on-source* signal. The additional night sky background noise produced by the stellar companion might artificially enhance the system acceptance in the ON region by adding photons to images which would otherwise be discarded by image cleaning or fail event selection cuts. This phenomenon might explain the relatively large significances derived for HMXB systems within the survey because high mass companion stars are more luminous than low mass ones. However, inhomogenous optical obscuration of the target systems is likely to distort or eliminate this effect. Indeed, absorption of the optical flux renders conclusive identification of an optical counterpart impossible for many of the surveyed systems [158, 159].

5.5 Summary

The VHE γ-ray signals corresponding to the positions of 125 X-ray binary systems have been analysed. Targets within 0.5° of the exclusion regions corresponding to known γ-ray sources were identified and were considered as subject to potential source confusion in subsequent analyses.

The γ-ray significance of each target was evaluated using the four possible combinations of the ring and reflected background models, and the standard and hard event selection cut. No individual targets were conclusively detected, although the overall distribution of target significances obtained using the ring background and hard cuts showed a tentative indication of a population-wide bias towards positive significances. Upper limits to the VHE γ-ray flux above the telescope threshold were derived for all targets.

Temporal analyses similar to those described in §3.10 were applied to all targets for which three or more runs with corresponding energy thresholds below 1 TeV were available. No evidence was found for secular, excess or periodic variability associated with any of the survey targets.

A stacking analysis was performed with the aim of identifying an underlying population of

faint but undetected γ-ray sources. The survey targets were segregated into high- and low-mass binary systems, and separate analyses were performed for each sub-sample. Monte Carlo studies were conducted to quantify the magnitude of systematic effects which could produce the observed results in the absence of a true γ-ray signal. It was revealed that a large systematic offset is required to reproduce the stacked significance derived for the HMXB sample using the ring background hard cuts. Although inconclusive, the results appear to favour a population of spectrally hard sources with an apparent indication of stronger γ-ray emission from the high-mass binary population. These characteristics would be consistent with the properties of known γ-ray binaries, all of which are HMXBs which exhibit hard γ-ray spectra.

Although no conclusive evidence was found for VHE γ-ray emission from any of the individual survey targets, there were some tentative indications that HMXBs may represent a faint, population of spectrally hard γ-ray sources. Additional observations, perhaps in conjunction with low energy coverage provided by the *Fermi* satellite, may help to reinforce or refute these indications.

Chapter 6

Future Directions

With only three confirmed examples, γ-ray binaries represent a rarified class of astrophysical object. Indeed, the numerous non-detections in this thesis appear to indicate that bright VHE γ-ray emission is not a common characteristic of X-ray binary systems. Nonetheless, the resultant scarcity of available data does not detract from the challenges associated with its interpretation. For example, while it might be tempting to assume that γ-ray production employs the same physical mechanisms in all three of the known γ-ray binaries [e.g. 85], the currently available data cannot confirm this hypothesis. In particular, the seemingly insurmountable uncertainty regarding the classifications of the compact objects in LS I $+61°303$ and LS 5039 significantly limits the power of observational data to constrain their individual radiative properties. Consequently, while further observations at multiple wavelengths may begin to disentangle the complex radiative processes operating within the known γ-ray binaries, it seems likely that obtaining conclusive answers will be problematic without a larger catalogue of example sources.

The next generation of ground-based Cherenkov telescopes may be useful in this respect. Upcoming instruments such as H.E.S.S. II, MAGIC II and ultimately, the Cherenkov Telescope Array (CTA) promise improved flux sensitivity and lower energy thresholds relative to the current generation of ground-based detectors. In combination with overlapping low energy γ-ray coverage provided by the *Fermi* satellite, the new telescopes are likely to prove invaluable for identifying

new γ-ray binaries and refining the observational characteristics of previously detected systems. Indeed, if there is any substance to the tentative indications presented in Chapter 5, then the enhanced capabilities of the new telescopes may reveal a faint population of previously undetectable γ-ray binary systems. These objects might be more distant counterparts of the known γ-ray binaries, or they could represent a distinct class of systems with an intrinsically lower γ-ray luminosity.

The three known γ-ray binaries appear to exhibit emission which is modulated in phase with the binary period. In contrast, the tentative detection of VHE γ-rays from Cygnus X-1 may be indicative of a separate class of binary systems which are transient, non-periodic γ-ray sources. Moreover, the results of [26] suggest that these sources may only produce detectable VHE γ-ray emission during bright broadband flaring episodes. As illustrated in Chapter 4, accurate prediction of flaring in X-ray binary systems is extremely difficult. Indeed, even if a flare is correctly anticipated, simultaneous Cherenkov telescope observations are often frustrated by the requirement for complete darkness and the vagaries of the weather. Nonetheless, further detections of flaring X-ray binaries are essential, not only for corroboration of the MAGIC detection, but also to constrain the radiative mechanisms responsible for the observed emission. To this end, the H.E.S.S. Collaboration has identified several likely binary systems, including the three systems discussed in Chapter 4, as *targets of opportunity* and will attempt to observe flares of these X-ray binaries whenever practical.

Finally, recent H.E.S.S. observations close to the Monoceros Loop supernova remnant led to the serendipitous discovery of a point-like γ-ray excess, HESS J0632+057. Subsequent observations with the *XMM-Newton* X-ray satellite revealed characteristics which are strongly reminiscent of LS I $+61°303$ [125]. Recent radio observations reveal significant flux variability on timescales of approximately one month [230]. Consequently, it appears increasingly likely that HESS J0632+057 will soon become the fourth confirmed γ-ray binary.

Appendix A

Data tables for the survey

Table A.1: Table showing the overall values of N_{ON}, N_{OFF}, α, and significance corresponding to the nominal positions of all targets in the survey.

Target	RA [°]	Dec [°]	Background	Cuts	N_{ON}	N_{OFF}	α	Significance [σ]
RX J0532.7-6926	83.18	-69.44	Reflected	Hard	19	335	0.057	-0.02
			Reflected	Standard	199	3122	0.069	-1.04
			Ring	Hard	19	152	0.132	-0.22
			Ring	Standard	199	1464	0.144	-0.74
1A 0535+262	84.73	26.32	Reflected	Hard	1	88	0.029	-1.08
			Reflected	Standard	18	797	0.032	-1.59
			Ring	Hard	1	21	0.130	-1.15
			Ring	Standard	18	188	0.142	-1.68
SAX J0635.2+0533	98.83	5.55	Reflected	Hard	52	991	0.051	0.23
			Reflected	Standard	530	9039	0.058	0.10
			Ring	Hard	52	359	0.131	0.66
			Ring	Standard	530	3556	0.143	0.87
4U 0900-40	135.53	-40.55	Reflected	Hard	17	332	0.054	-0.19
			Reflected	Standard	181	2906	0.061	0.22
			Ring	Hard	17	120	0.131	0.30
			Ring	Standard	181	1190	0.143	0.74
GRO J1008-57	152.45	-58.29	Reflected	Hard	13	412	0.035	-0.39
			Reflected	Standard	163	3865	0.042	0.04
			Ring	Hard	14	133	0.130	-0.78
			Ring	Standard	163	1156	0.145	-0.30
RX J1037.5-5647	159.40	-56.80	Reflected	Hard	6	219	0.023	0.43
			Reflected	Standard	38	1922	0.026	-1.70
			Ring	Hard	6	33	0.127	0.77
			Ring	Standard	38	277	0.145	-0.31
1A 1118-615	170.24	-61.92	Reflected	Hard	9	373	0.030	-0.65
			Reflected	Standard	109	3142	0.034	0.29
			Ring	Hard	9	77	0.132	-0.36
			Ring	Standard	109	782	0.144	-0.33
4U 1119-603	170.31	-60.62	Reflected	Hard	23	465	0.044	0.50
			Reflected	Standard	181	3697	0.049	-0.07

Target	RA [°]	Dec [°]	Background	Cuts	N_{ON}	N_{OFF}	α	Significance [σ]
			Ring	Hard	23	147	0.130	0.79
			Ring	Standard	181	1222	0.144	0.39
IGR J11215-5952	170.45	-59.86	Reflected	Hard	13	352	0.039	-0.18
			Reflected	Standard	128	3089	0.041	0.18
			Ring	Hard	14	101	0.131	0.19
			Ring	Standard	149	1030	0.144	0.06
4U 1223-624	186.66	-62.77	Reflected	Hard	14	370	0.036	0.22
			Reflected	Standard	137	3424	0.040	0.15
			Ring	Hard	14	83	0.128	0.91
			Ring	Standard	137	968	0.144	-0.16
IGR J12349-6434	188.73	-64.57	Reflected	Hard	6	113	0.029	1.32
			Reflected	Standard	46	1027	0.033	1.94
			Ring	Hard	6	25	0.125	1.33
			Ring	Standard	46	241	0.143	1.73
1H 1249-637	190.71	-63.06	Reflected	Hard	21	356	0.036	2.03
			Reflected	Standard	163	3208	0.041	2.61
			Ring	Hard	21	96	0.130	2.05
			Ring	Standard	163	873	0.144	2.95
4U 1258-61	195.32	-61.60	Reflected	Hard	10	195	0.041	0.63
			Reflected	Standard	67	1721	0.045	-1.15
			Ring	Hard	10	54	0.131	0.96
			Ring	Standard	67	484	0.144	-0.31
2RXP J130159.6-635806[†]	195.49	-63.97	Reflected	Hard	275	3275	0.069	3.04
			Reflected	Standard	2440	27200	0.080	5.60
			Ring	Hard	276	1634	0.132	3.71
			Ring	Standard	2440	15284	0.143	4.86
SAX J1324.4-6200	201.11	-62.01	Reflected	Hard	7	184	0.035	0.24
			Reflected	Standard	60	1654	0.047	-2.00
			Ring	Hard	7	52	0.127	0.15
			Ring	Standard	60	518	0.145	-1.69
4U 1323-62	201.65	-62.14	Reflected	Hard	11	239	0.037	0.67
			Reflected	Standard	90	2101	0.043	-0.05
			Ring	Hard	11	71	0.129	0.54
			Ring	Standard	90	573	0.145	0.72
1H 1348-633[‡]	209.54	-64.73	Reflected	Hard	2	99	0.068	-2.11
			Reflected	Standard	71	953	0.076	-0.17
			Ring	Hard	2	51	0.133	-2.07
			Ring	Standard	71	476	0.146	0.15
2S 1417-624	215.30	-62.70	Reflected	Hard	26	583	0.034	1.29
			Reflected	Standard	218	4972	0.039	1.75
			Ring	Hard	26	134	0.153	1.07
			Ring	Standard	218	1430	0.145	0.72
SAX J1452.8-5949	223.21	-59.82	Reflected	Hard	26	358	0.080	-0.50
			Reflected	Standard	243	3004	0.088	-1.30
			Ring	Hard	28	215	0.133	-0.11
			Ring	Standard	250	1878	0.145	-1.28
3A 1516-569	230.17	-57.17	Reflected	Hard	61	1040	0.057	0.20
			Reflected	Standard	551	8977	0.063	-0.77
			Ring	Hard	65	433	0.130	1.06
			Ring	Standard	551	3916	0.143	-0.42
4U 1538-52	235.60	-52.39	Reflected	Hard	26	477	0.047	0.74
			Reflected	Standard	190	3747	0.053	-0.61
			Ring	Hard	26	172	0.131	0.68
			Ring	Standard	190	1317	0.143	0.07

Target	RA [°]	Dec [°]	Background	Cuts	N_{ON}	N_{OFF}	α	Significance [σ]
XTE J1543-568	236.00	-56.77	Reflected	Hard	4	193	0.035	-1.12
			Reflected	Standard	44	1296	0.037	-0.66
			Ring	Hard	4	42	0.130	-0.63
			Ring	Standard	57	447	0.144	-0.88
XTE J1550-564	237.74	-56.48	Reflected	Hard	1	161	0.028	-2.01
			Reflected	Standard	27	1145	0.032	-1.71
			Ring	Hard	1	28	0.129	-1.57
			Ring	Standard	27	262	0.146	-1.80
1H 1555-552	238.59	-55.33	Reflected	Hard	7	200	0.041	-0.40
			Reflected	Standard	77	1724	0.046	-0.24
			Ring	Hard	7	57	0.130	-0.14
			Ring	Standard	77	553	0.144	-0.30
2S 1553-542	239.45	-54.41	Reflected	Hard	6	169	0.043	-0.49
			Reflected	Standard	86	1648	0.051	0.29
			Ring	Hard	8	77	0.127	-0.56
			Ring	Standard	86	613	0.143	-0.15
4U 1608-52‡	243.18	-52.42	Reflected	Hard	24	693	0.042	-0.94
			Reflected	Standard	255	5653	0.046	-0.28
			Ring	Hard	24	238	0.130	-1.22
			Ring	Standard	255	1905	0.146	-1.35
IGR J16195-4945‡	244.87	-49.76	Reflected	Hard	35	829	0.045	-0.32
			Reflected	Standard	319	6448	0.051	-0.61
			Ring	Hard	35	250	0.131	0.36
			Ring	Standard	319	2171	0.145	0.24
H 1617-155	244.98	-15.64	Reflected	Hard	9	191	0.054	-0.40
			Reflected	Standard	100	1758	0.062	-0.81
			Ring	Hard	9	68	0.131	0.02
			Ring	Standard	100	736	0.143	-0.48
4U 1624-49‡	247.01	-49.19	Reflected	Hard	49	768	0.051	1.43
			Reflected	Standard	338	5351	0.057	1.72
			Ring	Hard	49	296	0.132	1.45
			Ring	Standard	354	2244	0.144	1.57
IGR J16283-4838‡	247.04	-48.65	Reflected	Hard	41	851	0.046	0.28
			Reflected	Standard	351	6061	0.051	2.16
			Ring	Hard	41	303	0.131	0.20
			Ring	Standard	351	2334	0.144	0.74
IGR J16318-4848	247.95	-48.82	Reflected	Hard	36	883	0.049	-1.07
			Reflected	Standard	384	6718	0.053	1.40
			Ring	Hard	36	322	0.132	-0.95
			Ring	Standard	384	2579	0.145	0.49
IGR J16320-4751†	248.01	-47.87	Reflected	Hard	81	1031	0.039	5.45
			Reflected	Standard	435	7972	0.043	4.51
			Ring	Hard	85	378	0.132	4.17
			Ring	Standard	463	2655	0.146	3.50
4U 1630-47†	248.50	-47.39	Reflected	Hard	68	821	0.048	4.03
			Reflected	Standard	362	6165	0.052	2.29
			Ring	Hard	68	351	0.135	2.59
			Ring	Standard	362	2357	0.148	0.61
IGR J16358-4726†	248.99	-47.41	Reflected	Hard	84	850	0.049	5.63
			Reflected	Standard	433	6320	0.054	4.73
			Ring	Hard	84	343	0.132	4.73
			Ring	Standard	433	2421	0.146	3.86
GRS 1632-477‡	249.12	-47.83	Reflected	Hard	44	742	0.052	0.85
			Reflected	Standard	357	5698	0.061	0.58

Target	RA [°]	Dec [°]	Background	Cuts	N_{ON}	N_{OFF}	α	Significance [σ]
			Ring	Hard	44	367	0.134	-0.73
			Ring	Standard	357	2542	0.148	-0.96
AX J1639.0-4642‡	249.77	-46.70	Reflected	Hard	58	1077	0.043	1.62
			Reflected	Standard	415	9425	0.044	0.24
			Ring	Hard	58	332	0.133	1.87
			Ring	Standard	415	2876	0.145	-0.11
IGR J16418-4532	250.44	-45.52	Reflected	Hard	27	595	0.051	-0.65
			Reflected	Standard	398	8191	0.049	-0.15
			Ring	Hard	27	183	0.133	0.50
			Ring	Standard	398	2858	0.144	-0.68
4U 1642-45	251.45	-45.61	Reflected	Hard	32	673	0.044	0.47
			Reflected	Standard	468	7374	0.060	1.02
			Ring	Hard	35	228	0.133	0.80
			Ring	Standard	468	3059	0.144	1.18
IGR J16465-4507	251.65	-45.12	Reflected	Hard	29	795	0.037	-0.14
			Reflected	Standard	422	8312	0.051	0.06
			Ring	Hard	29	205	0.133	0.30
			Ring	Standard	422	2856	0.145	0.37
IGR J16479-4514	252.03	-45.20	Reflected	Hard	32	793	0.037	0.53
			Reflected	Standard	408	8074	0.053	-0.86
			Ring	Hard	34	202	0.131	1.30
			Ring	Standard	425	2879	0.145	0.39
IGR J16493-4348	252.34	-43.81	Reflected	Hard	18	391	0.040	0.55
			Reflected	Standard	145	2951	0.046	0.71
			Ring	Hard	18	108	0.133	0.87
			Ring	Standard	145	918	0.145	0.91
AX J1700-419‡	255.02	-41.96	Reflected	Hard	42	587	0.050	2.10
			Reflected	Standard	320	4605	0.063	1.77
			Ring	Hard	42	296	0.135	0.28
			Ring	Standard	320	2143	0.148	0.11
OAO 1657-415‡	255.20	-41.66	Reflected	Hard	33	584	0.055	0.15
			Reflected	Standard	293	4614	0.063	0.19
			Ring	Hard	33	257	0.134	-0.25
			Ring	Standard	293	2096	0.150	-1.09
4U 1659-487	255.71	-48.79	Reflected	Hard	38	541	0.062	0.70
			Reflected	Standard	288	3933	0.072	0.27
			Ring	Hard	38	236	0.130	1.20
			Ring	Standard	288	1923	0.143	0.73
4U 1700-37	255.99	-37.84	Reflected	Hard	28	839	0.048	-1.95
			Reflected	Standard	372	6674	0.054	0.58
			Ring	Hard	28	245	0.133	-0.77
			Ring	Standard	372	2302	0.145	1.91
3A 1702-363	256.44	-36.42	Reflected	Hard	19	350	0.034	1.87
			Reflected	Standard	109	2629	0.040	0.29
			Ring	Hard	19	59	0.133	3.09
			Ring	Standard	109	659	0.146	1.18
4U 1702-429	256.56	-43.04	Reflected	Hard	48	1127	0.033	1.63
			Reflected	Standard	314	8635	0.038	-0.71
			Ring	Hard	48	263	0.131	2.02
			Ring	Standard	314	2200	0.145	-0.30
4U 1705-44	257.23	-44.10	Reflected	Hard	65	1223	0.046	1.17
			Reflected	Standard	497	8883	0.052	1.38
			Ring	Hard	65	396	0.133	1.53
			Ring	Standard	497	3168	0.145	1.63

Target	RA [°]	Dec [°]	Background	Cuts	N_{ON}	N_{OFF}	α	Significance [σ]
IGR J17091-3624	257.26	-36.39	Reflected	Hard	3	324	0.028	-2.31
			Reflected	Standard	75	2707	0.031	-1.09
			Ring	Hard	3	61	0.136	-2.01
			Ring	Standard	75	585	0.147	-1.16
4U 1708-40‡	258.10	-40.84	Reflected	Hard	191	2792	0.057	2.28
			Reflected	Standard	1897	25666	0.069	2.82
			Ring	Hard	193	1249	0.131	2.06
			Ring	Standard	1929	13029	0.144	1.00
SAX J1712.6-3739‡	258.14	-37.64	Reflected	Hard	55	2105	0.030	-1.14
			Reflected	Standard	581	17601	0.035	-1.41
			Ring	Hard	56	449	0.129	-0.26
			Ring	Standard	600	4194	0.146	-0.40
1RXS J171824.2-402934‡	259.60	-40.49	Reflected	Hard	121	1583	0.074	0.31
			Reflected	Standard	1226	15244	0.084	-1.53
			Ring	Hard	121	739	0.133	2.06
			Ring	Standard	1226	8301	0.145	0.64
XTE J1723-376	260.91	-37.66	Reflected	Hard	11	475	0.035	-1.43
			Reflected	Standard	151	3746	0.040	0.12
			Ring	Hard	14	125	0.133	-0.63
			Ring	Standard	169	1137	0.147	0.14
EXO 1722-363	261.30	-36.28	Reflected	Hard	25	1064	0.033	-1.70
			Reflected	Standard	287	8404	0.037	-1.12
			Ring	Hard	25	257	0.132	-1.51
			Ring	Standard	287	2196	0.146	-1.79
4U 1724-307	261.89	-30.80	Reflected	Hard	10	435	0.024	-0.19
			Reflected	Standard	91	3191	0.027	0.36
			Ring	Hard	10	63	0.158	0.01
			Ring	Standard	91	608	0.148	0.11
X1724-356	261.91	-35.73	Reflected	Hard	53	971	0.053	0.15
			Reflected	Standard	459	7399	0.059	0.95
			Ring	Hard	53	370	0.133	0.52
			Ring	Standard	459	3023	0.145	0.89
4U 1728-337	262.99	-33.83	Reflected	Hard	68	1332	0.047	0.64
			Reflected	Standard	601	10034	0.053	2.72
			Ring	Hard	68	412	0.156	0.42
			Ring	Standard	613	3750	0.146	2.63
MXB 1730-335	263.35	-33.39	Reflected	Hard	53	1130	0.042	0.78
			Reflected	Standard	420	8649	0.049	-0.05
			Ring	Hard	53	327	0.133	1.29
			Ring	Standard	420	2787	0.146	0.59
GRS 1730-312	263.38	-31.22	Reflected	Hard	37	688	0.045	1.03
			Reflected	Standard	275	5257	0.055	-0.94
			Ring	Hard	43	266	0.133	1.17
			Ring	Standard	311	2248	0.145	-0.77
4U 1730-220	263.49	-22.04	Reflected	Hard	41	821	0.042	1.07
			Reflected	Standard	346	7116	0.049	-0.11
			Ring	Hard	41	266	0.132	0.89
			Ring	Standard	346	2298	0.144	0.74
SLX 1732-304	263.95	-30.48	Reflected	Hard	41	959	0.048	-0.78
			Reflected	Standard	355	7514	0.055	-2.90
			Ring	Hard	41	334	0.133	-0.47
			Ring	Standard	355	2820	0.145	-2.51
1734-292	264.35	-29.18	Reflected	Hard	107	2411	0.046	-0.42
			Reflected	Standard	983	18702	0.054	-0.70

Target	RA [°]	Dec [°]	Background	Cuts	N_{ON}	N_{OFF}	α	Significance [σ]
			Ring	Hard	107	747	0.157	-0.89
			Ring	Standard	983	6842	0.147	-0.66
SLX 1735-269	264.57	-27.00	Reflected	Hard	2	73	0.033	-0.28
			Reflected	Standard	24	493	0.038	1.09
			Ring	Hard	2	16	0.134	-0.10
			Ring	Standard	24	123	0.149	1.16
4U 1735-28	264.64	-28.48	Reflected	Hard	128	1813	0.057	2.25
			Reflected	Standard	976	13953	0.068	0.75
			Ring	Hard	128	673	0.134	3.50
			Ring	Standard	976	6231	0.147	1.91
XTE J1739-302‡	264.80	-30.34	Reflected	Hard	105	2624	0.039	0.30
			Reflected	Standard	897	20136	0.045	-0.19
			Ring	Hard	105	717	0.156	-0.60
			Ring	Standard	897	6109	0.146	0.14
RX J1739.4-2942	264.88	-29.70	Reflected	Hard	227	5177	0.044	0.11
			Reflected	Standard	2040	40062	0.050	0.77
			Ring	Hard	227	1495	0.132	1.90
			Ring	Standard	2052	13789	0.146	0.73
RX J1739.4-2942	264.89	-29.72	Reflected	Hard	237	5238	0.044	0.56
			Reflected	Standard	2151	41326	0.049	2.32
			Ring	Hard	239	1542	0.132	2.23
			Ring	Standard	2151	13968	0.146	2.21
GRS 1737-31‡	264.98	-30.98	Reflected	Hard	72	1616	0.042	0.49
			Reflected	Standard	598	12273	0.049	-0.13
			Ring	Hard	72	460	0.132	1.29
			Ring	Standard	598	4087	0.145	0.14
AX J1740.1-2847	265.05	-28.80	Reflected	Hard	287	6013	0.043	1.64
			Reflected	Standard	2492	48544	0.049	1.83
			Ring	Hard	287	1842	0.132	2.58
			Ring	Standard	2492	16395	0.145	2.12
SLX 1737-282	265.24	-28.31	Reflected	Hard	247	4908	0.051	-0.21
			Reflected	Standard	2282	39708	0.059	-0.91
			Ring	Hard	252	1671	0.133	1.88
			Ring	Standard	2282	15578	0.146	0.26
GRS 1739-278	265.65	-27.78	Reflected	Hard	239	4458	0.053	0.25
			Reflected	Standard	2232	36312	0.062	-0.46
			Ring	Hard	235	1535	0.133	1.97
			Ring	Standard	2232	14908	0.146	1.12
KS 1739-304‡	265.68	-30.51	Reflected	Hard	186	4408	0.042	0.03
			Reflected	Standard	1689	35635	0.047	0.40
			Ring	Hard	197	1546	0.133	-0.56
			Ring	Standard	1767	12282	0.147	-0.83
GC X-4†	265.95	-29.43	Reflected	Hard	517	8654	0.052	2.92
			Reflected	Standard	4453	69253	0.060	3.91
			Ring	Hard	523	3769	0.156	-2.54
			Ring	Standard	4504	30886	0.145	0.23
1E 1740.7-2942‡	265.98	-29.75	Reflected	Hard	529	9317	0.046	4.77
			Reflected	Standard	4210	75140	0.053	3.72
			Ring	Hard	538	3291	0.133	4.30
			Ring	Standard	4248	28360	0.146	1.72
GRS 1741.2-2859†	266.11	-29.01	Reflected	Hard	632	7009	0.069	6.07
			Reflected	Standard	5012	57557	0.080	5.32
			Ring	Hard	638	3962	0.156	0.67
			Ring	Standard	5050	32959	0.145	3.55

Target	RA [°]	Dec [°]	Background	Cuts	N_{ON}	N_{OFF}	α	Significance [σ]
GRO J1744-28†	266.14	-28.74	Reflected	Hard	506	6593	0.071	1.52
			Reflected	Standard	4687	55454	0.083	1.37
			Ring	Hard	513	3886	0.157	-3.71
			Ring	Standard	4708	33292	0.145	-1.73
RX J1744.7-2713	266.19	-27.23	Reflected	Hard	141	3671	0.039	-0.21
			Reflected	Standard	1367	30447	0.046	-0.68
			Ring	Hard	145	950	0.132	1.61
			Ring	Standard	1396	9165	0.146	1.52
KS 1741-293†	266.20	-29.35	Reflected	Hard	652	8493	0.058	6.68
			Reflected	Standard	5122	69213	0.066	7.65
			Ring	Hard	668	4008	0.133	5.25
			Ring	Standard	5198	33392	0.145	4.71
1741-322	266.26	-32.23	Reflected	Hard	21	766	0.034	-1.01
			Reflected	Standard	194	5778	0.039	-2.23
			Ring	Hard	21	203	0.134	-1.17
			Ring	Standard	194	1462	0.146	-1.30
GPS 1742-326	266.37	-32.69	Reflected	Hard	18	487	0.030	0.84
			Reflected	Standard	133	3689	0.034	0.56
			Ring	Hard	18	90	0.134	1.47
			Ring	Standard	133	819	0.148	1.00
GC X-2†	266.40	-29.45	Reflected	Hard	576	8197	0.057	4.54
			Reflected	Standard	4709	65685	0.065	6.90
			Ring	Hard	465	3537	0.156	-3.60
			Ring	Standard	4868	33377	0.145	0.32
AX J1745.6-2901†	266.40	-29.03	Reflected	Hard	2709	7251	0.071	63.35
			Reflected	Standard	9416	58872	0.082	55.89
			Ring	Hard	2721	3875	0.133	60.69
			Ring	Standard	9466	33536	0.145	53.65
1E 1742.5-2845†	266.43	-28.78	Reflected	Hard	749	7087	0.072	9.57
			Reflected	Standard	5477	56783	0.083	10.03
			Ring	Hard	752	3908	0.133	8.83
			Ring	Standard	5511	33593	0.145	8.34
XTE J1748-288†	267.02	-28.47	Reflected	Hard	582	8713	0.054	4.64
			Reflected	Standard	4667	71321	0.062	3.11
			Ring	Hard	588	3705	0.133	3.91
			Ring	Standard	4740	31771	0.145	1.61
AX J1749.1-2733‡	267.27	-27.55	Reflected	Hard	305	7560	0.036	1.83
			Reflected	Standard	2509	59972	0.041	0.80
			Ring	Hard	309	1928	0.133	3.02
			Ring	Standard	2574	17198	0.146	1.02
AX J1749.2-2725‡	267.29	-27.42	Reflected	Hard	233	5706	0.038	1.08
			Reflected	Standard	2054	46272	0.043	1.91
			Ring	Hard	234	1467	0.132	2.58
			Ring	Standard	2066	13336	0.147	2.33
GRO J1750-27‡	267.30	-26.64	Reflected	Hard	69	2001	0.037	-0.63
			Reflected	Standard	680	16215	0.042	-0.11
			Ring	Hard	71	474	0.133	0.93
			Ring	Standard	680	4430	0.146	1.20
SAX J1750.8-2900	267.60	-29.04	Reflected	Hard	349	7177	0.052	-1.36
			Reflected	Standard	3365	55527	0.062	-1.04
			Ring	Hard	349	2454	0.155	-1.51
			Ring	Standard	3365	22984	0.145	0.50
GX 1.1-01.0	268.07	-28.51	Reflected	Hard	235	5661	0.044	-0.90
			Reflected	Standard	2299	46512	0.052	-2.14

Target	RA [°]	Dec [°]	Background	Cuts	N_{ON}	N_{OFF}	α	Significance [σ]
			Ring	Hard	239	1704	0.132	0.83
			Ring	Standard	2299	15828	0.146	-0.13
IGR J17544-2619	268.61	-26.33	Reflected	Hard	87	1892	0.041	1.09
			Reflected	Standard	737	15104	0.047	0.72
			Ring	Hard	90	535	0.133	1.98
			Ring	Standard	737	4946	0.146	0.56
XTE J1755-324	268.87	-32.48	Reflected	Hard	5	132	0.029	0.55
			Reflected	Standard	36	1063	0.033	0.09
			Ring	Hard	5	22	0.155	0.74
			Ring	Standard	36	228	0.147	0.41
4U 1755-338	269.67	-33.81	Reflected	Hard	11	235	0.053	-0.40
			Reflected	Standard	98	1802	0.061	-1.07
			Ring	Hard	11	110	0.132	-0.90
			Ring	Standard	98	813	0.144	-1.69
4U 1758-25‡	270.28	-25.08	Reflected	Hard	40	945	0.036	1.05
			Reflected	Standard	322	8027	0.040	0.12
			Ring	Hard	40	186	0.132	2.65
			Ring	Standard	322	2025	0.148	1.20
GRS 1758-258	270.30	-25.74	Reflected	Hard	21	499	0.036	0.71
			Reflected	Standard	179	4227	0.040	0.89
			Ring	Hard	21	120	0.133	1.12
			Ring	Standard	179	1052	0.146	1.88
4U 1758-20	270.38	-20.53	Reflected	Hard	20	754	0.036	-1.42
			Reflected	Standard	48	1716	0.036	-1.76
			Ring	Hard	22	199	0.132	-0.79
			Ring	Standard	48	412	0.148	-1.60
SAX J1802.7-2017	270.67	-20.29	Reflected	Hard	37	1192	0.033	-0.41
			Reflected	Standard	63	1684	0.036	0.26
			Ring	Hard	37	284	0.132	-0.07
			Ring	Standard	63	416	0.147	0.21
2S 1803-245	271.71	-24.59	Reflected	Hard	12	322	0.032	0.47
			Reflected	Standard	86	2714	0.036	-1.26
			Ring	Hard	12	74	0.133	0.63
			Ring	Standard	86	653	0.147	-0.97
XTE J1806-246	271.71	-24.59	Reflected	Hard	12	318	0.032	0.52
			Reflected	Standard	86	2729	0.036	-1.33
			Ring	Hard	12	71	0.133	0.75
			Ring	Standard	86	649	0.147	-0.90
4U 1811-17‡	273.63	-17.16	Reflected	Hard	57	822	0.043	3.25
			Reflected	Standard	395	7471	0.051	0.74
			Ring	Hard	62	314	0.135	2.64
			Ring	Standard	428	2822	0.146	0.73
4U 1813-14	274.01	-14.04	Reflected	Hard	0	33	0.040	-1.61
			Reflected	Standard	11	352	0.045	-1.30
			Ring	Hard	0	7	0.134	-1.32
			Ring	Standard	11	114	0.150	-1.48
SAX J1818.6-1703	274.66	-17.05	Reflected	Hard	35	728	0.037	1.48
			Reflected	Standard	243	5995	0.042	-0.49
			Ring	Hard	35	165	0.132	2.43
			Ring	Standard	243	1690	0.146	-0.25
SAX J1819.3-2525	274.84	-25.43	Reflected	Hard	16	254	0.066	-0.21
			Reflected	Standard	163	2153	0.077	-0.29
			Ring	Hard	16	140	0.132	-0.55
			Ring	Standard	163	1163	0.143	-0.24

Target	RA [°]	Dec [°]	Background	Cuts	N_{ON}	N_{OFF}	α	Significance [σ]
RX J1826.2-1450†	276.56	-14.85	Reflected	Hard	1280	3519	0.085	38.95
			Reflected	Standard	4552	27691	0.097	31.15
			Ring	Hard	1283	2141	0.155	35.18
			Ring	Standard	4552	18662	0.143	30.36
XTE J1829-098	277.43	-9.86	Reflected	Hard	57	1302	0.037	1.13
			Reflected	Standard	517	11083	0.041	2.64
			Ring	Hard	57	315	0.134	2.00
			Ring	Standard	517	3136	0.146	2.50
H 1833-076‡	279.12	-7.61	Reflected	Hard	83	1466	0.047	1.67
			Reflected	Standard	769	12784	0.056	1.82
			Ring	Hard	87	585	0.132	1.00
			Ring	Standard	769	5296	0.145	-0.02
GS 1839-06†	280.43	-5.85	Reflected	Hard	145	2002	0.051	3.86
			Reflected	Standard	1215	17588	0.058	5.98
			Ring	Hard	145	1017	0.135	0.65
			Ring	Standard	1215	7541	0.146	3.05
GS 1839-04	280.45	-4.45	Reflected	Hard	71	1494	0.042	0.93
			Reflected	Standard	673	13395	0.048	1.09
			Ring	Hard	71	451	0.132	1.36
			Ring	Standard	673	4333	0.146	1.56
AX 1845.0-0433	281.26	-4.56	Reflected	Hard	64	1361	0.043	0.71
			Reflected	Standard	608	12497	0.047	0.58
			Ring	Hard	64	374	0.132	1.85
			Ring	Standard	608	3980	0.146	1.04
GS 1843+009	281.40	0.86	Reflected	Hard	14	231	0.037	1.63
			Reflected	Standard	85	2015	0.042	0.06
			Ring	Hard	14	57	0.132	1.94
			Ring	Standard	85	587	0.145	-0.02
2S 1845-024‡	282.07	-2.42	Reflected	Hard	107	2121	0.046	0.85
			Reflected	Standard	1010	18292	0.053	1.12
			Ring	Hard	107	806	0.131	0.10
			Ring	Standard	1010	6908	0.144	0.37
IGR J18483-0311‡	282.07	-3.18	Reflected	Hard	93	1598	0.050	1.48
			Reflected	Standard	711	13021	0.057	-1.29
			Ring	Hard	99	588	0.132	2.15
			Ring	Standard	758	5445	0.145	-1.04
EXO 1846-031‡	282.32	-3.06	Reflected	Hard	62	1048	0.066	-0.80
			Reflected	Standard	604	9111	0.070	-1.33
			Ring	Hard	64	444	0.130	0.75
			Ring	Standard	612	4422	0.144	-0.85
XTE J1855-026	283.88	-2.61	Reflected	Hard	2	122	0.029	-0.89
			Reflected	Standard	36	986	0.032	0.68
			Ring	Hard	2	22	0.133	-0.54
			Ring	Standard	36	197	0.145	1.23
XTE J1856+053	284.16	5.33	Reflected	Hard	2	46	0.033	0.35
			Reflected	Standard	12	418	0.038	-1.05
			Ring	Hard	2	9	0.135	0.60
			Ring	Standard	12	104	0.149	-0.87
XTE J1858+034‡	284.65	3.44	Reflected	Hard	22	381	0.048	0.83
			Reflected	Standard	185	2969	0.055	1.70
			Ring	Hard	22	144	0.134	0.58
			Ring	Standard	185	1149	0.144	1.35
XTE J1901+014	285.42	1.44	Reflected	Hard	38	735	0.045	0.82
			Reflected	Standard	303	6437	0.047	-0.11

Target	RA [°]	Dec [°]	Background	Cuts	N_{ON}	N_{OFF}	α	Significance [σ]
			Ring	Hard	39	180	0.132	2.65
			Ring	Standard	303	1909	0.145	1.48
4U 1901+03	285.90	3.19	Reflected	Hard	19	345	0.045	0.86
			Reflected	Standard	152	3175	0.050	-0.52
			Ring	Hard	19	127	0.130	0.56
			Ring	Standard	152	1150	0.144	-1.04
XTE J1906+09	286.20	9.04	Reflected	Hard	6	219	0.034	-0.57
			Reflected	Standard	78	2139	0.040	-0.85
			Ring	Hard	6	62	0.130	-0.72
			Ring	Standard	78	638	0.145	-1.43
4U 1907+09‡	287.41	9.83	Reflected	Hard	28	706	0.037	0.32
			Reflected	Standard	298	6945	0.041	0.80
			Ring	Hard	28	149	0.134	1.56
			Ring	Standard	298	1850	0.147	1.46
4U 1909+07	287.70	7.60	Reflected	Hard	18	407	0.039	0.49
			Reflected	Standard	135	3428	0.044	-1.18
			Ring	Hard	18	120	0.132	0.50
			Ring	Standard	135	1006	0.144	-0.80
3A 1909+048	287.96	4.98	Reflected	Hard	22	511	0.040	0.37
			Reflected	Standard	202	4948	0.044	-0.91
			Ring	Hard	26	161	0.133	0.90
			Ring	Standard	214	1477	0.145	-0.01
IGR J19140+0951†	288.52	9.88	Reflected	Hard	51	969	0.042	1.46
			Reflected	Standard	465	9477	0.048	0.53
			Ring	Hard	51	299	0.134	1.56
			Ring	Standard	465	2987	0.147	1.16
GRS 1915+105‡	288.82	10.97	Reflected	Hard	42	533	0.074	0.39
			Reflected	Standard	408	4996	0.085	-0.77
			Ring	Hard	42	268	0.131	1.04
			Ring	Standard	408	2912	0.144	-0.55
4U 1918+15	290.07	14.69	Reflected	Hard	1	59	0.041	-1.02
			Reflected	Standard	18	526	0.043	-0.96
			Ring	Hard	1	25	0.132	-1.42
			Ring	Standard	28	254	0.143	-1.37
4U 2129+12	322.49	12.17	Reflected	Hard	13	378	0.053	-1.64
			Reflected	Standard	184	3233	0.060	-0.79
			Ring	Hard	13	145	0.130	-1.34
			Ring	Standard	194	1391	0.143	-0.30

Table A.2: Table listing the livetimes (T_{live}) and threshold energies (E_{Thresh}) corresponding to the nominal positions of all targets in the survey, together with the derived integral flux upper limits above E_{Thresh}.

Target	Background	Cuts	T_{live} [h]	E_{Thresh} [TeV]	$F(E > E_{\mathrm{Thresh}})$
RX J0532.7-6926	Reflected	Hard	6.2	1.62	$< 4.393 \times 10^{-13}$
	Reflected	Standard	6.6	1.15	$< 6.272 \times 10^{-13}$
	Ring	Hard	6.2	1.62	$< 6.272 \times 10^{-13}$
	Ring	Standard	6.6	1.15	$< 6.196 \times 10^{-13}$
1A 0535+262	Reflected	Hard	1.1	1.91	$< 1.155 \times 10^{-12}$
	Reflected	Standard	1.1	0.99	$< 2.216 \times 10^{-12}$
	Ring	Hard	1.1	1.91	$< 2.216 \times 10^{-12}$
	Ring	Standard	1.1	0.99	$< 1.031 \times 10^{-12}$
SAX J0635.2+0533	Reflected	Hard	14.9	1.91	$< 2.237 \times 10^{-13}$
	Reflected	Standard	14.9	1.00	$< 2.885 \times 10^{-13}$
	Ring	Hard	14.9	1.91	$< 2.885 \times 10^{-13}$
	Ring	Standard	14.9	1.00	$< 3.346 \times 10^{-13}$
4U 0900-40	Reflected	Hard	4.9	1.84	$< 3.836 \times 10^{-13}$
	Reflected	Standard	4.9	0.99	$< 5.519 \times 10^{-13}$
	Ring	Hard	4.9	1.84	$< 5.519 \times 10^{-13}$
	Ring	Standard	4.9	0.99	$< 6.359 \times 10^{-13}$
GRO J1008-57	Reflected	Hard	4.9	1.70	$< 4.084 \times 10^{-13}$
	Reflected	Standard	5.6	0.93	$< 6.305 \times 10^{-13}$
	Ring	Hard	5.6	1.70	$< 6.305 \times 10^{-13}$
	Ring	Standard	5.6	0.93	$< 5.355 \times 10^{-13}$
RX J1037.5-5647	Reflected	Hard	2.1	1.19	$< 1.688 \times 10^{-12}$
	Reflected	Standard	2.1	0.64	$< 5.833 \times 10^{-13}$
	Ring	Hard	2.1	1.19	$< 5.833 \times 10^{-13}$
	Ring	Standard	2.1	0.64	$< 8.430 \times 10^{-13}$
1A 1118-615	Reflected	Hard	3.6	1.14	$< 9.876 \times 10^{-13}$
	Reflected	Standard	3.6	0.61	$< 2.236 \times 10^{-12}$
	Ring	Hard	3.6	1.14	$< 2.236 \times 10^{-12}$
	Ring	Standard	3.6	0.61	$< 1.452 \times 10^{-12}$
4U 1119-603	Reflected	Hard	4.9	1.30	$< 8.774 \times 10^{-13}$
	Reflected	Standard	4.9	0.70	$< 1.197 \times 10^{-12}$
	Ring	Hard	4.9	1.30	$< 1.197 \times 10^{-12}$
	Ring	Standard	4.9	0.70	$< 1.234 \times 10^{-12}$
IGR J11215-5952	Reflected	Hard	3.6	1.30	$< 7.382 \times 10^{-13}$
	Reflected	Standard	3.6	0.70	$< 1.502 \times 10^{-12}$
	Ring	Hard	4.6	1.30	$< 1.502 \times 10^{-12}$
	Ring	Standard	4.6	0.70	$< 1.092 \times 10^{-12}$
4U 1223-624	Reflected	Hard	13.7	1.13	$< 2.046 \times 10^{-13}$
	Reflected	Standard	13.7	0.60	$< 2.369 \times 10^{-13}$
	Ring	Hard	13.7	1.13	$< 2.369 \times 10^{-13}$
	Ring	Standard	13.7	0.60	$< 2.237 \times 10^{-13}$
IGR J12349-6434	Reflected	Hard	1.2	1.13	$< 5.076 \times 10^{-12}$
	Reflected	Standard	1.2	0.60	$< 6.740 \times 10^{-12}$
	Ring	Hard	1.2	1.13	$< 6.740 \times 10^{-12}$
	Ring	Standard	1.2	0.60	$< 6.470 \times 10^{-12}$
1H 1249-637	Reflected	Hard	17.3	1.12	$< 2.786 \times 10^{-13}$
	Reflected	Standard	17.3	0.60	$< 3.190 \times 10^{-13}$
	Ring	Hard	17.3	1.12	$< 3.190 \times 10^{-13}$
	Ring	Standard	17.3	0.60	$< 3.479 \times 10^{-13}$
4U 1258-61	Reflected	Hard	21.4	1.01	$< 1.239 \times 10^{-13}$
	Reflected	Standard	21.4	0.54	$< 6.860 \times 10^{-14}$

Target	Background	Cuts	T_{live} [h]	E_{Thresh} [TeV]	$F(E > E_{\mathrm{Thresh}})$
	Ring	Hard	21.4	1.01	$< 6.860 \times 10^{-14}$
	Ring	Standard	21.4	0.54	$< 9.606 \times 10^{-14}$
2RXP J130159.6-635806†	Reflected	Hard	68.5	1.87	$< 2.243 \times 10^{-13}$
	Reflected	Standard	70.5	1.65	$(1.747 \pm 0.32) \times 10^{-13}$
	Ring	Hard	68.9	1.87	$(1.747 \pm 0.32) \times 10^{-13}$
	Ring	Standard	70.5	1.65	$(1.399 \pm 0.29) \times 10^{-13}$
SAX J1324.4-6200	Reflected	Hard	2.6	1.08	$< 1.567 \times 10^{-12}$
	Reflected	Standard	2.6	0.58	$< 1.073 \times 10^{-12}$
	Ring	Hard	2.6	1.08	$< 1.073 \times 10^{-12}$
	Ring	Standard	2.6	0.58	$< 1.181 \times 10^{-12}$
4U 1323-62	Reflected	Hard	3.1	1.08	$< 1.458 \times 10^{-12}$
	Reflected	Standard	3.1	0.58	$< 2.297 \times 10^{-12}$
	Ring	Hard	3.1	1.08	$< 2.297 \times 10^{-12}$
	Ring	Standard	3.1	0.58	$< 2.637 \times 10^{-12}$
1H 1348-633‡	Reflected	Hard	2.1	1.06	$< 4.435 \times 10^{-13}$
	Reflected	Standard	2.4	1.08	$< 7.368 \times 10^{-13}$
	Ring	Hard	2.1	1.06	$< 7.368 \times 10^{-13}$
	Ring	Standard	2.4	1.08	$< 7.356 \times 10^{-13}$
2S 1417-624	Reflected	Hard	7.9	1.31	$< 7.774 \times 10^{-13}$
	Reflected	Standard	8.1	1.44	$< 5.602 \times 10^{-13}$
	Ring	Hard	7.9	1.31	$< 5.602 \times 10^{-13}$
	Ring	Standard	8.1	1.44	$< 3.884 \times 10^{-13}$
SAX J1452.8-5949	Reflected	Hard	8.3	1.01	$< 4.487 \times 10^{-13}$
	Reflected	Standard	8.9	0.55	$< 7.276 \times 10^{-13}$
	Ring	Hard	8.5	1.01	$< 7.276 \times 10^{-13}$
	Ring	Standard	9.1	0.55	$< 7.032 \times 10^{-13}$
3A 1516-569	Reflected	Hard	16.7	1.69	$< 2.726 \times 10^{-13}$
	Reflected	Standard	18.0	0.91	$< 2.645 \times 10^{-13}$
	Ring	Hard	18.0	1.69	$< 2.645 \times 10^{-13}$
	Ring	Standard	18.0	0.91	$< 2.898 \times 10^{-13}$
4U 1538-52	Reflected	Hard	5.6	1.81	$< 5.312 \times 10^{-13}$
	Reflected	Standard	5.6	0.99	$< 3.100 \times 10^{-13}$
	Ring	Hard	5.6	1.81	$< 3.100 \times 10^{-13}$
	Ring	Standard	5.6	0.99	$< 3.898 \times 10^{-13}$
XTE J1543-568	Reflected	Hard	2.2	1.91	$< 6.914 \times 10^{-13}$
	Reflected	Standard	1.8	1.02	$< 9.961 \times 10^{-13}$
	Ring	Hard	2.2	1.91	$< 9.961 \times 10^{-13}$
	Ring	Standard	2.2	1.02	$< 6.632 \times 10^{-13}$
XTE J1550-564	Reflected	Hard	1.3	0.78	$< 1.474 \times 10^{-12}$
	Reflected	Standard	1.3	0.43	$< 1.835 \times 10^{-12}$
	Ring	Hard	1.3	0.78	$< 1.835 \times 10^{-12}$
	Ring	Standard	1.3	0.43	$< 1.915 \times 10^{-12}$
1H 1555-552	Reflected	Hard	2.6	0.89	$< 1.500 \times 10^{-12}$
	Reflected	Standard	2.6	0.51	$< 2.064 \times 10^{-12}$
	Ring	Hard	2.6	0.89	$< 2.064 \times 10^{-12}$
	Ring	Standard	2.6	0.51	$< 1.985 \times 10^{-12}$
2S 1553-542	Reflected	Hard	2.6	1.21	$< 1.026 \times 10^{-12}$
	Reflected	Standard	3.0	0.65	$< 1.724 \times 10^{-12}$
	Ring	Hard	3.0	1.21	$< 1.724 \times 10^{-12}$
	Ring	Standard	3.0	0.65	$< 1.434 \times 10^{-12}$
4U 1608-52‡	Reflected	Hard	8.1	0.85	$< 5.086 \times 10^{-13}$
	Reflected	Standard	8.1	0.46	$< 1.155 \times 10^{-12}$
	Ring	Hard	8.1	0.85	$< 1.155 \times 10^{-12}$
	Ring	Standard	8.1	0.46	$< 8.110 \times 10^{-13}$

Target	Background	Cuts	$T_{\rm live}$ [h]	$E_{\rm Thresh}$ [TeV]	$F(E > E_{\rm Thresh})$
IGR J16195-4945‡	Reflected	Hard	8.4	1.04	$< 6.243 \times 10^{-13}$
	Reflected	Standard	8.4	0.57	$< 7.991 \times 10^{-13}$
	Ring	Hard	8.4	1.04	$< 7.991 \times 10^{-13}$
	Ring	Standard	8.4	0.57	$< 1.046 \times 10^{-12}$
H 1617-155	Reflected	Hard	3.9	1.73	$< 4.430 \times 10^{-13}$
	Reflected	Standard	3.9	0.90	$< 4.262 \times 10^{-13}$
	Ring	Hard	3.9	1.73	$< 4.262 \times 10^{-13}$
	Ring	Standard	3.9	0.90	$< 4.417 \times 10^{-13}$
4U 1624-49‡	Reflected	Hard	8.5	1.06	$< 1.059 \times 10^{-12}$
	Reflected	Standard	7.7	0.57	$< 1.563 \times 10^{-12}$
	Ring	Hard	8.5	1.06	$< 1.563 \times 10^{-12}$
	Ring	Standard	8.1	0.57	$< 1.521 \times 10^{-12}$
IGR J16283-4838‡	Reflected	Hard	8.1	1.06	$< 8.116 \times 10^{-13}$
	Reflected	Standard	8.1	0.57	$< 1.713 \times 10^{-12}$
	Ring	Hard	8.1	1.06	$< 1.713 \times 10^{-12}$
	Ring	Standard	8.1	0.57	$< 1.288 \times 10^{-12}$
IGR J16318-4848	Reflected	Hard	9.8	0.82	$< 4.836 \times 10^{-13}$
	Reflected	Standard	9.8	0.47	$< 1.662 \times 10^{-12}$
	Ring	Hard	9.8	0.82	$< 1.662 \times 10^{-12}$
	Ring	Standard	9.8	0.47	$< 1.375 \times 10^{-12}$
IGR J16320-4751†	Reflected	Hard	10.3	0.86	$(1.344 \pm 0.30) \times 10^{-12}$
	Reflected	Standard	10.3	0.47	$(1.540 \pm 0.36) \times 10^{-12}$
	Ring	Hard	10.7	0.86	$(1.540 \pm 0.36) \times 10^{-12}$
	Ring	Standard	10.7	0.47	$(1.192 \pm 0.35) \times 10^{-12}$
4U 1630-47†	Reflected	Hard	8.7	0.74	$(1.246 \pm 0.36) \times 10^{-12}$
	Reflected	Standard	8.7	0.42	$< 2.415 \times 10^{-12}$
	Ring	Hard	8.7	0.74	$< 2.415 \times 10^{-12}$
	Ring	Standard	8.7	0.42	$< 1.732 \times 10^{-12}$
IGR J16358-4726†	Reflected	Hard	9.1	0.73	$(1.768 \pm 0.38) \times 10^{-12}$
	Reflected	Standard	9.1	0.42	$(1.954 \pm 0.44) \times 10^{-12}$
	Ring	Hard	9.1	0.73	$(1.954 \pm 0.44) \times 10^{-12}$
	Ring	Standard	9.1	0.42	$(1.658 \pm 0.45) \times 10^{-12}$
GRS 1632-477‡	Reflected	Hard	9.1	0.74	$< 1.089 \times 10^{-12}$
	Reflected	Standard	9.1	0.42	$< 1.598 \times 10^{-12}$
	Ring	Hard	9.1	0.74	$< 1.598 \times 10^{-12}$
	Ring	Standard	9.1	0.42	$< 1.035 \times 10^{-12}$
AX J1639.0-4642‡	Reflected	Hard	10.2	1.93	$< 5.720 \times 10^{-13}$
	Reflected	Standard	11.6	1.64	$< 1.750 \times 10^{-13}$
	Ring	Hard	10.2	1.93	$< 1.750 \times 10^{-13}$
	Ring	Standard	11.6	1.64	$< 1.609 \times 10^{-13}$
IGR J16418-4532	Reflected	Hard	6.6	1.90	$< 3.097 \times 10^{-13}$
	Reflected	Standard	11.5	1.96	$< 1.621 \times 10^{-13}$
	Ring	Hard	6.6	1.90	$< 1.621 \times 10^{-13}$
	Ring	Standard	11.5	1.96	$< 1.375 \times 10^{-13}$
4U 1642-45	Reflected	Hard	6.7	1.87	$< 5.123 \times 10^{-13}$
	Reflected	Standard	12.0	1.98	$< 2.228 \times 10^{-13}$
	Ring	Hard	7.1	1.87	$< 2.228 \times 10^{-13}$
	Ring	Standard	12.0	1.98	$< 2.273 \times 10^{-13}$
IGR J16465-4507	Reflected	Hard	6.7	1.90	$< 4.154 \times 10^{-13}$
	Reflected	Standard	11.5	1.97	$< 1.754 \times 10^{-13}$
	Ring	Hard	6.7	1.90	$< 1.754 \times 10^{-13}$
	Ring	Standard	11.5	1.97	$< 1.940 \times 10^{-13}$
IGR J16479-4514	Reflected	Hard	6.2	1.89	$< 6.016 \times 10^{-13}$
	Reflected	Standard	11.1	1.97	$< 1.262 \times 10^{-13}$

Target	Background	Cuts	$T_{\rm live}$ [h]	$E_{\rm Thresh}$ [TeV]	$F(E > E_{\rm Thresh})$
	Ring	Hard	6.7	1.89	$< 1.262 \times 10^{-13}$
	Ring	Standard	11.5	1.97	$< 1.874 \times 10^{-13}$
IGR J16493-4348	Reflected	Hard	3.4	0.62	$< 2.154 \times 10^{-12}$
	Reflected	Standard	3.4	0.36	$< 3.391 \times 10^{-12}$
	Ring	Hard	3.4	0.62	$< 3.391 \times 10^{-12}$
	Ring	Standard	3.4	0.36	$< 3.607 \times 10^{-12}$
AX J1700-419‡	Reflected	Hard	7.2	0.80	$< 1.530 \times 10^{-12}$
	Reflected	Standard	7.2	0.44	$< 2.145 \times 10^{-12}$
	Ring	Hard	7.2	0.80	$< 2.145 \times 10^{-12}$
	Ring	Standard	7.2	0.44	$< 1.539 \times 10^{-12}$
OAO 1657-415‡	Reflected	Hard	6.8	0.80	$< 9.782 \times 10^{-13}$
	Reflected	Standard	6.8	0.44	$< 1.505 \times 10^{-12}$
	Ring	Hard	6.8	0.80	$< 1.505 \times 10^{-12}$
	Ring	Standard	6.8	0.44	$< 1.017 \times 10^{-12}$
4U 1659-487	Reflected	Hard	8.4	1.31	$< 6.085 \times 10^{-13}$
	Reflected	Standard	8.4	0.71	$< 6.456 \times 10^{-13}$
	Ring	Hard	8.4	1.31	$< 6.456 \times 10^{-13}$
	Ring	Standard	8.4	0.71	$< 7.342 \times 10^{-13}$
4U 1700-37	Reflected	Hard	8.1	0.95	$< 2.768 \times 10^{-13}$
	Reflected	Standard	8.1	0.51	$< 1.079 \times 10^{-12}$
	Ring	Hard	8.1	0.95	$< 1.079 \times 10^{-12}$
	Ring	Standard	8.1	0.51	$< 1.458 \times 10^{-12}$
3A 1702-363	Reflected	Hard	2.4	0.57	$< 4.002 \times 10^{-12}$
	Reflected	Standard	2.4	0.32	$< 4.063 \times 10^{-12}$
	Ring	Hard	2.4	0.57	$< 4.063 \times 10^{-12}$
	Ring	Standard	2.4	0.32	$< 4.808 \times 10^{-12}$
4U 1702-429	Reflected	Hard	10.2	0.79	$< 1.171 \times 10^{-12}$
	Reflected	Standard	10.2	0.44	$< 8.508 \times 10^{-13}$
	Ring	Hard	10.2	0.79	$< 8.508 \times 10^{-13}$
	Ring	Standard	10.2	0.44	$< 9.418 \times 10^{-13}$
4U 1705-44	Reflected	Hard	14.2	0.64	$< 9.886 \times 10^{-13}$
	Reflected	Standard	14.2	0.37	$< 1.518 \times 10^{-12}$
	Ring	Hard	14.2	0.64	$< 1.518 \times 10^{-12}$
	Ring	Standard	14.2	0.37	$< 1.595 \times 10^{-12}$
IGR J17091-3624	Reflected	Hard	2.2	0.67	$< 7.313 \times 10^{-13}$
	Reflected	Standard	2.2	0.37	$< 2.214 \times 10^{-12}$
	Ring	Hard	2.2	0.67	$< 2.214 \times 10^{-12}$
	Ring	Standard	2.2	0.37	$< 2.117 \times 10^{-12}$
4U 1708-40‡	Reflected	Hard	41.0	1.94	$< 2.708 \times 10^{-13}$
	Reflected	Standard	48.2	1.95	$< 1.403 \times 10^{-13}$
	Ring	Hard	41.4	1.94	$< 1.403 \times 10^{-13}$
	Ring	Standard	48.6	1.95	$< 1.042 \times 10^{-13}$
SAX J1712.6-3739‡	Reflected	Hard	16.3	1.88	$< 1.753 \times 10^{-13}$
	Reflected	Standard	17.9	1.64	$< 7.881 \times 10^{-14}$
	Ring	Hard	16.7	1.88	$< 7.881 \times 10^{-14}$
	Ring	Standard	18.3	1.64	$< 1.052 \times 10^{-13}$
1RXS J171824.2-402934‡	Reflected	Hard	27.3	1.93	$< 1.999 \times 10^{-13}$
	Reflected	Standard	32.3	1.86	$< 5.831 \times 10^{-14}$
	Ring	Hard	27.3	1.93	$< 5.831 \times 10^{-14}$
	Ring	Standard	32.3	1.86	$< 1.121 \times 10^{-13}$
XTE J1723-376	Reflected	Hard	3.9	0.74	$< 6.467 \times 10^{-13}$
	Reflected	Standard	3.9	0.40	$< 2.266 \times 10^{-12}$
	Ring	Hard	4.3	0.74	$< 2.266 \times 10^{-12}$
	Ring	Standard	4.3	0.40	$< 2.233 \times 10^{-12}$

Target	Background	Cuts	$T_{\rm live}$ [h]	$E_{\rm Thresh}$ [TeV]	$F(E > E_{\rm Thresh})$
EXO 1722-363	Reflected	Hard	8.7	1.08	$< 2.836 \times 10^{-13}$
	Reflected	Standard	8.7	0.58	$< 5.283 \times 10^{-13}$
	Ring	Hard	8.7	1.08	$< 5.283 \times 10^{-13}$
	Ring	Standard	8.7	0.58	$< 4.130 \times 10^{-13}$
4U 1724-307	Reflected	Hard	3.3	0.65	$< 1.299 \times 10^{-12}$
	Reflected	Standard	3.3	0.36	$< 2.558 \times 10^{-12}$
	Ring	Hard	3.3	0.65	$< 2.558 \times 10^{-12}$
	Ring	Standard	3.3	0.36	$< 2.192 \times 10^{-12}$
X1724-356	Reflected	Hard	11.2	1.07	$< 5.157 \times 10^{-13}$
	Reflected	Standard	11.2	0.58	$< 7.455 \times 10^{-13}$
	Ring	Hard	11.2	1.07	$< 7.455 \times 10^{-13}$
	Ring	Standard	11.2	0.58	$< 7.665 \times 10^{-13}$
4U 1728-337	Reflected	Hard	15.0	0.88	$< 6.014 \times 10^{-13}$
	Reflected	Standard	14.5	0.49	$< 1.198 \times 10^{-12}$
	Ring	Hard	15.0	0.88	$< 1.198 \times 10^{-12}$
	Ring	Standard	15.0	0.49	$< 1.169 \times 10^{-12}$
MXB 1730-335	Reflected	Hard	10.9	0.90	$< 7.489 \times 10^{-13}$
	Reflected	Standard	10.9	0.49	$< 7.222 \times 10^{-13}$
	Ring	Hard	10.9	0.90	$< 7.222 \times 10^{-13}$
	Ring	Standard	10.9	0.49	$< 8.888 \times 10^{-13}$
GRS 1730-312	Reflected	Hard	8.5	0.75	$< 9.517 \times 10^{-13}$
	Reflected	Standard	9.0	0.41	$< 6.581 \times 10^{-13}$
	Ring	Hard	9.8	0.75	$< 6.581 \times 10^{-13}$
	Ring	Standard	9.8	0.41	$< 7.145 \times 10^{-13}$
4U 1730-220	Reflected	Hard	8.9	1.09	$< 6.739 \times 10^{-13}$
	Reflected	Standard	8.9	0.56	$< 6.272 \times 10^{-13}$
	Ring	Hard	8.9	1.09	$< 6.272 \times 10^{-13}$
	Ring	Standard	8.9	0.56	$< 8.063 \times 10^{-13}$
SLX 1732-304	Reflected	Hard	12.3	1.54	$< 2.259 \times 10^{-13}$
	Reflected	Standard	12.3	0.86	$< 1.108 \times 10^{-13}$
	Ring	Hard	12.3	1.54	$< 1.108 \times 10^{-13}$
	Ring	Standard	12.3	0.86	$< 1.212 \times 10^{-13}$
1734-292	Reflected	Hard	26.1	1.48	$< 1.938 \times 10^{-13}$
	Reflected	Standard	26.5	1.32	$< 8.910 \times 10^{-14}$
	Ring	Hard	26.1	1.48	$< 8.910 \times 10^{-14}$
	Ring	Standard	26.5	1.32	$< 9.055 \times 10^{-14}$
SLX 1735-269	Reflected	Hard	0.4	0.44	$< 1.390 \times 10^{-11}$
	Reflected	Standard	0.4	0.25	$< 2.123 \times 10^{-11}$
	Ring	Hard	0.4	0.44	$< 2.123 \times 10^{-11}$
	Ring	Standard	0.4	0.25	$< 2.276 \times 10^{-11}$
4U 1735-28	Reflected	Hard	22.2	1.48	$< 4.497 \times 10^{-13}$
	Reflected	Standard	22.6	1.31	$< 1.481 \times 10^{-13}$
	Ring	Hard	22.2	1.48	$< 1.481 \times 10^{-13}$
	Ring	Standard	22.6	1.31	$< 1.927 \times 10^{-13}$
XTE J1739-302[‡]	Reflected	Hard	27.5	1.54	$< 2.231 \times 10^{-13}$
	Reflected	Standard	27.2	0.83	$< 2.189 \times 10^{-13}$
	Ring	Hard	27.5	1.54	$< 2.189 \times 10^{-13}$
	Ring	Standard	27.2	0.83	$< 2.425 \times 10^{-13}$
RX J1739.4-2942	Reflected	Hard	54.1	1.73	$< 1.464 \times 10^{-13}$
	Reflected	Standard	54.6	1.35	$< 9.917 \times 10^{-14}$
	Ring	Hard	54.1	1.73	$< 9.917 \times 10^{-14}$
	Ring	Standard	54.9	1.35	$< 9.728 \times 10^{-14}$
RX J1739.4-2942	Reflected	Hard	54.4	1.72	$< 1.685 \times 10^{-13}$
	Reflected	Standard	55.6	1.35	$< 1.367 \times 10^{-13}$

Target	Background	Cuts	$T_{\rm live}$ [h]	$E_{\rm Thresh}$ [TeV]	$F(E > E_{\rm Thresh})$
	Ring	Hard	54.8	1.72	$< 1.367 \times 10^{-13}$
	Ring	Standard	55.6	1.35	$< 1.334 \times 10^{-13}$
GRS 1737-31‡	Reflected	Hard	18.0	1.54	$< 2.940 \times 10^{-13}$
	Reflected	Standard	18.0	0.83	$< 2.463 \times 10^{-13}$
	Ring	Hard	18.0	1.54	$< 2.463 \times 10^{-13}$
	Ring	Standard	18.0	0.83	$< 2.635 \times 10^{-13}$
AX J1740.1-2847	Reflected	Hard	71.8	1.73	$< 1.693 \times 10^{-13}$
	Reflected	Standard	73.0	1.37	$< 9.097 \times 10^{-14}$
	Ring	Hard	71.8	1.73	$< 9.097 \times 10^{-14}$
	Ring	Standard	73.0	1.37	$< 9.774 \times 10^{-14}$
SLX 1737-282	Reflected	Hard	63.7	1.72	$< 1.059 \times 10^{-13}$
	Reflected	Standard	66.3	1.35	$< 4.254 \times 10^{-14}$
	Ring	Hard	65.0	1.72	$< 4.254 \times 10^{-14}$
	Ring	Standard	66.3	1.35	$< 6.292 \times 10^{-14}$
GRS 1739-278	Reflected	Hard	65.1	1.71	$< 1.172 \times 10^{-13}$
	Reflected	Standard	66.3	1.35	$< 5.076 \times 10^{-14}$
	Ring	Hard	64.6	1.71	$< 5.076 \times 10^{-14}$
	Ring	Standard	66.3	1.35	$< 7.904 \times 10^{-14}$
KS 1739-304‡	Reflected	Hard	45.1	1.70	$< 1.542 \times 10^{-13}$
	Reflected	Standard	46.4	1.33	$< 9.288 \times 10^{-14}$
	Ring	Hard	47.7	1.70	$< 9.288 \times 10^{-14}$
	Ring	Standard	49.0	1.33	$< 6.335 \times 10^{-14}$
GC X-4†	Reflected	Hard	112.5	1.71	$< 1.788 \times 10^{-13}$
	Reflected	Standard	115.5	1.36	$(5.818 \pm 1.51) \times 10^{-14}$
	Ring	Hard	113.8	1.71	$(5.818 \pm 1.51) \times 10^{-14}$
	Ring	Standard	116.4	1.36	$< 5.457 \times 10^{-14}$
1E 1740.7-2942‡	Reflected	Hard	112.6	1.74	$(1.371 \pm 0.31) \times 10^{-13}$
	Reflected	Standard	117.3	1.38	$(5.529 \pm 1.50) \times 10^{-14}$
	Ring	Hard	114.7	1.74	$(5.529 \pm 1.50) \times 10^{-14}$
	Ring	Standard	117.7	1.38	$< 7.655 \times 10^{-14}$
GRS 1741.2-2859†	Reflected	Hard	115.8	1.71	$(1.682 \pm 0.30) \times 10^{-13}$
	Reflected	Standard	118.4	1.35	$(7.723 \pm 1.48) \times 10^{-14}$
	Ring	Hard	117.1	1.71	$(7.723 \pm 1.48) \times 10^{-14}$
	Ring	Standard	119.3	1.35	$(5.326 \pm 1.51) \times 10^{-14}$
GRO J1744-28†	Reflected	Hard	114.4	1.71	$< 1.282 \times 10^{-13}$
	Reflected	Standard	117.9	1.35	$< 6.622 \times 10^{-14}$
	Ring	Hard	115.8	1.71	$< 6.622 \times 10^{-14}$
	Ring	Standard	118.4	1.35	$< 2.724 \times 10^{-14}$
RX J1744.7-2713	Reflected	Hard	45.8	1.74	$< 1.127 \times 10^{-13}$
	Reflected	Standard	47.1	1.35	$< 5.058 \times 10^{-14}$
	Ring	Hard	46.6	1.74	$< 5.058 \times 10^{-14}$
	Ring	Standard	47.5	1.35	$< 9.175 \times 10^{-14}$
KS 1741-293†	Reflected	Hard	116.4	1.71	$(1.928 \pm 0.31) \times 10^{-13}$
	Reflected	Standard	121.1	1.35	$(1.123 \pm 0.15) \times 10^{-13}$
	Ring	Hard	119.8	1.71	$(1.123 \pm 0.15) \times 10^{-13}$
	Ring	Standard	122.9	1.35	$(7.190 \pm 1.55) \times 10^{-14}$
1741-322	Reflected	Hard	7.3	0.70	$< 5.190 \times 10^{-13}$
	Reflected	Standard	7.3	0.39	$< 5.234 \times 10^{-13}$
	Ring	Hard	7.3	0.70	$< 5.234 \times 10^{-13}$
	Ring	Standard	7.3	0.39	$< 6.941 \times 10^{-13}$
GPS 1742-326	Reflected	Hard	3.8	0.53	$< 2.196 \times 10^{-12}$
	Reflected	Standard	3.8	0.30	$< 3.465 \times 10^{-12}$
	Ring	Hard	3.8	0.53	$< 3.465 \times 10^{-12}$
	Ring	Standard	3.8	0.30	$< 3.617 \times 10^{-12}$

Target	Background	Cuts	$T_{\rm live}$ [h]	$E_{\rm Thresh}$ [TeV]	$F(E > E_{\rm Thresh})$
GC X-2†	Reflected	Hard	112.8	1.71	$(1.303 \pm 0.30) \times 10^{-13}$
	Reflected	Standard	114.9	1.36	$(1.007 \pm 0.15) \times 10^{-13}$
	Ring	Hard	95.2	1.70	$(1.007 \pm 0.15) \times 10^{-13}$
	Ring	Standard	118.8	1.36	$< 5.625 \times 10^{-14}$
AX J1745.6-2901†	Reflected	Hard	118.4	1.71	$(2.567 \pm 0.06) \times 10^{-12}$
	Reflected	Standard	121.4	1.35	$(9.174 \pm 0.20) \times 10^{-13}$
	Ring	Hard	118.8	1.71	$(9.174 \pm 0.20) \times 10^{-13}$
	Ring	Standard	121.8	1.35	$(9.082 \pm 0.20) \times 10^{-13}$
1E 1742.5-2845†	Reflected	Hard	117.0	1.71	$(2.745 \pm 0.32) \times 10^{-13}$
	Reflected	Standard	119.6	1.35	$(1.455 \pm 0.15) \times 10^{-13}$
	Ring	Hard	117.9	1.71	$(1.455 \pm 0.15) \times 10^{-13}$
	Ring	Standard	120.5	1.35	$(1.249 \pm 0.15) \times 10^{-13}$
XTE J1748-288†	Reflected	Hard	118.7	1.73	$(1.277 \pm 0.29) \times 10^{-13}$
	Reflected	Standard	121.3	1.35	$< 9.541 \times 10^{-14}$
	Ring	Hard	120.4	1.73	$< 9.541 \times 10^{-14}$
	Ring	Standard	123.0	1.35	$< 7.352 \times 10^{-14}$
AX J1749.1-2733‡	Reflected	Hard	76.3	1.73	$< 1.780 \times 10^{-13}$
	Reflected	Standard	77.2	1.37	$< 6.905 \times 10^{-14}$
	Ring	Hard	76.8	1.73	$< 6.905 \times 10^{-14}$
	Ring	Standard	79.3	1.37	$< 7.176 \times 10^{-14}$
AX J1749.2-2725‡	Reflected	Hard	60.5	1.74	$< 1.590 \times 10^{-13}$
	Reflected	Standard	61.6	1.36	$< 9.256 \times 10^{-14}$
	Ring	Hard	60.4	1.74	$< 9.256 \times 10^{-14}$
	Ring	Standard	62.1	1.36	$< 1.023 \times 10^{-13}$
GRO J1750-27‡	Reflected	Hard	17.9	1.20	$< 2.803 \times 10^{-13}$
	Reflected	Standard	18.7	0.64	$< 3.936 \times 10^{-13}$
	Ring	Hard	18.7	1.20	$< 3.936 \times 10^{-13}$
	Ring	Standard	18.7	0.64	$< 5.536 \times 10^{-13}$
SAX J1750.8-2900	Reflected	Hard	95.8	1.73	$< 5.903 \times 10^{-14}$
	Reflected	Standard	98.4	1.37	$< 3.614 \times 10^{-14}$
	Ring	Hard	95.8	1.73	$< 3.614 \times 10^{-14}$
	Ring	Standard	98.4	1.37	$< 6.049 \times 10^{-14}$
GX 1.1-01.0	Reflected	Hard	71.3	1.75	$< 7.663 \times 10^{-14}$
	Reflected	Standard	73.8	1.38	$< 2.714 \times 10^{-14}$
	Ring	Hard	72.1	1.75	$< 2.714 \times 10^{-14}$
	Ring	Standard	73.8	1.38	$< 5.318 \times 10^{-14}$
IGR J17544-2619	Reflected	Hard	16.9	0.82	$< 7.305 \times 10^{-13}$
	Reflected	Standard	17.3	0.45	$< 8.579 \times 10^{-13}$
	Ring	Hard	17.3	0.82	$< 8.579 \times 10^{-13}$
	Ring	Standard	17.3	0.45	$< 8.546 \times 10^{-13}$
XTE J1755-324	Reflected	Hard	1.3	0.58	$< 4.799 \times 10^{-12}$
	Reflected	Standard	1.3	0.32	$< 4.306 \times 10^{-12}$
	Ring	Hard	1.3	0.58	$< 4.306 \times 10^{-12}$
	Ring	Standard	1.3	0.32	$< 4.400 \times 10^{-12}$
4U 1755-338	Reflected	Hard	3.4	0.56	$< 1.183 \times 10^{-12}$
	Reflected	Standard	3.4	0.32	$< 1.564 \times 10^{-12}$
	Ring	Hard	3.4	0.56	$< 1.564 \times 10^{-12}$
	Ring	Standard	3.4	0.32	$< 1.328 \times 10^{-12}$
4U 1758-25‡	Reflected	Hard	7.4	0.70	$< 1.441 \times 10^{-12}$
	Reflected	Standard	7.4	0.39	$< 1.631 \times 10^{-12}$
	Ring	Hard	7.4	0.70	$< 1.631 \times 10^{-12}$
	Ring	Standard	7.4	0.39	$< 2.212 \times 10^{-12}$
GRS 1758-258	Reflected	Hard	3.8	0.67	$< 1.902 \times 10^{-12}$
	Reflected	Standard	3.8	0.37	$< 2.915 \times 10^{-12}$

Target	Background	Cuts	$T_{\rm live}$ [h]	$E_{\rm Thresh}$ [TeV]	$F(E > E_{\rm Thresh})$
	Ring	Hard	3.8	0.67	$< 2.915 \times 10^{-12}$
	Ring	Standard	3.8	0.37	$< 3.658 \times 10^{-12}$
4U 1758-20	Reflected	Hard	6.3	0.94	$< 3.824 \times 10^{-13}$
	Reflected	Standard	1.3	0.28	$< 2.824 \times 10^{-12}$
	Ring	Hard	6.7	0.94	$< 2.824 \times 10^{-12}$
	Ring	Standard	1.3	0.28	$< 3.263 \times 10^{-12}$
SAX J1802.7-2017	Reflected	Hard	10.6	0.94	$< 4.489 \times 10^{-13}$
	Reflected	Standard	1.3	0.28	$< 6.545 \times 10^{-12}$
	Ring	Hard	10.6	0.94	$< 6.545 \times 10^{-12}$
	Ring	Standard	1.3	0.28	$< 6.889 \times 10^{-12}$
2S 1803-245	Reflected	Hard	2.7	0.69	$< 2.001 \times 10^{-12}$
	Reflected	Standard	2.7	0.37	$< 1.963 \times 10^{-12}$
	Ring	Hard	2.7	0.69	$< 1.963 \times 10^{-12}$
	Ring	Standard	2.7	0.37	$< 2.051 \times 10^{-12}$
XTE J1806-246	Reflected	Hard	2.7	0.69	$< 2.018 \times 10^{-12}$
	Reflected	Standard	2.7	0.37	$< 1.919 \times 10^{-12}$
	Ring	Hard	2.7	0.69	$< 1.919 \times 10^{-12}$
	Ring	Standard	2.7	0.37	$< 2.104 \times 10^{-12}$
4U 1811-17[‡]	Reflected	Hard	7.1	1.03	$< 1.508 \times 10^{-12}$
	Reflected	Standard	7.9	0.55	$< 9.267 \times 10^{-13}$
	Ring	Hard	7.9	1.03	$< 9.267 \times 10^{-13}$
	Ring	Standard	8.3	0.55	$< 9.663 \times 10^{-13}$
4U 1813-14	Reflected	Hard	0.4	0.50	$< 5.438 \times 10^{-12}$
	Reflected	Standard	0.4	0.26	$< 5.845 \times 10^{-12}$
	Ring	Hard	0.4	0.50	$< 5.845 \times 10^{-12}$
	Ring	Standard	0.4	0.26	$< 6.381 \times 10^{-12}$
SAX J1818.6-1703	Reflected	Hard	5.5	1.07	$< 1.179 \times 10^{-12}$
	Reflected	Standard	5.5	0.55	$< 7.911 \times 10^{-13}$
	Ring	Hard	5.5	1.07	$< 7.911 \times 10^{-13}$
	Ring	Standard	5.5	0.55	$< 8.951 \times 10^{-13}$
SAX J1819.3-2525	Reflected	Hard	3.5	0.78	$< 1.079 \times 10^{-12}$
	Reflected	Standard	3.5	0.44	$< 1.498 \times 10^{-12}$
	Ring	Hard	3.5	0.78	$< 1.498 \times 10^{-12}$
	Ring	Standard	3.5	0.44	$< 1.569 \times 10^{-12}$
RX J1826.2-1450[†]	Reflected	Hard	67.4	1.94	$(1.649 \pm 0.06) \times 10^{-12}$
	Reflected	Standard	68.2	1.48	$(5.160 \pm 0.19) \times 10^{-13}$
	Ring	Hard	67.8	1.94	$(5.160 \pm 0.19) \times 10^{-13}$
	Ring	Standard	68.2	1.48	$(5.188 \pm 0.19) \times 10^{-13}$
XTE J1829-098	Reflected	Hard	12.3	0.86	$< 7.932 \times 10^{-13}$
	Reflected	Standard	12.3	0.46	$< 1.481 \times 10^{-12}$
	Ring	Hard	12.3	0.86	$< 1.481 \times 10^{-12}$
	Ring	Standard	12.3	0.46	$< 1.451 \times 10^{-12}$
H 1833-076[‡]	Reflected	Hard	18.6	1.52	$< 3.946 \times 10^{-13}$
	Reflected	Standard	19.4	0.76	$< 5.050 \times 10^{-13}$
	Ring	Hard	19.0	1.52	$< 5.050 \times 10^{-13}$
	Ring	Standard	19.4	0.76	$< 3.325 \times 10^{-13}$
GS 1839-06[†]	Reflected	Hard	31.0	1.99	$(1.618 \pm 0.46) \times 10^{-13}$
	Reflected	Standard	31.4	1.35	$(1.750 \pm 0.31) \times 10^{-13}$
	Ring	Hard	31.0	1.99	$(1.750 \pm 0.31) \times 10^{-13}$
	Ring	Standard	31.4	1.35	$< 1.926 \times 10^{-13}$
GS 1839-04	Reflected	Hard	19.5	1.92	$< 2.402 \times 10^{-13}$
	Reflected	Standard	20.0	1.07	$< 2.535 \times 10^{-13}$
	Ring	Hard	19.5	1.92	$< 2.535 \times 10^{-13}$
	Ring	Standard	20.0	1.07	$< 2.735 \times 10^{-13}$

Target	Background	Cuts	$T_{\rm live}$ [h]	$E_{\rm Thresh}$ [TeV]	$F(E > E_{\rm Thresh})$
AX 1845.0-0433	Reflected	Hard	18.2	1.92	$< 2.258 \times 10^{-13}$
	Reflected	Standard	18.7	1.02	$< 2.429 \times 10^{-13}$
	Ring	Hard	18.2	1.92	$< 2.429 \times 10^{-13}$
	Ring	Standard	18.7	1.02	$< 2.610 \times 10^{-13}$
GS 1843+009	Reflected	Hard	2.9	1.00	$< 1.474 \times 10^{-12}$
	Reflected	Standard	2.9	0.52	$< 1.302 \times 10^{-12}$
	Ring	Hard	2.9	1.00	$< 1.302 \times 10^{-12}$
	Ring	Standard	2.9	0.52	$< 1.265 \times 10^{-12}$
2S 1845-024‡	Reflected	Hard	31.0	1.92	$< 1.758 \times 10^{-13}$
	Reflected	Standard	31.4	1.06	$< 1.763 \times 10^{-13}$
	Ring	Hard	31.0	1.92	$< 1.763 \times 10^{-13}$
	Ring	Standard	31.4	1.06	$< 1.440 \times 10^{-13}$
IGR J18483-0311‡	Reflected	Hard	22.2	1.93	$< 2.543 \times 10^{-13}$
	Reflected	Standard	22.7	1.02	$< 1.080 \times 10^{-13}$
	Ring	Hard	24.4	1.93	$< 1.080 \times 10^{-13}$
	Ring	Standard	24.4	1.02	$< 1.096 \times 10^{-13}$
EXO 1846-031‡	Reflected	Hard	18.6	1.90	$< 1.352 \times 10^{-13}$
	Reflected	Standard	19.0	1.02	$< 1.146 \times 10^{-13}$
	Ring	Hard	19.0	1.90	$< 1.146 \times 10^{-13}$
	Ring	Standard	19.5	1.02	$< 1.296 \times 10^{-13}$
XTE J1855-026	Reflected	Hard	1.3	1.07	$< 1.874 \times 10^{-12}$
	Reflected	Standard	1.3	0.55	$< 3.193 \times 10^{-12}$
	Ring	Hard	1.3	1.07	$< 3.193 \times 10^{-12}$
	Ring	Standard	1.3	0.55	$< 2.601 \times 10^{-12}$
XTE J1856+053	Reflected	Hard	0.2	0.58	$< 1.713 \times 10^{-11}$
	Reflected	Standard	0.2	0.30	$< 9.234 \times 10^{-12}$
	Ring	Hard	0.2	0.58	$< 9.234 \times 10^{-12}$
	Ring	Standard	0.2	0.30	$< 9.813 \times 10^{-12}$
XTE J1858+034‡	Reflected	Hard	4.5	1.16	$< 9.629 \times 10^{-13}$
	Reflected	Standard	4.5	0.61	$< 1.543 \times 10^{-12}$
	Ring	Hard	4.5	1.16	$< 1.543 \times 10^{-12}$
	Ring	Standard	4.5	0.61	$< 1.568 \times 10^{-12}$
XTE J1901+014	Reflected	Hard	9.8	0.85	$< 7.601 \times 10^{-13}$
	Reflected	Standard	10.2	0.78	$< 3.826 \times 10^{-13}$
	Ring	Hard	10.2	1.55	$< 3.826 \times 10^{-13}$
	Ring	Standard	10.2	0.78	$< 5.429 \times 10^{-13}$
4U 1901+03	Reflected	Hard	4.7	1.43	$< 7.206 \times 10^{-13}$
	Reflected	Standard	4.7	0.72	$< 6.412 \times 10^{-13}$
	Ring	Hard	4.7	1.43	$< 6.412 \times 10^{-13}$
	Ring	Standard	4.7	0.72	$< 5.279 \times 10^{-13}$
XTE J1906+09	Reflected	Hard	3.1	1.69	$< 5.184 \times 10^{-13}$
	Reflected	Standard	3.1	0.86	$< 6.158 \times 10^{-13}$
	Ring	Hard	3.1	1.69	$< 6.158 \times 10^{-13}$
	Ring	Standard	3.1	0.86	$< 4.616 \times 10^{-13}$
4U 1907+09‡	Reflected	Hard	10.3	1.59	$< 3.204 \times 10^{-13}$
	Reflected	Standard	10.3	0.85	$< 6.379 \times 10^{-13}$
	Ring	Hard	10.3	1.59	$< 6.379 \times 10^{-13}$
	Ring	Standard	10.3	0.85	$< 6.815 \times 10^{-13}$
4U 1909+07	Reflected	Hard	5.2	1.62	$< 5.320 \times 10^{-13}$
	Reflected	Standard	5.2	0.85	$< 4.231 \times 10^{-13}$
	Ring	Hard	5.2	1.62	$< 4.231 \times 10^{-13}$
	Ring	Standard	5.2	0.85	$< 4.033 \times 10^{-13}$
3A 1909+048	Reflected	Hard	6.3	1.22	$< 6.048 \times 10^{-13}$
	Reflected	Standard	6.8	0.65	$< 5.240 \times 10^{-13}$

Target	Background	Cuts	$T_{\rm live}$ [h]	$E_{\rm Thresh}$ [TeV]	$F(E > E_{\rm Thresh})$
	Ring	Hard	7.2	1.22	$< 5.240 \times 10^{-13}$
	Ring	Standard	7.2	0.65	$< 6.569 \times 10^{-13}$
IGR J19140+0951[†]	Reflected	Hard	14.8	1.69	$< 3.726 \times 10^{-13}$
	Reflected	Standard	14.8	0.87	$< 4.878 \times 10^{-13}$
	Ring	Hard	14.8	1.69	$< 4.878 \times 10^{-13}$
	Ring	Standard	14.8	0.87	$< 5.092 \times 10^{-13}$
GRS 1915+105[‡]	Reflected	Hard	10.6	1.28	$< 4.295 \times 10^{-13}$
	Reflected	Standard	10.6	0.69	$< 4.840 \times 10^{-13}$
	Ring	Hard	10.6	1.28	$< 4.840 \times 10^{-13}$
	Ring	Standard	10.6	0.69	$< 5.309 \times 10^{-13}$
4U 1918+15	Reflected	Hard	0.9	1.16	$< 1.629 \times 10^{-12}$
	Reflected	Standard	0.9	0.62	$< 2.454 \times 10^{-12}$
	Ring	Hard	1.3	1.26	$< 2.454 \times 10^{-12}$
	Ring	Standard	1.3	0.67	$< 1.373 \times 10^{-12}$
4U 2129+12	Reflected	Hard	7.7	0.94	$< 2.147 \times 10^{-13}$
	Reflected	Standard	7.3	0.50	$< 7.639 \times 10^{-13}$
	Ring	Hard	7.7	0.94	$< 7.639 \times 10^{-13}$
	Ring	Standard	7.7	0.50	$< 8.138 \times 10^{-13}$

Table A.3: Table listing the variability properties corresponding to the nominal positions of all targets in the survey. Values are listed which correspond to the false alarm probabilities for secular ($P_{\rm fa}^{\rm sec}$) and excess ($P_{\rm fa}^{\rm add}$) variability, in addition to the maximum calculated Lomb-Scargle power ($z_{\rm max}$) and the best fitting Lomb-Scargle period ($P_{\rm best}$). If a periodicity has been identified at lower energies, then the corresponding period ($P_{\rm known}$) is also given.

Target	Background	Cuts	Slope	$P_{\rm fa}^{\rm sec}$	$P_{\rm fa}^{\rm add}$	$z_{\rm max}$	$P_{\rm best}$ [d]	$P_{\rm known}$ [d]
SAX J0635.2+0533	Reflected	Hard	-	-	-	-	-	-
	Reflected	Standard	-6.877×10^{-16}	0.360374	0.0968809	-	-	-
	Ring	Hard	-	-	-	-	-	-
	Ring	Standard	-8.895×10^{-16}	0.175197	0.0776413	-	-	-
4U 0900-40	Reflected	Hard	-	-	-	-	-	-
	Reflected	Standard	-3.284×10^{-16}	0.944232	0.69643	-	-	-
	Ring	Hard	-	-	-	-	-	-
	Ring	Standard	-2.390×10^{-15}	0.597251	0.730967	-	-	-
RX J1037.5-5647	Reflected	Hard	-	-	-	-	-	-
	Reflected	Standard	2.089×10^{-14}	0.264128	0.539713	-	-	-
	Ring	Hard	-	-	-	-	-	-
	Ring	Standard	1.079×10^{-14}	0.530836	0.742525	-	-	-
4U 1223-624	Reflected	Hard	-	-	-	-	-	-
	Reflected	Standard	3.951×10^{-14}	0.255056	0.413254	-	-	-
	Ring	Hard	-	-	-	-	-	-
	Ring	Standard	2.163×10^{-14}	0.516045	0.621426	-	-	-
1H 1249-637	Reflected	Hard	-	-	-	-	-	-
	Reflected	Standard	2.078×10^{-14}	0.576712	0.724441	-	-	-
	Ring	Hard	-	-	-	-	-	-
	Ring	Standard	2.012×10^{-14}	0.639691	0.513824	-	-	-
4U 1258-61	Reflected	Hard	-	-	-	-	-	-
	Reflected	Standard	-8.449×10^{-13}	0.372013	0.859561	-	-	-
	Ring	Hard	-	-	-	-	-	-
	Ring	Standard	-2.104×10^{-12}	0.0917405	0.460013	-	-	-
2RXP J130159.6-635806†	Reflected	Hard	-1.342×10^{-15}	0.079469	0.808324	-	-	-
	Reflected	Standard	-2.563×10^{-16}	0.272739	0.214251	8.18224	0.668292	-
	Ring	Hard	-1.744×10^{-15}	0.938246	0.895591	-	-	-
	Ring	Standard	-9.838×10^{-17}	0.515408	0.690897	10.1186	0.688075	-
SAX J1324.4-6200	Reflected	Hard	-	-	-	-	-	-
	Reflected	Standard	-4.049×10^{-13}	0.574551	0.376796	-	-	-
	Ring	Hard	-	-	-	-	-	-
	Ring	Standard	3.899×10^{-14}	0.913194	0.664108	-	-	-
4U 1323-62	Reflected	Hard	-	-	-	-	-	-
	Reflected	Standard	5.389×10^{-13}	0.23364	0.546668	-	-	-
	Ring	Hard	-	-	-	-	-	-
	Ring	Standard	7.272×10^{-13}	0.0239652	0.385963	-	-	-
2S 1417-624	Reflected	Hard	-	-	-	-	-	-
	Reflected	Standard	-3.304×10^{-15}	0.74375	0.480295	-	-	-
	Ring	Hard	-	-	-	-	-	-
	Ring	Standard	-7.970×10^{-17}	0.992741	0.473068	-	-	-
SAX J1452.8-5949	Reflected	Hard	-	-	-	-	-	-
	Reflected	Standard	1.957×10^{-13}	0.244515	0.162209	-	-	-
	Ring	Hard	-	-	-	-	-	-
	Ring	Standard	2.659×10^{-15}	0.89247	0.733655	-	-	-
3A 1516-569	Reflected	Hard	2.308×10^{-15}	0.0112622	0.979833	-	-	-
	Reflected	Standard	2.105×10^{-16}	0.645259	0.792408	4.43193	0.621335	16.6
	Ring	Hard	-	-	-	-	-	-
	Ring	Standard	-6.157×10^{-17}	0.846181	0.811336	8.23043	0.984752	16.6

Target	Background	Cuts	Slope	$P_{\rm fa}^{\rm sec}$	$P_{\rm fa}^{\rm add}$	$z_{\rm max}$	$P_{\rm best}$ [d]	$P_{\rm known}$ [d]
4U 1538-52	Reflected	Hard	-	-	-	-	-	-
	Reflected	Standard	2.300×10^{-15}	0.407931	0.555336	-	-	-
	Ring	Hard	-	-	-	-	-	-
	Ring	Standard	2.317×10^{-15}	0.187198	0.718695	-	-	-
XTE J1543-568	Reflected	Hard	-	-	-	-	-	-
	Reflected	Standard	-	-	-	-	-	-
	Ring	Hard	-	-	-	-	-	-
	Ring	Standard	-1.165×10^{-12}	0.688712	0.998157	-	-	-
1H 1555-552	Reflected	Hard	-	-	-	-	-	-
	Reflected	Standard	-5.712×10^{-14}	0.407842	0.657382	-	-	-
	Ring	Hard	-	-	-	-	-	-
	Ring	Standard	-3.561×10^{-14}	0.558442	0.810531	-	-	-
2S 1553-542	Reflected	Hard	-	-	-	-	-	-
	Reflected	Standard	-9.836×10^{-14}	0.159526	0.0550772	-	-	-
	Ring	Hard	-	-	-	-	-	-
	Ring	Standard	-5.608×10^{-14}	0.367911	0.00132583	-	-	-
4U 1608-52‡	Reflected	Hard	-	-	-	-	-	-
	Reflected	Standard	-1.206×10^{-15}	0.152721	0.453902	-	-	-
	Ring	Hard	-	-	-	-	-	-
	Ring	Standard	7.141×10^{-17}	0.910212	0.823686	-	-	-
IGR J16195-4945‡	Reflected	Hard	-	-	-	-	-	-
	Reflected	Standard	7.343×10^{-16}	0.740826	0.390842	-	-	-
	Ring	Hard	-	-	-	-	-	-
	Ring	Standard	-4.709×10^{-16}	0.815818	0.586044	-	-	-
H 1617-155	Reflected	Hard	-	-	-	-	-	-
	Reflected	Standard	-1.742×10^{-13}	0.433429	0.703732	-	-	-
	Ring	Hard	-	-	-	-	-	-
	Ring	Standard	-4.107×10^{-14}	0.822405	0.873167	-	-	-
4U 1624-49‡	Reflected	Hard	-	-	-	-	-	-
	Reflected	Standard	-7.659×10^{-17}	0.976382	0.592303	-	-	-
	Ring	Hard	-	-	-	-	-	-
	Ring	Standard	-1.338×10^{-15}	0.514219	0.868328	-	-	-
IGR J16283-4838‡	Reflected	Hard	-	-	-	-	-	-
	Reflected	Standard	5.329×10^{-16}	0.838967	0.669271	-	-	-
	Ring	Hard	-	-	-	-	-	-
	Ring	Standard	2.466×10^{-15}	0.204052	0.886987	-	-	-
IGR J16318-4848	Reflected	Hard	-	-	-	-	-	-
	Reflected	Standard	-5.328×10^{-15}	0.116744	0.524876	-	-	-
	Ring	Hard	-	-	-	-	-	-
	Ring	Standard	-4.729×10^{-16}	0.902448	0.0962923	-	-	-
IGR J16320-4751†	Reflected	Hard	-4.367×10^{-15}	0.398488	0.747991	-	-	-
	Reflected	Standard	-2.709×10^{-15}	0.538245	0.167816	2.14296	0.63438	8.96
	Ring	Hard	-8.329×10^{-16}	0.816029	0.899731	-	-	-
	Ring	Standard	-1.539×10^{-15}	0.716797	0.12812	2.53165	1.13148	8.96
4U 1630-47†	Reflected	Hard	2.446×10^{-15}	0.618163	0.88595	-	-	-
	Reflected	Standard	6.814×10^{-16}	0.828477	0.928585	-	-	-
	Ring	Hard	7.416×10^{-17}	0.976678	0.980385	-	-	-
	Ring	Standard	3.421×10^{-15}	0.330299	0.801766	-	-	-
IGR J16358-4726†	Reflected	Hard	-1.056×10^{-16}	0.953603	0.998958	-	-	-
	Reflected	Standard	2.876×10^{-15}	0.571589	0.369863	-	-	-
	Ring	Hard	1.368×10^{-15}	0.36059	0.998534	-	-	-
	Ring	Standard	1.023×10^{-16}	0.979001	0.379834	-	-	-
GRS 1632-477‡	Reflected	Hard	-	-	-	-	-	-
	Reflected	Standard	5.784×10^{-15}	0.068343	0.760268	-	-	-

Target	Background	Cuts	Slope	$P_{\rm fa}^{\rm sec}$	$P_{\rm fa}^{\rm add}$	$z_{\rm max}$	$P_{\rm best}$ [d]	$P_{\rm known}$ [d]
	Ring	Hard	-	-	-	-	-	-
	Ring	Standard	5.431×10^{-15}	0.119569	0.395113	-	-	-
AX J1639.0-4642‡	Reflected	Hard	-	-	-	-	-	-
	Reflected	Standard	9.729×10^{-16}	0.551795	0.925834	-	-	-
	Ring	Hard	-7.098×10^{-15}	0.388585	0.987495	-	-	-
	Ring	Standard	2.202×10^{-15}	0.0979265	0.946709	-	-	-
IGR J16418-4532	Reflected	Hard	-	-	-	-	-	-
	Reflected	Standard	-2.410×10^{-15}	0.840655	0.881003	-	-	-
	Ring	Hard	-	-	-	-	-	-
	Ring	Standard	-9.964×10^{-16}	0.934568	0.899739	-	-	-
4U 1642-45	Reflected	Hard	-	-	-	-	-	-
	Reflected	Standard	-1.172×10^{-15}	0.948001	0.211731	-	-	-
	Ring	Hard	-	-	-	-	-	-
	Ring	Standard	2.119×10^{-15}	0.894643	0.467179	-	-	-
IGR J16465-4507	Reflected	Hard	-	-	-	-	-	-
	Reflected	Standard	-3.492×10^{-14}	0.463163	0.00970485	-	-	-
	Ring	Hard	-	-	-	-	-	-
	Ring	Standard	-1.432×10^{-15}	0.940498	0.178458	-	-	-
IGR J16479-4514	Reflected	Hard	-	-	-	-	-	-
	Reflected	Standard	-2.545×10^{-15}	0.878813	0.847621	-	-	-
	Ring	Hard	-	-	-	-	-	-
	Ring	Standard	7.363×10^{-15}	0.383184	0.966474	-	-	-
IGR J16493-4348	Reflected	Hard	-	-	-	-	-	-
	Reflected	Standard	-1.858×10^{-14}	0.596137	0.323331	-	-	-
	Ring	Hard	-	-	-	-	-	-
	Ring	Standard	-8.109×10^{-16}	0.98026	0.339719	-	-	-
AX J1700-419‡	Reflected	Hard	-	-	-	-	-	-
	Reflected	Standard	8.970×10^{-15}	0.151361	0.0292711	-	-	-
	Ring	Hard	-	-	-	-	-	-
	Ring	Standard	4.163×10^{-15}	0.287475	0.245891	-	-	-
OAO 1657-415‡	Reflected	Hard	-	-	-	-	-	-
	Reflected	Standard	-2.485×10^{-15}	0.659768	0.368099	-	-	-
	Ring	Hard	-	-	-	-	-	-
	Ring	Standard	-4.327×10^{-16}	0.902688	0.840439	-	-	-
4U 1659-487	Reflected	Hard	-	-	-	-	-	-
	Reflected	Standard	-2.637×10^{-13}	0.626049	0.446585	-	-	-
	Ring	Hard	-	-	-	-	-	-
	Ring	Standard	1.161×10^{-15}	0.65002	0.498895	-	-	-
4U 1700-37	Reflected	Hard	-	-	-	-	-	-
	Reflected	Standard	-3.475×10^{-15}	0.12017	0.0400653	-	-	-
	Ring	Hard	-	-	-	-	-	-
	Ring	Standard	-3.844×10^{-15}	0.0898371	0.0395381	-	-	-
4U 1702-429	Reflected	Hard	-	-	-	-	-	-
	Reflected	Standard	1.987×10^{-16}	0.844882	0.141215	-	-	-
	Ring	Hard	-	-	-	-	-	-
	Ring	Standard	7.076×10^{-16}	0.406833	0.319352	-	-	-
4U 1705-44	Reflected	Hard	-	-	-	-	-	-
	Reflected	Standard	-8.749×10^{-16}	0.723806	0.380801	1.51134	1.0013	-
	Ring	Hard	-	-	-	-	-	-
	Ring	Standard	1.260×10^{-15}	0.631453	0.399339	2.14942	1.0013	-
4U 1708-40‡	Reflected	Hard	-	-	-	-	-	-
	Reflected	Standard	6.611×10^{-16}	0.296139	0.576255	8.2257	0.716296	-
	Ring	Hard	-	-	-	-	-	-
	Ring	Standard	5.952×10^{-16}	0.185424	0.513844	7.96567	0.596094	-

Target	Background	Cuts	Slope	$P_{\rm fa}^{\rm sec}$	$P_{\rm fa}^{\rm add}$	$z_{\rm max}$	$P_{\rm best}$ [d]	$P_{\rm known}$ [d]
SAX J1712.6-3739‡	Reflected	Hard	-7.562×10^{-15}	0.034398	0.84182	-	-	-
	Reflected	Standard	8.770×10^{-16}	0.152968	0.384157	17.1472	0.716864	-
	Ring	Hard	-	-	-	-	-	-
	Ring	Standard	1.731×10^{-16}	0.777018	0.259594	11.9911	0.716864	-
1RXS J171824.2-402934‡	Reflected	Hard	-	-	-	-	-	-
	Reflected	Standard	-1.325×10^{-15}	0.0479291	0.596356	-	-	-
	Ring	Hard	-	-	-	-	-	-
	Ring	Standard	-1.240×10^{-15}	0.00807465	0.408763	7.86413	0.724957	-
XTE J1723-376	Reflected	Hard	-	-	-	-	-	-
	Reflected	Standard	-3.740×10^{-15}	0.330941	0.575661	-	-	-
	Ring	Hard	-	-	-	-	-	-
	Ring	Standard	-5.851×10^{-15}	0.185583	0.205705	-	-	-
EXO 1722-363	Reflected	Hard	-	-	-	-	-	-
	Reflected	Standard	-7.823×10^{-16}	0.271432	0.45249	-	-	-
	Ring	Hard	-	-	-	-	-	-
	Ring	Standard	-4.979×10^{-16}	0.387719	0.860971	-	-	-
4U 1724-307	Reflected	Hard	-	-	-	-	-	-
	Reflected	Standard	-5.821×10^{-16}	0.900626	0.0137695	-	-	-
	Ring	Hard	-	-	-	-	-	-
	Ring	Standard	3.866×10^{-16}	0.924542	0.0358524	-	-	-
X1724-356	Reflected	Hard	-	-	-	-	-	-
	Reflected	Standard	-3.702×10^{-16}	0.808659	0.0341375	-	-	-
	Ring	Hard	-	-	-	-	-	-
	Ring	Standard	1.592×10^{-16}	0.845289	0.137381	8.38922	4.71721	-
4U 1728-337	Reflected	Hard	-	-	-	-	-	-
	Reflected	Standard	-8.938×10^{-16}	0.317392	0.497295	-	-	-
	Ring	Hard	-	-	-	-	-	-
	Ring	Standard	-8.660×10^{-17}	0.918864	0.123407	7.76566	16.0384	-
MXB 1730-335	Reflected	Hard	-	-	-	-	-	-
	Reflected	Standard	1.221×10^{-15}	0.106542	0.481673	-	-	-
	Ring	Hard	-	-	-	-	-	-
	Ring	Standard	1.000×10^{-15}	0.158003	0.689367	-	-	-
GRS 1730-312	Reflected	Hard	-	-	-	-	-	-
	Reflected	Standard	2.433×10^{-15}	0.0321207	0.210143	-	-	-
	Ring	Hard	-	-	-	-	-	-
	Ring	Standard	1.553×10^{-15}	0.0667366	0.147977	-	-	-
4U 1730-220	Reflected	Hard	-	-	-	-	-	-
	Reflected	Standard	-6.537×10^{-16}	0.756882	0.0694566	-	-	-
	Ring	Hard	-	-	-	-	-	-
	Ring	Standard	3.964×10^{-16}	0.835573	0.194173	-	-	-
SLX 1732-304	Reflected	Hard	-	-	-	-	-	-
	Reflected	Standard	2.421×10^{-16}	0.569746	0.0438419	-	-	-
	Ring	Hard	-	-	-	-	-	-
	Ring	Standard	-7.883×10^{-17}	0.687713	0.757753	9.02795	1.00114	-
1734-292	Reflected	Hard	2.827×10^{-15}	0.438364	0.770175	-	-	-
	Reflected	Standard	-7.385×10^{-17}	0.750675	0.245071	8.19207	2.73265	-
	Ring	Hard	-	-	-	-	-	-
	Ring	Standard	7.289×10^{-18}	0.970806	0.582788	7.56296	3.3507	-
4U 1735-28	Reflected	Hard	1.293×10^{-15}	0.152452	0.984609	-	-	-
	Reflected	Standard	1.568×10^{-16}	0.65133	0.885308	12.3842	1.98785	-
	Ring	Hard	-1.607×10^{-16}	0.834203	0.997262	-	-	-
	Ring	Standard	2.004×10^{-17}	0.95705	0.759471	16.8277	1.73861	-
XTE J1739-302‡	Reflected	Hard	-	-	-	-	-	-
	Reflected	Standard	5.885×10^{-17}	0.919741	0.203899	9.06797	0.598819	-

Target	Background	Cuts	Slope	$P_{\rm fa}^{\rm sec}$	$P_{\rm fa}^{\rm add}$	$z_{\rm max}$	$P_{\rm best}$ [d]	$P_{\rm known}$ [d]
	Ring	Hard	-	-	-	-	-	-
	Ring	Standard	-5.957×10^{-17}	0.745988	0.0979458	7.16285	0.585146	-
RX J1739.4-2942	Reflected	Hard	5.165×10^{-16}	0.611189	0.999615	-	-	-
	Reflected	Standard	3.683×10^{-17}	0.807707	0.10615	7.16297	5.05748	-
	Ring	Hard	7.859×10^{-16}	0.635609	0.973772	-	-	-
	Ring	Standard	1.915×10^{-18}	0.989515	0.127339	6.96393	0.964487	-
RX J1739.4-2942	Reflected	Hard	6.676×10^{-17}	0.872658	0.999995	-	-	-
	Reflected	Standard	4.886×10^{-17}	0.730986	0.412242	7.65947	29.3826	-
	Ring	Hard	-9.678×10^{-16}	0.343166	0.998432	-	-	-
	Ring	Standard	7.889×10^{-18}	0.955781	0.300716	7.50842	2.03322	-
GRS 1737-31‡	Reflected	Hard	-	-	-	-	-	-
	Reflected	Standard	1.897×10^{-16}	0.265481	0.896586	4.51985	0.664433	-
	Ring	Hard	-	-	-	-	-	-
	Ring	Standard	7.052×10^{-17}	0.720025	0.483957	4.83212	0.504812	-
AX J1740.1-2847	Reflected	Hard	-6.842×10^{-16}	0.754091	0.958035	-	-	-
	Reflected	Standard	-3.634×10^{-16}	0.0960341	0.665442	9.85091	0.508824	-
	Ring	Hard	-6.279×10^{-17}	0.964178	0.984202	-	-	-
	Ring	Standard	-3.425×10^{-16}	0.0653095	0.432416	10.1942	0.805814	-
SLX 1737-282	Reflected	Hard	1.188×10^{-15}	0.121569	0.999925	-	-	-
	Reflected	Standard	2.007×10^{-16}	0.304805	0.208281	5.22658	0.603116	-
	Ring	Hard	2.723×10^{-16}	0.745516	0.999308	-	-	-
	Ring	Standard	1.968×10^{-16}	0.285205	0.358649	4.66842	0.511341	-
GRS 1739-278	Reflected	Hard	-4.239×10^{-16}	0.525752	0.998019	-	-	-
	Reflected	Standard	3.889×10^{-16}	0.0746814	0.208988	7.30822	0.686784	-
	Ring	Hard	1.339×10^{-15}	0.800925	0.998456	-	-	-
	Ring	Standard	2.317×10^{-16}	0.203452	0.561121	7.21364	0.616227	-
KS 1739-304‡	Reflected	Hard	1.846×10^{-15}	0.0621874	0.96004	-	-	-
	Reflected	Standard	-9.738×10^{-17}	0.485996	0.139466	10.4344	0.859465	-
	Ring	Hard	1.867×10^{-15}	0.364767	0.953786	-	-	-
	Ring	Standard	-3.662×10^{-17}	0.737223	0.736189	7.81907	0.915762	-
GC X-4†	Reflected	Hard	-2.817×10^{-16}	0.728399	0.975329	-	-	-
	Reflected	Standard	-1.879×10^{-16}	0.378288	0.0051718	7.07842	0.554908	-
	Ring	Hard	-2.444×10^{-16}	0.5887	0.999997	7.25188	3.5287	-
	Ring	Standard	-1.177×10^{-16}	0.427173	0.0471924	5.41276	0.531058	-
1E 1740.7-2942‡	Reflected	Hard	-4.844×10^{-17}	0.889772	0.999999	9.87927	0.578213	-
	Reflected	Standard	-3.384×10^{-16}	0.00483427	0.521454	12.0916	1.27482	-
	Ring	Hard	5.108×10^{-17}	0.836991	1	7.87708	1.3713	-
	Ring	Standard	-1.148×10^{-16}	0.253887	0.194666	11.8539	1.58618	-
GRS 1741.2-2859†	Reflected	Hard	4.515×10^{-16}	0.401676	0.999968	15.6366	0.98356	-
	Reflected	Standard	-5.326×10^{-17}	0.773615	0.94207	4.51643	0.505516	-
	Ring	Hard	-2.516×10^{-16}	0.537783	1	9.3827	0.731675	-
	Ring	Standard	-2.802×10^{-17}	0.827901	0.730509	6.68931	0.716169	-
GRO J1744-28†	Reflected	Hard	3.901×10^{-16}	0.707109	0.995872	-	-	-
	Reflected	Standard	-5.277×10^{-16}	0.0146842	0.000142023	10.311	0.825029	11.8342
	Ring	Hard	4.100×10^{-16}	0.323369	1	8.32368	0.681492	11.8342
	Ring	Standard	-2.388×10^{-16}	0.0995508	0.00201301	12.0826	0.825108	11.8342
RX J1744.7-2713	Reflected	Hard	7.055×10^{-16}	0.862577	0.767834	-	-	-
	Reflected	Standard	3.925×10^{-17}	0.87864	0.011966	14.3382	0.911556	-
	Ring	Hard	1.148×10^{-15}	0.54536	0.972646	-	-	-
	Ring	Standard	8.364×10^{-17}	0.671605	0.143016	10.2547	10.8486	-
KS 1741-293†	Reflected	Hard	-6.761×10^{-16}	0.202358	0.999964	4.77872	1.0763	-
	Reflected	Standard	-4.221×10^{-16}	0.0268768	0.152596	6.29278	0.72823	-
	Ring	Hard	8.425×10^{-17}	0.816058	1	5.21138	0.812515	-
	Ring	Standard	-2.907×10^{-16}	0.0425286	0.188441	8.07972	0.741553	-

Target	Background	Cuts	Slope	$P_{\rm fa}^{\rm sec}$	$P_{\rm fa}^{\rm add}$	$z_{\rm max}$	$P_{\rm best}$ [d]	$P_{\rm known}$ [d]
1741-322	Reflected	Hard	-	-	-	-	-	-
	Reflected	Standard	1.811×10^{-15}	0.0641902	0.180643	-	-	-
	Ring	Hard	-	-	-	-	-	-
	Ring	Standard	1.222×10^{-15}	0.165769	0.464513	-	-	-
GPS 1742-326	Reflected	Hard	-	-	-	-	-	-
	Reflected	Standard	2.164×10^{-15}	0.20268	0.523878	-	-	-
	Ring	Hard	-	-	-	-	-	-
	Ring	Standard	1.380×10^{-15}	0.480828	0.376013	-	-	-
GC X-2†	Reflected	Hard	-2.850×10^{-16}	0.457535	0.999998	6.56502	0.575949	-
	Reflected	Standard	2.275×10^{-16}	0.190114	0.241614	7.22592	0.979534	-
	Ring	Hard	5.415×10^{-16}	0.317489	0.999998	5.172	0.912538	-
	Ring	Standard	4.161×10^{-16}	0.0022418	0.49478	6.72115	0.658849	-
AX J1745.6-2901†	Reflected	Hard	-6.583×10^{-16}	0.412412	0.0366295	13.7442	13.4417	0.35
	Reflected	Standard	-7.357×10^{-16}	0.0505523	0.00198824	14.7921	0.510428	0.35
	Ring	Hard	-1.340×10^{-15}	0.0353871	0.00645099	12.3148	0.517795	0.35
	Ring	Standard	-4.130×10^{-16}	0.0335405	0.00803167	15.1654	0.997434	0.35
1E 1742.5-2845†	Reflected	Hard	7.875×10^{-17}	0.870918	0.999989	4.88483	0.994517	-
	Reflected	Standard	-7.645×10^{-17}	0.653513	0.948389	7.29254	2.81033	-
	Ring	Hard	3.995×10^{-16}	0.255893	1	6.0616	0.824641	-
	Ring	Standard	-2.263×10^{-16}	0.0898128	0.439529	8.17451	0.506916	-
XTE J1748-288†	Reflected	Hard	9.034×10^{-16}	0.32853	0.999446	8.37298	0.819817	-
	Reflected	Standard	2.065×10^{-16}	0.271367	0.517987	9.81004	0.622087	-
	Ring	Hard	5.109×10^{-16}	0.287728	0.999953	7.44802	2.11477	-
	Ring	Standard	9.681×10^{-17}	0.495318	0.0363893	9.55494	0.677517	-
AX J1749.1-2733‡	Reflected	Hard	-3.591×10^{-16}	0.609968	0.999869	-	-	-
	Reflected	Standard	-2.840×10^{-17}	0.846476	0.801041	6.16881	0.567661	-
	Ring	Hard	-8.593×10^{-16}	0.398906	0.993524	-	-	-
	Ring	Standard	-1.629×10^{-16}	0.252974	0.752235	5.56863	0.612789	-
AX J1749.2-2725‡	Reflected	Hard	-8.667×10^{-16}	0.0886425	0.999992	-	-	-
	Reflected	Standard	4.182×10^{-17}	0.792834	0.582634	7.65752	0.604984	-
	Ring	Hard	-1.203×10^{-15}	0.0509084	0.99884	-	-	-
	Ring	Standard	-4.086×10^{-17}	0.791243	0.583513	9.98899	0.604984	-
GRO J1750-27‡	Reflected	Hard	-	-	-	-	-	-
	Reflected	Standard	-4.226×10^{-16}	0.45179	0.0925608	8.39043	0.881924	29.8
	Ring	Hard	-	-	-	-	-	-
	Ring	Standard	-2.369×10^{-16}	0.664483	0.192006	8.85256	0.881924	29.8
SAX J1750.8-2900	Reflected	Hard	-2.353×10^{-16}	0.762358	0.997775	-	-	-
	Reflected	Standard	-7.105×10^{-17}	0.70706	0.0703362	7.51089	0.82279	-
	Ring	Hard	6.786×10^{-16}	0.347497	0.994797	-	-	-
	Ring	Standard	-5.763×10^{-17}	0.719184	0.0270787	8.5094	0.54614	-
GX 1.1-01.0	Reflected	Hard	9.767×10^{-16}	0.339251	0.989039	-	-	-
	Reflected	Standard	-1.263×10^{-16}	0.539135	0.277417	7.94773	0.912976	-
	Ring	Hard	9.296×10^{-16}	0.398367	0.974679	-	-	-
	Ring	Standard	-6.756×10^{-17}	0.66456	0.166577	8.21073	0.504878	-
IGR J17544-2619	Reflected	Hard	1.068×10^{-15}	0.598148	0.889142	-	-	-
	Reflected	Standard	-1.903×10^{-16}	0.8497	0.536906	9.58689	0.672143	-
	Ring	Hard	4.664×10^{-14}	0.335059	0.873121	-	-	-
	Ring	Standard	8.505×10^{-16}	0.192143	0.969379	4.58824	0.719662	-
4U 1755-338	Reflected	Hard	-	-	-	-	-	-
	Reflected	Standard	2.181×10^{-13}	0.631444	0.0209626	-	-	-
	Ring	Hard	-	-	-	-	-	-
	Ring	Standard	2.525×10^{-13}	0.561319	0.064724	-	-	-
4U 1758-25‡	Reflected	Hard	-	-	-	-	-	-
	Reflected	Standard	-3.421×10^{-16}	0.862815	0.616555	-	-	-

Target	Background	Cuts	Slope	$P_{\rm fa}^{\rm sec}$	$P_{\rm fa}^{\rm add}$	$z_{\rm max}$	$P_{\rm best}$ [d]	$P_{\rm known}$ [d]
	Ring	Hard	-	-	-	-	-	-
	Ring	Standard	-5.156×10^{-16}	0.810689	0.439936	-	-	-
GRS 1758-258	Reflected	Hard	-	-	-	-	-	-
	Reflected	Standard	-1.235×10^{-15}	0.612025	0.396054	-	-	-
	Ring	Hard	-	-	-	-	-	-
	Ring	Standard	9.918×10^{-17}	0.964586	0.45353	-	-	-
2S 1803-245	Reflected	Hard	-	-	-	-	-	-
	Reflected	Standard	3.779×10^{-15}	0.778705	0.116157	-	-	-
	Ring	Hard	-	-	-	-	-	-
	Ring	Standard	1.281×10^{-14}	0.283095	0.138034	-	-	-
XTE J1806-246	Reflected	Hard	-	-	-	-	-	-
	Reflected	Standard	6.638×10^{-15}	0.608326	0.108694	-	-	-
	Ring	Hard	-	-	-	-	-	-
	Ring	Standard	1.433×10^{-14}	0.244635	0.0860378	-	-	-
4U 1811-17‡	Reflected	Hard	-4.397×10^{-14}	0.0463528	0.935211	-	-	-
	Reflected	Standard	1.437×10^{-14}	0.243008	0.347091	-	-	-
	Ring	Hard	-2.096×10^{-14}	0.117479	0.989116	-	-	-
	Ring	Standard	2.769×10^{-15}	0.794927	0.370399	-	-	-
SAX J1818.6-1703	Reflected	Hard	-	-	-	-	-	-
	Reflected	Standard	1.599×10^{-15}	0.875425	0.866062	-	-	-
	Ring	Hard	-	-	-	-	-	-
	Ring	Standard	-2.208×10^{-17}	0.998381	0.829315	-	-	-
SAX J1819.3-2525	Reflected	Hard	-	-	-	-	-	-
	Reflected	Standard	-5.051×10^{-15}	0.6129	0.00339799	-	-	-
	Ring	Hard	-	-	-	-	-	-
	Ring	Standard	1.597×10^{-16}	0.97743	0.00921412	-	-	-
XTE J1829-098	Reflected	Hard	-	-	-	-	-	-
	Reflected	Standard	-1.253×10^{-15}	0.0806615	0.262304	-	-	-
	Ring	Hard	-	-	-	-	-	-
	Ring	Standard	-1.528×10^{-15}	0.0103036	0.358693	12.4393	0.713006	-
H 1833-076‡	Reflected	Hard	-1.350×10^{-16}	0.932906	0.955506	-	-	-
	Reflected	Standard	-1.333×10^{-16}	0.667452	0.874707	4.22906	0.684009	-
	Ring	Hard	1.763×10^{-15}	0.64862	0.876942	-	-	-
	Ring	Standard	-7.906×10^{-17}	0.800031	0.702414	3.87356	0.748979	-
GS 1839-06†	Reflected	Hard	-1.599×10^{-15}	0.250479	0.933773	-	-	-
	Reflected	Standard	-4.026×10^{-16}	0.0345633	0.437836	10.8426	16.8468	-
	Ring	Hard	-3.180×10^{-15}	0.0468601	0.835363	-	-	-
	Ring	Standard	-3.594×10^{-16}	0.0206431	0.725524	11.4983	0.957621	-
GS 1839-04	Reflected	Hard	-	-	-	-	-	-
	Reflected	Standard	-3.342×10^{-16}	0.276042	0.114314	11.8123	0.777894	-
	Ring	Hard	-	-	-	-	-	-
	Ring	Standard	-1.841×10^{-16}	0.465804	0.0476309	12.692	0.532758	-
AX 1845.0-0433	Reflected	Hard	-	-	-	-	-	-
	Reflected	Standard	4.134×10^{-17}	0.879894	0.0264029	18.3515	5.40313	-
	Ring	Hard	-	-	-	-	-	-
	Ring	Standard	-4.459×10^{-17}	0.843215	0.147617	11.7701	5.40313	-
GS 1843+009	Reflected	Hard	-	-	-	-	-	-
	Reflected	Standard	-2.935×10^{-15}	0.389231	0.503335	-	-	-
	Ring	Hard	-	-	-	-	-	-
	Ring	Standard	-3.124×10^{-15}	0.496654	0.230818	-	-	-
2S 1845-024‡	Reflected	Hard	-	-	-	-	-	-
	Reflected	Standard	-4.505×10^{-16}	0.0270722	0.656102	6.04733	0.503348	241
	Ring	Hard	-	-	-	-	-	-
	Ring	Standard	-1.246×10^{-16}	0.488493	0.347817	7.99616	0.559158	241

Target	Background	Cuts	Slope	$P_{\rm fa}^{\rm sec}$	$P_{\rm fa}^{\rm add}$	$z_{\rm max}$	$P_{\rm best}$ [d]	$P_{\rm known}$ [d]
IGR J18483-0311‡	Reflected	Hard	-	-	-	-	-	-
	Reflected	Standard	-5.842×10^{-17}	0.877778	0.527419	-	-	-
	Ring	Hard	-	-	-	-	-	-
	Ring	Standard	-5.582×10^{-17}	0.741233	0.83761	6.24866	0.808879	-
EXO 1846-031‡	Reflected	Hard	-	-	-	-	-	-
	Reflected	Standard	1.924×10^{-17}	0.94783	0.387062	-	-	-
	Ring	Hard	-	-	-	-	-	-
	Ring	Standard	4.683×10^{-18}	0.983019	0.265229	6.07713	1.14353	-
XTE J1858+034‡	Reflected	Hard	-	-	-	-	-	-
	Reflected	Standard	-1.799×10^{-15}	0.3332	0.956818	-	-	-
	Ring	Hard	-	-	-	-	-	-
	Ring	Standard	-6.304×10^{-15}	0.00818281	0.786425	-	-	-
XTE J1901+014	Reflected	Hard	-	-	-	-	-	-
	Reflected	Standard	2.836×10^{-16}	0.768096	0.43607	-	-	-
	Ring	Hard	-	-	-	-	-	-
	Ring	Standard	1.900×10^{-16}	0.767484	0.49235	7.44182	0.538479	-
4U 1901+03	Reflected	Hard	-	-	-	-	-	-
	Reflected	Standard	-4.199×10^{-15}	0.35395	0.432561	-	-	-
	Ring	Hard	-	-	-	-	-	-
	Ring	Standard	-3.214×10^{-15}	0.39965	0.324271	-	-	-
XTE J1906+09	Reflected	Hard	-	-	-	-	-	-
	Reflected	Standard	-1.232×10^{-14}	0.0206871	0.0118656	-	-	-
	Ring	Hard	-	-	-	-	-	-
	Ring	Standard	-1.115×10^{-14}	0.0123372	0.0164013	-	-	-
4U 1907+09‡	Reflected	Hard	-	-	-	-	-	-
	Reflected	Standard	3.878×10^{-17}	0.961326	0.209697	-	-	-
	Ring	Hard	-	-	-	-	-	-
	Ring	Standard	-5.211×10^{-16}	0.419394	0.346251	7.30546	0.515453	8.38
4U 1909+07	Reflected	Hard	-	-	-	-	-	-
	Reflected	Standard	-6.260×10^{-16}	0.681533	0.319225	-	-	-
	Ring	Hard	-	-	-	-	-	-
	Ring	Standard	-1.347×10^{-15}	0.370778	0.173439	-	-	-
3A 1909+048	Reflected	Hard	-	-	-	-	-	-
	Reflected	Standard	-3.021×10^{-16}	0.849112	0.640595	-	-	-
	Ring	Hard	-	-	-	-	-	-
	Ring	Standard	-9.399×10^{-16}	0.395744	0.933194	-	-	-
IGR J19140+0951†	Reflected	Hard	-	-	-	-	-	-
	Reflected	Standard	-1.017×10^{-16}	0.831819	0.215284	13.0576	0.892939	13.558
	Ring	Hard	-	-	-	-	-	-
	Ring	Standard	-6.136×10^{-16}	0.110662	0.285843	8.52887	1.88246	13.558
GRS 1915+105‡	Reflected	Hard	-	-	-	-	-	-
	Reflected	Standard	-2.007×10^{-16}	0.94923	0.775506	-	-	-
	Ring	Hard	-	-	-	-	-	-
	Ring	Standard	-5.949×10^{-16}	0.378499	0.447908	-	-	-
4U 1918+15	Reflected	Hard	-	-	-	-	-	-
	Reflected	Standard	-	-	-	-	-	-
	Ring	Hard	-	-	-	-	-	-
	Ring	Standard	1.060×10^{-12}	0.624467	0.173381	-	-	-
4U 2129+12	Reflected	Hard	-	-	-	-	-	-
	Reflected	Standard	2.610×10^{-14}	0.0585306	0.272621	-	-	-
	Ring	Hard	-	-	-	-	-	-
	Ring	Standard	2.087×10^{-14}	0.0543469	0.491773	-	-	-

Appendix B

Recovering data from bad runs

As explained in §3.2, it is the policy of the H.E.S.S. collaboration to truncate manually and discard *entire* observation runs that are obtained under sub-optimal atmospheric conditions. While this conservative approach undoubtedly preserves the integrity of the resultant data, it inevitably impairs observational efficiency. For example, scattered cloud cover during telescope operation often results in sporadic obscuration of the observational target. Runs affected in this manner would likely contain substantial amounts of high-quality data which might be recoverable if the episodes of atmospheric degradation could be reliably identified.

B.1 Identifying Good Time Intervals

The construction and application of *Good Time Intervals* (GTIs) is commonplace within the X-ray astronomy community and also among users of the *Fermi* γ-ray observatory. A GTI simply describes the union of all times within an observation which fulfil predefined data quality criteria. Subsequent analyses may then refer to a generated GTI and discard individual photons that were detected during periods with nominally poor data quality. The ability to define GTIs for individual H.E.S.S. observations would eliminate the requirement to terminate manually runs which are subject to transient periods of degradation, and significantly improve the operational efficiency of the instrument.

Although the telescope-mounted radiometers discussed in §3.2.4 provide a measurement of atmospheric quality which is independent of the telescope efficiency, they can only detect variations in luminosity temperature of the the night sky [58] and cannot be used as absolute calibrators. In contrast, the comparison of the observed and expected trigger rates as described in §3.2.4 does provide an absolute metric for atmospheric quality, but is also strongly dependent upon the array performance at the time of observation. Consequently, by considering simultaneous measurements of the radiometer temperature and array trigger rate, one may construct a reliable diagnostic for the levels of target obscuration, allowing segments of unreliable data to be identified and discarded.

Figure B.1 illustrates a custom graphical user interface (GUI) which was implemented to facilitate straightforward identification of transient obscuration episodes[1]. The two graphical panels embedded in the GUI illustrate the array trigger rate (top panel) and the average telescope radiometer temperature (bottom panel) as a function of time since the start of the observation. To enhance the contrast of variations which indicate sporadic cloud cover, the trigger rate (R) and radiometer temperature (T) are both corrected to counteract their dependence on varying zenith angle (Z) within a run. Specifically,

$$R_{\text{corr}} = \frac{R_{\text{uncorr}}}{-0.2566 + 1.564 \cos Z - 0.307 \cos^2 Z} \tag{B.1}$$

$$T_{\text{corr}} = \left[\frac{(T_{\text{uncorr}} + 100)^4}{(\sec Z)^{0.32}} \right]^{\frac{1}{4}} \tag{B.2}$$

where (B.1) is extracted from the standard H.E.S.S. *Heidelberg* analysis suite and (B.2) was derived by [73]. Furthermore, the mean radiometer temperatures ($\bar{T}_{\text{corr}}$) are normalised between zero and unity to compensate for the lack of an absolute calibration.

The red shaded areas in Figure B.1 are periods of unacceptable data have been automatically identified by the program using a simple function of the radiometer and trigger rate data.

[1]The source code for the graphical user interface, as well as that required to implement GTI filtering within the standard *Heidelberg* analysis, is presented in Appendix E.1

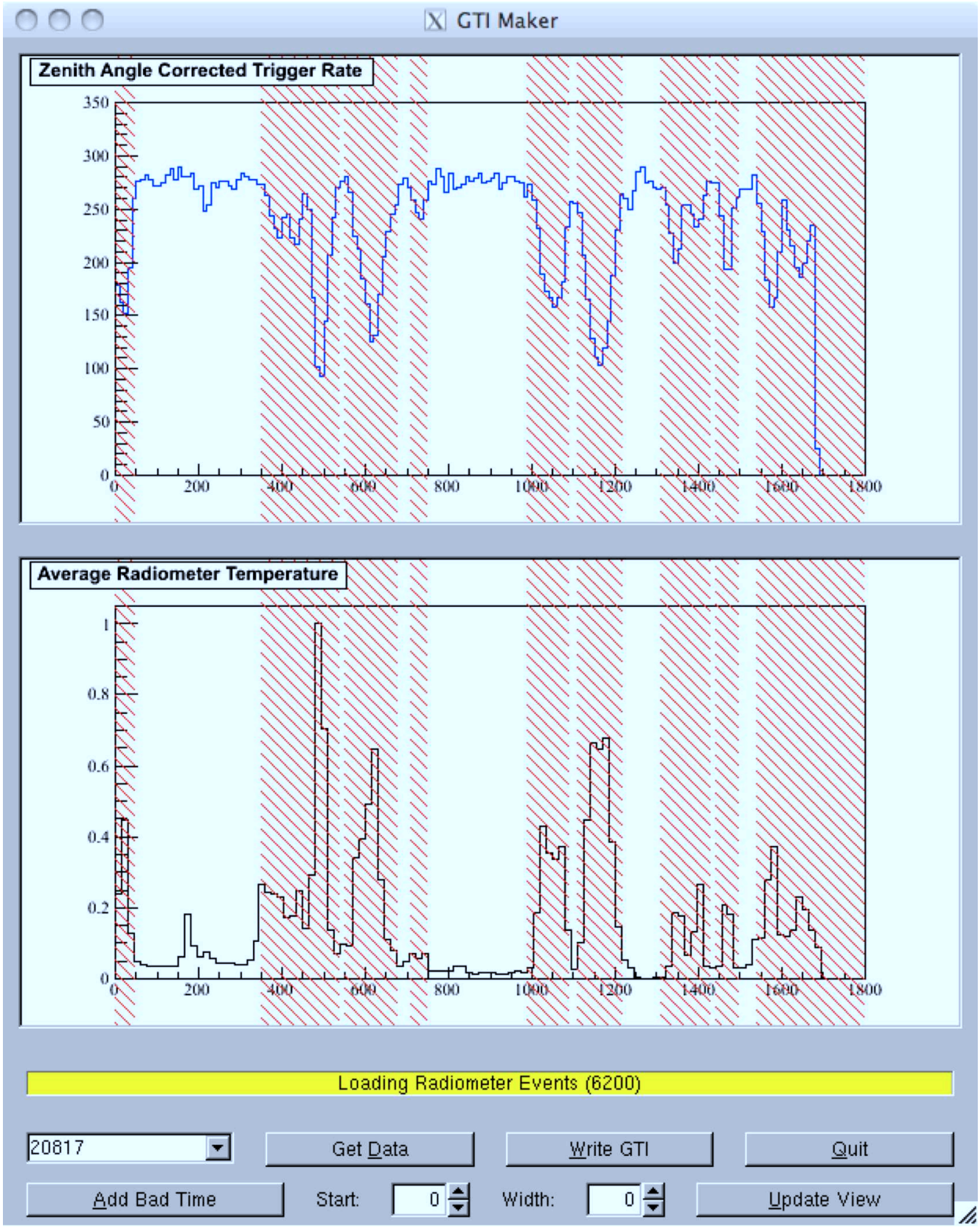

Figure B.1: A screenshot of the GUI application which facilitates definition of GTIs for a given observation run. The graphical windows plot the time evolution of the array trigger rate (*top panel*) and the normalised, mean radiometer temperatures (*bottom panel*). Both plots are corrected to compensate for varying zenith angle within a run. The red shaded areas indicate the automatically identified intervals which are likely to yield unreliable data.

Specifically, data is considered unusable if the following inequalities hold:

$$R_{\mathrm{corr}} < 250 \quad \mathrm{s}^{-1} \tag{B.3}$$

$$\left|\frac{dR_{\mathrm{corr}}}{dt}\right| > 5 \times 10^{-3} \quad \mathrm{s}^{-2} \tag{B.4}$$

$$\left|\frac{d\bar{T}_{\mathrm{corr}}}{dt}\right| > 4 \times 10^{-3} \quad \mathrm{Ks}^{-1} \tag{B.5}$$

The time derivatives are calculated by fitting fifth order splines to the data which may then be analytically differentiated. As is evident from Figure B.1, these simple criteria are remarkably successful in identifying observational intervals which are likely to yield unacceptably poor data quality. Interactive refinement of the automatically defined intervals is possible by dragging the interval boundaries within the GUI windows, and new intervals can be added using the controls beneath the embedded displays. Once a satisfactory GTI has been defined, the results can be saved and used to time-filter events in any of the standard *Heidelberg* analyses.

B.2 Application to the Crab Nebula

Establishing the utility of IACT data recovered from nominally bad runs requires application of the GTI technique to a known γ-ray source with well established, non-varying observational characteristics. Accordingly, a limited case study has been performed using the Crab Nebula, which is the *de facto* standard candle in the VHE γ-ray domain. Assembling a suitable dataset of sporadically obscured runs was complicated by the aforementioned H.E.S.S. policy of judicious run truncation, and only four appropriate observations were identified within the entire Crab Nebula dataset. GTIs were constructed for each run and used to filter events within the standard spectral analysis described in §3.11. Further spectral analyses were performed using the obscured dataset without application of the GTI filtering, and also using a control dataset of four nominally good observations. The control runs were chosen to closely match the zenith angles and observational epochs of those in the obscured dataset.

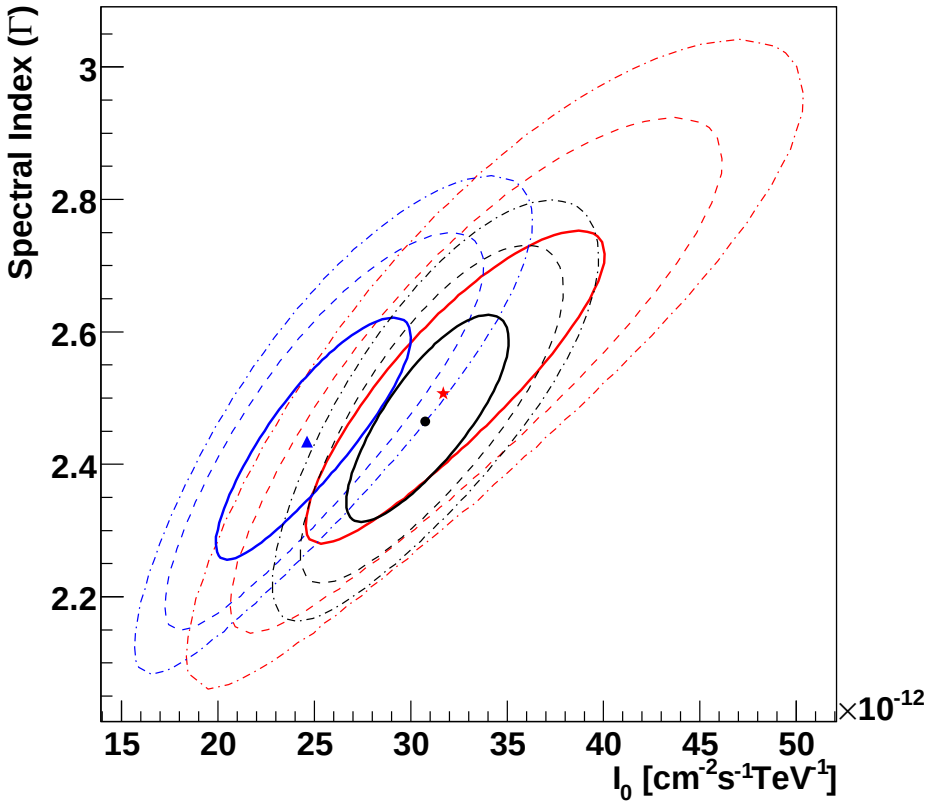

Figure B.2: Parameter confidence level contours for power law ($dN/dE = I_0 E^{-\Gamma}$) spectral fits to VHE γ-ray spectra of the Crab Nebula. The three colours correspond to the data from four nominally good runs (*black*), four nominally bad runs with GTI filtering applied (*red*), and the same nominally bad runs without GTI filtering (*blue*). The individual contours correspond to 68% confidence (*solid*), 95% confidence (*dashed*) and 99% confidence (*dot-dashed*)

Figure B.2 plots confidence contours for power law fits to each of the derived spectra. The black contours correspond to the spectrum obtained from the nominally good observations, while the red and blue contours correspond to the obscured data set with and without GTI filtering. The results derived using the unfiltered analysis and those corresponding to the nominally good runs differ at the $\sim 2\sigma$ level. In contrast, application of the GTI filter yields spectral parameters which are more consistent with the unobscured data, differing by $< 1\sigma$. Moreover, these results agree well with the more detailed analysis of H.E.S.S. Crab Nebula observations presented by [11]. Although these preliminary indications are encouraging, it should be noted that the limitations of the available dataset prevent robust conclusions from being drawn. Indeed, with so few γ-ray

events available it was inevitable that the GTI filtering would produce the comparatively large spectral uncertainties that are evident in Figure B.2. Nonetheless, while further evaluation of GTI filtering technique is undoubtedly required before a change in H.E.S.S. observational policy could be recommended, the initial results suggest that it may represent a viable method for improving the efficiency of IACT arrays.

Appendix C

Mathematical formulation of the Hillas parameters

The material in this appendix is primarily adapted from [91]. The pixels of a Cherenkov camera image are parameterised angular co-ordinates x_i and y_i and their amplitudes n_i. The following *moments* are then defined as summations over all pixels in the image.

$$\langle x \rangle = \frac{\sum n_i x_i}{\sum n_i} \qquad \langle y \rangle = \frac{\sum n_i y_i}{\sum n_i}$$

$$\langle x^2 \rangle = \frac{\sum n_i x_i^2}{\sum n_i} \qquad \langle y^2 \rangle = \frac{\sum n_i y_i^2}{\sum n_i}$$

$$\langle x^3 \rangle = \frac{\sum n_i x_i^3}{\sum n_i} \qquad \langle y^3 \rangle = \frac{\sum n_i y_i^3}{\sum n_i}$$

$$\langle xy \rangle = \frac{\sum n_i x_i^2 y_i}{\sum n_i} \qquad \langle x^2 y \rangle = \frac{\sum n_i x_i y_i}{\sum n_i}$$

$$\langle xy^2 \rangle = \frac{\sum n_i x_i y_i^2}{\sum n_i}$$

Functions of these moments then define the *spreads* of the Cherenkov image in various directions.

$$\sigma_{x^2} = \langle x^2 \rangle - \langle x \rangle^2 \qquad \sigma_{y^2} = \langle y^2 \rangle - \langle y \rangle^2 \qquad \sigma_{xy} = \langle xy \rangle - \langle x \rangle \langle y \rangle$$

$$\sigma_{x^3} = \langle x^3 \rangle - 3\langle x \rangle^2 \langle x \rangle + 2\langle y^2 \rangle \qquad \sigma_{y^3} = \langle y^3 \rangle - 3\langle y \rangle^2 \langle y \rangle + 2\langle y^3 \rangle$$

$$\sigma_{xy^2} = \langle xy^2 \rangle - \langle x \rangle \langle y^2 \rangle - 2\langle xy \rangle \langle y \rangle + 2\langle x \rangle^2 \langle y \rangle^2$$

$$\sigma_{x^2y} = \langle x^2 y \rangle - \langle x^2 \rangle \langle y \rangle - 2\langle xy \rangle \langle x \rangle + 2\langle x \rangle^2 \langle y \rangle$$

The Hillas parameters are then defined as specific combinations of the moments and spreads defined above.

$$d = \sigma_{y^2} - \sigma_{x^2} \qquad s = \sqrt{d^2 + 4(\sigma_{xy})^2}$$

$$u = 1 - \frac{d}{s} \qquad v = 2 - u$$

$$w = \sqrt{4(\langle y^2 \rangle - \langle x^2 \rangle)^2 \langle xy \rangle^2} \qquad \tan\phi = \frac{(d+s)\langle y \rangle + 2\sigma_{xy}\langle x \rangle}{2\sigma_{xy}\langle y \rangle - (d-s)\langle x \rangle}$$

$$\text{length} = \sqrt{\frac{\sigma_{x^2} + \sigma_{y^2} + s}{2}} \qquad \text{width} = \sqrt{\frac{\sigma_{x^2} + \sigma_{y^2} - s}{2}}$$

$$\text{miss} = \sqrt{\frac{1}{3}(u\langle x \rangle^2 + v\langle y \rangle^2 - \left(\frac{2\sigma_{xy}\langle x \rangle \langle y \rangle}{s}\right)} \qquad \text{distance} = \sqrt{\langle x \rangle^2 + \langle y \rangle^2}$$

$$\text{azwidth} = \sqrt{\frac{\langle x \rangle^2 \langle y^2 \rangle - 2\langle x \rangle \langle y \rangle \langle xy \rangle + \langle x^2 \rangle \langle y \rangle^2}{(\text{distance})^2}}$$

$$\sigma'_{x^3} = \sigma_{x^3} \cos^3\phi + 3\sigma_{x^2y} \cos^2\phi \sin\phi + 3\sigma^2_{xy} \cos\phi \sin^2\phi + \sigma_{y^3} \sin^3\phi$$

$$\text{asymmetry} = \frac{\sqrt[3]{\sigma'_{x^3}}}{\text{length}}$$

Appendix D

The Compton Scattering Angle

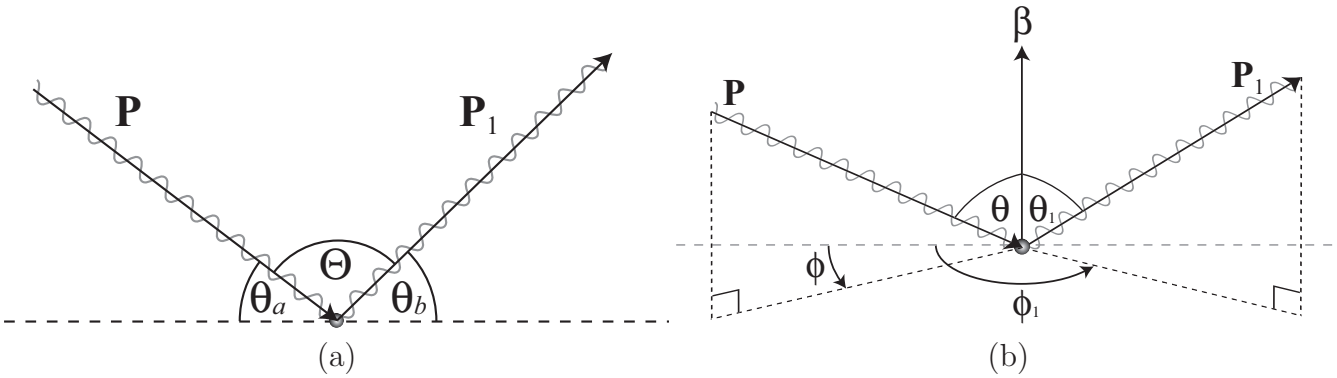

Figure D.1: Compton scattering geometry in the electron rest frame a) in the plane of the scattering b) in terms of a arbitrary spherical polar coordinate system.

Consider the scattering event illustrated in Figure D.1. In the plane of the scattering (Figure D.1(a)), the scalar product of the initial and final photon four-momenta is given by:

$$\mathbf{P} \cdot \mathbf{P}_1 = P^\mu (P_1)_\mu = P^0 P_1^0 - \vec{p} \cdot \vec{p_1} \tag{D.1}$$

Where $\vec{p}$ and $\vec{p_1}$ are respectively the three-momenta of the photon before and after scattering.

Consequently,

$$\begin{aligned}
\mathbf{P}\cdot\mathbf{P}_1 &= \frac{\epsilon\epsilon_1}{c^2}\left(1-\begin{bmatrix}-\cos\theta_a\\ \sin\theta_a\\ 0\end{bmatrix}\cdot\begin{bmatrix}\cos\theta_b\\ \sin\theta_b\\ 0\end{bmatrix}\right)\\
&= \frac{\epsilon\epsilon_1}{c^2}\left(1+\cos\theta_a\cos\theta_b-\sin\theta_a\sin\theta_b\right)\\
&= \frac{\epsilon\epsilon_1}{c^2}(1+\cos(\theta_a+\theta_b))\\
&= \frac{\epsilon\epsilon_1}{c^2}(1-\cos(\pi-(\theta_a+\theta_b)))\\
&= \frac{\epsilon\epsilon_1}{c^2}(1-\cos\Theta) \qquad \text{(D.2)}
\end{aligned}$$

Now, $\mathbf{P}\cdot\mathbf{P}_1$ is re-evaluated using an alternative and more general coordinate system in which the electron velocity vector β parallels the x-axis (Figure D.1(b)). In this configuration, the four-momenta before and after scattering are:

$$\mathbf{P}=\frac{\epsilon}{c}\begin{bmatrix}1\\ \cos\theta\\ \sin\theta\sin\phi\\ \sin\theta\cos\phi\end{bmatrix},\qquad \mathbf{P}_1=\frac{\epsilon_1}{c}\begin{bmatrix}1\\ \cos\theta_1\\ \sin\theta_1\sin\phi_1\\ \sin\theta_1\cos\phi_1\end{bmatrix} \qquad \text{(D.3)}$$

Evaluating the scalar product,

$$\begin{aligned}
\mathbf{P}\cdot\mathbf{P}_1 &= \frac{\epsilon\epsilon_1}{c^2}(1-\cos\theta\cos\theta_1-\sin\theta\sin\theta_1\sin\phi\sin\phi_1-\sin\theta\sin\theta_1\cos\phi\cos\phi_1)\\
&= \frac{\epsilon\epsilon_1}{c^2}(1-\cos\theta\cos\theta_1-\sin\theta\sin\theta_1(\sin\phi\sin\phi_1+\cos\phi\cos\phi_1))\\
&= \frac{\epsilon\epsilon_1}{c^2}(1-\cos\theta\cos\theta_1-\sin\theta\sin\theta_1\cos(\phi-\phi_1)) \qquad \text{(D.4)}
\end{aligned}$$

Finally, combining (D.2) and (D.4) yields the angular dependencies of the scattering in the electron

rest frame.

$$\begin{aligned} 1 - \cos\Theta &= 1 - \cos\theta\cos\theta_1 - \sin\theta\sin\theta_1\cos(\phi - \phi_1) \\ \implies \cos\Theta &= \cos\theta\cos\theta_1 + \sin\theta\sin\theta_1\cos(\phi - \phi_1) \end{aligned} \tag{D.5}$$

Appendix E

Source Code

E.1 Analysis Tools

The following sections describe the files that reside in the *Analysis Software* directory on the attached compact disk and contain the C++ source code for the custom implemented analysis tools used to generate the results presented in this thesis. Although all presented code is original, many of these files include headers from the ROOT software framework as well as the standard *Heidelberg* analysis suite which was introduced in Chapter 3. Accordingly, successful compilation and linking of the code requires existing installations of both packages.

E.1.1 Durham Analysis

E.1.1.1 include/Event.hh, src/Event.C

Declaration and definition of the `Event` class, which forms the basis of a custom implemented event-wise high level analysis scheme. This approach preserves the information associated with each photon that is detected, providing superior flexibility at the point of data analysis. In contrast the standard *Heidelberg* analysis software groups γ-ray-like events into immutable bins at reduction time and event-wise information is lost.

E.1.1.2 include/RunInfo.hh, src/RunInfo.C

Declaration and definition of the `RunInfo` class, which functions as an extensible data structure to encapsulate run-wise data such as target coordinates for use by classes which inherit from `DataSetPlotter`.

E.1.1.3 include/LightCurveEvent.hh, src/LightCurveEvent.C

Declaration and definition of the `LightCurveEvent` class, which inherits from `Event` and encapsulates the event-wise information which it necessary to produce γ-ray light curves.

E.1.1.4 include/LightCurveMaker.hh, src/LightCurveMaker.C

Declaration and definition of the `LightCurveMaker` class. This class inherits from the `Maker` class which is the base class of all functional classes of the standard H.E.S.S. data reduction chain. This class extracts the event-wise information required to produce γ-ray light curves and uses it to construct `LightCurveEvent`s which are stored for later analysis by the `LightCurvePlotter` class.

E.1.1.5 include/DataSetPlotter.hh, include/DataSetPlotter.icc

Declaration and definition of the `DataSetPlotter` class, which forms the basis for all analysis tools which form part of the event-wise scheme. This is a template class which defines several methods to facilitate reading, filtering and plotting of data which is stored using the `RunInfo` class or descendants of the `Event` class.

E.1.1.6 include/LightCurvePlotter.hh, src/LightCurvePlotter.C

Declaration and definition of the `LightCurvePlotter` class, which inherits from `DataSetPlotter` and defines the methods necessary to produce γ-ray light curves from stored `LightCurveEvent`s. The class also exposes much of its functionality via graphical user interface which allows interactive re-binning, and adjustment of flux units and energy thresholds as well as providing easy access to the functionality of related classes such as the `BayesianBlocks` and `LombScargle` classes.

E.1.1.7 include/BayesianBlocks.hh, src/BayesianBlocks.C

Declaration and definition of the `BayesianBlocks` class, which implements the method of [220] to identify statistically significant changes in γ-ray trigger rate given a sequence of event times.

E.1.1.8 include/LombScargle.hh, include/LombScargle.icc

Declaration and definition of the `LombScargle` class, which implements the Lomb-Scargle periodogram discussed at length in §3.10.3. In addition, the `LombScargle` class defines methods for determining peak false alarm probabilities using Monte Carlo simulations.

E.1.1.9 include/ConfBand.hh, src/ConfBand.C

Declaration and definition of the `ConfBand` class, which is used to draw a graphical band which illustrates the range of a parameter space which is consistent (at a specified confidence level) with a functional fit to data.

E.1.1.10 include/FluxConfBand.hh, src/FluxConfBand.C

Declaration and definition of the `FluxConfBand` class, which implements similar functionality to `ConfBand` but also interfaces with the `FluxGraph` class defined in the standard *Heidelberg* analysis. This class was required to produce the spectral plots presented in §3.11.

E.1.1.11 include/ULGraph.hh, src/ULGraph.C

Declaration and definition of the `ULGraph` class, which is used to draw graphs of upper limits consisting of horizontal error bars and downward pointing arrows.

E.1.1.12 include/ULFluxGraph.hh, src/ULFluxGraph.C

Declaration and definition of the `ULFluxGraph` class, implements similar functionality to `ULGraph`but also interfaces with the `FluxGraph` class defined in the standard *Heidelberg* analysis. This class was required to produce the spectral plots presented in §3.11.

E.1.1.13 include/SpecUtils.hh, src/SpecUtils.C

Declaration and definition of the `SpecUtils` class, which defines a number of static methods which provide a streamlined interface to the somewhat complicated standard *Heidelberg* spectral analysis classes.

E.1.1.14 include/Units.hh

Defines several enumeration types which are used by classes inheriting from `DataSetPlotter` to define unit names and conversion factors.

E.1.2 TCompoundFit

E.1.2.1 include/hjdmanip.h

Declaration and definition of the `FPLatex` class, which is designed to operate as a C++ I/O stream manipulator which outputs floating point numbers as textual representations which are can be parsed by the LaTeX typesetting system.

E.1.2.2 include/TCompoundFormula.h, src/TCompoundFormula.cpp

Declaration and definition of the `TCompoundFormula` class, which inherits from the `TFormula` class defined by the ROOT software framework. The class encapsulates an arbitrary number mathematical functions which it can combine using a variety of arithmetic operators. The class also defines multiple methods for drawing the resultant compound function. The power spectra presented in Figure 4.2 were drawn using this class.

E.1.2.3 include/TCompoundFit.h, src/TCompoundFit.cpp

Declaration and definition of the `TCompoundFit` class, which is designed to streamline the process of fitting complicated compound functions to data using the ROOT software framework. The broad functionality of this class is loosely based upon the `XSPEC` package [28]. The class enables

the user to interactively construct and fit `TCompoundFormula` objects to data and also provides an interface (via the `TFitFunctions` class) to the classes derived from `TFitFunctor`, facilitating straightforward composition and fitting of user-defined numerical models. The power spectra fits presented in Figure 4.2 and the radiative model fits presented in Chapters 3 and 4 were accomplished using this class.

E.1.2.4 include/TFitFunctor.h

Declaration and definition of the `TFitFunctor` class and its descendants, `Lorentzian` and `SSCSpec`. `TFitFunctor` is an abstract base class which is designed to provide a unified function object interface for user-defined numerical models. `Lorentzian` implements a lorentzian peak function, while `SSCSpec` encapsulates (via the `SSC` class described in Appendix E.2) the functionality of the synchrotron self-Compton model described in §2.7.1.

E.1.2.5 include/TFitFunctions.h, TFitFunctions.cpp

Declaration and definition of the `TFitFunctions` class, which is a helper class that enumerates the available descendants of `TFitFunctor` to `TCompoundFit` and acts as a factory class which constructs and returns objects of the requisite type for fitting.

E.1.3 GTI Maker Application

E.1.3.1 include/GTI.hh, src/GTI.C

Declaration and definition of the `GTI` class, which encapsulates data regarding good time intervals which have been identified using the `gtimaker` class.

E.1.3.2 include/gtiproc.hh, src/gtiproc.C

Declaration and definition of the `gtiproc` class, which inherits from the aforementioned `Maker` class and operates as an early component in the standard H.E.S.S. data reduction chain. `gtiproc` searches for a valid good time interval file associated with the run which is currently being reduced.

If an appropriate file is found, processing of events which were detected during periods of nominally bad time is suppressed.

E.1.3.3 include/gtimaker.hh, src/gtimaker.C

Declaration and definition of the `gtimaker` class, which provides the graphical user interface described in Appendix B and processes the user input to create, serialise and save instances of the `GTI` class for later processing by `gtiproc`.

E.2 Radiative Models

The following sections describe the files that reside in the *Physical Simulations* directory on the attached compact disk and contain the C++ source code for the custom implemented radiative emission and absorption models outlined in Chapter 2. Although all presented code is original, many of these files include headers from the ROOT software framework. Accordingly, successful compilation and linking of the code requires an existing installation this package.

E.2.0.4 include/Approximator.h, src/Approximator.cpp

Declaration and definition of the `Approximator` class, which is used to generate Chebyshev polynomial approximations to numerically generate functions. The use of such approximations can greatly increase evaluation speed particularly if the model requires extensive evaluation of nested numerical integrals with computationally expensive integrand functions. If the integrands can be accurately approximated by a simple polynomial expression, the computational cost of the numerous function evaluations required by numerical quadrature algorithms is significantly reduced.

E.2.0.5 include/Absorption.h, src/Absorption.cpp

Declaration and definition of the `Absorption` and `Orbital` classes, which are used to implement the γ-ray absorption model introduced in §2.7.3. `Absorption` encapsulates the aspects of the model which simulate the actual absorption process, while `Orbital` solves the equations of orbital mechanics to determine parameters such as the orbital separation at a given orbital phase.

E.2.0.6 include/SSC.h, src/SSC.cpp

Declaration and definition of the `Electrons`, `Synchrotron`, `CompIso`, `SSC`, `CompDB` and `CompDisk` classes.

`Electrons` is a helper class which encapsulates the properties of an astrophysical electron population in its own rest frame. The shape of the electron spectrum is defined phenomenologically, with pure power law, broken power law, and exponentially cut off power law spectra options currently

implemented. The power law slopes, cut off and break energies, and the overall internal energy are input parameters and are used to self-consistently determine an appropriate normalisation for the spectrum.

`Synchrotron` implements the synchrotron component of the SSC model introduced in §2.7.1, while `CompIso` implements the inverse-Compton component assuming that the synchrotron photon distribution is isotropic in the rest frame of the scattering electrons. `SSC` is a helper class which encapsulates the `Synchrotron` and `CompIso` classes behind a unified interface, ensuring that the input parameters are consistent for both classes. `SSC` is also used by the `SSCSpec` class described in §E.1.

`CompDB` and `CompDisk` are implementations of models described by [75]. `CompDB` simulates the γ-ray emission produced by inverse-Compton scattering of stellar photons by electrons entrained in a relativistic jet. Similarly, `CompDisk` models inverse-Compton scattering of soft photons emitted by an accretion flow.

E.2.0.7 include/JetWind.h, src/JetWind.cpp

Declaration and definition of the `JetWind` class, which implements the neutral pion creation and decay model introduced in §2.7.2. `JetWind` uses the `Orbital` class to predict orbital variations in the emitted flux of VHE γ-rays due to neutral pion decay.

Bibliography

[1] A. W. Guthmann, M. Georganopoulos, A. Marcowith, & K. Manolakou , editor. *Relativistic Flows in Astrophysics*, volume 589 of *Lecture Notes in Physics, Berlin Springer Verlag*, 2002.

[2] V. A. Acciari, M. Beilicke, G. Blaylock, S. M. Bradbury, J. H. Buckley, V. Bugaev, Y. Butt, K. L. Byrum, O. Celik, A. Cesarini, L. Ciupik, Y. C. K. Chow, P. Cogan, P. Colin, W. Cui, M. K. Daniel, C. Duke, T. Ergin, A. D. Falcone, S. J. Fegan, J. P. Finley, P. Fortin, L. F. Fortson, D. Gall, K. Gibbs, G. H. Gillanders, J. Grube, R. Guenette, D. Hanna, E. Hays, J. Holder, D. Horan, S. B. Hughes, C. M. Hui, T. B. Humensky, P. Kaaret, D. B. Kieda, J. Kildea, A. Konopelko, H. Krawczynski, F. Krennrich, M. J. Lang, S. LeBohec, K. Lee, G. Maier, A. McCann, M. McCutcheon, J. Millis, P. Moriarty, R. Mukherjee, T. Nagai, R. A. Ong, D. Pandel, J. S. Perkins, F. Pizlo, M. Pohl, J. Quinn, K. Ragan, P. T. Reynolds, H. J. Rose, M. Schroedter, G. H. Sembroski, A. W. Smith, D. Steele, S. P. Swordy, J. A. Toner, L. Valcarcel, V. V. Vassiliev, R. Wagner, S. P. Wakely, J. E. Ward, T. C. Weekes, A. Weinstein, R. J. White, D. A. Williams, S. A. Wissel, M. Wood, and B. Zitzer. VERITAS Observations of the γ-Ray Binary LS I +61 303. ApJ, 679:1427–1432, June 2008.

[3] F. Aharonian, A. Akhperjanian, J. Barrio, K. Bernlöhr, H. Börst, H. Bojahr, O. Bolz, J. Contreras, J. Cortina, S. Denninghoff, V. Fonseca, J. Gonzalez, N. Götting, G. Heinzelmann, G. Hermann, A. Heusler, W. Hofmann, D. Horns, A. Ibarra, C. Iserlohe, I. Jung, R. Kankanyan, M. Kestel, J. Kettler, A. Kohnle, A. Konopelko, H. Kornmeyer, D. Kranich, H. Krawczynski, H. Lampeitl, M. Lopez, E. Lorenz, F. Lucarelli, N. Magnussen, O. Mang, H. Meyer, R. Mirzoyan, A. Moralejo, E. Ona, L. Padilla, M. Panter, R. Plaga, A. Plyashesh-

nikov, J. Prahl, G. Pühlhofer, G. Rauterberg, A. Röhring, W. Rhode, G. P. Rowell, V. Sahakian, M. Samorski, M. Schilling, F. Schröder, M. Siems, W. Stamm, M. Tluczykont, H. J. Völk, C. A. Wiedner, and W. Wittek. Evidence for TeV gamma ray emission from Cassiopeia A. A&A, 370:112–120, April 2001.

[4] F. Aharonian, A. Akhperjanian, M. Beilicke, K. Bernlöhr, H.-G. Börst, H. Bojahr, O. Bolz, T. Coarasa, J. L. Contreras, J. Cortina, S. Denninghoff, M. V. Fonseca, M. Girma, N. Götting, G. Heinzelmann, G. Hermann, A. Heusler, W. Hofmann, D. Horns, I. Jung, R. Kankanyan, M. Kestel, A. Kohnle, A. Konopelko, H. Kornmeyer, D. Kranich, H. Lampeitl, M. Lopez, E. Lorenz, F. Lucarelli, O. Mang, H. Meyer, R. Mirzoyan, A. Moralejo, E. Ona-Wilhelmi, M. Panter, A. Plyasheshnikov, G. Pühlhofer, R. de los Reyes, W. Rhode, J. Ripken, G. Rowell, V. Sahakian, M. Samorski, M. Schilling, M. Siems, D. Sobzynska, W. Stamm, M. Tluczykont, V. Vitale, H. J. Völk, C. A. Wiedner, and W. Wittek. Is the giant radio galaxy M 87 a TeV gamma-ray emitter? A&A, 403:L1–L5, May 2003.

[5] F. Aharonian, A. G. Akhperjanian, G. Anton, U. B. de Almeida, A. R. Bazer-Bachi, Y. Becherini, B. Behera, W. Benbow, K. Bernlöhr, C. Boisson, A. Bochow, V. Borrel, E. Brion, J. Brucker, P. Brun, R. Bühler, T. Bulik, I. Büsching, T. Boutelier, P. M. Chadwick, A. Charbonnier, R. C. G. Chaves, A. Cheesebrough, L.-M. Chounet, A. C. Clapson, G. Coignet, M. Dalton, M. K. Daniel, I. D. Davids, B. Degrange, C. Deil, H. J. Dickinson, A. Djannati-Ataï, W. Domainko, L. O. Drury, F. Dubois, G. Dubus, J. Dyks, M. Dyrda, K. Egberts, D. Emmanoulopoulos, P. Espigat, C. Farnier, F. Feinstein, A. Fiasson, A. Förster, G. Fontaine, M. Füßling, S. Gabici, Y. A. Gallant, L. Gérard, B. Giebels, J.-F. Glicenstein, B. Glück, P. Goret, D. Göhring, D. Hauser, M. Hauser, S. Heinz, G. Heinzelmann, G. Henri, G. Hermann, J. A. Hinton, A. Hoffmann, W. Hofmann, M. Holleran, S. Hoppe, D. Horns, A. Jacholkowska, O. C. de Jager, C. Jahn, I. Jung, K. Katarzyński, U. Katz, S. Kaufmann, E. Kendziorra, M. Kerschhaggl, D. Khangulyan, B. Khélifi, D. Keogh, W. Kluźniak, T. Kneiske, N. Komin, K. Kosack, G. Lamanna, I. J. Latham, J.-P. Lenain, T. Lohse, V. Marandon, J. M. Martin, O. Martineau-Huynh, A. Marcowith, D. Maurin,

T. J. L. McComb, M. C. Medina, R. Moderski, E. Moulin, M. Naumann-Godo, M. de Naurois, D. Nedbal, D. Nekrassov, J. Niemiec, S. J. Nolan, S. Ohm, J.-F. Olive, E. de Oña Wilhelmi, K. J. Orford, M. Ostrowski, M. Panter, M. P. Arribas, G. Pedaletti, G. Pelletier, P.-O. Petrucci, S. Pita, G. Pühlhofer, M. Punch, A. Quirrenbach, B. C. Raubenheimer, M. Raue, S. M. Rayner, M. Renaud, F. Rieger, J. Ripken, L. Rob, S. Rosier-Lees, G. Rowell, B. Rudak, C. B. Rulten, J. Ruppel, V. Sahakian, A. Santangelo, R. Schlickeiser, F. M. Schöck, R. Schröder, U. Schwanke, S. Schwarzburg, S. Schwemmer, A. Shalchi, M. Sikora, J. L. Skilton, H. Sol, D. Spangler, Ł. Stawarz, R. Steenkamp, C. Stegmann, G. Superina, A. Szostek, P. H. Tam, J.-P. Tavernet, R. Terrier, O. Tibolla, M. Tluczykont, C. van Eldik, G. Vasileiadis, C. Venter, L. Venter, J. P. Vialle, P. Vincent, J. Vink, M. Vivier, H. J. Völk, F. Volpe, S. J. Wagner, M. Ward, A. A. Zdziarski, and A. Zech. Discovery of Very High Energy γ-Ray Emission from Centaurus A with H.E.S.S. ApJ, 695:L40–L44, April 2009.

[6] F. Aharonian, A. G. Akhperjanian, K.-M. Aye, A. R. Bazer-Bachi, M. Beilicke, W. Benbow, D. Berge, P. Berghaus, K. Bernlöhr, C. Boisson, O. Bolz, V. Borrel, I. Braun, F. Breitling, A. M. Brown, J. B. Gordo, P. M. Chadwick, L.-M. Chounet, R. Cornils, L. Costamante, B. Degrange, H. J. Dickinson, A. Djannati-Ataï, L. O. Drury, G. Dubus, D. Emmanoulopoulos, P. Espigat, F. Feinstein, P. Fleury, G. Fontaine, Y. Fuchs, S. Funk, Y. A. Gallant, B. Giebels, S. Gillessen, J. F. Glicenstein, P. Goret, C. Hadjichristidis, M. Hauser, G. Heinzelmann, G. Henri, G. Hermann, J. A. Hinton, W. Hofmann, M. Holleran, D. Horns, A. Jacholkowska, O. C. de Jager, B. Khélifi, N. Komin, A. Konopelko, I. J. Latham, R. Le Gallou, A. Lemière, M. Lemoine-Goumard, N. Leroy, T. Lohse, A. Marcowith, J.-M. Martin, O. Martineau-Huynh, C. Masterson, T. J. L. McComb, M. de Naurois, S. J. Nolan, A. Noutsos, K. J. Orford, J. L. Osborne, M. Ouchrif, M. Panter, G. Pelletier, S. Pita, G. Pühlhofer, M. Punch, B. C. Raubenheimer, M. Raue, J. Raux, S. M. Rayner, A. Reimer, O. Reimer, J. Ripken, L. Rob, L. Rolland, G. Rowell, V. Sahakian, L. Saugé, S. Schlenker, R. Schlickeiser, C. Schuster, U. Schwanke, M. Siewert, H. Sol, D. Spangler, R. Steenkamp, C. Stegmann, J.-P. Tavernet, R. Terrier, C. G. Théoret, M. Tluczykont, G. Vasileiadis, C. Venter, P. Vincent,

H. J. Völk, and S. J. Wagner. Discovery of Very High Energy Gamma Rays Associated with an X-ray Binary. *Science*, 309:746–749, July 2005.

[7] F. Aharonian, A. G. Akhperjanian, K.-M. Aye, A. R. Bazer-Bachi, M. Beilicke, W. Benbow, D. Berge, P. Berghaus, K. Bernlöhr, C. Boisson, O. Bolz, I. Braun, F. Breitling, A. M. Brown, J. Bussons Gordo, P. M. Chadwick, L.-M. Chounet, R. Cornils, L. Costamante, B. Degrange, A. Djannati-Ataï, L. O'C. Drury, G. Dubus, D. Emmanoulopoulos, P. Espigat, F. Feinstein, P. Fleury, G. Fontaine, Y. Fuchs, S. Funk, Y. A. Gallant, B. Giebels, S. Gillessen, J. F. Glicenstein, P. Goret, C. Hadjichristidis, M. Hauser, G. Heinzelmann, G. Henri, G. Hermann, J. A. Hinton, W. Hofmann, M. Holleran, D. Horns, O. C. de Jager, S. Johnston, B. Khélifi, J. G. Kirk, N. Komin, A. Konopelko, I. J. Latham, R. Le Gallou, A. Lemière, M. Lemoine-Goumard, N. Leroy, O. Martineau-Huynh, T. Lohse, A. Marcowith, C. Masterson, T. J. L. McComb, M. de Naurois, S. J. Nolan, A. Noutsos, K. J. Orford, J. L. Osborne, M. Ouchrif, M. Panter, G. Pelletier, S. Pita, G. Pühlhofer, M. Punch, B. C. Raubenheimer, M. Raue, J. Raux, S. M. Rayner, I. Redondo, A. Reimer, O. Reimer, J. Ripken, L. Rob, L. Rolland, G. Rowell, V. Sahakian, L. Saugé, S. Schlenker, R. Schlickeiser, C. Schuster, U. Schwanke, M. Siewert, O. Skjæraasen, H. Sol, R. Steenkamp, C. Stegmann, J.-P. Tavernet, R. Terrier, C. G. Théoret, M. Tluczykont, G. Vasileiadis, C. Venter, P. Vincent, H. J. Völk, and S. J. Wagner. Discovery of the binary pulsar PSR B1259-63 in very-high-energy gamma rays around periastron with HESS. A&A, 442:1–10, October 2005.

[8] F. Aharonian, A. G. Akhperjanian, K.-M. Aye, A. R. Bazer-Bachi, M. Beilicke, W. Benbow, D. Berge, P. Berghaus, K. Bernlöhr, C. Boisson, O. Bolz, I. Braun, F. Breitling, A. M. Brown, J. Bussons Gordo, P. M. Chadwick, L.-M. Chounet, R. Cornils, L. Costamante, B. Degrange, A. Djannati-Ataï, L. O'C. Drury, G. Dubus, D. Emmanoulopoulos, P. Espigat, F. Feinstein, P. Fleury, G. Fontaine, Y. Fuchs, S. Funk, Y. A. Gallant, B. Giebels, S. Gillessen, J. F. Glicenstein, P. Goret, C. Hadjichristidis, M. Hauser, G. Heinzelmann, G. Henri, G. Hermann, J. A. Hinton, W. Hofmann, M. Holleran, D. Horns, O. C. de Jager, B. Khélifi, N. Komin, A. Konopelko, I. J. Latham, R. Le Gallou, A. Lemière, M. Lemoine, N. Leroy, T. Lohse,

A. Marcowith, C. Masterson, T. J. L. McComb, M. de Naurois, S. J. Nolan, A. Noutsos, K. J. Orford, J. L. Osborne, M. Ouchrif, M. Panter, G. Pelletier, S. Pita, G. Pühlhofer, M. Punch, B. C. Raubenheimer, M. Raue, J. Raux, S. M. Rayner, I. Redondo, A. Reimer, O. Reimer, J. Ripken, L. Rob, L. Rolland, G. Rowell, V. Sahakian, L. Saugé, S. Schlenker, R. Schlickeiser, C. Schuster, U. Schwanke, M. Siewert, H. Sol, R. Steenkamp, C. Stegmann, J.-P. Tavernet, R. Terrier, C. G. Théoret, M. Tluczykont, G. Vasileiadis, C. Venter, P. Vincent, H. J. Völk, and S. J. Wagner. Observations of Mkn 421 in 2004 with HESS at large zenith angles. A&A, 437:95–99, July 2005.

[9] F. Aharonian, A. G. Akhperjanian, K.-M. Aye, A. R. Bazer-Bachi, M. Beilicke, W. Benbow, D. Berge, P. Berghaus, K. Bernlöhr, O. Bolz, C. Boisson, C. Borgmeier, F. Breitling, A. M. Brown, P. M. Chadwick, V. R. Chitnis, L.-M. Chounet, R. Cornils, L. Costamante, B. Degrange, O. C. de Jager, A. Djannati-Ataï, L. O. '. Drury, T. Ergin, P. Espigat, F. Feinstein, P. Fleury, G. Fontaine, S. Funk, Y. A. Gallant, B. Giebels, S. Gillessen, P. Goret, J. Guy, C. Hadjichristidis, M. Hauser, G. Heinzelmann, G. Henri, G. Hermann, J. Hinton, W. Hofmann, M. Holleran, D. Horns, I. Jung, B. Khélifi, N. Komin, A. Konopelko, I. J. Latham, R. L. Gallou, M. Lemoine, A. Lemière, N. Leroy, T. Lohse, A. Marcowith, C. Masterson, T. J. L. McComb, M. de Naurois, S. J. Nolan, A. Noutsos, K. J. Orford, J. L. Osborne, M. Ouchrif, M. Panter, G. Pelletier, S. Pita, M. Pohl, G. Pühlhofer, M. Punch, B. C. Raubenheimer, M. Raue, J. Raux, S. M. Rayner, I. Redondo, A. Reimer, O. Reimer, J. Ripken, M. Rivoal, L. Rob, L. Rolland, G. Rowell, V. Sahakian, L. Sauge, S. Schlenker, R. Schlickeiser, C. Schuster, U. Schwanke, M. Siewert, H. Sol, R. Steenkamp, C. Stegmann, J.-P. Tavernet, C. G. Théoret, M. Tluczykont, D. J. van der Walt, G. Vasileiadis, P. Vincent, B. Visser, H. J. Volk, and S. J. Wagner. Calibration of cameras of the H.E.S.S. detector. *Astroparticle Physics*, 22:109–125, November 2004.

[10] F. Aharonian, A. G. Akhperjanian, J. A. Barrio, K. Bernloehr, J. J. G. Beteta, S. M. Bradbury, J. L. Contreras, J. Cortina, A. Daum, T. Deckers, E. Feigl, J. Fernandez, V. Fonseca, A. Frass, B. Funk, J. C. Gonzalez, V. Haustein, G. Heinzelmann, M. Hemberger, G. Her-

mann, M. Hess, A. Heusler, W. Hofmann, I. Holl, D. Horns, R. Kankanian, O. Kirstein, C. Koehler, A. Konopelko, H. Kornmayer, D. Kranich, H. Krawczynski, H. Lampeitl, A. Lindner, E. Lorenz, N. Magnussen, H. Meyer, R. Mirzoyan, H. Moeller, A. Moralejo, L. Padilla, M. Panter, D. Petry, R. Plaga, J. Prahl, C. Prosch, G. Puehlhofer, G. Rauterberg, W. Rhode, R. Rivero, A. Roehring, V. Sahakian, M. Samorski, J. A. Sanchez, D. Schmele, T. Schmidt, W. Stamm, M. Ulrich, H. J. Voelk, S. Westerhoff, B. Wiebel-Sooth, C. A. Wiedner, M. Willmer, and H. Wirth. Measurement of the flux, spectrum, and variability of TeV γ-rays from MKN 501 during a state of high activity. A&A, 327:L5–L8, November 1997.

[11] F. Aharonian, A. G. Akhperjanian, A. R. Bazer-Bachi, M. Beilicke, W. Benbow, D. Berge, K. Bernlöhr, C. Boisson, O. Bolz, V. Borrel, I. Braun, F. Breitling, A. M. Brown, R. Bühler, I. Büsching, S. Carrigan, P. M. Chadwick, L.-M. Chounet, R. Cornils, L. Costamante, B. Degrange, H. J. Dickinson, A. Djannati-Ataï, L. O'C. Drury, G. Dubus, K. Egberts, D. Emmanoulopoulos, P. Espigat, F. Feinstein, E. Ferrero, A. Fiasson, G. Fontaine, S. Funk, S. Funk, Y. A. Gallant, B. Giebels, J. F. Glicenstein, P. Goret, C. Hadjichristidis, D. Hauser, M. Hauser, G. Heinzelmann, G. Henri, G. Hermann, J. A. Hinton, W. Hofmann, M. Holleran, D. Horns, A. Jacholkowska, O. C. de Jager, B. Khélifi, N. Komin, A. Konopelko, K. Kosack, I. J. Latham, R. Le Gallou, A. Lemière, M. Lemoine-Goumard, T. Lohse, J. M. Martin, O. Martineau-Huynh, A. Marcowith, C. Masterson, T. J. L. McComb, M. de Naurois, D. Nedbal, S. J. Nolan, A. Noutsos, K. J. Orford, J. L. Osborne, M. Ouchrif, M. Panter, G. Pelletier, S. Pita, G. Pühlhofer, M. Punch, B. C. Raubenheimer, M. Raue, S. M. Rayner, A. Reimer, O. Reimer, J. Ripken, L. Rob, L. Rolland, G. Rowell, V. Sahakian, L. Saugé, S. Schlenker, R. Schlickeiser, U. Schwanke, H. Sol, D. Spangler, F. Spanier, R. Steenkamp, C. Stegmann, G. Superina, J.-P. Tavernet, R. Terrier, C. G. Théoret, M. Tluczykont, C. van Eldik, G. Vasileiadis, C. Venter, P. Vincent, H. J. Völk, S. J. Wagner, and M. Ward. Observations of the Crab nebula with HESS. A&A, 457:899–915, October 2006.

[12] F. Aharonian, A. G. Akhperjanian, A. R. Bazer-Bachi, M. Beilicke, W. Benbow, D. Berge, K. Bernlöhr, C. Boisson, O. Bolz, V. Borrel, I. Braun, F. Breitling, A. M. Brown, P. M. Chad-

wick, L.-M. Chounet, R. Cornils, L. Costamante, B. Degrange, H. J. Dickinson, A. Djannati-Ataï, L. O. Drury, G. Dubus, D. Emmanoulopoulos, P. Espigat, F. Feinstein, G. Fontaine, Y. Fuchs, S. Funk, Y. A. Gallant, B. Giebels, S. Gillessen, J. F. Glicenstein, P. Goret, C. Hadjichristidis, M. Hauser, G. Heinzelmann, G. Henri, G. Hermann, J. A. Hinton, W. Hofmann, M. Holleran, D. Horns, A. Jacholkowska, O. C. de Jager, B. Khélifi, N. Komin, A. Konopelko, I. J. Latham, R. Le Gallou, A. Lemière, M. Lemoine-Goumard, N. Leroy, T. Lohse, J. M. Martin, O. Martineau-Huynh, A. Marcowith, C. Masterson, T. J. L. McComb, M. de Naurois, S. J. Nolan, A. Noutsos, K. J. Orford, J. L. Osborne, M. Ouchrif, M. Panter, G. Pelletier, S. Pita, G. Pühlhofer, M. Punch, B. C. Raubenheimer, M. Raue, J. Raux, S. M. Rayner, A. Reimer, O. Reimer, J. Ripken, L. Rob, L. Rolland, G. Rowell, V. Sahakian, L. Saugé, S. Schlenker, R. Schlickeiser, C. Schuster, U. Schwanke, M. Siewert, H. Sol, D. Spangler, R. Steenkamp, C. Stegmann, J.-P. Tavernet, R. Terrier, C. G. Théoret, M. Tluczykont, G. Vasileiadis, C. Venter, P. Vincent, H. J. Völk, and S. J. Wagner. The H.E.S.S. Survey of the Inner Galaxy in Very High Energy Gamma Rays. ApJ, 636:777–797, January 2006.

[13] F. Aharonian, A. G. Akhperjanian, A. R. Bazer-Bachi, M. Beilicke, W. Benbow, D. Berge, K. Bernlöhr, C. Boisson, O. Bolz, V. Borrel, I. Braun, F. Breitling, A. M. Brown, P. M. Chadwick, L.-M. Chounet, R. Cornils, L. Costamante, B. Degrange, H. J. Dickinson, A. Djannati-Ataï, L. O'C. Drury, G. Dubus, D. Emmanoulopoulos, P. Espigat, F. Feinstein, G. Fontaine, Y. Fuchs, S. Funk, Y. A. Gallant, B. Giebels, S. Gillessen, J. F. Glicenstein, P. Goret, C. Hadjichristidis, M. Hauser, G. Heinzelmann, G. Henri, G. Hermann, J. A. Hinton, W. Hofmann, M. Holleran, D. Horns, A. Jacholkowska, O. C. de Jager, B. Khélifi, N. Komin, A. Konopelko, I. J. Latham, R. Le Gallou, A. Lemière, M. Lemoine-Goumard, N. Leroy, T. Lohse, J. M. Martin, O. Martineau-Huynh, A. Marcowith, C. Masterson, T. J. L. McComb, M. de Naurois, S. J. Nolan, A. Noutsos, K. J. Orford, J. L. Osborne, M. Ouchrif, M. Panter, G. Pelletier, S. Pita, G. Pühlhofer, M. Punch, B. C. Raubenheimer, M. Raue, J. Raux, S. M. Rayner, A. Reimer, O. Reimer, J. Ripken, L. Rob, L. Rolland, G. Rowell, V. Sahakian, L. Saugé, S. Schlenker, R. Schlickeiser, C. Schuster, U. Schwanke, M. Siewert, H. Sol, D. Spangler,

R. Steenkamp, C. Stegmann, J.-P. Tavernet, R. Terrier, C. G. Théoret, M. Tluczykont, G. Vasileiadis, C. Venter, P. Vincent, H. J. Völk, and S. J. Wagner. Multi-wavelength observations of PKS 2155-304 with HESS. A&A, 442:895–907, November 2005.

[14] F. Aharonian, A. G. Akhperjanian, A. R. Bazer-Bachi, M. Beilicke, W. Benbow, D. Berge, K. Bernlöhr, C. Boisson, O. Bolz, V. Borrel, I. Braun, A. M. Brown, R. Bühler, I. Büsching, S. Carrigan, P. M. Chadwick, L.-M. Chounet, R. Cornils, L. Costamante, B. Degrange, H. J. Dickinson, A. Djannati-Ataï, L. O'C. Drury, G. Dubus, K. Egberts, D. Emmanoulopoulos, P. Espigat, F. Feinstein, E. Ferrero, A. Fiasson, G. Fontaine, S. Funk, M. Füßling, Y. A. Gallant, B. Giebels, J. F. Glicenstein, P. Goret, C. Hadjichristidis, D. Hauser, M. Hauser, G. Heinzelmann, G. Henri, G. Hermann, J. A. Hinton, A. Hoffmann, W. Hofmann, M. Holleran, D. Horns, A. Jacholkowska, O. C. de Jager, E. Kendziorra, B. Khélifi, N. Komin, A. Konopelko, K. Kosack, I. J. Latham, R. Le Gallou, A. Lemière, M. Lemoine-Goumard, T. Lohse, J. M. Martin, O. Martineau-Huynh, A. Marcowith, C. Masterson, G. Maurin, T. J. L. McComb, E. Moulin, M. de Naurois, D. Nedbal, S. J. Nolan, A. Noutsos, K. J. Orford, J. L. Osborne, M. Ouchrif, M. Panter, G. Pelletier, S. Pita, G. Pühlhofer, M. Punch, B. C. Raubenheimer, M. Raue, S. M. Rayner, A. Reimer, O. Reimer, J. Ripken, L. Rob, L. Rolland, G. Rowell, V. Sahakian, A. Santangelo, L. Saugé, S. Schlenker, R. Schlickeiser, R. Schröder, U. Schwanke, S. Schwarzburg, A. Shalchi, H. Sol, D. Spangler, F. Spanier, R. Steenkamp, C. Stegmann, G. Superina, J.-P. Tavernet, R. Terrier, M. Tluczykont, C. van Eldik, G. Vasileiadis, C. Venter, P. Vincent, H. J. Völk, S. J. Wagner, and M. Ward. 3.9 day orbital modulation in the TeV γ-ray flux and spectrum from the X-ray binary LS 5039. A&A, 460:743–749, December 2006.

[15] F. Aharonian and H.E.S.S. Collaboration. Detection of TeV γ-ray emission from the shell-type supernova remnant RX J0852.0-4622 with HESS. A&A, 437:L7–L10, July 2005.

[16] F. Aharonian and H.E.S.S. Collaboration. H.E.S.S. observations of PKS 2155-304. A&A, 430:865–875, February 2005.

[17] F. Aharonian and H.E.S.S. Collaboration. Upper limits to the SN1006 multi-TeV gamma-ray flux from HESS observations. A&A, 437:135–139, July 2005.

[18] F. Aharonian and The H.E.S.S. Collaboration. Discovery of very high energy γ-rays associated with an X-ray binary. *Science*, 308:Unknown, July 2005.

[19] F. A. Aharonian. TeV gamma rays from BL Lac objects due to synchrotron radiation of extremely high energy protons. *New Astronomy*, 5:377–395, November 2000.

[20] F. A. Aharonian. *Very high energy cosmic gamma radiation : a crucial window on the extreme Universe*. 2004.

[21] F. A. Aharonian, A. G. Akhperjanian, J. A. Barrio, K. Bernlöhr, H. Bojahr, J. L. Contreras, J. Cortina, A. Daum, T. Deckers, V. Fonseca, J. C. Gonzalez, G. Heinzelmann, M. Hemberger, G. Hermann, M. Heß, A. Heusler, W. Hofmann, H. Hohl, D. Horns, A. Ibarra, R. Kankanyan, O. Kirstein, C. Köhler, A. Konopelko, H. Kornmeyer, D. Kranich, H. Krawczynski, H. Lampeitl, A. Lindner, E. Lorenz, N. Magnussen, H. Meyer, R. Mirzoyan, A. Moralejo, L. Padilla, M. Panter, D. Petry, R. Plaga, A. Plyasheshnikov, J. Prahl, G. Pühlhofer, G. Rauterberg, C. Renault, W. Rhode, V. Sahakian, M. Samorski, D. Schmele, F. Schröder, W. Stamm, H. J. Völk, B. Wiebel-Sooth, C. Wiedner, M. Willmer, and H. Wirth. The temporal characteristics of the TeV gamma-radiation from MKN 501 in 1997. I. Data from the stereoscopic imaging atmospheric Cherenkov telescope system of HEGRA. A&A, 342:69–86, February 1999.

[22] F. A. Aharonian, A. G. Akhperjanian, A. R. Bazer-Bachi, M. Beilicke, W. Benbow, D. Berge, K. Bernlöhr, C. Boisson, O. Bolz, V. Borrel, I. Braun, F. Breitling, A. M. Brown, P. M. Chadwick, L.-M. Chounet, R. Cornils, L. Costamante, B. Degrange, H. J. Dickinson, A. Djannati-Ataï, L. O'C. Drury, G. Dubus, D. Emmanoulopoulos, P. Espigat, F. Feinstein, G. Fontaine, Y. Fuchs, S. Funk, Y. A. Gallant, B. Giebels, S. Gillessen, J. F. Glicenstein, P. Goret, C. Hadjichristidis, M. Hauser, G. Heinzelmann, G. Henri, G. Hermann, J. A. Hinton, W. Hofmann,

M. Holleran, D. Horns, A. Jacholkowska, O. C. de Jager, B. Khélifi, N. Komin, A. Konopelko, I. J. Latham, R. Le Gallou, A. Lemière, M. Lemoine-Goumard, N. Leroy, T. Lohse, J. M. Martin, O. Martineau-Huynh, A. Marcowith, C. Masterson, T. J. L. McComb, M. de Naurois, S. J. Nolan, A. Noutsos, K. J. Orford, J. L. Osborne, M. Ouchrif, M. Panter, G. Pelletier, S. Pita, G. Pühlhofer, M. Punch, B. C. Raubenheimer, M. Raue, J. Raux, S. M. Rayner, A. Reimer, O. Reimer, J. Ripken, L. Rob, L. Rolland, G. Rowell, V. Sahakian, L. Saugé, S. Schlenker, R. Schlickeiser, C. Schuster, U. Schwanke, M. Siewert, H. Sol, D. Spangler, R. Steenkamp, C. Stegmann, J.-P. Tavernet, R. Terrier, C. G. Théoret, M. Tluczykont, G. Vasileiadis, C. Venter, P. Vincent, H. J. Völk, and S. J. Wagner. A possible association of the new VHE γ-ray source HESS J1825 137 with the pulsar wind nebula G 18.0 0.7. A&A, 442:L25–L29, November 2005.

[23] F. A. Aharonian and A. M. Atoyan. On the emissivity of pi^0-decay gamma radiation in the vicinity of accelerators of galactic cosmic rays. A&A, 309:917–928, May 1996.

[24] J. Albert, E. Aliu, H. Anderhub, L. A. Antonelli, P. Antoranz, M. Backes, C. Baixeras, J. A. Barrio, H. Bartko, D. Bastieri, J. K. Becker, W. Bednarek, K. Berger, E. Bernardini, C. Bigongiari, A. Biland, R. K. Bock, G. Bonnoli, P. Bordas, V. Bosch-Ramon, T. Bretz, I. Britvitch, M. Camara, E. Carmona, A. Chilingarian, S. Commichau, J. L. Contreras, J. Cortina, M. T. Costado, S. Covino, V. Curtef, F. Dazzi, A. DeAngelis, E. De-Cea del Pozo, R. de los Reyes, B. DeLotto, M. DeMaria, F. DeSabata, C. Delgado Mendez, A. Dominguez, D. Dorner, M. Doro, M. Errando, M. Fagiolini, D. Ferenc, E. Fernández, R. Firpo, M. V. Fonseca, L. Font, N. Galante, R. J. G. López, M. Garczarczyk, M. Gaug, F. Goebel, M. Hayashida, A. Herrero, D. Höhne, J. Hose, C. C. Hsu, S. Huber, T. Jogler, D. Kranich, A. La Barbera, A. Laille, E. Leonardo, E. Lindfors, S. Lombardi, F. Longo, M. López, E. Lorenz, P. Majumdar, G. Maneva, N. Mankuzhiyil, K. Mannheim, L. Maraschi, M. Mariotti, M. Martínez, D. Mazin, M. Meucci, M. Meyer, J. M. Miranda, R. Mirzoyan, S. Mizobuchi, M. Moles, A. Moralejo, D. Nieto, K. Nilsson, J. Ninkovic, N. Otte, I. Oya, M. Panniello, R. Paoletti, J. M. Paredes, M. Pasanen, D. Pascoli, F. Pauss, R. G. Pegna,

M. A. Perez-Torres, M. Persic, L. Peruzzo, A. Piccioli, F. Prada, E. Prandini, N. Puchades, A. Raymers, W. Rhode, M. Ribó, J. Rico, M. Rissi, A. Robert, S. Rügamer, A. Saggion, T. Y. Saito, M. Salvati, M. Sanchez-Conde, P. Sartori, K. Satalecka, V. Scalzotto, V. Scapin, R. Schmitt, T. Schweizer, M. Shayduk, K. Shinozaki, S. N. Shore, N. Sidro, A. Sierpowska-Bartosik, A. Sillanpää, D. Sobczynska, F. Spanier, A. Stamerra, L. S. Stark, L. Takalo, F. Tavecchio, P. Temnikov, D. Tescaro, M. Teshima, M. Tluczykont, D. F. Torres, N. Turini, H. Vankov, A. Venturini, V. Vitale, R. M. Wagner, W. Wittek, V. Zabalza, F. Zandanel, R. Zanin, and J. Zapatero. Periodic Very High Energy γ-Ray Emission from LS I +61°303 Observed with the MAGIC Telescope. ApJ, 693:303–310, March 2009.

[25] J. Albert, E. Aliu, H. Anderhub, P. Antoranz, A. Armada, M. Asensio, C. Baixeras, J. A. Barrio, M. Bartelt, H. Bartko, D. Bastieri, S. R. Bavikadi, W. Bednarek, K. Berger, C. Bigongiari, A. Biland, E. Bisesi, R. K. Bock, P. Bordas, V. Bosch-Ramon, T. Bretz, I. Britvitch, M. Camara, E. Carmona, A. Chilingarian, S. Ciprini, J. A. Coarasa, S. Commichau, J. L. Contreras, J. Cortina, V. Curtef, V. Danielyan, F. Dazzi, A. De Angelis, R. de los Reyes, B. De Lotto, E. Domingo-Santamaría, D. Dorner, M. Doro, M. Errando, M. Fagiolini, D. Ferenc, E. Fernández, R. Firpo, J. Flix, M. V. Fonseca, L. Font, M. Fuchs, N. Galante, M. Garczarczyk, M. Gaug, M. Giller, F. Goebel, D. Hakobyan, M. Hayashida, T. Hengstebeck, D. Höhne, J. Hose, C. C. Hsu, P. G. Isar, P. Jacon, O. Kalekin, R. Kosyra, D. Kranich, M. Laatiaoui, A. Laille, T. Lenisa, P. Liebing, E. Lindfors, S. Lombardi, F. Longo, J. López, M. López, E. Lorenz, F. Lucarelli, P. Majumdar, G. Maneva, K. Mannheim, O. Mansutti, M. Mariotti, M. Martínez, K. Mase, D. Mazin, C. Merck, M. Meucci, M. Meyer, J. M. Miranda, R. Mirzoyan, S. Mizobuchi, A. Moralejo, K. Nilsson, E. Oña-Wilhelmi, R. Orduña, N. Otte, I. Oya, D. Paneque, R. Paoletti, J. M. Paredes, M. Pasanen, D. Pascoli, F. Pauss, N. Pavel, R. Pegna, M. Persic, L. Peruzzo, A. Piccioli, M. Poller, G. Pooley, E. Prandini, A. Raymers, W. Rhode, M. Ribó, J. Rico, B. Riegel, M. Rissi, A. Robert, G. E. Romero, S. Rügamer, A. Saggion, A. Sánchez, P. Sartori, V. Scalzotto, V. Scapin, R. Schmitt, T. Schweizer, M. Shayduk, K. Shinozaki, S. N. Shore,

N. Sidro, A. Sillanpää, D. Sobczynska, A. Stamerra, L. S. Stark, L. Takalo, P. Temnikov, D. Tescaro, M. Teshima, N. Tonello, A. Torres, D. F. Torres, N. Turini, H. Vankov, V. Vitale, R. M. Wagner, T. Wibig, W. Wittek, R. Zanin, and J. Zapatero. Variable Very-High-Energy Gamma-Ray Emission from the Microquasar LS I +61 303. *Science*, 312:1771–1773, June 2006.

[26] J. Albert, E. Aliu, H. Anderhub, P. Antoranz, A. Armada, C. Baixeras, J. A. Barrio, H. Bartko, D. Bastieri, J. K. Becker, W. Bednarek, K. Berger, C. Bigongiari, A. Biland, R. K. Bock, P. Bordas, V. Bosch-Ramon, T. Bretz, I. Britvitch, M. Camara, E. Carmona, A. Chilingarian, J. A. Coarasa, S. Commichau, J. L. Contreras, J. Cortina, M. T. Costado, V. Curtef, V. Danielyan, F. Dazzi, A. De Angelis, C. Delgado, R. de los Reyes, B. De Lotto, E. Domingo-Santamaría, D. Dorner, M. Doro, M. Errando, M. Fagiolini, D. Ferenc, E. Fernández, R. Firpo, J. Flix, M. V. Fonseca, L. Font, M. Fuchs, N. Galante, R. J. García-López, M. Garczarczyk, M. Gaug, M. Giller, F. Goebel, D. Hakobyan, M. Hayashida, T. Hengstebeck, A. Herrero, D. Höhne, J. Hose, C. C. Hsu, P. Jacon, T. Jogler, R. Kosyra, D. Kranich, R. Kritzer, A. Laille, E. Lindfors, S. Lombardi, F. Longo, J. López, M. López, E. Lorenz, P. Majumdar, G. Maneva, K. Mannheim, O. Mansutti, M. Mariotti, M. Martínez, D. Mazin, C. Merck, M. Meucci, M. Meyer, J. M. Miranda, R. Mirzoyan, S. Mizobuchi, A. Moralejo, D. Nieto, K. Nilsson, J. Ninkovic, E. Oña-Wilhelmi, N. Otte, I. Oya, M. Panniello, R. Paoletti, J. M. Paredes, M. Pasanen, D. Pascoli, F. Pauss, R. Pegna, M. Persic, L. Peruzzo, A. Piccioli, E. Prandini, N. Puchades, A. Raymers, W. Rhode, M. Ribó, J. Rico, M. Rissi, A. Robert, S. Rügamer, A. Saggion, T. Saito, A. Sánchez, P. Sartori, V. Scalzotto, V. Scapin, R. Schmitt, T. Schweizer, M. Shayduk, K. Shinozaki, S. N. Shore, N. Sidro, A. Sillanpää, D. Sobczynska, A. Stamerra, L. S. Stark, L. Takalo, P. Temnikov, D. Tescaro, M. Teshima, D. F. Torres, N. Turini, H. Vankov, V. Vitale, R. M. Wagner, T. Wibig, W. Wittek, F. Zandanel, R. Zanin, and J. Zapatero. Very High Energy Gamma-Ray Radiation from the Stellar Mass Black Hole Binary Cygnus X-1. ApJ, 665:L51–L54, August 2007.

[27] A. N. Argue, D. L. Jauncey, D. D. Morabito, and R. A. Preston. The radio and optical

identification of Circinus X-1. MNRAS, 209:11P–14P, July 1984.

[28] K. A. Arnaud. XSPEC: The First Ten Years. In G. H. Jacoby and J. Barnes, editors, *ASP Conf. Ser. 101: Astronomical Data Analysis Software and Systems V*, page 17, 1996.

[29] A. M. Atoyan and F. A. Aharonian. Modelling of the non-thermal flares in the Galactic microquasar GRS 1915+105. MNRAS, 302:253–276, January 1999.

[30] C. Bailyn, D. Maitra, M. Buxton, L. Jeanty, and D. Gonzalez. X-ray and Optical Activity in V4641 Sgr (=SAX 1819.3-2525). *The Astronomer's Telegram*, 171:1, August 2003.

[31] J. A. Bellido and for the Pierre Auger Collaboration. Mass Composition Studies of the Highest Energy Cosmic Rays. *ArXiv e-prints*, January 2009.

[32] T. Belloni, M. Klein-Wolt, M. Méndez, M. van der Klis, and J. van Paradijs. A model-independent analysis of the variability of GRS 1915+105. A&A, 355:271–290, March 2000.

[33] T. Belloni, M. Mendez, A. R. King, M. van der Klis, and J. van Paradijs. A Unified Model for the Spectral Variability in GRS 1915+105. ApJ, 488:L109+, October 1997.

[34] T. Belloni, D. Psaltis, and M. van der Klis. A Unified Description of the Timing Features of Accreting X-Ray Binaries. ApJ, 572:392–406, June 2002.

[35] W. Benbow. The standard h.e.s.s. analysis technique. In *Towards a Network of Atmospheric Cherenkov Detectors VII*, pages 163–171, April 2005.

[36] W. Benbow and H.E.S.S. Collaboration. The Status and Performance of H.E.S.S. In *AIP Conf. Proc. 745: High Energy Gamma-Ray Astronomy*, pages 611–616, February 2005.

[37] D. Berge, S. Funk, and J. Hinton. Background modelling in very-high-energy γ-ray astronomy. A&A, 466:1219–1229, May 2007.

[38] K. Bernlohr. Impact of atmospheric parameters on the atmospheric Cherenkov technique*. *Astroparticle Physics*, 12:255–268, January 2000.

[39] K. Bernlöhr, O. Carrol, R. Cornils, S. Elfahem, P. Espigat, S. Gillessen, G. Heinzelmann, G. Hermann, W. Hofmann, D. Horns, I. Jung, R. Kankanyan, A. Katona, B. Khelifi, H. Krawczynski, M. Panter, M. Punch, S. Rayner, G. Rowell, M. Tluczykont, and R. van Staa. The optical system of the H.E.S.S. imaging atmospheric Cherenkov telescopes. Part I: layout and components of the system. *Astroparticle Physics*, 20:111–128, November 2003.

[40] P. R. Bevington and D. K. Robinson. *Data reduction and error analysis for the physical sciences*. McGraw-Hill, 1992.

[41] J. M. Blondin and M. P. Owen. Wind Accretion VS Roche Lobe Overflow in HMXBs. In D. T. Wickramasinghe, G. V. Bicknell, & L. Ferrario, editor, *IAU Colloq. 163: Accretion Phenomena and Related Outflows*, volume 121 of *Astronomical Society of the Pacific Conference Series*, page 361, 1997.

[42] J. M. Blondin, I. R. Stevens, and T. R. Kallman. Enhanced winds and tidal streams in massive X-ray binaries. ApJ, 371:684–695, April 1991.

[43] G. R. Blumenthal and R. J. Gould. Bremsstrahlung, Synchrotron Radiation, and Compton Scattering of High-Energy Electrons Traversing Dilute Gases. *Reviews of Modern Physics*, 42:237–271, 1970.

[44] V. Bosch-Ramon and J. M. Paredes. A numerical model for the γ-ray emission of the microquasar LS 5039. A&A, 417:1075–1081, April 2004.

[45] V. Bosch-Ramon, J. M. Paredes, M. Ribó, J. M. Miller, P. Reig, and J. Martí. Orbital X-Ray Variability of the Microquasar LS 5039. ApJ, 628:388–394, July 2005.

[46] V. Bosch-Ramon, G. E. Romero, and J. M. Paredes. A broadband leptonic model for gamma-ray emitting microquasars. A&A, 447:263–276, February 2006.

[47] M. Böttcher and C. D. Dermer. Photon-Photon Absorption of Very High Energy Gamma Rays from Microquasars: Application to LS 5039. ApJ, 634:L81–L84, November 2005.

[48] S. Boutloukos, M. van der Klis, D. Altamirano, M. Klein-Wolt, R. Wijnands, P. G. Jonker, and R. P. Fender. Discovery of Twin kHz QPOs in the Peculiar X-Ray Binary Circinus X-1. ApJ, 653:1435–1444, December 2006.

[49] W. N. Brandt, A. C. Fabian, T. Dotani, F. Nagase, H. Inoue, T. Kotani, and Y. Segawa. ASCA observations of the iron K complex of Circinus X-1 near zero phase: spectral evidence for partial covering. MNRAS, 283:1071–1082, December 1996.

[50] W. N. Brandt and N. S. Schulz. The Discovery of Broad P Cygni X-Ray Lines from Circinus X-1 with the Chandra High-Energy Transmission Grating Spectrometer. ApJ, 544:L123–L127, December 2000.

[51] M. Buxton, D. Maitra, C. Bailyn, L. Jeanty, and D. Gonzalez. Optical Outburst of V4641 (=SAX J1819.3-2525). *The Astronomer's Telegram*, 170:1, August 2003.

[52] D. Campbell-Wilson and R. W. Hunstead. Sax J1819.3-2525. IAU Circ., 7908:2, May 2002.

[53] J. Casares, I. Ribas, J. M. Paredes, J. Martí, and C. Allende Prieto. Orbital parameters of the microquasar LS I +61 303. MNRAS, 360:1105–1109, July 2005.

[54] J. Casares, M. Ribó, I. Ribas, J. M. Paredes, J. Martí, and A. Herrero. A possible black hole in the γ-ray microquasar LS 5039. MNRAS, 364:899–908, December 2005.

[55] A. J. Castro-Tirado, S. Brandt, N. Lund, I. Lapshov, R. A. Sunyaev, A. A. Shlyapnikov, S. Guziy, and E. P. Pavlenko. Discovery and observations by watch of the X-ray transient GRS 1915+105. ApJS, 92:469–472, June 1994.

[56] P. A. Čerenkov. Visible Radiation Produced by Electrons Moving in a Medium with Velocities Exceeding that of Light . *Phys. Rev.*, 52:378, August 1937.

[57] P. M. Chadwick and et al. Simultaneous X-ray and VHE gamma-ray observations of microquasars. In *International Cosmic Ray Conference*, volume 4 of *International Cosmic Ray Conference*, page 263, 2005.

[58] P. M. Chadwick, K. Lyons, T. J. L. McComb, K. J. Orford, J. L. Osborne, S. M. Rayner, S. E. Shaw, and K. E. Turver. Sensing atmospheric conditions using MIR radiometers. In B. L. Dingus, M. H. Salamon, & D. B. Kieda, editor, *American Institute of Physics Conference Series*, volume 515 of *American Institute of Physics Conference Series*, pages 393–397, June 2000.

[59] C. Chapuis and S. Corbel. On the optical extinction and distance of ¡ASTROBJ¿GRS 1915+105¡/ASTROBJ¿. A&A, 414:659–665, February 2004.

[60] S. Chaty, I. F. Mirabel, P. A. Duc, J. E. Wink, and L. F. Rodriguez. Infrared and millimeter observations of the galactic superluminal source GRS 1915+105. A&A, 310:825–830, June 1996.

[61] M. J. Church, G. S. Halai, and M. Bałucińska-Church. An explanation of the Z-track sources. A&A, 460:233–244, December 2006.

[62] J. S. Clark, P. A. Charles, W. I. Clarkson, and M. J. Coe. Near IR spectroscopy of the X-ray binary ¡ASTROBJ¿Circinus X-1¡/ASTROBJ¿. A&A, 400:655–658, March 2003.

[63] J. S. Clark, P. Reig, S. P. Goodwin, V. M. Larionov, P. Blay, M. J. Coe, J. Fabregat, I. Negueruela, I. Papadakis, and I. A. Steele. On the radio emitting high mass X-ray binary ¡ASTROBJ¿LS 5039¡/ASTROBJ¿. A&A, 376:476–483, September 2001.

[64] W. I. Clarkson, P. A. Charles, and N. Onyett. X-ray behaviour of Circinus X-1 - I. X-ray dips as a diagnostic of periodic behaviour. MNRAS, 348:458–468, February 2004.

[65] M. H. Cohen, W. Cannon, G. H. Purcell, D. B. Shaffer, J. J. Broderick, K. I. Kellermann, and D. L. Jauncey. The Small-Scale Structure of Radio Galaxies and Quasi-Stellar Sources at 3.8 Centimeters. ApJ, 170:207, December 1971.

[66] J. A. Combi, S. A. Cellone, J. Martí, M. Ribó, I. F. Mirabel, and J. Casares. Optical polarimetric observations of the microquasar ¡ASTROBJ¿LS 5039¡/ASTROBJ¿. A&A, 427:959–963, December 2004.

[67] P. S. Coppi. The Physics of Hybrid Thermal/Non-Thermal Plasmas. In J. Poutanen and R. Svensson, editors, *High Energy Processes in Accreting Black Holes*, volume 161 of *Astronomical Society of the Pacific Conference Series*, page 375, 1999.

[68] P. S. Coppi. EQPAIR: A Hybrid Thermal/Non-Thermal Model for the Spectra of X-Ray Binaries. In *Bulletin of the American Astronomical Society*, volume 32, page 1217, October 2000.

[69] S. Corbel, R. P. Fender, A. K. Tzioumis, J. A. Tomsick, J. A. Orosz, J. M. Miller, R. Wijnands, and P. Kaaret. Large-Scale, Decelerating, Relativistic X-ray Jets from the Microquasar XTE J1550-564. *Science*, 298:196–199, October 2002.

[70] J. Cronin, K. Gaisser, T, and S. P. Swordy. *Sci. Amer.*, 276:44, 1997.

[71] A. Cumming, G. W. Marcy, and R. P. Butler. The Lick Planet Search: Detectability and Mass Thresholds. ApJ, 526:890–915, December 1999.

[72] A. D'Aí, R. Iaria, T. Di Salvo, G. Lavagetto, and N. R. Robba. A Complex Environment around Circinus X-1. ApJ, 671:2006–2016, December 2007.

[73] Michael Daniel. *The attenuation of atmospheric Cherenkov photons*. PhD thesis, 2002.

[74] M. de Naurois and H. E. S. S. Collaboration. Application of an Analysis Method Based on a Semi-Analytical Shower Model to the First H.E.S.S. Telescope. In *28th International Cosmic Ray Conference*, volume 5 of *International Cosmic Ray Conference*, page 2907, Tsukuba, July 2003.

[75] C. D. Dermer and M. Böttcher. Gamma Rays from Compton Scattering in the Jets of Microquasars: Application to LS 5039. ApJ, 643:1081–1097, June 2006.

[76] C. D. Dermer and R. Schlickeiser. Model for the High-Energy Emission from Blazars. ApJ, 416:458, October 1993.

[77] C. D. Dermer, S. J. Sturner, and R. Schlickeiser. Nonthermal Compton and Synchrotron Processes in the Jets of Active Galactic Nuclei. ApJS, 109:103, March 1997.

[78] V. Dhawan, W. M. Goss, and L. F. Rodríguez. Small-Scale Structure in Galactic H I Absorption toward GRS 1915+105. ApJ, 540:863–868, September 2000.

[79] V. Dhawan, I. F. Mirabel, and L. F. Rodríguez. AU-Scale Synchrotron Jets and Superluminal Ejecta in GRS 1915+105. ApJ, 543:373–385, November 2000.

[80] G. Q. Ding, J. L. Qu, and T. P. Li. Evolution of Hard X-Ray Spectra along the Branches in Circinus X-1. ApJ, 596:L219–L222, October 2003.

[81] C. Done. Galactic black hole binary systems. *Advances in Space Research*, 28:255–265, 2001.

[82] C. Done, M. Gierliński, and A. Kubota. Modelling the behaviour of accretion flows in X-ray binaries. Everything you always wanted to know about accretion but were afraid to ask. A&A Rev., 15:1–66, December 2007.

[83] C. Done, G. Wardziński, and M. Gierliński. GRS 1915+105: the brightest Galactic black hole. MNRAS, 349:393–403, April 2004.

[84] L. O. Drury, F. A. Aharonian, and H. J. Voelk. The gamma-ray visibility of supernova remnants. A test of cosmic ray origin. A&A, 287:959–971, July 1994.

[85] G. Dubus. Gamma-ray absorption in massive X-ray binaries. A&A, 451:9–18, May 2006.

[86] G. Dubus. Gamma-ray binaries: pulsars in disguise? A&A, 456:801–817, September 2006.

[87] S. S. Eikenberry, K. Matthews, E. H. Morgan, R. A. Remillard, and R. W. Nelson. Evidence for a Disk-Jet Interaction in the Microquasar GRS 1915+105. ApJ, 494:L61+, February 1998.

[88] H. Falcke and P. L. Biermann. The jet-disk symbiosis. I. Radio to X-ray emission models for quasars. A&A, 293:665–682, January 1995.

[89] H. Falcke and P. L. Biermann. The jet/disk symbiosis. III. What the radio cores in GRS 1915+105, NGC 4258, M 81 and SGR A* tell us about accreting black holes. A&A, 342:49–56, February 1999.

[90] G. G. Fazio, H. F. Helmken, E. O'Mongain, and T. C. Weekes. Detection of High-Energy Gamma Rays from the Crab Nebula. ApJ, 175:L117+, August 1972.

[91] D. J. Fegan. γ/hadron separation at TeV energies. *J. Phys. G: Nucl. Part. Phys.*, 23:1013–1060, 1997.

[92] G. J Feldman and R. D Cousins. Unified approach to the classical statistical analysis of small signals. *Phys. Rev*, D57:3837, 1998.

[93] R. Fender. *Jets from X-ray binaries*, pages 381–419. April 2006.

[94] R. Fender and T. Belloni. GRS 1915+105 and the Disc-Jet Coupling in Accreting Black Hole Systems. ARA&A, 42:317–364, September 2004.

[95] R. Fender, R. Spencer, T. Tzioumis, K. Wu, M. van der Klis, J. van Paradijs, and H. Johnston. An Asymmetric Arcsecond Radio Jet from Circinus X-1. ApJ, 506:L121–L125, October 1998.

[96] R. Fender, K. Wu, H. Johnston, T. Tzioumis, P. Jonker, R. Spencer, and M. van der Klis. An ultra-relativistic outflow from a neutron star accreting gas from a companion. Nature, 427:222–224, January 2004.

[97] R. P. Fender, T. M. Belloni, and E. Gallo. Towards a unified model for black hole X-ray binary jets. MNRAS, 355:1105–1118, December 2004.

[98] R. P. Fender, S. T. Garrington, D. J. McKay, T. W. B. Muxlow, G. G. Pooley, R. E. Spencer, A. M. Stirling, and E. B. Waltman. MERLIN observations of relativistic ejections from GRS 1915+105. MNRAS, 304:865–876, April 1999.

[99] R. P. Fender, G. G. Pooley, C. Brocksopp, and S. J. Newell. Rapid infrared flares in GRS 1915+105: evidence for infrared synchrotron emission. MNRAS, 290:L65–L69, October 1997.

[100] J. D. Finke, C. D. Dermer, and M. Böttcher. Synchrotron Self-Compton Analysis of TeV X-Ray-Selected BL Lacertae Objects. ApJ, 686:181–194, October 2008.

[101] S. Funk, G. Hermann, J. Hinton, D. Berge, K. Bernlöhr, W. Hofmann, P. Nayman, F. Toussenel, and P. Vincent. The trigger system of the H.E.S.S. telescope array. *Astroparticle Physics*, 22:285–296, November 2004.

[102] G. Ghisellini, A. Celotti, G. Fossati, L. Maraschi, and A. Comastri. A theoretical unifying scheme for gamma-ray bright blazars. MNRAS, 301:451–468, December 1998.

[103] G. Ghisellini and L. Maraschi. Bulk acceleration in relativistic jets and the spectral properties of blazars. ApJ, 340:181–189, May 1989.

[104] M. Gierliński, C. Done, and K. Page. Reprocessing of X-rays in the outer accretion disc of the black hole binary XTE J1817-330. MNRAS, 392:1106–1114, January 2009.

[105] D. R. Gies and C. T. Bolton. The optical spectrum of HDE 226868 = Cygnus X-1. II Spectrophotometry and mass estimates. ApJ, 304:371–393, May 1986.

[106] V. L. Ginzburg and S. I. Syrovatskii. Developments in the Theory of Synchrotron Radiation and its Reabsorption. ARA&A, 7:375, 1969.

[107] I. S. Glass. Longterm Infrared Behaviour of CIRCINUS-X-1. MNRAS, 268:742, June 1994.

[108] M. Gliozzi, G. Bodo, and G. Ghisellini. The bulk kinetic power of the jets of GRS 1915+105. MNRAS, 303:L37–L40, March 1999.

[109] V. P. Goranskij. GM Sagittarii: Strange Light Changes in a Binary System. *Informational Bulletin on Variable Stars*, 3464:1, May 1990.

[110] W. M. Goss and U. Mebold. The distance of CIR X-1. MNRAS, 181:255–258, November 1977.

[111] R. J. Gould and G. P. Schréder. Pair Production in Photon-Photon Collisions. *Physical Review*, 155:1404–1407, March 1967.

[112] R. M. Green. *Spherical astronomy*. 1985.

[113] P. C. Gregory and A. R. Taylor. New highly variable radio source, possible counterpart of gamma-ray source CG135+1. Nature, 272:704–706, April 1978.

[114] J. Greiner, J. G. Cuby, and M. J. McCaughrean. An unusually massive stellar black hole in the Galaxy. Nature, 414:522–525, November 2001.

[115] J. Greiner, J. G. Cuby, M. J. McCaughrean, A. J. Castro-Tirado, and R. E. Mennickent. Identification of the donor in the X-ray binary GRS 1915+105. A&A, 373:L37–L40, July 2001.

[116] P. W. Guilbert, A. C. Fabian, and M. J. Rees. Spectral and variability constraints on compact sources. MNRAS, 205:593–603, November 1983.

[117] E. T. Harlaftis and J. Greiner. The rotational broadening and the mass of the donor star of GRS 1915+105. A&A, 414:L13–L16, January 2004.

[118] R. C. Hartman, D. L. Bertsch, S. D. Bloom, A. W. Chen, P. Deines-Jones, J. A. Esposito, C. E. Fichtel, D. P. Friedlander, S. D. Hunter, L. M. McDonald, P. Sreekumar, D. J. Thompson, B. B. Jones, Y. C. Lin, P. F. Michelson, P. L. Nolan, W. F. Tompkins, G. Kanbach, H. A. Mayer-Hasselwander, A. Mücke, M. Pohl, O. Reimer, D. A. Kniffen, E. J. Schneid, C. von Montigny, R. Mukherjee, and B. L. Dingus. The Third EGRET Catalog of High-Energy Gamma-Ray Sources. ApJS, 123:79–202, July 1999.

[119] A. Haungs, A. K. Razdan, C. L. Bhat, R. C. Rannot, and H. Rebel. First results on

characterization of Cherenkov images through combined use of Hillas, fractal and wavelet parameters. *Astroparticle Physics*, 12:145–156, November 1999.

[120] S. Heinz, N. S. Schulz, W. N. Brandt, and D. K. Galloway. Evidence of a Parsec-Scale X-Ray Jet from the Accreting Neutron Star Circinus X-1. ApJ, 663:L93–L96, July 2007.

[121] W. Hermsen, B. N. Swanenburg, G. F. Bignami, G. Boella, R. Buccheri, L. Scarsi, G. Kanbach, H. A. Mayer-Hasselwander, J. L. Masnou, and J. A. Paul. New high energy gamma-ray sources observed by COS B. Nature, 269:494, October 1977.

[122] V. F. Hess. Beobachtungen der durchdringenden Strahlung bei sieben Freiballonfahrten. *Sitzungsberichte der mathematisch-naturw*, pages 2001–2032, 1912.

[123] H.E.S.S. Collaboration, F. Acero, F. Aharonian, A. G. Akhperjanian, G. Anton, U. Barres de Almeida, A. R. Bazer-Bachi, Y. Becherini, B. Behera, K. Bernlöhr, A. Bochow, C. Boisson, J. Bolmont, V. Borrel, J. Brucker, F. Brun, P. Brun, T. Bulik, I. Büsching, T. Boutelier, P. M. Chadwick, A. Charbonnier, R. C. G. Chaves, A. Cheesebrough, J. Conrad, L.-M. Chounet, A. C. Clapson, G. Coignet, M. Dalton, M. K. Daniel, I. D. Davids, B. Degrange, C. Deil, H. J. Dickinson, A. Djannati-Ataï, W. Domainko, L. O. Drury, F. Dubois, G. Dubus, J. Dyks, M. Dyrda, K. Egberts, P. Eger, P. Espigat, L. Fallon, C. Farnier, S. Fegan, F. Feinstein, A. Fiasson, A. Förster, G. Fontaine, M. Füßling, S. Gabici, Y. A. Gallant, L. Gérard, D. Gerbig, B. Giebels, J. F. Glicenstein, B. Glück, P. Goret, D. Göring, M. Hauser, S. Heinz, G. Heinzelmann, G. Henri, G. Hermann, J. A. Hinton, A. Hoffmann, W. Hofmann, P. Hofverberg, M. Holleran, S. Hoppe, D. Horns, A. Jacholkowska, O. C. de Jager, C. Jahn, I. Jung, K. Katarzyński, U. Katz, S. Kaufmann, M. Kerschhaggl, D. Khangulyan, B. Khélifi, D. Keogh, D. Klochkov, W. Kluźniak, T. Kneiske, N. Komin, K. Kosack, R. Kossakowski, G. Lamanna, J.-P. Lenain, T. Lohse, V. Marandon, A. Marcowith, J. Masbou, D. Maurin, T. J. L. McComb, M. C. Medina, J. Méhault, R. Moderski, E. Moulin, M. Naumann-Godo, M. de Naurois, D. Nedbal, D. Nekrassov, B. Nicholas, J. Niemiec, S. J. Nolan, S. Ohm, J.-F. Olive, E. de Oña Wilhelmi, K. J. Orford, M. Ostrowski, M. Panter, M. Paz Arribas,

G. Pedaletti, G. Pelletier, P.-O. Petrucci, S. Pita, G. Pühlhofer, M. Punch, A. Quirrenbach, B. C. Raubenheimer, M. Raue, S. M. Rayner, O. Reimer, M. Renaud, R. de Los Reyes, F. Rieger, J. Ripken, L. Rob, S. Rosier-Lees, G. Rowell, B. Rudak, C. B. Rulten, J. Ruppel, F. Ryde, V. Sahakian, A. Santangelo, R. Schlickeiser, F. M. Schöck, A. Schönwald, U. Schwanke, S. Schwarzburg, S. Schwemmer, A. Shalchi, I. Sushch, M. Sikora, J. L. Skilton, H. Sol, Ł. Stawarz, R. Steenkamp, C. Stegmann, F. Stinzing, G. Superina, A. Szostek, P. H. Tam, J.-P. Tavernet, R. Terrier, O. Tibolla, M. Tluczykont, C. van Eldik, G. Vasileiadis, C. Venter, L. Venter, J. P. Vialle, P. Vincent, M. Vivier, H. J. Völk, F. Volpe, S. Vorobiov, S. J. Wagner, M. Ward, A. A. Zdziarski, and A. Zech. H.E.S.S. upper limits on very high energy gamma-ray emission from the microquasar GRS 1915+105. A&A, 508:1135–1140, December 2009.

[124] A. M. Hillas. Cerenkov light images of EAS produced by primary gamma. *NASA. Goddard Space Flight Center 19th Intern. Cosmic Ray Conf., Vol. 3 p 445-448 (SEE N85-34862 23-93)*, 3:445–448, August 1985.

[125] J. A. Hinton, J. L. Skilton, S. Funk, J. Brucker, F. A. Aharonian, G. Dubus, A. Fiasson, Y. Gallant, W. Hofmann, A. Marcowith, and O. Reimer. HESS J0632+057: A New Gamma-Ray Binary? ApJ, 690:L101–L104, January 2009.

[126] R. M. Hjellming. Recurrence of Radio Counterpart of V4641 Sgr (=XTE J1819-254). *The Astronomer's Telegram*, 61:1, July 2000.

[127] R. M. Hjellming, M. P. Rupen, R. W. Hunstead, D. Campbell-Wilson, A. J. Mioduszewski, B. M. Gaensler, D. A. Smith, R. J. Sault, R. P. Fender, R. E. Spencer, C. J. de la Force, A. M. S. Richards, S. T. Garrington, S. A. Trushkin, F. D. Ghigo, E. B. Waltman, and M. McCollough. Light Curves and Radio Structure of the 1999 September Transient Event in V4641 Sagittarii (=XTE J1819-254=SAX J1819.3-2525). ApJ, 544:977–992, December 2000.

[128] W. Hofmann and H. E. S. S. Collaboration. Status of the H.E.S.S. Project. In *International Cosmic Ray Conference*, volume 5 of *International Cosmic Ray Conference*, page 2811, July 2003.

[129] J. R. Hörandel. Models of the knee in the energy spectrum of cosmic rays. *Astroparticle Physics*, 21:241–265, June 2004.

[130] J. H. Horne and S. L. Baliunas. A prescription for period analysis of unevenly sampled time series. ApJ, 302:757–763, March 1986.

[131] R. Iaria, L. Burderi, T. Di Salvo, A. La Barbera, and N. R. Robba. A Hard Tail in the X-Ray Broadband Spectrum of Circinus X-1 at the Periastron: A Peculiar Z Source. ApJ, 547:412–419, January 2001.

[132] R. Iaria, A. D'Aí, G. Lavagetto, T. Di Salvo, N. R. Robba, and L. Burderi. Chandra Observation of Cir X-1 near the Periastron Passage: Evidence for an X-Ray Jet? ApJ, 673:1033–1043, February 2008.

[133] R. Iaria, T. Di Salvo, L. Burderi, and N. R. Robba. Spectral Evolution of Circinus X-1 along Its Orbit. ApJ, 561:321–328, November 2001.

[134] R. Iaria, M. Spanò, T. Di Salvo, N. R. Robba, L. Burderi, R. Fender, M. van der Klis, and F. Frontera. On the Soft Excess in the X-Ray Spectrum of Circinus X-1: Revisitation of the Distance to Circinus X-1. ApJ, 619:503–516, January 2005.

[135] J. in 't Zand, J. Heise, A. Bazzano, M. Cocchi, L. di Ciolo, and J. M. Muller. SAX J1819.3-2525. IAU Circ., 7119:1, March 1999.

[136] K. Jahoda, C. B. Markwardt, Y. Radeva, A. H. Rots, M. J. Stark, J. H. Swank, T. E. Strohmayer, and W. Zhang. Calibration of the Rossi X-Ray Timing Explorer Proportional Counter Array. ApJS, 163:401–423, April 2006.

[137] J. M. Jauch and F. Rohrlich. *The theory of photons and electrons. The relativistic quantum field theory of charged particles with spin one-half.* Springer Verlag, 1976.

[138] H. M. Johnston, R. Fender, and K. Wu. High-resolution optical and infrared spectroscopic observations of CIR X-1. MNRAS, 308:415–423, September 1999.

[139] H. M. Johnston, K. Wu, R. Fender, and J. G. Cullen. Secular and orbital variability of Cir X-1 observed in optical spectra. MNRAS, 328:1193–1199, December 2001.

[140] F. C. Jones. Calculated Spectrum of Inverse-Compton-Scattered Photons. *Physical Review*, 167:1159–1169, March 1968.

[141] P. G. Jonker and G. Nelemans. The distances to Galactic low-mass X-ray binaries: consequences for black hole luminosities and kicks. MNRAS, 354:355–366, October 2004.

[142] P. G. Jonker, G. Nelemans, and C. G. Bassa. Detection of the radial velocity curve of the B5-A0 supergiant companion star of Cir X-1? MNRAS, 374:999–1005, January 2007.

[143] C. R. Kaiser, K. F. Gunn, C. Brocksopp, and J. L. Sokoloski. Revision of the Properties of the GRS 1915+105 Jets: Clues from the Large-Scale Structure. ApJ, 612:332–341, September 2004.

[144] P. M. W. Kalberla, W. B. Burton, D. Hartmann, E. M. Arnal, E. Bajaja, R. Morras, and W. G. L. Pöppel. The Leiden/Argentine/Bonn (LAB) Survey of Galactic HI. Final data release of the combined LDS and IAR surveys with improved stray-radiation corrections. A&A, 440:775–782, September 2005.

[145] L. J. Kaluzienski, S. S. Holt, E. A. Boldt, and P. J. Serlemitsos. Evidence for a 16.6 day period from Circinus X-1. ApJ, 208:L71–L75, September 1976.

[146] N. S. Kardashev. Nonstationarity of Spectra of Young Sources of Nonthermal Radio Emission. *Soviet Astronomy*, 6:317, December 1962.

[147] T. Kato, M. Uemura, R. Stubbings, T. Watanabe, and B. Monard. Preoutburst Activity of V4641 Sgr = SAX J1819.3-2525: Possible Existence of 2.5-Day Period. *Information Bulletin on Variable Stars*, 4777:1, October 1999.

[148] D. Khangulyan, F. Aharonian, and V. Bosch-Ramon. On the formation of TeV radiation in LS 5039. MNRAS, 383:467–478, January 2008.

[149] L. Kiss and S. Meszaros. Optical spectroscopy of V4641 Sgr. *The Astronomer's Telegram*, 299:1, July 2004.

[150] M. Klein-Wolt, R. P. Fender, G. G. Pooley, T. Belloni, S. Migliari, E. H. Morgan, and M. van der Klis. Hard X-ray states and radio emission in GRS 1915+105. MNRAS, 331:745–764, April 2002.

[151] A. Konigl. Relativistic jets as X-ray and gamma-ray sources. ApJ, 243:700–709, February 1981.

[152] D. A. Leahy, W. Darbro, R. F. Elsner, M. C. Weisskopf, S. Kahn, P. G. Sutherland, and J. E. Grindlay. On searches for pulsed emission with application to four globular cluster X-ray sources - NGC 1851, 6441, 6624, and 6712. ApJ, 266:160–170, March 1983.

[153] J. C. Lee, C. S. Reynolds, R. Remillard, N. S. Schulz, E. G. Blackman, and A. C. Fabian. High-Resolution Chandra HETGS and Rossi X-Ray Timing Explorer Observations of GRS 1915+105: A Hot Disk Atmosphere and Cold Gas Enriched in Iron and Silicon. ApJ, 567:1102–1111, March 2002.

[154] W. H. G. Lewin, J. van Paradijs, and E. P. J. van den Heuvel. *X-ray Binaries*. January 1997.

[155] W. H. G. Lewin, J. van Paradijs, and M. van der Klis. A review of quasi-periodic oscillations in low-mass X-ray binaries. *Space Science Reviews*, 46:273–378, September 1988.

[156] T.-P. Li and Y.-Q. Ma. Analysis methods for results in gamma-ray astronomy. ApJ, 272:317–324, September 1983.

[157] C. Lindstrøm, J. Griffin, L. L. Kiss, M. Uemura, A. Derekas, S. Mészáros, and P. Székely. New clues on outburst mechanisms and improved spectroscopic elements of the black hole binary V4641 Sagittarii*. MNRAS, 363:882–890, November 2005.

[158] Q. Z. Liu, J. van Paradijs, and E. P. J. van den Heuvel. A catalogue of high-mass X-ray binaries. A&AS, 147:25–49, November 2000.

[159] Q. Z. Liu, J. van Paradijs, and E. P. J. van den Heuvel. A catalogue of low-mass X-ray binaries. A&A, 368:1021–1054, March 2001.

[160] Q. Z. Liu, J. van Paradijs, and E. P. J. van den Heuvel. Catalogue of high-mass X-ray binaries in the Galaxy (4th edition). A&A, 455:1165–1168, September 2006.

[161] Q. Z. Liu, J. van Paradijs, and E. P. J. van den Heuvel. A catalogue of low-mass X-ray binaries in the Galaxy, LMC, and SMC (Fourth edition). A&A, 469:807–810, July 2007.

[162] N. R. Lomb. Least-squares frequency analysis of unequally spaced data. Ap&SS, 39:447–462, February 1976.

[163] M. S. Longair. *High Energy Astrophysics*, volume 2. Cambridge University Press, 2004.

[164] M. S. Longair. *High Energy Astrophysics*, volume 1. Cambridge University Press, 2004.

[165] D. Maitra and C. D. Bailyn. X-Ray Observations of V4641 SGR (SAX J1819.3-2525) during the Brief and Violent Outburst of 2003. ApJ, 637:992–1001, February 2006.

[166] J. Malzac, P. Lubiński, A. A. Zdziarski, M. Cadolle Bel, M. Türler, and P. Laurent. An intense state of hard X-ray emission of Cyg X-1 observed by INTEGRAL coincident with TeV measurements. A&A, 492:527–534, December 2008.

[167] L. Maraschi and A. Treves. A model for LSI61 deg 303. MNRAS, 194:1P–5P, January 1981.

[168] B. Margon, M. Lampton, S. Bowyer, and R. Cruddace. A Pulsing X-Ray Source in Circinus. ApJ, 169:L23, October 1971.

[169] C. B. Markwardt and J. H. Swank. Sax J1819.3-2525. IAU Circ., 7906:3, May 2002.

[170] C. B. Markwardt, J. H. Swank, and E. H. Morgan. GM Sagittarii and SAX J1819.3-2525 = XTE J1819-254. IAU Circ., 7257:2, September 1999.

[171] J. Marti, J. M. Paredes, and M. Ribo. The system LS 5039: a new massive radio emitting X-ray binary. A&A, 338:L71–L74, October 1998.

[172] A. Martocchia, C. Motch, and I. Negueruela. The low X-ray state of LS 5039 / RX J1826.2-1450. A&A, 430:245–253, January 2005.

[173] A. Mastichiadis. Radiative Processes in Relativistic Outflows. In A. W. Guthmann, M. Georganopoulos, A. Marcowith, & K. Manolakou , editor, *Relativistic Flows in Astrophysics*, volume 589 of *Lecture Notes in Physics, Berlin Springer Verlag*, page 1, 2002.

[174] D. Mazin and M. Raue. New limits on the density of the extragalactic background light in the optical to the far infrared from the spectra of all known TeV blazars. A&A, 471:439–452, August 2007.

[175] M. L. McCollough, M. H. Finger, and P. M. Woods. GM Sagittarii and SAX J1819.3-2525 = XTE J1819-254. IAU Circ., 7257:1, September 1999.

[176] M. V. McSwain and D. R. Gies. Wind Accretion and Binary Evolution of the Microquasar LS 5039. ApJ, 568:L27–L30, March 2002.

[177] A. Merloni, T. Di Matteo, and A. C. Fabian. Magnetic flares and the optical variability of the X-ray transient XTE J1118+480. MNRAS, 318:L15–L19, October 2000.

[178] R. P. Mignani, A. De Luca, P. A. Caraveo, and I. F. Mirabel. HST observations rule out the association between Cir X-1 and SNR G321.9-0.3. A&A, 386:487–491, May 2002.

[179] G. Miley and B. Margon. A search for extended radio emission around the nearby X-ray QSO 0241 + 622. A&A, 79:360, November 1979.

[180] I. F. Mirabel and L. F. Rodriguez. A Superluminal Source in the Galaxy. Nature, 371:46, September 1994.

[181] I. F. Mirabel and L. F. Rodríguez. Sources of Relativistic Jets in the Galaxy. ARA&A, 37:409–443, 1999.

[182] G. Mohanty, S. Biller, D. A. Carter-Lewis, D. J. Fegan, A. M. Hillas, R. C. Lamb, T. C. Weekes, M. West, and J. Zweerink. Measurement of TeV gamma-ray spectra with the Cherenkov imaging technique. *Astroparticle Physics*, 9:15–43, June 1998.

[183] A. Moneti. Optical and infrared observations of Circinus X-1. A&A, 260:L7–L10, July 1992.

[184] C. Motch, F. Haberl, K. Dennerl, M. Pakull, and E. Janot-Pacheco. New massive X-ray binary candidates from the ROSAT Galactic Plane Survey. I. Results from a cross-correlation with OB star catalogues. A&A, 323:853–875, July 1997.

[185] A. Mücke and R. J. Protheroe. A proton synchrotron blazar model for flaring in Markarian 501. *Astroparticle Physics*, 15:121–136, March 2001.

[186] P. Murdin, D. L. Jauncey, I. Lerche, G. D. Nicolson, L. J. Kaluzienski, S. S. Holt, and R. F. Haynes. Binary model of Circinus X-1. I - Eccentricity from combined X-ray and radio observations. A&A, 87:292–298, July 1980.

[187] B. Nicholas and G. Rowell. H.E.S.S Observations of the Microquasars Cir X-1, Cyg X-1 and 4U 1755-33. In F. A. Aharonian, W. Hofmann, & F. Rieger, editor, *American Institute of Physics Conference Series*, volume 1085 of *American Institute of Physics Conference Series*, pages 245–248, December 2008.

[188] G. D. Nicolson. Circinus X-1 – Return to high radio flaring state. *The Astronomer's Telegram*, 985:1, January 2007.

[189] S. J. Nolan, G. Pühlhofer, and P. M. Chadwick. Active Atmospheric Calibration for H.E.S.S. Applied to PKS 2155-304. In *30th International Cosmic Ray Conference*, volume 3 of *International Cosmic Ray Conference*, pages 1009–1012, Mérida, 2008.

[190] A. V. Olinto. The Highest Energy Cosmic Rays. In *AIP Conf. Proc. 745: High Energy Gamma-Ray Astronomy*, pages 48–59, February 2005.

[191] T. Oosterbroek, M. van der Klis, E. Kuulkers, J. van Paradijs, and W. H. G. Lewin. Circinus X-1 revisited: Fast-timing properties in relation to spectral state. A&A, 297:141–158, May 1995.

[192] J. A. Orosz, E. Kuulkers, M. van der Klis, J. E. McClintock, M. R. Garcia, P. J. Callanan, C. D. Bailyn, R. K. Jain, and R. A. Remillard. A Black Hole in the Superluminal Source SAX J1819.3-2525 (V4641 Sgr). ApJ, 555:489–503, July 2001.

[193] J. M. Paredes, J. Martí, M. Ribó, and M. Massi. Discovery of a High-Energy Gamma-Ray-Emitting Persistent Microquasar. *Science*, 288:2340–2342, June 2000.

[194] J. M. Paredes, M. Ribó, E. Ros, J. Martí, and M. Massi. Confirmation of persistent radio jets in the microquasar ¡ASTROBJ¿LS 5039¡/ASTROBJ¿. A&A, 393:L99–L102, October 2002.

[195] P. M. S. Parkinson, D. M. Tournear, E. D. Bloom, W. B. Focke, K. T. Reilly, K. S. Wood, P. S. Ray, M. T. Wolff, and J. D. Scargle. Long-Term X-Ray Variability of Circinus X-1. ApJ, 595:333–341, September 2003.

[196] M. Prouza and R. Šmída. The Galactic magnetic field and propagation of ultra-high energy cosmic rays. A&A, 410:1–10, October 2003.

[197] M. Punch, C. W. Akerlof, M. F. Cawley, M. Chantell, D. J. Fegan, S. Fennell, J. A. Gaidos, J. Hagan, A. M. Hillas, Y. Jiang, A. D. Kerrick, R. C. Lamb, M. A. Lawrence, D. A. Lewis, D. I. Meyer, G. Mohanty, K. S. O'Flaherty, P. T. Reynolds, A. C. Rovero, M. S. Schubnell,

G. Sembroski, T. C. Weekes, and C. Wilson. Detection of TeV photons from the active galaxy Markarian 421. Nature, 358:477, August 1992.

[198] M. J. Rees. Appearance of Relativistically Expanding Radio Sources. Nature, 211:468–470, July 1966.

[199] P. Reig, M. Ribó, J. M. Paredes, and J. Martí. Long-term X-ray variability of the microquasar system LS 5039/RX J1826.2-1450. A&A, 405:285–290, July 2003.

[200] R. A. Remillard and J. E. McClintock. X-Ray Properties of Black-Hole Binaries. ARA&A, 44:49–92, September 2006.

[201] M. Revnivtsev, M. Gilfanov, and E. Churazov. High frequencies in the power spectrum of Cyg X-1 in the hard and soft spectral states. A&A, 363:1013–1018, November 2000.

[202] M. Revnivtsev, M. Gilfanov, E. Churazov, and R. Sunyaev. Super-Eddington outburst of V4641 Sgr. A&A, 391:1013–1022, September 2002.

[203] M. Revnivtsev, I. Khamitov, R. Burenin, M. Pavlinsky, R. Sunyaev, Z. Aslan, I. Bikmaev, and N. Sakhibullin. Optical observations of V4641 Sgr. *The Astronomer's Telegram*, 297:1, July 2004.

[204] M. Ribó. *Discovery and study of the microquasar LS 5039 and a search for new microquasars*. PhD thesis, AA(Departament d'Astronomia i Meteorologia, Universitat de Barcelona, Av. Diagonal 647, E-08028 Barcelona, Spain), 2002.

[205] M. Ribó. Microquasars. In J. Romney and M. Reid, editors, *ASP Conf. Ser. 340: Future Directions in High Resolution Astronomy*, page 269, December 2005.

[206] M. Ribó, P. Reig, J. Martí, and J. M. Paredes. X-ray and radio observations of RX J1826.2-1450/LS 5039. A&A, 347:518–523, July 1999.

[207] G. E. Romero, H. R. Christiansen, and M. Orellana. Hadronic High-Energy Gamma-Ray Emission from the Microquasar LS I +61 303. ApJ, 632:1093–1098, October 2005.

[208] G. E. Romero, D. F. Torres, M. M. Kaufman Bernadó, and I. F. Mirabel. Hadronic gamma-ray emission from windy microquasars. A&A, 410:L1–L4, October 2003.

[209] G. E. Romero, D. F. Torres, M. M. Kaufman Bernadó, and I. F. Mirabel. Hadronic gamma-ray emission from windy microquasars. A&A, 410:L1–L4, October 2003.

[210] H. J. Rose. Cherenkov Telescope Calibration using Muon Ring Images. In *24th International Cosmic Ray Conference*, volume 3 of *International Cosmic Ray Conference*, page 464, Rome, 1995.

[211] G. P. Rowell. A new template background estimate for source searching in TeV gamma -ray astronomy. A&A, 410:389–396, October 2003.

[212] M. P. Rupen, V. Dhawan, and A. J. Mioduszewski. V4641 Sagittarii. IAU Circ., 7928:2, June 2002.

[213] M. P. Rupen, V. Dhawan, and A. J. Mioduszewski. Further radio observations of V4641 Sgr (= SAX J1819.3-2525). *The Astronomer's Telegram*, 175:1, August 2003.

[214] M. P. Rupen, V. Dhawan, and A. J. Mioduszewski. V4641 Sgr: continued radio flaring. *The Astronomer's Telegram*, 303:1, July 2004.

[215] M. P. Rupen, A. J. Mioduszewski, and V. Dhawan. Strong radio flare in V4641 Sgr (= SAX J1819.3-2525). *The Astronomer's Telegram*, 172:1, August 2003.

[216] M. P. Rupen, A. J. Mioduszewski, and V. Dhawan. Radio Reappearance of V4641 Sgr. *The Astronomer's Telegram*, 296:1, July 2004.

[217] D. M. Russell, R. P. Fender, R. I. Hynes, C. Brocksopp, J. Homan, P. G. Jonker, and M. M. Buxton. Global optical/infrared-X-ray correlations in X-ray binaries: quantifying disc and jet contributions. MNRAS, 371:1334–1350, September 2006.

[218] G. B. Rybicki and A. P. Lightman. *Radiative Processes in Astrophysics*. John Wiley & Sons, Inc., 1979.

[219] J. D. Scargle. Studies in astronomical time series analysis. II - Statistical aspects of spectral analysis of unevenly spaced data. ApJ, 263:835–853, December 1982.

[220] J. D. Scargle. Studies in Astronomical Time Series Analysis. V. Bayesian Blocks, a New Method to Analyze Structure in Photon Counting Data. ApJ, 504:405, September 1998.

[221] V. Schönfelder. *The Universe in Gamma Rays*. 2001.

[222] N. S. Schulz and W. N. Brandt. Variability of the X-Ray P Cygni Line Profiles from Circinus X-1 near Zero Phase. ApJ, 572:971–983, June 2002.

[223] N. S. Schulz, T. E. Kallman, D. K. Galloway, and W. N. Brandt. The Variable Warm Absorber in Circinus X-1. ApJ, 672:1091–1102, January 2008.

[224] A. Schwarzenberg-Czerny. Period Search in Large Datasets. *Baltic Astronomy*, 7:43–69, March 1998.

[225] A. Schwarzenberg-Czerny. An astronomer's guide to period searching. In C. Sterken, editor, *Interplay of Periodic, Cyclic and Stochastic Variability in Selected Areas of the H-R Diagram*, volume 292 of *Astronomical Society of the Pacific Conference Series*, page 383, March 2003.

[226] C. Senkbeil and B. Sault. Radio observations of V4641 Sgr at 6 and 3 cm. *The Astronomer's Telegram*, 302:1, July 2004.

[227] R. E. Shirey, H. V. Bradt, and A. M. Levine. The Complete "Z" Track of Circinus X-1. ApJ, 517:472–487, May 1999.

[228] R. E. Shirey, H. V. Bradt, A. M. Levine, and E. H. Morgan. Absorption Dips and QPOs in the Eccentric Neutron-star Binary Circinus X-1. *Bulletin of the American Astronomical Society*, 30:1288, December 1998.

[229] R. E. Shirey, A. M. Levine, and H. V. Bradt. Scattering and Iron Fluorescence Revealed during Absorption Dips in Circinus X-1. ApJ, 524:1048–1058, October 1999.

[230] J. L. Skilton, M. Pandey-Pommier, J. A. Hinton, C. C. Cheung, F. A. Aharonian, J. Brucker, G. Dubus, A. Fiasson, S. Funk, Y. Gallant, A. Marcowith, and O. Reimer. The radio counterpart of the likely TeV binary HESSJ0632+057. MNRAS, 399:317–322, October 2009.

[231] P. Soleri, V. Tudose, R. P. Fender, and M. van der Klis. Simultaneous X-ray/Radio Observations of Cir X-1. In *Proceedings of "Bursts, Pulses and Flickering: wide-field monitoring of the dynamic radio sky". 12-15 June 2007, Kerastari, Tripolis, Greece., p.37*, 2007.

[232] R. T. Stewart, J. L. Caswell, R. F. Haynes, and G. J. Nelson. Circinus X-1 - A runaway binary with curved radio jets. MNRAS, 261:593–598, April 1993.

[233] R. Stubbings and A. Pearce. GM Sagittarii and SAX J1819.3-2525 = XTE J1819-254. IAU Circ., 7253:1, September 1999.

[234] J. Swank. X-ray Reappearance of V4641 Sgr. *The Astronomer's Telegram*, 295:1, July 2004.

[235] G. Taubes. Pattern Emerges in Cosmic Ray Mystery. *Science*, 262:1649, December 1993.

[236] A. F. Tennant, A. C. Fabian, and R. A. Shafer. Observation of type I X-ray bursts from CIR X-1. MNRAS, 221:27P–31P, July 1986.

[237] A. F. Tennant, A. C. Fabian, and R. A. Shafer. The discovery of X-ray bursts from CIR X-1. MNRAS, 219:871–881, April 1986.

[238] A. Toor. Millisecond X-ray bursts from Circinus X-1. ApJ, 215:L57–L60, July 1977.

[239] S. P. Trudolyubov. On the Two Types of Steady Hard X-Ray States of GRS 1915+105. ApJ, 558:276–282, September 2001.

[240] V. Tudose, R. P. Fender, C. R. Kaiser, A. K. Tzioumis, M. van der Klis, and R. E. Spencer. The large-scale jet-powered radio nebula of Circinus X-1. MNRAS, 372:417–424, October 2006.

[241] V. Tudose, R. P. Fender, M. Linares, D. Maitra, and M. van der Klis. The disc-jet coupling in the neutron star X-ray binary Aquila X-1. MNRAS, page 1465, October 2009.

[242] V. Tudose, R. P. Fender, A. K. Tzioumis, R. E. Spencer, and M. van der Klis. A decade of radio imaging the relativistic outflow in the peculiar X-ray binary Circinus X-1. MNRAS, 390:447–464, October 2008.

[243] M. van der Klis. *Rapid X-ray Variability*, pages 39–112. Cambridge University Press, April 2006.

[244] J. van Paradijs and J. E. McClintock. Absolute visual magnitudes of low-mass X-ray binaries. A&A, 290:133–136, October 1994.

[245] O. Vilhu. Mass transfer from the donor of GRS 1915+105. A&A, 388:936–939, June 2002.

[246] T. C. Weekes. *Very high energy gamma-ray astronomy*. 2003.

[247] T. C. Weekes, M. F. Cawley, D. J. Fegan, K. G. Gibbs, A. M. Hillas, P. W. Kowk, R. C. Lamb, D. A. Lewis, D. Macomb, N. A. Porter, P. T. Reynolds, and G. Vacanti. Observation of TeV gamma rays from the Crab nebula using the atmospheric Cerenkov imaging technique. ApJ, 342:379–395, July 1989.

[248] J. A. J. Whelan, S. K. Mayo, D. T. Wickramasinghe, P. G. Murdin, B. A. Peterson, T. G. Hawarden, A. J. Longmore, R. F. Haynes, W. M. Goss, L. W. Simons, J. L. Caswell, A. G. Little, and W. B. McAdam. The optical and radio counterpart of Circinus X-1 /3U 1516-56/. MNRAS, 181:259–271, November 1977.

[249] A. A. Zdziarski, M. Gierliński, A. R. Rao, S. V. Vadawale, and J. Mikołajewska. GRS 1915+105: the distance, radiative processes and energy-dependent variability. MNRAS, 360:825–838, July 2005.

[250] A. A. Zdziarski, J. E. Grove, J. Poutanen, A. R. Rao, and S. V. Vadawale. OSSE and

RXTE Observations of GRS 1915+105: Evidence for Nonthermal Comptonization. ApJ, 554:L45–L48, June 2001.

[251] M. Zechmeister and M. Kürster. The generalised Lomb-Scargle periodogram. A new formalism for the floating-mean and Keplerian periodograms. A&A, 496:577–584, March 2009.

[252] W. Zhang, A. B. Giles, K. Jahoda, Y. Soong, J. H. Swank, and E. H. Morgan. Laboratory performance of the proportional counter array experiment for the X-ray Timing Explorer. In O. H. Siegmund, editor, *Society of Photo-Optical Instrumentation Engineers (SPIE) Conference Series*, volume 2006 of *Society of Photo-Optical Instrumentation Engineers (SPIE) Conference Series*, pages 324–333, November 1993.